2026 • 30 • 6

Online ISSN 2500-3259

Сетевое издание

ВАВИЛОВСКИЙ ЖУРНАЛ ГЕНЕТИКИ И СЕЛЕКЦИИ

VAVILOV JOURNAL OF GENETICS AND BREEDING

Основан в 1997 г.
Периодичность 8 выпусков в год
doi 10.18699/vjgb-26-85

Учредители

Сибирское отделение Российской академии наук

Федеральное государственное бюджетное научное учреждение «Федеральный исследовательский центр Институт цитологии и генетики Сибирского отделения Российской академии наук»

Межрегиональная общественная организация Вавиловское общество генетиков и селекционеров

Главный редактор

А.В. Кочетов – академик РАН, д-р биол. наук, профессор РАН (Россия)

Заместители главного редактора

Н.А. Колчанов – академик РАН, д-р биол. наук, профессор (Россия)
И.Н. Леонова – д-р биол. наук (Россия)
Н.Б. Рубцов – д-р биол. наук, профессор (Россия)

Ответственный секретарь

Г.В. Орлова – канд. биол. наук (Россия)

Редакционная коллегия

Е.Е. Андронов – д-р биол. наук (Россия)
Ю.С. Аульченко – д-р биол. наук (Великобритания)
О.С. Афанасенко – академик РАН, д-р биол. наук (Россия)
Д.А. Афонников – д-р биол. наук, доцент (Россия)
Л.И. Афтанас – академик РАН, д-р мед. наук (Россия)
Л.А. Беспалова – академик РАН, д-р с.-х. наук (Россия)
А. Бёрнер – д-р наук (Германия)
Н.П. Бондарь – канд. биол. наук (Россия)
П.М. Бородин – д-р биол. наук, проф. (Россия)
А.В. Васильев – чл.-кор. РАН, д-р биол. наук (Россия)
М.И. Воевода – академик РАН, д-р мед. наук (Россия)
Т.А. Гавриленко – д-р биол. наук (Россия)
Н.Е. Грунтенко – д-р биол. наук (Россия)
С.А. Демаков – д-р биол. наук (Россия)
И.К. Захаров – д-р биол. наук, проф. (Россия)
И.А. Захаров-Гезехус – чл.-кор. РАН, д-р биол. наук (Россия)
С.Г. Инге-Вечтомов – академик РАН, д-р биол. наук (Россия)
А.В. Кильчевский – академик НАНБ, д-р биол. наук (Беларусь)
Б.Р. Кулуев – д-р биол. наук (Россия)
Д.М. Ларкин – канд. биол. наук (Великобритания)
С.А. Лашин – д-р биол. наук (Россия)
Ж. Ле Гуи – д-р наук (Франция)
И.Н. Лебедев – чл.-кор. РАН, д-р биол. наук, проф. (Россия)
Л.А. Лутова – д-р биол. наук, проф. (Россия)
В.Ю. Макеев – чл.-кор. РАН, д-р физ.-мат. наук (Россия)
И.В. Максимов – д-р биол. наук (Россия)
Б.А. Малярчук – д-р биол. наук (Россия)
Ю.Г. Матушкин – канд. биол. наук (Россия)
С.П. Медведев – канд. биол. наук (Россия)
В.И. Молодин – академик РАН, д-р ист. наук (Россия)
М.П. Мошкин – д-р биол. наук, проф. (Россия)
Л.Ю. Новикова – д-р с.-х. наук (Россия)
Е.К. Потокина – д-р биол. наук (Россия)
В.П. Пузырев – академик РАН, д-р мед. наук (Россия)
Д.В. Пышный – чл.-кор. РАН, д-р хим. наук (Россия)
Е.Ю. Рыкова – д-р биол. наук (Россия)
Е.А. Салина – чл.-кор. РАН, д-р биол. наук, проф. (Россия)
В.А. Степанов – академик РАН, д-р биол. наук (Россия)
И.А. Тихонович – академик РАН, д-р биол. наук (Россия)
Е.К. Хлесткина – чл.-кор. РАН, д-р биол. наук, проф. РАН (Россия)
Э.К. Хуснутдинова – чл.-кор. РАО, академик АН Республики Башкортостан, д-р биол. наук (Россия)
М. Чен – д-р биол. наук (Китайская Народная Республика)
Е.В. Шахтшнейдер – д-р мед. наук (Россия)
С.В. Шестаков – академик РАН, д-р биол. наук (Россия)
С.В. Шеховцов – д-р биол. наук (Россия)
Н.С. Юдин – канд. биол. наук (Россия)
Н.К. Янковский – академик РАН, д-р биол. наук (Россия)

2026 • 30 • 6

Online ISSN 2500-3259

Online edition

VAVILOVSKII ZHURNAL GENETIKI I SELEKTSII

VAVILOV JOURNAL OF GENETICS AND BREEDING

Founded in 1997
Publication frequency: 8 issues a year
doi 10.18699/vjgb-26-85

Founders

Siberian Branch of the Russian Academy of Sciences

Federal Research Center Institute of Cytology and Genetics of the Siberian Branch of the Russian Academy of Sciences

The Vavilov Society of Geneticists and Breeders

Editor-in-Chief

A.V. Kochetov, Full Member of the Russian Academy of Sciences, Dr. Sci. (Biology), Professor of the RAS, Russia

Deputy Editor-in-Chief

N.A. Kolchanov, Full Member of the Russian Academy of Sciences, Dr. Sci. (Biology), Russia
I.N. Leonova, Dr. Sci. (Biology), Russia
N.B. Rubtsov, Professor, Dr. Sci. (Biology), Russia

Executive Secretary

G.V. Orlova, Cand. Sci. (Biology), Russia

Editorial board

O.S. Afanasenko, Full Member of the RAS, Dr. Sci. (Biology), Russia
D.A. Afonnikov, Associate Professor, Dr. Sci. (Biology), Russia
L.I. Aftanas, Full Member of the RAS, Dr. Sci. (Medicine), Russia
E.E. Andronov, Dr. Sci. (Biology), Russia
Yu.S. Aulchenko, Dr. Sci. (Biology), United Kingdom
L.A. Bespalova, Full Member of the RAS, Dr. Sci. (Agricul.), Russia
N.P. Bondar, Cand. Sci. (Biology), Russia
P.M. Borodin, Professor, Dr. Sci. (Biology), Russia
A. Börner, Dr. Sci., Germany
M. Chen, Dr. Sci. (Biology), People's Republic of China
S.A. Demakov, Dr. Sci. (Biology), Russia
T.A. Gavrilenko, Dr. Sci. (Biology), Russia
N.E. Gruntenko, Dr. Sci. (Biology), Russia
S.G. Inge-Vechtomov, Full Member of the RAS, Dr. Sci. (Biology), Russia
E.K. Khlestkina, Corr. Member of the RAS, Professor of the RAS, Dr. Sci. (Biology), Russia
E.K. Khusnutdinova, Corr. Member of the RAE, Full Member of the AS of Bashkortostan, Dr. Sci. (Biology), Russia
A.V. Kilchevsky, Full Member of the NAS of Belarus, Dr. Sci. (Biology), Belarus
B.R. Kuluev, Dr. Sci. (Biology), Russia
D.M. Larkin, Cand. Sci. (Biology), Great Britain
S.A. Lashin, Dr. Sci. (Biology), Russia
J. Le Gouis, Dr. Sci., France
I.N. Lebedev, Corr. Member of the RAS, Professor, Dr. Sci. (Biology), Russia
L.A. Lutova, Professor, Dr. Sci. (Biology), Russia
V.Yu. Makeev, Corr. Member of the RAS, Dr. Sci. (Physics and Mathem.), Russia
I.V. Maksimov, Dr. Sci. (Biology), Russia
B.A. Malyarchuk, Dr. Sci. (Biology), Russia
Yu.G. Matushkin, Cand. Sci. (Biology), Russia
S.P. Medvedev, Cand. Sci. (Biology), Russia
V.I. Molodin, Full Member of the RAS, Dr. Sci. (History), Russia
M.P. Moshkin, Professor, Dr. Sci. (Biology), Russia
L.Yu. Novikova, Dr. Sci. (Agricul.), Russia
E.K. Potokina, Dr. Sci. (Biology), Russia
V.P. Puzyrev, Full Member of the RAS, Dr. Sci. (Medicine), Russia
D.V. Pyshnyi, Corr. Member of the RAS, Dr. Sci. (Chemistry), Russia
E.Y. Rykova, Dr. Sci. (Biology), Russia
E.A. Salina, Corr. Member of the RAS, Professor, Dr. Sci. (Biology), Russia
E.V. Shakhtshneider, Dr. Sci. (Medicine), Russia
S.V. Shekhovtsov, Dr. Sci. (Biology), Russia
S.V. Shestakov, Full Member of the RAS, Dr. Sci. (Biology), Russia
V.A. Stepanov, Full Member of the RAS, Dr. Sci. (Biology), Russia
I.A. Tikhonovich, Full Member of the RAS, Dr. Sci. (Biology), Russia
A.V. Vasiliev, Corr. Member of the RAS, Dr. Sci. (Biology), Russia
M.I. Voevoda, Full Member of the RAS, Dr. Sci. (Medicine), Russia
N.K. Yankovsky, Full Member of the RAS, Dr. Sci. (Biology), Russia
N.S. Yudin, Cand. Sci. (Biology), Russia
I.K. Zakharov, Professor, Dr. Sci. (Biology), Russia
I.A. Zakharov-Gezekhus, Corr. Member of the RAS, Dr. Sci. (Biology), Russia

ВАВИЛОВСКИЙ ЖУРНАЛ ГЕНЕТИКИ И СЕЛЕКЦИИ • VAVILOV JOURNAL OF GENETICS AND BREEDING

СОДЕРЖАНИЕ • 2026 • 30 • 6

Генетика и селекция растений

843 ОРИГИНАЛЬНОЕ ИССЛЕДОВАНИЕ
Холодовая акклиматизация растений томата связана с дифференциальной экспрессией генов семейства *SlLHC*, метаболизма каротиноидов и накопления/деградации хлорофиллов. *М.А. Филюшин, А.В. Щенникова, Е.З. Кочиева*

854 ОРИГИНАЛЬНОЕ ИССЛЕДОВАНИЕ
Пребридинговые исследования линий яровой мягкой пшеницы, несущих транслокацию T1BS.1BL-1S#F7L-1BL с геном *Lr51*. *С.Н. Сибикеев, А.Е. Дружин, З.Е. Фитилева, И.В. Борисов*

Физиологическая генетика

863 ОРИГИНАЛЬНОЕ ИССЛЕДОВАНИЕ
Способность FGF21 снижать выраженность признаков неалкогольной жировой болезни печени у мышей зависит от пола и диеты. *Н.Ю. Балыбина, Е.Н. Макарова, Т.В. Яковлева, А.Ю. Казанцева, Н.М. Бажан*

875 ОРИГИНАЛЬНОЕ ИССЛЕДОВАНИЕ
Влияние отбора по поведению на уровень глюкозы в крови у серебристо-черных лисиц после рестрикционного стресса. *Р.Г. Гулевич, С.Г. Шихевич, Д.В. Шепелева, А.В. Харламова*

Генетика животных

883 ОРИГИНАЛЬНОЕ ИССЛЕДОВАНИЕ
Полногеномное исследование генетических детерминант преждевременного старения крыс OXYS. *В.М. Петрова, М.С. Протасова, А.Д. Манахов, Н.А. Стефанова, Н.Г. Колосова, Е.И. Рогаев*

899 ОРИГИНАЛЬНОЕ ИССЛЕДОВАНИЕ
Эпигенетическая регуляция транскрипционной активности генов, связанных с нейропротекторным действием цефтриаксона, в головном мозге у крыс на модели спорадической болезни Альцгеймера: участие гистоновой деацетилазы 1. *А.А. Баширзаде, М.А. Тихонова, В.М. Беличенко, Л.А. Федосеева, М.Д. Беляев, Т.-И. Ренн, Х.-М. Чан, Н.Г. Колосова, Н.Д. Беляев, Т.Г. Амстиславская (на англ. языке)*

908 ОРИГИНАЛЬНОЕ ИССЛЕДОВАНИЕ
Влияние мутантных генов *APP* и *PSEN1* на асимметрию гиппокампа у мышей 5xFAD – трансгенной модели болезни Альцгеймера. *Е.Ю. Брусенцев, И.Н. Рожкова, В.С. Козенева, И.Д. Чекашов, Т.А. Рахманова, О.Б. Шевелев, С.Я. Амстиславский*

921 ОРИГИНАЛЬНОЕ ИССЛЕДОВАНИЕ
Оценка таксономического и генетического разнообразия лесных мышей рода *Apodemus* степной зоны Центрального Предкавказья. *Ф.А. Темботова, А.Х. Амшокова, М.С. Гудова, Е.П. Кононенко*

Медицинская генетика

938 ОРИГИНАЛЬНОЕ ИССЛЕДОВАНИЕ
Особенности метилирования ДНК в пораженных тканях аорты при дилатации/аневризме и расслоении восходящего отдела. *И.А. Гончарова, А.А. Зарубин, А.В. Марков, С.А. Шипулина, Н.П. Бабушкина, Ю.А. Королёва, А.А. Слепцов, М.С. Назаренко*

949 ОРИГИНАЛЬНОЕ ИССЛЕДОВАНИЕ
Клинический случай Х-сцепленной гипогидротической эктодермальной дисплазии, вызванной дупликацией Xq13.1, затрагивающей ген *EDA*. *В.И. Степаненко, И.Ж. Жалсанова, Е.А. Фонова, А.С. Зуев, С.Н. Государкина, Т.Н. Киреева, Е.Г. Равжаева, А.А. Агафонова, Г.Н. Сеитова, А.С. Монахова, Н.А. Скрябин*

Палеогенетика

955 ОРИГИНАЛЬНОЕ ИССЛЕДОВАНИЕ
Генетический анализ представителя воинской знати из могильника черняховской культуры Дальний (Выдрин) в Курской области. *Е.В. Рождественских, Т.В. Андреева, С.С. Кунижева, А.Д. Манахов, М.С. Гашева, О.А. Радюш, И.К. Решетова, М.В. Добровольская, Е.И. Рогаев*

Биоинформатика и системная биология

964 ОРИГИНАЛЬНОЕ ИССЛЕДОВАНИЕ
Обнаружение болезней земляники садовой с помощью БПЛА на основе сегментации мультиспектральных изображений методами глубокого машинного обучения. *А.Ф. Чешкова, В.С. Риксен, О.В. Елкин*

973 ОРИГИНАЛЬНОЕ ИССЛЕДОВАНИЕ
Визуальный анализ генотипов щавеля (*Rumex* spp.) биплот-методом с использованием морфологических признаков. *Н. Сабагния, М. Мохеббини, М. Джанмохаммади, М. Эрфани, К. Фарманпур-Калалаг (на англ. языке)*

© Сибирское отделение Российской академии наук, 2026
© Институт цитологии и генетики СО РАН, 2026
Вавиловский журнал генетики и селекции, 2026

VAVILOVSKII ZHURNAL GENETIKI I SELEKTSII • VAVILOV JOURNAL OF GENETICS AND BREEDING

CONTENTS • 2026 • 30 • 6

Plant genetics and breeding

843 ORIGINAL ARTICLE
Cold acclimation of tomato plants is associated with differential expression of genes of the *SlLHC* family, carotenoid metabolism, and chlorophyll accumulation/degradation. *M.A. Filyushin, A.V. Shchennikova, E.Z. Kochieva*

854 ORIGINAL ARTICLE
Prebreeding studies of spring bread wheat lines, carrying T1BS.1BL-1S#F7L-1BL translocation with *Lr51* gene. *S.N. Sibikeev, A.E. Druzhin, Z.E. Fitileva, I.V. Borisov*

Physiological genetics

863 ORIGINAL ARTICLE
The ability of FGF21 to ameliorate signs of non-alcoholic fatty liver disease in mice depends on sex and diet. *N.Yu. Balybina, E.N. Makarova, T.V. Jakovleva, A.Yu. Kazantseva, N.M. Bazhan*

875 ORIGINAL ARTICLE
Effect of selection for behavior on the blood glucose level in foxes exposed to restriction stress. *R.G. Gulevich, S.G. Shikhevich, D.V. Shepeleva, A.V. Kharlamova*

Animal genetics

883 ORIGINAL ARTICLE
Whole genome sequencing identifies genetic variants associated with senescence-accelerated phenotype of OXYS rats. *V.M. Petrova, M.S. Protasova, A.D. Manakhov, N.A. Stefanova, N.G. Kolosova, E.I. Rogaev*

899 ORIGINAL ARTICLE
Epigenetic regulation of the transcriptional activity of genes mediating the neuroprotective activity of ceftriaxone in the brain in a rat model of sporadic Alzheimer disease: the involvement of histone deacetylase 1. *A.A. Bashirzade, M.A. Tikhonova, V.M. Belichenko, L.A. Fedoseeva, M.D. Belyaev, T.-Y. Renn, H.-M. Chang, N.G. Kolosova, N.D. Belyaev, T.G. Amstislavskaya*

908 ORIGINAL ARTICLE
The influence of mutant genes *APP* and *PSEN1* on hippocampal asymmetry in 5xFAD mice, transgenic model of Alzheimer disease. *E.Yu. Brusentsev, I.N. Rozhkova, V.S. Kozeneva, I.D. Chekashov, T.A. Rakhmanova, O.B. Shevelev, S.Ya. Amstislavsky*

921 ORIGINAL ARTICLE
Assessment of taxonomic and genetic diversity of wood mice of the genus *Apodemus* in the steppe zone of the Central Ciscaucasia. *F.A. Tembotova, A.Kh. Amshokova, M.S. Gudova, E.P. Kononenko*

Medical genetics

938 ORIGINAL ARTICLE
DNA methylation analysis of aortic wall tissue in ascending aortic dilatation/aneurysm and dissection. *I.A. Goncharova, A.A. Zarubin, A.V. Markov, S.A. Shipulina, N.P. Babushkina, Iu.A. Koroleva, A.A. Sleptcov, M.S. Nazarenko*

949 ORIGINAL ARTICLE
A clinical case of X-linked hypohidrotic ectodermal dysplasia caused by an Xq13.1 duplication affecting the *EDA* gene. *V.I. Stepanenko, I.Zh. Zhalsanova, E.A. Fonova, A.S. Zuev, S.N. Gosudarkina, T.N. Kireeva, E.G. Ravzhaeva, A.A. Agafonova, G.N. Seitova, A.S. Monakhova, N.A. Skryabin*

Paleogenetics

955 ORIGINAL ARTICLE
Genetic analysis of a representative of the military nobility from the Dal'niy (Vydrin) burial ground of the Chernyakhov culture in the Kursk region. *E.V. Rozhdestvenskikh, T.V. Andreeva, S.S. Kunizheva, A.D. Manakhov, M.S. Gasheva, O.A. Radyush, I.K. Reshetova, M.V. Dobrovolskaya, E.I. Rogaev*

Bioinformatics and systems biology

964 ORIGINAL ARTICLE
UAV-based disease detection in strawberry by multispectral image segmentation invoking deep learning. *A.F. Cheshkova, V.S. Riksen, O.V. Elkin*

973 ORIGINAL ARTICLE
Visual analysis of sorrel (*Rumex* spp.) genotypes by the biplot method using morphological characters. *N. Sabaghnia, M. Mohebodini, M. Janmohammadi, M. Erfani, K. Farmanpour-Kalalagh*

© Siberian Branch RAS, 2026
© Institute of Cytology and Genetics, SB RAS, 2026
Vavilov Journal of Genetics and Breeding, 2026

Vavilovskii Zhurnal Genetiki i Selektsii
Vavilov Journal of Genetics and Breeding. 2026;30(6):843-853

doi 10.18699/vjgb-26-86

Cold acclimation of tomato plants is associated with differential expression of genes of the *SlLHC* family, carotenoid metabolism, and chlorophyll accumulation/degradation

M.A. Filyushin, A.V. Shchennikova, E.Z. Kochieva

Institute of Bioengineering, Research Center of Biotechnology of the Russian Academy of Sciences, Moscow, Russia
michel7753@mail.ru

Abstract. Tomato (*Solanum lycopersicum* L.) is sensitive to cold stress. The plant's adaptive response to low temperatures is accompanied by cellular osmoregulation and a decrease in the rate of photosynthesis due to disruption of the antennae of photosystems I and II, including proteins of the light-harvesting complex (LHC) family that bind chlorophylls *a*/*b* and carotenoids. In this study, a transcriptome analysis of differential expression of *SlLHC* family genes, carotenoid and abscisic acid (ABA) biosynthesis genes, as well as *ORANGE* and *STAY-GREEN* genes associated with chlorophyll accumulation and degradation, was performed for the first time during two cycles (I and II) of "cold stress (12 h) – recovery (60 h)". The tomato cultivar Otradnyi was used for the analysis. 12 h before the end of the recovery period of the second cycle (II-48), the content of chlorophylls *a*/*b* and carotenoids in plant leaves was shown to be significantly decreased. It was revealed that 12 h of cold exposure in both cycles (I-12, II-12) suppressed the expression of most *LHC* family genes. At the same time points, a significant increase in the transcript levels of the *NSY*, *CCD-like*, *LeNCED1* and *NCED6* genes associated with ABA synthesis was detected. Genes, expression profile of which differed between the primary and repeated cycles of cold exposure, were identified. Based on these data, a list of candidate genes for cold stress memory markers in plants was compiled: 10 *SlLHC* family genes (*Cab-1A*, *Cab-1D*, *CAB12*, *CAB5*-LOC101257186, *SEP2*, *OHP2*-LOC101259223, *OHP1* and *LIL3-2*-LOC101247899) and five genes associated with ABA synthesis (*VDE*, *CCD4*, *CCD-like*, *LeNCED1* and *NCED6*). The obtained results are important for identifying and understanding the involvement of photosynthesis-related genes in the response to cold stress and determining cold tolerance of tomato plants, and can be used in breeding cold-resistant varieties.

Key words: *Solanum lycopersicum* L.; cold stress; LHC protein family; chlorophyll *a*/*b*-binding proteins; carotenoid biosynthesis; ABA; gene expression

For citation: Filyushin M.A., Shchennikova A.V., Kochieva E.Z. Cold acclimation of tomato plants is associated with differential expression of genes of the *SlLHC* family, carotenoid metabolism, and chlorophyll accumulation/degradation. *Vavilovskii Zhurnal Genetiki i Selektsii = Vavilov J Genet Breed*. 2026;30(6):843-853. doi 10.18699/vjgb-26-86

Funding. The work was supported by the Russian Science Foundation (grant No. 24-16-00043, transcriptome analysis) and the Ministry of Science and Higher Education of the Russian Federation (obtaining and preparing plants, biochemical analysis).

Холодовая акклиматизация растений томата связана с дифференциальной экспрессией генов семейства *SlLHC*, метаболизма каротиноидов и накопления/деградации хлорофиллов

М.А. Филюшин, А.В. Щенникова, Е.З. Кочиева

Федеральный исследовательский центр «Фундаментальные основы биотехнологии» Российской академии наук, Москва, Россия
michel7753@mail.ru

Аннотация. Растения томата (*Solanum lycopersicum* L.) чувствительны к воздействию холодового стресса, адаптационный ответ на который связан с клеточной осморегуляцией и снижением скорости фотосинтеза за счет нарушения работы антенн фотосистем I и II, включающих белки семейства Light-Harvesting Complex (LHC), связывающие хлорофиллы *a*/*b* и каротиноиды. В настоящей работе впервые проведен транскриптомный анализ дифференциальной экспрессии генов семейства *SlLHC*, генов биосинтеза каротиноидов и абсцизовой кислоты (АБК), а также генов *ORANGE* и *STAY-GREEN*, связанных с синтезом и деградацией хлорофиллов, в динамике двух циклов (I и II) «холодовой стресс (12 ч) – восстановление (60 ч)». Для анализа использован сорт томата

© Filyushin M.A., Shchennikova A.V., Kochieva E.Z., 2026
This work is licensed under a Creative Commons Attribution 4.0 License

Отрадный. Показано, что за 12 ч до завершения периода восстановления второго цикла (II-48) в листьях растения значительно уменьшается количество хлорофиллов *a*/*b* и каротиноидов. Выявлено, что 12 ч холодового воздействия в обоих циклах (I-12, II-12) подавляют экспрессию большинства генов семейства *LHC*. В тех же точках обнаружено значимое повышение уровня транскриптов генов *NSY*, *CCD-like*, *LeNCED1* и *NCED6*, связанных с синтезом АБК. Определены гены, профиль экспрессии которых различается между первичным и повторным циклами холодового воздействия. На основании этих данных составлен список генов-кандидатов в маркеры памяти растений о холодовом стрессе: десять генов семейства *SlLHC* (*Cab-1A*, *Cab-1D*, *CAB12*, *CAB5*-LOC101257186, *SEP2*, *OHP2*-LOC101259223, *OHP1* и *LIL3-2*-LOC101247899) и пять генов, ассоциированных с синтезом АБК (*VDE*, *CCD4*, *CCD-like*, *LeNCED1* и *NCED6*). Полученные результаты важны для определения и осмысления участия генов, связанных с фотосинтезом, в ответе на холодовой стресс и определении холодостойкости растений томата, и могут быть использованы в селекции холодостойких сортов.
Ключевые слова: *Solanum lycopersicum* L.; холодовой стресс; семейство белков LHC; хлорофилл *a*/*b*-связывающие белки; биосинтез каротиноидов; АБК; экспрессия генов

Introduction

The survival, productivity, and geographic distribution of plants are limited by unfavorable environmental conditions. Among the most serious factors, cold stress can have both less destructive (chilling) and more destructive (freezing) forms (Kidokoro et al., 2022). Unable to move, plants are forced to adapt to stressful conditions, including low temperatures (Browse, Xin, 2001), which is accompanied by physiological and molecular genetic changes (Ding et al., 2024). Primary stress triggers epigenetic modifications in the genome, thus improving plant adaptation to recurrent events and forming stress memory (Villagómez-Aranda et al., 2022). Genes that exhibit differences in expression patterns between priming and repeats, as well as during recovery periods, are considered markers of stress memory (Friedrich et al., 2019; Bäurle, Trindade, 2020; Jacques et al., 2021; Aina et al., 2024).

In the plant response to cold stress, one of the significant groups of genes is associated with photosynthesis, the reduction of which stimulates cellular osmoregulation (Yamori et al. 2014). The latter is achieved by stomatal closure under the action of abscisic acid (ABA) (Sreenivasulu et al., 2012; Agurla et al., 2018), formed during the oxidative cleavage of the carotenoid 9′-*cis*-neoxanthin (Nakashima, Yamaguchi-Shinozaki, 2013; Chen et al., 2020; Xu et al., 2023).

Cold-induced inhibition of photosynthesis is characterized by impaired light energy capture by the light-harvesting complexes (antennae) of photosystems I and II and electron transfer in thylakoids (Ashraf, Harris, 2013). The antennae include proteins of the Light-Harvesting Complex (LHC) family, which are embedded in the thylakoid membrane and noncovalently bind to chlorophylls *a* and/or *b*, altering their optical properties (Klimmek et al., 2006). The resulting set of different chlorophyll forms ensures the transfer of energy from absorbed quanta to the reaction centers of the photosystems (Li et al., 2025). Also, LHC proteins are involved in chlorophyll degradation by interacting with the STAY-GREEN (SGR) protein and chlorophyll catabolism enzymes (CCE) (Pietrzykowska et al., 2014). The LHC family includes chlorophyll *a*/*b*-binding proteins (CAB or Lhca/b), photosystem II protein psbS, Light-Harvesting-like proteins (LIL, also including Light-Inducible proteins (ELIP), One-Helix proteins (OHP), Stress-Enhanced proteins (SEP)), and ferrochelatases (FC or FeCh) (Jansson, 1999; Klimmek et al., 2006).

In addition to LHC proteins and chlorophylls *a*/*b*, antenna complexes include carotenoids (β-carotene, xanthophylls of the lutein and violaxanthin cycles), which are involved in the capture of light quanta in spectral ranges weakly absorbed by chlorophylls, followed by the transfer of excitation energy to chlorophyll molecules (Li et al., 2025). Furthermore, carotenoids (primarily violaxanthin, antheroxanthin, and zeaxanthin) protect the photosynthetic apparatus from excess excitation energy and prevent its destruction by neutralizing singlet oxygen and triplet chlorophyll (Li et al., 2025).

The ORANGE (OR) protein plays an important role in regulating chlorophyll and carotenoid levels in green plant tissues. For example, the expression level of *SlOR* and *SlOR-like* genes in the stems and leaves of tomato *Solanum lycopersicum* L. is positively associated with the levels of chlorophylls and carotenoids in leaf cells (Gao et al., 2025). However, overexpression of the *OR* gene in the model species *Arabidopsis thaliana* L. suppresses chlorophyll biosynthesis and thylakoid membrane development (Tee, 2019).

The *LHC* gene family has been identified in various plant species, including *A. thaliana* (30, 32, or 34 genes), poplar *Populus* spp. (36 or 39), cotton *Gossypium hirsutum* L. (86), and apple *Malus* × *domestica* Borkh. (27 or 42) (Klimmek et al., 2006; Zhao et al., 2020; Zhang et al., 2021; Lan et al., 2022).

Tomato plants (*S. lycopersicum*), an important vegetable crop, are sensitive to temperatures below 12 °C (Mesa et al., 2022) and are therefore grown primarily indoors in most regions of the Russian Federation due to the risk of sudden temperature fluctuations and recurrent spring cold spells or frosts. During the development of stress resistance, the parameters of photosynthesis undergo significant changes, including the expression of photosynthetic proteins (Neilson et al., 2011; Soualiou et al., 2023), so studying tomato *LHC* genes may be promising for the breeding of new varieties.

The number of *LHC* genes in *S. lycopersicum*, as in other plant species, is not precisely defined and depends on the specific study: 40 (Lan et al., 2022) or 39 (Meng et al., 2025). Most *LHC* genes contain stress-associated *cis*-regulatory elements in their promoters. These genes are differentially expressed in response to drought, cold, and salinity, may play an important role in many biological processes, and are shown to be regulated by circadian rhythms (Piechulla et al., 1998;

Lan et al., 2022; Meng et al., 2025). The transcript level of *SlLHC* genes increases during plant adaptation to salt stress (Ikuyinminu et al., 2023) and is positively related to the rate of photosynthesis (Yan et al., 2023).

The aim of this study was a transcriptome analysis of leaves of the cold-resistant tomato cultivar Otradnyi in terms of changes in the expression of *LHC* genes, genes of the carotenoid biosynthesis pathway, as well as genes associated with the synthesis of carotenoids and chlorophyll in chloroplasts, the formation of ABA and the degradation of chlorophylls, in response to two cycles of "cold stress – post-stress recovery". The results obtained are important for understanding the involvement of photosynthesis-related genes in the cold stress response and cold tolerance of tomato plants, with the potential to identify markers of cold stress memory among these genes.

Materials and methods

In the study, we used plants of the tomato *S. lycopersicum* cold-resistant cv. Otradnyi (code 8006741, https://gossortrf.ru/registry/) bred by the Federal Scientific Vegetable Center (FSVC, Moscow Region). This cultivar is early ripening and resistant to salinity (Filyushin et al., 2025; data from the originators).

Tomato cv. Otradnyi seeds (the 2024 harvest) were used to obtain seedlings at the 5–7 leaf stage (light/dark – 16 h/8 h, 23 °C/18 °C; dark phase 23:00–7:00; Photosynthetic Photon Flux (PPF) – 190 μM/(m^2·s)). Plants were subjected to two cycles of cold stress; controls were incubated under normal conditions (23 °C). Each cycle consisted of a cooling phase of 12 h at 3 °C (20:00–8:00) (I-12 and II-12) followed by a post-stress recovery period (memory phase) of 60 h under normal conditions (Fig. 1). The cycles followed one after another and in total took 144 h (12+60+12+60).

The use of two cycles was motivated by the signature of stress memory marker genes, implying differences in the expression patterns of such genes between priming and re-exposure (Friedrich et al., 2019; Bäurle, Trindade, 2020; Jacques et al., 2021; Aina et al., 2024). That is, if the expression profile of the genes we analyzed under two-cycle stress shows significant intercycle differences, such genes can become candidates for stress memory markers. In addition, we used a 60-h recovery period, since another characteristic of stress memory marker genes is the failure to return to normal expression values for a long time (more than 24 h) after stress (Friedrich et al., 2019; Bäurle, Trindade, 2020; Jacques et al., 2021; Aina et al., 2024).

Over the course of two cycles (a total of 144 h), no visible differences were found between the experimental plants and the controls. In both cold treatment cycles, no signs of leaf wilting were observed in the stressed samples (apparently due to the cold tolerance of the cv. Otradnyi). There were also no significant differences in plant height, leaf number and size between the control and experimental groups, as well as within them.

At the end of cold exposure (12 h, 8:00) and after 48 h of recovery (8:00) of the first (I) and second (II) cycles, leaf samples were collected from the experimental and control plants. In the recovery phase (60 h), a 48-h point (I-48 and II-48) was chosen, 12 h before the end of the post-stress period, so that sampling was carried out at the same time of day (8:00) both during stress and recovery. The choice was determined by the dependence of the expression of the analyzed photosynthesis genes on circadian rhythms (Piechulla et al., 1998; Meng et al., 2025). This temporal coordination, combined with a parallel cultured control for normalization, should improve the accuracy of interpretation of the resulting biochemical and transcriptomic data.

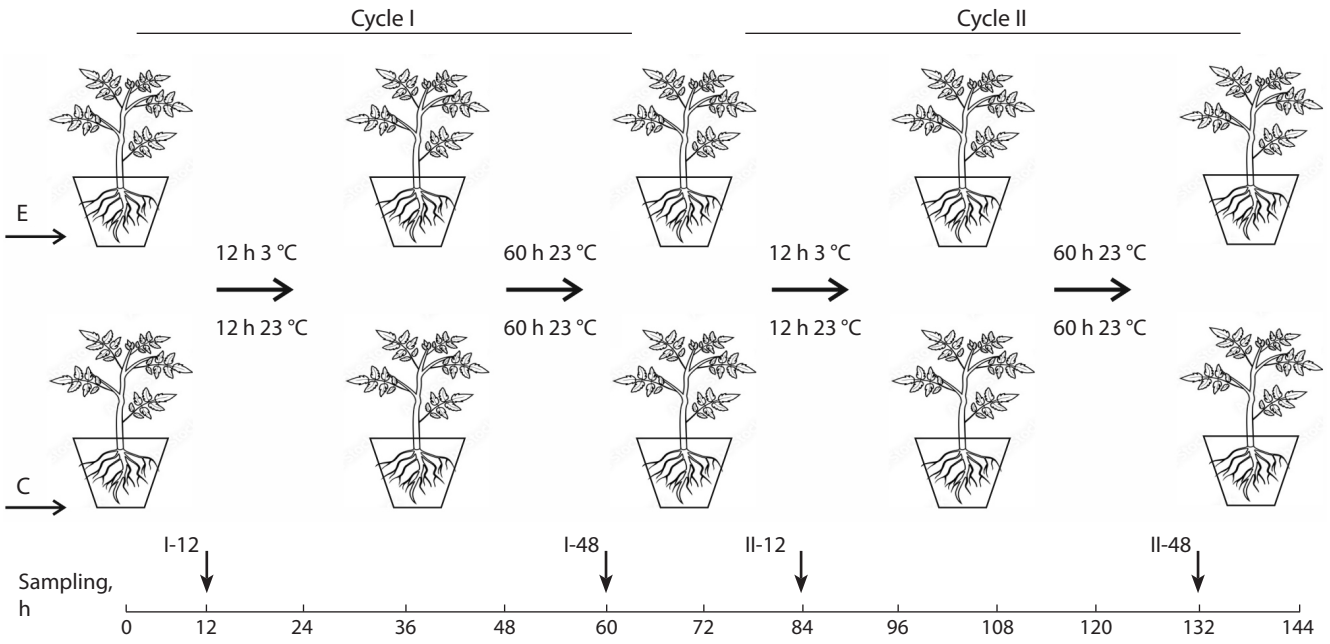


Fig. 1. Schematic representation of two-cycle (I, II) exposure to cold stress with subsequent recovery on tomato plants of the cv. Otradnyi.

The samples were analyzed for chlorophylls *a*/*b* and carotenoids (two biological and three analytical replicates); one biological replicate was a pool of leaves from two independent plants for each measurement point. The concentrations (mg/g fresh weight (FW)) of chlorophylls *a* and *b* and total carotenoids were determined in chloroform-methanol (3:1, v/v) extracts according to (Efremov et al., 2020), with absorption spectra recorded on an Eppendorf BioSpectrometer® basic (Eppendorf, Germany). The following formulas were used to calculate pigment concentrations:

Chlorophyll *a* (Chl*a*) =

$$11.47\times(A_{666} - A_{750}) - 2\times(A_{648} - A_{750}),$$

Chlorophyll *b* (Chl*b*) =

$$21.85\times(A_{648} - A_{750}) - 4.53\times(A_{666} - A_{750}),$$

Total carotenoids =

$$[1000\times(A_{480} - A_{750}) - 1.33\times\text{Chl}a - 23.93\times\text{Chl}b]/202,$$

where A_{666}, A_{648}, A_{750} and A_{480} are the absorption values at the indicated wavelengths.

The significance ($p < 0.05$) of differences between values was determined using Two-way ANOVA ("multiple comparisons, corrected with Bonferroni test") in GraphPad Prism v. 8 ("GraphPad Software Inc.", USA; https://www.graphpad.com/scientific-software/prism/).

For subsequent transcriptome analysis, total RNA was isolated from the same leaf samples (RNeasy Plant Mini Kit, Qiagen, USA) and used to obtain mRNA libraries (NEBNext® mRNA Library Prep Reagent Set for Illumina; New England BioLabs, USA), which were sequenced on the Illumina HiSeq2500 platform (Illumina Inc., USA). Based on the obtained reads, coding sequences were assembled using Trinity v3.5.13 (https://github.com/trinityrnaseq/trinityrnaseq/wiki) and TransDecoder v5.1.0 (https://github.com/TransDecoder/TransDecoder) and then annotated with NCBI-Blast (https://www.ncbi.nlm.nih.gov/). Relative transcript levels were estimated as RPKM (number of reads per 1 kb transcripts per million mapped reads).

Differentially expressed genes (DEGs) between the control and experimental plants in two cycles at the end of stress (I-12, II-12) and the recovery period (I-48, II-48) were identified using the DESeq2 method (Love et al., 2014). Differences in transcript levels were considered significant if the expression change was ≥2 (absolute log2FoldChange [FC] ≥ 1; padj (P-value adjusted, or false discovery rate) < 0.05). Next, the annotation was used to search for tomato *LHC* superfamily genes, carotenoid metabolism pathway genes, as well as *OR*, *OR-like*, and *SGR* genes, both among the primary gene list and among the DEGs. Changes in gene expression profiles during the experiment were visualized using heatmaps (Excel).

Results

In this study, we examined the effect of two "cold stress – recovery" cycles (I, II) on metabolite content and photosynthesis-related gene expression in leaves of the cold-tolerant tomato cv. Otradnyi. Leaves were collected from experimental plants (parallel to control samples) at two points in each cycle: at the end of the 12-h stress period (I-12, II-12); and 12 h before the end of the 60-hour recovery phase (I-48, II-48).

Tissue samples were used for chlorophyll *a* and *b* and total carotenoid content analysis. At point I-48, both in the control and the experimental group, the obtained values were significantly lower than at the other three points (II-48, I-12, and II-12). The exception was carotenoids: their content at point I-48 differed from I-12, but not from II-12, but was similar in the control and experimental groups (Fig. 2). In addition, in the experimental group, the amount of all analyzed pigments decreased significantly at the end of the recovery period of the second cycle (II-48) (Fig. 2).

The same leaf samples were used to obtain transcriptomes for subsequent analysis of the expression dynamics of photosynthesis-related genes. A preliminary list of genes of interest was compiled based on transcriptome annotations from SolGenomics, including studies (Lan et al., 2022; Meng et al., 2025), and NCBI (see the Table). The former study identified 24 *Lhca/b*, 10 *Lil*, one *Psbs*, and five *FCII* genes in tomato (Lan et al., 2022). The latter publication reported 29 *Lhca/b*, seven *Lil*, one *Psbs*, and two *FCII* genes (Meng et al., 2025).

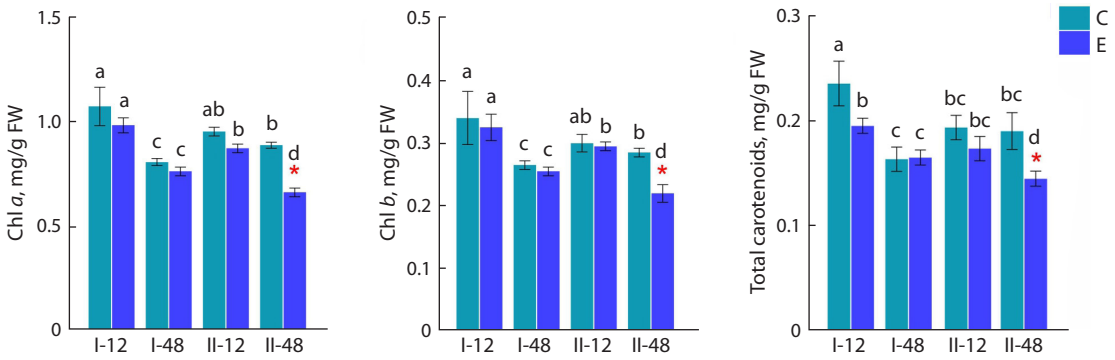


Fig. 2. Dynamics of the content (mg/g FW) of chlorophylls *a* and *b* and total carotenoids in the leaves of tomato cv. Otradnyi plants in response to cold stress and recovery.

In each of the two exposure cycles (I, II), measurements were taken at the end of stress exposure (I-12, II-12) and after 48 h of the recovery period (I-48, II-48). The value $^{a-d}$ $p < 0.05$ – for statistically significant differences between the experiment (E) and the control (C) at each of the points; a significant difference between the experiment and the control at point II-48 is additionally indicated by a red asterisk.

List of genes analyzed in the study

Superfamily *LHC*		
Solyc gene ID[1]	NCBI gene ID[2]	Annotation of the encoded protein (NCBI)
02g070940 02g070950 02g070970 02g071010 02g071030	LOC101264784	Chlorophyll *a*/*b*-binding protein Cab-1B (CAB1B)
02g070990	LOC101266182	CAB1B homolog, 100 %-cover, identity 99.25 %
02g070980	LOC104645884	Chlorophyll *a*/*b*-binding protein Cab-1A (Cab-1A)
02g071000	LOC104645883	Chlorophyll *a*/*b*-binding protein 1D (Cab-1D)
03g005760	LOC101267774	Chlorophyll *a*/*b*b-binding protein 1-like
03g005770	LOC101245729	Chlorophyll *a*/*b*-binding protein
03g005780	LOC108491835	Chlorophyll *a*/*b*-binding protein Cab-3C (Cab-3C)
12g006140	LOC543976	Chlorophyll *a*/*b*-binding protein 5, chloroplastic (CAB5)
07g063600	LOC101268123	Chlorophyll *a*/*b*-binding protein 13, chloroplastic-like
12g011450	LOC101243766	Chlorophyll *a*/*b*-binding protein 13, chloroplastic (CAB13)
09g014520	LOC101249002	Chlorophyll *a*/*b*-binding protein CP29.1, chloroplastic
06g063370	LOC101266527	Chlorophyll *a*/*b*-binding protein Cab9 (CAB9)
01g105030	LOC101256629	Chlorophyll *a*/*b*-binding protein CP24 10A, chloroplastic (CAB-10A)
04g082930 04g082920	LOC101246628	Chlorophyll *a*/*b*-binding protein 7, chloroplastic
01g105050	LOC101256131	Chlorophyll *a*/*b*-binding protein CP24 10B, chloroplastic-like (LHCP)
05g056050	LOC101253380	Chlorophyll *a*/*b*-binding protein 6A, chloroplastic
05g056070	LOC544310	Chlorophyll *a*/*b*-binding protein precursor (CAB6A)
10g006230	LOC101264376	Chlorophyll *a*/*b*-binding protein 7, chloroplastic-like (CAB7)
10g007690	LOC101253628	Type III chlorophyll *a*/*b*-binding protein (CAB-8)
12g011280	LOC101265617	Chlorophyll *a*/*b*-binding protein 8, chloroplastic-like
03g115900	LOC101268669	Chlorophyll *a*/*b*-binding protein CAB11 (CAB11)
06g069730	LOC101256006	Chlorophyll *a*/*b*-binding protein Cab12 (CAB12)
–	LOC101265886	Chlorophyll *a*/*b*-binding protein 1C, chloroplastic
–	LOC101263969	Chlorophyll *a*/*b*-binding protein
–	LOC101268491	Chlorophyll *a*/*b*-binding protein 3C, chloroplastic-like
–	LOC543975	Chlorophyll *a*/*b*-binding protein precursor (CAB4)
11g042640	LOC101267576	Uncharacterized (CAB-like)
07g022900	LOC101257186	Photosystem I chlorophyll *a*/*b*-binding protein 5, chloroplastic
12g009200	LOC101252151	photosystem I chlorophyll *a*/*b*-binding protein 6, chloroplastic
09g082690	LOC101257109	Early light inducible protein (ELIP)
09g082700	LOC138337022	ELIP homolog 97 %-cover, identity 84.74 %
01g107660	LOC101252927	Stress enhanced protein 1-like protein
04g053130	LOC101250395	Stress enhanced protein 2, chloroplastic
12g056620	LOC101259223	Light-harvesting complex-like protein OHP2, chloroplastic
04g071930	LOC101253996	Light-harvesting complex-like protein OHP2, chloroplastic
03g094000	LOC101247899	Light-harvesting complex-like protein 3 isotype 2, chloroplastic
08g007180	LOC101260362	Light-harvesting complex-like protein 3 isotype 1, chloroplastic
08g077880	LOC101248227	Light-harvesting complex-like protein 3 isotype 2, chloroplastic
09g011010	LOC101262449	Light-harvesting complex-like protein OHP1, chloroplastic
05g018650	LOC101247019	Ferrochelatase-2, chloroplastic
10g084140	LOC101248153	Ferrochelatase-2, chloroplastic
08g065480	LOC101263738	Ferrochelatase-2, chloroplastic
06g060340	LOC101260830	Photosystem II subunit S (psbS)

Table (end)

Carotenoid metabolism		
Annotation of the encoded protein (NCBI)	NCBI gene ID	Functional activity of the encoded protein
Phytoene synthase 1, chloroplastic (Psy1)	LOC543988	Carotenoid synthesis (ElShamey et al., 2025)
Phytoene synthase 2, chloroplastic (PSY2)	LOC543964	
Phytoene synthase 3	LOC101267734	
Phytoene desaturase (pds)	LOC544073	
15-*cis*-phytoene desaturase, chloroplastic/chromoplastic	LOC101244544	
Prolycopene isomerase, chloroplastic (CRTISO)	LOC101267857	
15-*cis*-ζ-carotene isomerase (Z-ISO)	LOC101253762	
ζ-carotene desaturase (zds)	LOC543629	
Lycopene-ε-cyclase (CrtL-e-1)	LOC544129	
Lycopene-β-cyclase, chloroplastic	LOC101267662	
Lycopene-β-cyclase (LCY1)	LOC544104	
Lycopene-β-cyclase, chromoplastic (NSY) = neoxanthin synthase, chloroplastic	LOC543649	
B-carotene isomerase D27, chloroplastic	LOC101266539	
B-carotene hydroxylase (CrtR-b1)	LOC544133	
B-carotene hydroxylase (CrtR-b2)	LOC544297	
Zeaxanthin epoxidase, chloroplastic	LOC101252420	
Zeaxanthin epoxidase, chloroplastic (ZEP)	LOC544162	
Violaxanthin de-epoxidase (VDE)	LOC543696	
Carotenoid cleavage dioxygenase 7 (CCD7)	LOC100313501	SGL and ABA synthesis (ElShamey et al., 2025)
Carotenoid cleavage dioxygenase 4, chloroplastic	LOC101250535	
Carotenoid cleavage dioxygenase 1A (LeCCD1A)	LOC543935	
Carotenoid cleavage dioxygenase 1B (LeCCD1B)	LOC544269	
Carotenoid 9,10(9',10')-cleavage dioxygenase-like	LOC101255364	
NCED1 9-*cis*-epoxycarotenoid dioxygenase (LeNCED1)	LOC544163	
NCED2 9-*cis*-epoxycarotenoid dioxygenase 2	LOC100316877	
9-*cis*-epoxycarotenoid dioxygenase NCED6, chloroplastic	LOC101246826	
Synthesis of chlorophylls and carotenoids in chloroplasts		
Annotation of the encoded protein (NCBI)	NCBI gene ID	Functional activity of the encoded protein
ORANGE protein-like	LOC101244466	Negatively regulate chlorophyll biosynthesis, thylakoid membrane development, and *ELIP* gene expression in *A. thaliana* (Tee, 2019). Positively influence the growth and stress resistance of tomato plants (Gao et al., 2025)
Protein ORANGE-LIKE, chloroplastic	LOC101247247	
Chlorophyll degradation		
Annotation of the encoded protein (NCBI)	NCBI gene ID	Functional activity of the encoded protein
G protein STAY-GREEN	LOC101260158	Interact with LHC proteins and chlorophyll catabolism enzymes (Pietrzykowska et al., 2014)
Protein STAY-GREEN homolog, chloroplastic-like	LOC101258237	
Senescence-inducible chloroplast stay-green protein 1 (SGR1)	LOC778212	

[1] Current Tomato Genome version SL4.0 and Annotation ITAG4.0, from September 2019 (https://www.solgenomics.net/organism/Solanum_lycopersicum/genome), using data of (Lan et al., 2022; Meng et al., 2025).
[2] SLM_r2.1 (GCF_036512215.1), assembly and annotation of the tomato genome, September 3, 2024 (updates October 2024–September 2025; https://www.ncbi.nlm.nih.gov/datasets/genome/GCF_036512215.1/).

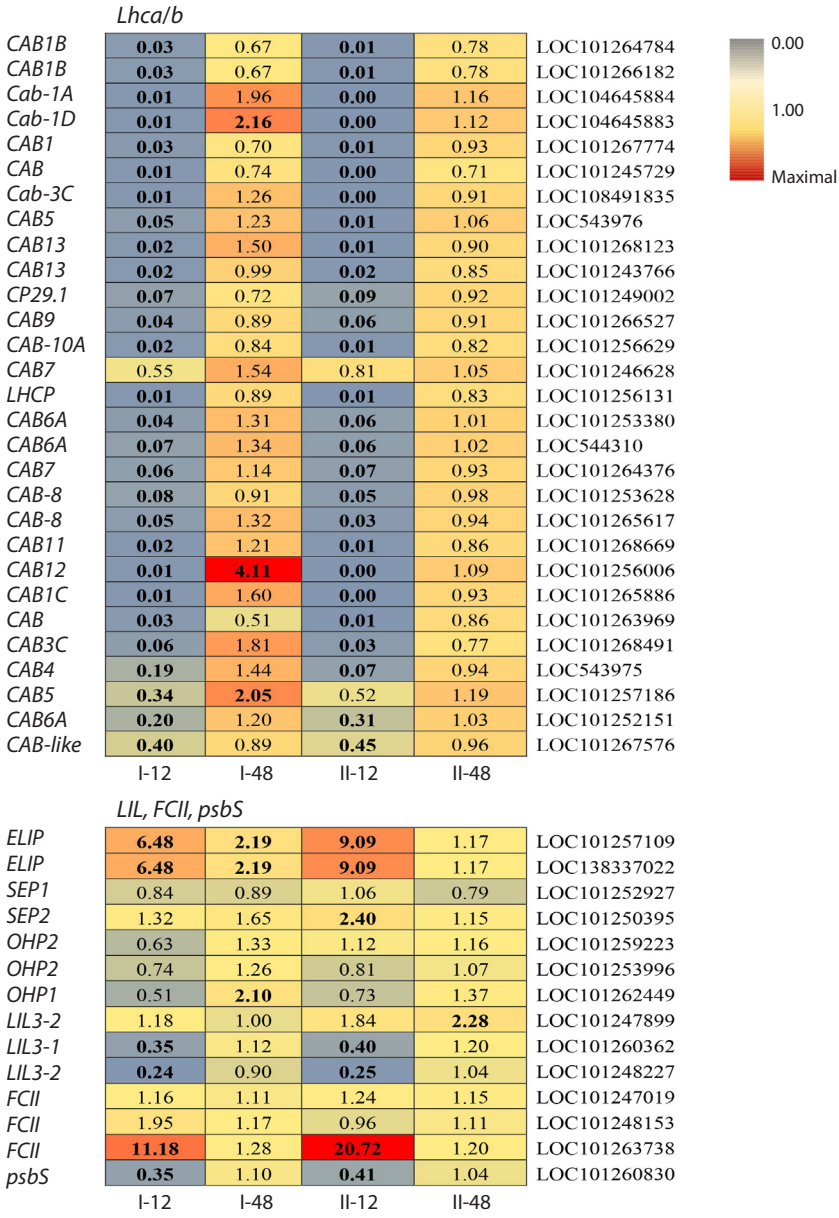


Fig. 3. Heatmap of changes in *LHC* superfamily gene expression in the leaves of the tomato cv. Otradnyi (*S. lycopersicum*) in response to two cycles (I, II) of "cold stress – recovery", constructed using our transcriptome data for points I-12, II-12 (end of stress) and I-48, II-48 (recovery period).

Here and in Figure 4: cells show RPKM values rounded to two decimal places; statistically significant differences from the control (taken as 1.00) are highlighted in bold. The cell color gradient corresponds to a decrease (shades of gray) or increase (shades of red) in gene expression compared to the control (1.00, yellow color).

We further relied on NCBI data, where the current version of the tomato genome is dated September 3, 2024, compared to SolGenomics (September 2019).

According to NCBI data, the tomato *LHC* family includes 43 genes (29 – *Lhca/b*, 10 – *Lil*, 1 – *psbS*, 3 – *FCII*) (see the Table). In addition, 18 genes of the carotenoid biosynthesis pathway, eight deoxygenase genes (catalyzing the conversion of carotenoids to the phytohormones strigolactones (SGL) and ABA), two homologous *OR* genes (synthesis of chlorophylls and carotenoids in chloroplasts) and three homologous *SGR* genes (chlorophyll degradation) were identified in tomato genome (see the Table).

The obtained transcriptome data were used to assess changes in the expression of the genes we selected (see the Table) in tomato leaves during two cycles of "cold stress – recovery" (Fig. 3 and 4).

It was shown that in both stress cycles after 12 h of cold exposure (I-12, II-12), the expression of *Lhca/b* genes decreased significantly (≥2-fold). The exceptions were *CAB7*-LOC101246628 (I-12, II-12) and *CAB5*-LOC101257186 (II-12), the level of transcripts of which also decreased at both points, however, less significantly (<2-fold). By the end of the recovery period of both cycles (I-48, II-48), the expression of *Lhca/b* genes returned to control values, with

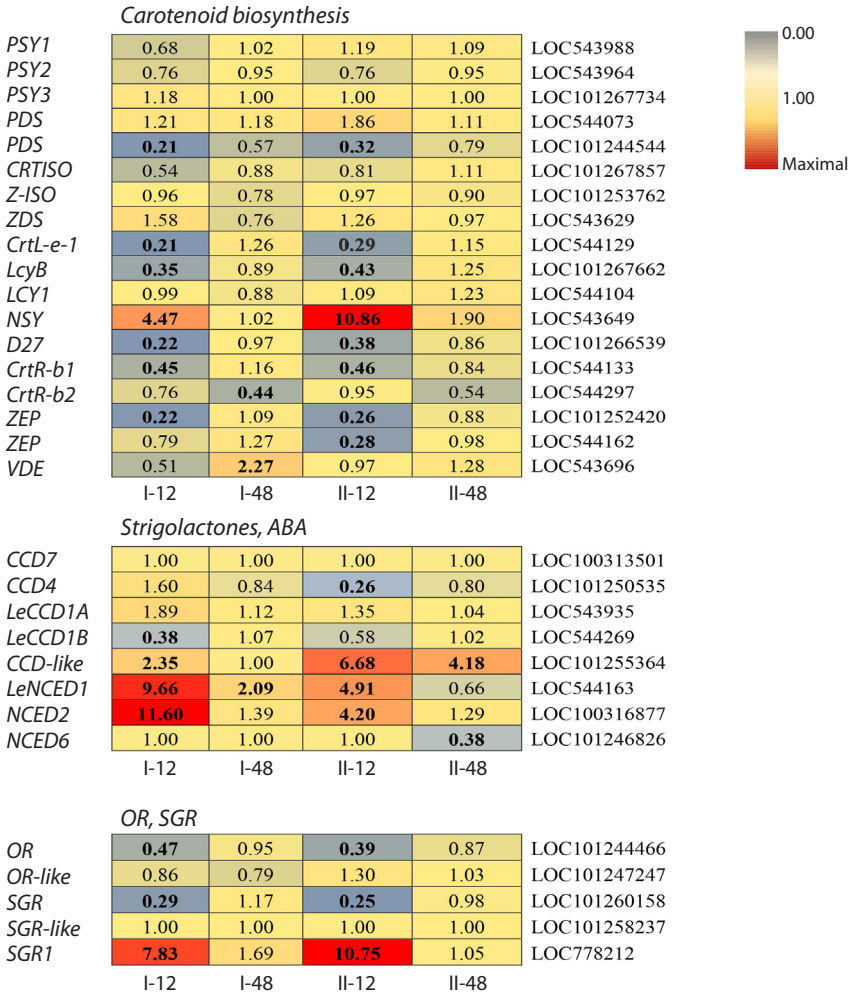


Fig. 4. Heatmap of changes in the expression of carotenoid, SGL and ABA biosynthesis genes, as well as *OR* and *SGR* genes, in the leaves of tomato cv. Otradnyi in response to two cycles (I, II) of "cold stress – recovery".

Constructed using the transcriptome data obtained for points I-12, II-12 (end of stress) and I-48, II-48 (recovery period).

the exception of an increased level of *Cab-1D*, *CAB12* and *CAB5*-LOC101257186 transcripts (I-48) (Fig. 3).

Among the other gene groups of the *LHC* family, the expression of both the *ELIP* genes and one of the ferrochelatases (LOC101263738) increases significantly towards the end of stress (I-12, II-12) and after recovery maintains an elevated value (I-48) or returns to the control level (II-48). The expression of two *LIL3* genes (LOC101260362, LOC101248227) and the *psbS* and *OHP1* genes, on the contrary, decreases in response to stress (I-12, II-12) and, upon recovery, returns to the control (I-48, II-48; except for the induction of *OHP1* in I-48). The remaining genes showed no significant changes in expression across the two stress – recovery cycles, with the exception of *SEP2* (upregulation, II-12) and one of *LIL3-2*-LOC101247899 (upregulation, II-48) (Fig. 3).

The previously formulated stress memory marker feature states that markers are genes, expression of which changes differently in response to the first and repeated stressful events, and to the recovery periods separating them (Friedrich et al., 2019; Bäurle, Trindade, 2020; Jacques et al., 2021). Given this, the *Cab-1A*, *Cab-1D*, *CAB12*, *CAB5*-LOC101257186, *ELIP*, *SEP2*, *OHP2*-LOC101259223, *OHP1* and *LIL3-2*-LOC101247899 genes, which showed intercycle differences in expression dynamics, may be considered candidates for such markers (Fig. 3).

In addition to the *LHC* family genes, transcriptome analysis of the carotenoid biosynthesis genes was performed. As a result, no significant response to both "cold stress – recovery" cycles was found for the genes of all three phytoene synthases (*PSY1–3*), one of the two *PDS*-LOC544073, *CRTISO*, *Z-ISO*, *ZDS*, and *LCY1* (Fig. 4). The second *PDS*-LOC101244544, *CrtL-e-1*, *LcyB*, *D27*, *CrtR-b1*, and one of the two *ZEP* genes showed the same expression dynamics: a decrease (I-12, II-12) and a return to the control level (I-48, II-48); the expression of the second *ZEP* gene had similar dynamics, except for a less significant decrease at point I-12 (Fig. 4). The level of *CrtR-b2* transcripts, on the contrary, decreased after the recovery periods (I-48, II-48). Two genes deserve special mention. The expression of the first one encoding neoxanthin synthase (*NSY*) was significantly increased in response to cold exposure (I-12, II-12) and returned to control levels after the recovery period (I-48, II-48). The level of transcripts of the second gene

encoding violaxanthin de-epoxidase (*VDE*) decreased in the first stress cycle (I-12), and then increased (I-48), and in the second cycle did not differ from the control (Fig. 4).

Among the genes encoding dioxygenases involved in the pathway for converting carotenoids into phytohormones (SGL, ABA), *CCD7* and *LeCCD1A* showed no significant response to two "cold stress – recovery" cycles. *CCD4* and *NCED6* expression differed from the control profile only by a decrease at points II-12 and II-48, respectively. The transcript levels of the *LeCCD1B* and *NCED2* genes significantly decreased and increased, respectively, after stress (I-12, II-12). The *CCD-like* and *LeNCED1* genes had transcript levels significantly higher than the control, except at points I-48 and II-48, respectively (Fig. 4).

Of the genes associated with chlorophyll synthesis and degradation, two (*OR-like*, *SGR-like*) showed no differences from the control, two (*OR*, *SGR*) had significantly reduced transcript levels after stress (I-12, II-12), and one (*SGR1*) had an increased level at the same points (I-12, II-12) (Fig. 4).

Given the definition of a stress memory marker (Friedrich et al., 2019; Bäurle, Trindade, 2020; Jacques et al., 2021), the following genes may be considered candidates: *VDE*, *CCD4*, *CCD-like*, *LeNCED1*, and *NCED6* (Fig. 4).

Discussion

The plant adaptive response to cold stress is closely linked to cellular osmoregulation mediated by ABA-induced stomatal closure (Sreenivasulu et al., 2012; Agurla et al., 2018). 9′-*cis*-neoxanthin serves as a precursor of ABA, and its increased synthesis in response to stress can be accompanied by a decrease in the content of violaxanthin cycle xanthophylls important for photosynthesis, leading to a decrease in the rate of photosynthesis (Nakashima, Yamaguchi-Shinozaki, 2013; Yamori et al. 2014; Chen et al., 2020; Xu et al., 2023). This disrupts the function of the antennae of photosystems I and II (Ashraf, Harris, 2013), which include proteins of the LHC family that bind chlorophylls *a*/*b* and carotenoids (Klimmek et al., 2006; Li et al., 2025). Studying *LHC* genes is therefore important for understanding their role in the cold stress response and determining plant cold tolerance.

Since the available information on the *S. lycopersicum LHC* genes varies (Lan et al., 2022; Meng et al., 2025), the first step was the identification of genes of this family using the above-mentioned publications and GenBank data (SolGenomics and NCBI). The results obtained differed from those of the studies (Lan et al., 2022; Meng et al., 2025) that used only the SolGenomics database, both in terms of the number and composition of the *LHC* family (see the Table). Our data are believed to be the most reliable since they are based on the latest version of the *S. lycopersicum* genome available in the NCBI database (from 2024 *vs*. 2019 in SolGenomics).

Considering the involvement of carotenoids in photosynthesis, the list of genes for analysis also included known genes of the carotenoid metabolism pathway (ElShamey et al., 2025), as well as *SGR* and *OR* genes associated with chlorophyll degradation (Pietrzykowska et al., 2014) and chlorophyll/carotenoid synthesis (Tee, 2019; Gao et al., 2025), respectively (see the Table).

Having selected the cold-resistant cv. Otradnyi for the study, we carried out two consecutive "cold stress – recovery" cycles (I, II), where each cycle included 12-h cooling (3 °C) followed by 60 h of normal conditions (Fig. 1). Since the level of *LHC* gene transcripts is regulated by circadian rhythms (Piechulla et al., 1998; Meng et al., 2025), we used control plants grown in parallel at normal temperature (23 °C), taking readings at the same points as the experiment.

Measurement of chlorophyll *a*/*b* and carotenoid contents in leaves collected at the end of the 12-h stress period (I-12, II-12) and during the recovery phase (I-48, II-48) showed that the amounts of all analyzed pigments decreased significantly at the end of the second cycle (II-48) (Fig. 2). This may suggest a more effective plant response to repeated cold stress due to a possible decrease in the rate of photosynthesis and an increase in osmoregulation, in accordance with data (Sreenivasulu et al., 2012; Agurla et al., 2018). That is, stress memory may have occurred in plants during the first cycle "cold stress – recovery", which could be reflected in transcriptomic data.

The same tomato leaf samples were used to obtain transcriptomes and analyze changes in the expression of genes of interest (see the Table): *LHC* family, carotenoid metabolism, *SGR* and *OR* genes. The observed decrease in transcript levels of most *LHC* genes and half of the carotenoid biosynthesis genes at the end of the stress exposure (I-12, II-12) (Fig. 3 and 4) may suggest a decrease in the rate of photosynthesis in tomato leaves in response to low temperature, since the rate of photosynthesis is positively associated with *LHC* gene expression (Yan et al., 2023). A sharp increase in the expression of the *SGR1* gene (Fig. 4), involved in chlorophyll degradation (Pietrzykowska et al., 2014), and a decrease in the expression of the *OR* gene (Fig. 4), positively associated with chlorophyll biogenesis and the development of thylakoid membranes (Tee, 2019), may also be associated with a decrease in photosynthesis. At the same time, a significant increase in the expression of the *NSY*, *CCD-like*, *LeNCED1*, and *NCED6* genes (Fig. 4) in I-12 and II-12 leaves may suggest increased ABA production (ElShamey et al., 2025), associated with stomatal closure in response to cold stress (Sreenivasulu et al., 2012; Agurla et al., 2018).

Previously, it was shown that the level of *S. lycopersicum LHC* gene transcripts increases during tomato plant adaptation to salt stress (Ikuyinminu et al., 2023). The discrepancy with our data (Fig. 3) can be explained both by the use of a different stress factor and by the use of the biostimulant PSI-475 by the authors before watering the plants with a saline solution (Ikuyinminu et al., 2023).

The publication (Meng et al., 2025) also presents data on the expression of *S. lycopersicum LHC* genes in response to a single-cycle 24-h cold stress. In particular, it was shown that the level of *SlLhcb1.11* (LOC108491835) gene transcripts decreases and *SlELIP1* (LOC101257109) increases (Meng et al., 2025), which is completely consistent with our results (Fig. 3). Silencing of *SlLhcb1.11* or *SlELIP1* in tomato plants leads to a decrease in chlorophyll content, impaired photosynthesis and cold resistance (Meng et al., 2025), indicating an important role of these genes in the adaptive response of *S. lycopersicum*. According to our data, the *SlELIP1* gene

may be a candidate for stress memory markers, since its expression profile differs between the first and second recovery periods (Fig. 3). In addition to *SlELIP1*, a number of genes correspond to the stress memory marker definition (Friedrich et al., 2019; Bäurle, Trindade, 2020; Jacques et al., 2021): *Cab-1A*, *Cab-1D*, *CAB12*, *CAB5*-LOC101257186, *SEP2*, *OHP2*-LOC101259223, *OHP1* and *LIL3-2*-LOC101247899, *VDE*, *CCD4*, *CCD-like*, *LeNCED1* and *NCED6* (Fig. 3 and 4).

Conclusion

Overall, in this study, we performed the first transcriptome analysis of the differential expression of *SlLHC* genes, carotenoid metabolism genes, and genes associated with chlorophyll synthesis and degradation in the leaves of a cold-tolerant tomato genotype during two consecutive cycles "cold stress – recovery". Signs of a possible decrease in the rate of photosynthesis were obtained: a decrease in the chlorophyll and carotenoid content at the end of the second cycle recovery (II-48) and a decrease in the transcript levels of most *LHC* family genes at the end of each chilling stage (I-12, II-12). At points I-12 and II-12, an increase in the expression of the *NSY*, *CCD-like*, *LeNCED1*, and *NCED6* genes was also detected, which may indicate a possible increase in ABA synthesis in response to low temperature. Based on the obtained expression dynamics, among the analyzed genes, candidates for the role of markers of tomato cold stress memory were identified, namely 10 *SlLHC* genes and five genes associated with ABA synthesis.

References

Agurla S., Gahir S., Munemasa S., Murata Y., Raghavendra A.S. Mechanism of stomatal closure in plants exposed to drought and cold stress. In: Iwaya-Inoue M., Sakurai M., Uemura M. (Eds) Survival Strategies in Extreme Cold and Desiccation. Advances in Experimental Medicine and Biology. Vol. 1081. Springer, 2018;215-232. doi 10.1007/978-981-13-1244-1_12

Aina O., Bakare O.O., Fadaka A.O., Keyster M., Klein A. Plant biomarkers as early detection tools in stress management in food crops: a review. *Planta.* 2024;259(3):60. doi 10.1007/s00425-024-04333-1

Ashraf M., Harris P.J.C. Photosynthesis under stressful environments: an overview. *Photosynthetica*. 2013;51:163-190. doi 10.1007/s11099-013-0021-6

Bäurle I., Trindade I. Chromatin regulation of somatic abiotic stress memory. *J Exp Bot.* 2020;71(17):5269-5279. doi 10.1093/jxb/eraa098

Browse J., Xin Z. Temperature sensing and cold acclimation. *Curr Opin Plant Biol.* 2001;4:241-246. doi 10.1016/s1369-5266(00)00167-9

Chen K., Li G.J., Bressan R.A., Song C.P., Zhu J.K., Zhao Y. Abscisic acid dynamics, signaling, and functions in plants. *J Integr Plant Biol.* 2020;62(1):25-54. doi 10.1111/jipb.12899

Ding Y., Shi Y., Yang S. Regulatory networks underlying plant responses and adaptation to cold stress. *Annu Rev Genet.* 2024;58(1):43-65. doi 10.1146/annurev-genet-111523-102226

Efremov G.I., Slugina M.A., Shchennikova A.V., Kochieva E.Z. Differential regulation of phytoene synthase PSY1 during fruit carotenogenesis in cultivated and wild tomato species (*Solanum* section Lycopersicon). *Plants.* 2020;9(9):1169. doi 10.3390/plants9091169

ElShamey E., Zeng Y., Ding Y., Yang J. Functional phytochemicals in tomatoes: biosynthesis, gene regulation, and human health implications. *Front Plant Sci.* 2025;16:1662388. doi 10.3389/fpls.2025.1662388

Filyushin M.A., Shchennikova A.V., Kochieva E.Z. Differential expression profile of DREB2 subfamily transcription factor genes in the dynamics of salt stress and post-stress recovery in tomato plants. *Vavilovskii Zhurnal Genetiki i Selektsii = Vavilov J Genet Breed.* 2025;29(8):1213-1220. doi 10.18699/vjgb-25-128

Friedrich T., Faivre L., Bäurle I., Schubert D. Chromatin-based mechanisms of temperature memory in plants. *Plant Cell Environ.* 2019;42(3):762-770. doi 10.1111/pce.13373

Gao Y., Zhou X., Huang H., Wang C., Xiao X., Wen J., Wu J., Zhou S., de Dios V.R., Rodríguez L.G., Yao Y., Liu J., Deng H. ORANGE proteins mediate adaptation to high light and resistance to *Pseudomonas syringae* in tomato by regulating chlorophylls and carotenoids accumulation. *Int J Biol Macromol.* 2025;306(Pt.4):141739. doi 10.1016/j.ijbiomac.2025.141739

Ikuyinminu E., Goñi O., Łangowski Ł., O'Connell S. Transcriptome, biochemical and phenotypic analysis of the effects of a precision engineered biostimulant for inducing salinity stress tolerance in tomato. *Int J Mol Sci.* 2023;24(8):6988. doi 10.3390/ijms24086988

Jacques C., Salon C., Barnard R.L., Vernoud V., Prudent M. Drought stress memory at the plant cycle level: a review. *Plants* (*Basel*). 2021;10(9):1873. doi 10.3390/plants10091873

Jansson S. A guide to the *Lhc* genes and their relatives in *Arabidopsis*. *Trends Plant Sci.* 1999;4(6):236-240. doi 10.1016/s1360-1385(99)01419-3

Kidokoro S., Shinozaki K., Yamaguchi-Shinozaki K. Transcriptional regulatory network of plant cold-stress responses. *Trends Plant Sci.* 2022;27(9):922-935. doi 10.1016/j.tplants.2022.01.008

Klimmek F., Sjödin A., Noutsos C., Leister D., Jansson S. Abundantly and rarely expressed *Lhc* protein genes exhibit distinct regulation patterns in plants. *Plant Physiol.* 2006;140(3):793-804. doi 10.1104/pp.105.073304

Lan Y., Song Y., Zhao F., Cao Y., Luo D., Qiao D., Cao Y., Xu H. Phylogenetic, structural and functional evolution of the LHC gene family in plant species. *Int J Mol Sci.* 2022;24(1):488. doi 10.3390/ijms24010488

Li Y., Cao T., Guo Y., Grimm B., Li X., Duanmu D., Lin R. Regulatory and retrograde signaling networks in the chlorophyll biosynthetic pathway. *J Integr Plant Biol.* 2025;67(4):887-911. doi 10.1111/jipb.13837

Love M.I., Huber W., Anders S. Moderated estimation of fold change and dispersion for RNA-seq data with DESeq2. *Genome Biol.* 2014;15(12):550. doi 10.1186/s13059-014-0550-8

Meng F., Ma M., Li S., Liang P., Liang Y., Shi H., Huang S., Su H., Deng Y., Akram M.A., Shen X., Feng R., Zhan X., Ma F. Genome-wide identification of light-harvesting chlorophyll a/b-binding (LHC) gene family in tomato and functional analysis of *SlLhcb1.11* and *SlELIP1* under cold stress. *Genomics.* 2025;117(2):111022. doi 10.1016/j.ygeno.2025.111022

Mesa T., Polo J., Arabia A., Caselles V., Munné-Bosch S. Differential physiological response to heat and cold stress of tomato plants and its implication on fruit quality. *J Plant Physiol.* 2022;268:153581. doi 10.1016/j.jplph.2021.153581

Nakashima K., Yamaguchi-Shinozaki K. ABA signaling in stress-response and seed development. *Plant Cell Rep.* 2013;32(7):959-970. doi 10.1007/s00299-013-1418-1

Neilson K.A., Mariani M., Haynes P.A. Quantitative proteomic analysis of cold-responsive proteins in rice. *Proteomics.* 2011;11(9):1696-1706. doi 10.1002/pmic.201000727

Piechulla B., Merforth N., Rudolph B. Identification of tomato *Lhc* promoter regions necessary for circadian expression. *Plant Mol Biol.* 1998;38(4):655-662. doi 10.1023/a:1006094015513

Pietrzykowska M., Suorsa M., Semchonok D.A., Tikkanen M., Boekema E.J., Aro E.-M., Jansson S. The light-harvesting chlorophyll *a/b* binding proteins Lhcb1 and Lhcb2 play complementary roles during state transitions in *Arabidopsis*. *Plant Cell*. 2014;26(9):3646-3660. doi 10.1105/tpc.114.127373

Soualiou S., Duan F., Li X., Zhou W. Nitrogen supply alleviates cold stress by increasing photosynthesis and nitrogen assimilation in maize seedlings. *J Exp Bot.* 2023;74(10):3142-3162. doi 10.1093/jxb/erad073

Sreenivasulu N., Harshavardhan V.T., Govind G., Seiler C., Kohli A. Contrapuntal role of ABA: does it mediate stress tolerance or plant growth retardation under long-term drought stress? *Gene.* 2012; 506(2):265-273. doi 10.1016/j.gene.2012.06.076

Tee E.E. Orange is the new green: Arabidopsis ORANGE represses chloroplast biogenesis. *Plant Cell.* 2019;31(12):2824-2825. doi 10.1105/tpc.19.00670

Villagómez-Aranda A.L., Feregrino-Pérez A.A., García-Ortega L.F., González-Chavira M.M., Torres-Pacheco I., Guevara-González R.G. Activating stress memory: eustressors as potential tools for plant breeding. *Plant Cell Rep.* 2022;41(7):1481-1498. doi 10.1007/s00299-022-02858-x

Xu C., Wang Y., Yang H., Tang Y., Liu B., Hu X., Hu Z. Cold acclimation alleviates photosynthetic inhibition and oxidative damage induced by cold stress in citrus seedlings. *Plant Signal Behav.* 2023; 18(1):2285169. doi 10.1080/15592324.2023.2285169

Yamori W., Hikosaka K., Way D.A. Temperature response of photosynthesis in C_3, C_4, and CAM plants: temperature acclimation and temperature adaptation. *Photosynth Res.* 2014;119(1-2):101-117. doi 10.1007/s11120-013-9874-6

Yan J., Liu J., Yang S., Jiang C., Liu Y., Zhang N., Sun X., … Liu Y., Sun Z., Qi M., Wang F., Li T. Light quality regulates plant biomass and fruit quality through a photoreceptor-dependent HY5-LHC/CYCB module in tomato. *Hortic Res.* 2023;10(12):uhad219. doi 10.1093/hr/uhad219

Zhang Q., Ma C., Wang X., Ma Q., Fan S., Zhang C. Genome-wide identification of the light-harvesting chlorophyll *a/b* binding (Lhc) family in *Gossypium hirsutum* reveals the influence of *GhLhcb2.3* on chlorophyll *a* synthesis. *Plant Biol* (*Stuttg*). 2021;23(5):831-842. doi 10.1111/plb.13294

Zhao S., Gao H., Luo J., Wang H., Dong Q., Wang Y., Yang K., Mao K., Ma F. Genome-wide analysis of the light-harvesting chlorophyll *a/b*-binding gene family in apple (*Malus domestica*) and functional characterization of *MdLhcb4.3*, which confers tolerance to drought and osmotic stress. *Plant Physiol Biochem.* 2020;154:517-529. doi 10.1016/j.plaphy.2020.06.022

Conflict of interest. The authors declare no conflict of interest.
Received March 11, 2026. Revised May 12, 2026. Accepted May 13, 2026.

PLANT GENETICS AND BREEDING
Original article

Vavilovskii Zhurnal Genetiki i Selektsii
Vavilov Journal of Genetics and Breeding. 2026;30(6):854-862

doi 10.18699/vjgb-26-87

Prebreeding studies of spring bread wheat lines, carrying T1BS.1BL-1S#F7L-1BL translocation with *Lr51* gene

S.N. Sibikeev [1], A.E. Druzhin [1], Z.E. Fitileva [1], I.V. Borisov [1, 2]

[1] Federal Center of Agriculture Research of the South-East Region, Saratov, Russia
[2] Institute of Biochemistry and Physiology of Plants and Microorganisms – Subdivision of Saratov Scientific Centre of the Russian Academy of Sciences, Saratov, Russia
sibikeev_sergey@mail.ru

Abstract. One of the sources of bread wheat resistance to the *Puccinia triticina* is the *Lr51* gene in the T1BS.1BL-1S#F7L-1BL translocation, from *Aegilops speltoides* Tausch. However, it is little used in the practical breeding of *Triticum aestivum* L. The main reason is the fear of the negative impact of translocation on important agronomic features. This paper presents the results of pre-breeding studies of lines-analogues of spring bread wheat cultivar Saratovskaya 68 – L6 and L7, carrying T1BS.1BL-1S#F7L-1BL translocation, compared with the recipient – Saratovskaya 68 and the standard – Saratovskaya 76. The presence of the *Lr51* gene was confirmed by PCR analysis with markers S30-13L and AGA7-759R. Lines L6 and L7 are resistant to saratov populations of *P. triticina*. The lines-analogues are cytologically stable. The presence of translocation in L6 and L7 did not significantly influence for plant height and lodging resistance. In lines-analogues, the duration of the germination-earing period is at the level of recipient and standard cultivars. For grain productivity, lines L6 and L7 do not significantly differ from Saratovskaya 68. However, lines L6 and L7 surpassed Saratovskaya 76 in 2024, but there were no differences for 2023–2025 period. Analysis of the structure of the elements productivity of the main ear for average 2023–2025 period showed that at the lines L6 and L7 no differences with the cultivar-recipient for all traits. But comparisons with Saratovskaya 76, show significant differences in favor of lines with translocation in terms of ear density, while L7 also had significant differences for grain weight from the ear and number grains in spikelet.The presence of the T1BS.1BL-1S#F7L-1BL translocation in L6 and L7 did not significantly affect the protein content, as well as the indicators of flour and bread, except for the volume and porosity of bread. Lines L6 and L7 were inferior to Saratovskaya 76 in terms of elasticity, the ratio of elasticity to extensibility (P/L), and the volume of bread, but surpassed the strength of flour (W). In general, in terms of cytological stability and the entire range of breeding-valuable indicators, the effect of T1BS.1BL-1S#F7L-1BL translocation in the genotype of the Saratovskaya 68 is assessed as neutral, and lines L6 and L7 have breeding significance for leaf rust resistance.

Key words: spring bread wheat; lines-analogous of cultivar Saratovskaya 68; T1BS.1BL-1S#F7L-1BL; resistance to leaf rust; influence for grain productivity and bread making quality

For citation: Sibikeev S.N., Druzhin A.E., Fitileva Z.E., Borisov I.V. Prebreeding studies of spring bread wheat lines, carrying T1BS.1BL-1S#F7L-1BL translocation with *Lr51* gene. *Vavilovskii Zhurnal Genetiki i Selektsii = Vavilov J Genet Breed*. 2026;30(6):854-862. doi 10.18699/vjgb-26-87

Funding. The research was carried out with the support of the Ministry of Science and Higher Education of the Russian Federation, project FWNF-2025-0003.

Пребридинговые исследования линий яровой мягкой пшеницы, несущих транслокацию T1BS.1BL-1S#F7L-1BL с геном *Lr51*

С.Н. Сибикеев [1], А.Е. Дружин [1], З.Е. Фитилева [1], И.В. Борисов [1, 2]

[1] Федеральный аграрный научный центр Юго-Востока, Саратов, Россия
[2] Институт биохимии и физиологии растений и микроорганизмов – обособленное структурное подразделение Федерального исследовательского центра «Саратовский научный центр РАН», Саратов, Россия
sibikeev_sergey@mail.ru

Аннотация. Одним из эффективных генов устойчивости к возбудителю листовой ржавчины (*Puccinia triticina*) у мягкой пшеницы (*T. aestivum* L.) является ген *Lr51*, интродуцированный в геном мягкой пшеницы от *Aegilops speltoides* Tausch в составе транслокации T1BS.1BL-1S#F7L-1BL. Однако этот ген редко используют в практической селекции из-за опасения негативного влияния чужеродной транслокации на агрономические важные признаки. В данной работе представлены результаты пребридинговых исследований яровых линий мягкой пшеницы Л6 и Л7, несущих T1BS.1BL-1S#F7L-1BL транслокацию, по сравнению с сортом-реципиентом

© Sibikeev S.N., Druzhin A.E., Fitileva Z.E., Borisov I.V., 2026
This work is licensed under a Creative Commons Attribution 4.0 License

Саратовская 68 и сортом-стандартом Саратовская 76 по комплексу селекционно значимых признаков. Наличие гена *Lr51* в генотипе линий Л6 и Л7 подтверждено ПЦР-анализом с использованием маркеров S30-13L и AGA7-759R. Фитопатологическая оценка линий Л6 и Л7 в условиях искусственного и естественного инфекционного фона к локальной популяции листовой ржавчины, распространенной в Саратовской области, показала их высокий уровень устойчивости в сравнении с сортом-реципиентом. По оценке цитологической стабильности линий, мейотический индекс составляет 98.2 и 99.7 у линий Л6 и Л7 соответственно. Наличие транслокации у Л6 и Л7 не влияло значимо на высоту растений и устойчивость к полеганию. У линий-аналогов продолжительность периода всходы–колошение оказалась на уровне сорта-реципиента и сорта-стандарта. По продуктивности зерна линии Л6 и Л7 также не отличались достоверно от сортов Саратовская 68 и Саратовская 76, по данным полевых испытаний за период 2023–2025 гг. Анализ структуры продуктивности главного колоса у линий Л6 и Л7 выявил отсутствие различий с сортом-реципиентом по всем показателям. По сравнению с сортом Саратовская 76 были достоверные различия в пользу линий-аналогов по плотности колоса, а у Л7 также по весу зерна с колоса и озерненности колоска. Наличие транслокации T1BS.1BL-1S#F7L-1BL у Л6 и Л7 незначимо повлияло на содержание белка, а также на качество муки и хлеба. Однако обе линии уступали сорту-реципиенту по таким признакам, как объем и пористость хлеба. Линии Л6 и Л7 уступали сорту Саратовская 76 по упругости, отношению упругости к растяжимости, объему хлеба, но превзошли по силе муки. В целом, с учетом цитологической стабильности и комплексу селекционно ценных показателей, влияние T1BS.1BL-1S#F7L-1BL транслокации в генотипе сорта Саратовская 68 оценивается как нейтральное, а линии Л6 и Л7 имеют селекционную значимость по устойчивости к листовой ржавчине.

Ключевые слова: яровая мягкая пшеница; линии-аналоги сорта Саратовская 68; T1BS.1BL-1S#F7L-1BL транслокация; устойчивость к листовой ржавчине; влияние на продуктивность и качество зерна

Introduction

Bread wheat (*Triticum aestivum* L. em. Thell) is one of the main food crops. Wheat accounts for over 27 % of the total global grain production. Intensive breeding for increased productivity of this crop has led to a significant reduction of its gene pool in terms of resistance genes to diseases and pests. The susceptibility of bread wheat varieties to diseases leads to huge losses in grain yield and a decrease in its quality. For example, average losses from leaf rust in Russia and foreign countries are 4–6 %, and under epiphytotic conditions of this pathogen, grain yield losses can reach 50–70 % (Dymchenko et al., 1990). In recent decades, an increase in the harmfulness of the disease spectrum of bread wheat has been noted for the Lower and Middle Volga regions of Russia. A severe stem rust epiphytotic was observed in 2016, a severe leaf rust and septoria leaf spot epiphytotic in 2017, a severe tan spot epiphytotic in 2019, a local but severe stem rust epiphytotic in 2020 and simultaneous moderate epiphytotics of stripe and leaf rust, powdery mildew, and tan spot in 2025. There is constant pressure on bread wheat plants from fungal diseases. Thus, the importance of increasing the yield of cultivated plants through resistance to biotic factors, which include a large group of phytopathogens, is sharply increasing. To avoid economically significant losses from bread wheat diseases, including rust species, constant scientifically based breeding for resistance to pathogens is necessary. This work should be based on knowledge of the pathogen's biology, its virulence, the resistance genetics of cultivated crops varieties, and a sufficient number and diversity of resistance genes to pathogens, i. e., it should be anticipatory (McIntosh, Brown, 1997). The most difficult task is to expand the genetic diversity of resistance genes to pathogens. For example, studies by O.A. Baranova (2020) on a set of 32 new bread wheat cultivars entered into the State Register of Selection Achievements of the Russian Federation for 2017–2018 showed that only 11 cultivars have high effectiveness against the stem rust pathogen. Of these, seven cultivars are protected by one gene *Sr31*, three cultivars by a combination of *Sr31*+*Sr57* and one cultivar *Sr31*+*Sr28*. Studies by E.I. Gultyaeva et al. (2025) on a set of 28 winter and 16 spring bread wheat cultivars approved for use in 2024 showed that seven winter and five spring bread wheat cultivars are resistant to the leaf rust pathogen, i. e., 25 and 37 %. However, only one winter bread wheat cultivar is resistant to the stripe rust pathogen.

Currently, effective resistance to pathogens in the majority of wheat cultivars is due to the presence of resistance genes introgressed from wild and cultivated relatives of bread wheat, rather than their own resistance genes. The species *Aegilops speltoides* Tausch 2*n* = 14, genome S (Schneider et al., 2008) should be particularly highlighted. Twelve identified genes transferred from this species are known, including six genes for resistance to leaf rust (*Lr28*, *Lr35*, *Lr36*, *Lr47*, *Lr51*, *Lr66*), three to stem rust (*Sr32*, *Sr39*, *Sr47*) and three to powdery mildew (*Pm12*, *Pm32*, *Pm53*) (grainsgenes.org/GG3/wgc, accessed February 11, 2026). I.G. Adonina et al. (2012) identified the T5BS.5BL-5SL translocation from *Ae. speltoides*, which carries an effective gene for leaf rust resistance, designated as *LrASP5*. Among the identified genes, the gene *Lr51* (laboratory designation *LrF7*), obtained from crossing the bread wheat cultivar Neepawa with *Ae. speltoides* source F, should be noted, and then six backcrosses were made to the cultivar Neepawa and a highly resistant line F7 to the leaf rust pathogen was obtained (Dvorak, 1977). In this line, a translocation from chromosome 1S *Ae. speltoides* to chromosome 1BL of the cultivar Neepawa – T1BS.1BL-1S#F7L-1BL (Dvorak, Knott, 1980) was localized. Later, in one derivative line from F7 – F-7-3, an intercalary translocation from 1S to 1BL ranging from 14 to 32 cM was established, including the loci *XAga7* and *Xmwg710* (Helguera et al., 2005). The gene *Lr51* for resistance to the leaf rust pathogen is semidominant and highly effective both in Russia (Gultyaeva et al., 2024, 2025), and abroad, particularly in the USA (Helguera et al., 2005). Despite the effectiveness of resistance, this gene is rarely used in commercial bread wheat cultivars. It is known

from the sources available to us that the *Lr51* gene has been identified in ten Egyptian bread wheat cultivars (Ashraf et al., 2015). Among Russian cultivars, this gene has not been identified (Gultyaeva et al., 2025). At the National Center of Grain named after P.P. Lukyanenko (FSBSO "NCG P.P. Lukyanenko"), a series of lines with combinations of *Lr51* with *Lr* genes have been obtained: *Lr10*, *Lr26*, *Lr28*, *Lr34*, *Lr35*, *Lr50*. The number of *Lr* genes in the combinations ranged from two to five (Davoyan, 2022). The reasons for the rare use of the translocation with *Lr51* are unclear. It is hypothesized that this translocation may negatively affect for agronomically valuable traits and reduce grain productivity overall (Helguera et al., 2005). However, there is no data on prebreeding studies of the T1BS.1BL-1S#F7L-1BL translocation; information on the impact of this translocation for grain yield and bread making quality is absent. The purpose of our research is: based on the results of a three-year study of spring bread wheat lines-analogous with T1BS.1BL-1S#F7L-1BL translocation, identify the influence of translocation on cytological stability, agronomically important traits, grain productivity and bread making quality, and thus determine its breeding value.

Materials and methods

The material used included the following samples:

Spring bread wheat cultivar Saratovskaya 68, which belongs to the erythrospermum variety, is valuable for quality, resistant to drought, susceptible to leaf and stem rust pathogens, and contains a gene *Lr10* ineffective against the leaf rust pathogen (Gultyaeva et al., 2020).

Spring bread wheat cultivar Saratovskaya 76 – a standard approved by the State Commission of the Russian Federation for the Testing and Protection of Selection Achievements for the Saratov region.

L6 and L7 lines are analogues of spring bread wheat cultivar Saratovskaya 68. Pedigree: Saratovskaya 68/F-7-3*3// Saratovskaya 68. Lines analogues were obtained after crossing with line F-7-3 and triple backcrossing with cultivar Saratovskaya 68, where the pedigree of the near-isogenic line F-7-3 = Neepawa*6/*Triticum speltoides*, contains translocation T1BS.1BL-1S#F7L-1BL with the gene *Lr51*. The line F-7-3 was kindly provided by Doctor of Biological Sciences E.I. Gultyaeva (FSBSI VIZR, Saint Petersburg, Pushkino). Lines L6 and L7 belong to the erythrospermum variety and are highly resistant to the leaf rust pathogen.

Cytogenetic studies. The cytological stability was assessed by studying chromosome behavior during microsporogenesis in meiosis. Meiosis stages in microsporogenesis were studied on temporary squashed preparations of anthers. Spikes of lines L6 and L7 were cut before emerging from the leaf sheath and fixed in a mixture of 96 % ethanol and glacial acetic acid (3:1). Twenty-four hours after fixation, the material was transferred to 70 % ethyl alcohol, where it was stored until analysis at t = +2–4 °C. Schiff reagent was used as a dye staff. For each line, 100–200 microsporocytes at meiosis stages (metaphase I and II, anaphase I and II, telophase I and II, tetrads) were analyzed. Slides were analyzed on a microscope Axio Scope A 1 (Carl Zeiss) with objectives N-ACHROPLAN 40x/0.65 and N-ACHROPLAN 100x/1.25 0;1.

Phytopathological analysis. Under field conditions, the degree of resistance to the leaf rust pathogen was evaluated according to the reaction type of the Mains and Jackson scale (1926), where: 0 – absence of symptoms; 0; – necroses without pustules; 1 – very small pustules surrounded by necrosis; 2 – medium-sized pustules surrounded by necrosis or chlorosis; 3 – medium-sized pustules without necrosis; 4 – large pustules without necrosis, X – pustules on the same leaf of different types, with chloroses and necroses present. Plants with infection types 0–2 were classified as resistant (R), and 3, 4, and X (S) – as susceptible. The percentage of rust infection was assessed according to the R.F. Peterson et al. (1948) scale.

For laboratory evaluation, mixed Saratov populations of *Puccinia triticina* with artificially increased presence of pathotype *pp19*, virulent to gene *Lr19* were used. Seedlings (three-leaf stage), grown in soil-filled containers, were sprayed with an aqueous spore suspension of the population with the addition of Tween 80 detergent. The suspension concentration was 1 mg inoculum per 1 mL of water. After plant inoculation, a dark period was created for 20 hours at 100 % relative humidity, then seedlings were grown at a temperature of 20–22 °C, with a photoperiod of 16 h day/8 h night. The type of reaction to the pathogen of seedlings was determined according to the Mains and Jackson scale (1926).

Molecular genetic analysis. For PCR analysis, DNA was isolated from five-day-old wheat seedlings using the cetyltrimethylammonium bromide (CTAB) method (Murray, Thompson, 1980). For the identification of the resistance gene *Lr51* CAPS-marker was used, for the gene AGA7, located in *Ae. speltoides* translocation, containing *Lr51*. Primers S30-13L 5′-GCATCAACAAGATATTCGTTATGACC-3′ and AGA7-759R 5′-TGGCTGCTCAGAAAACTGGACC-3′ proposed in the work by M. Helguera et al. (2005) were used. Amplification was carried out on T100 Thermal Cycler (BioRad) amplifiers. Restriction was performed using the endonuclease PstI (SibEnzyme). Separation of amplification products was carried out in a 2 % agarose gel stained with ethidium bromide. The positive control was near-isogenic line F 7-3, and the negative control was the recipient cultivar Saratovskaya 68. GeneRulerTM 100bp DNA Ladder ("Evrogene") was used as a molecular weight marker. PCR was performed in duplicate.

Evaluation of grain productivity indicators, physical and baking properties of dough and bread in lines L6, L7, and the standard cultivar Saratovskaya 76 was conducted in 2023–2025. Experimental material was randomly sown in plots of 7 m^2 in 3-fold repetition on the experimental field of Federal Center of Agriculture Research of the South-East Region in Saratov. Sowing rate was 400 grains per 1 m^2. In addition to phenological observations and direct assessment of grain yield, studies of the elements of main spike productivity were conducted: spike length, number of spikelets and grains, grain weight per spike, spike density, grain set per spikelet (as a generalized fertility indicator), which were determined for 15 spikes of the studied lines and the standard cultivar. Bread making quality traits were evaluated by the content of crude gluten, the strength of which was determined using the Gluten Deformation Meter – IDK-3M ("PLAUN"), as well as by

Table 1. Hydrothermal coefficients for the Saratov meteorological station (Federal Center of Agriculture Research of the South-East Region) for 2023–2025

Saratov meteorological station (FCAR of the South-East Region)	2023				2024				2025		
	V	VI	VII	VIII	IV	V	VI	VII	V	VI	VII
Hydrothermal coefficient	0.8	1.1	0.6	0.4	0.3	0.2	0.8	0.1	1.1	0.8	0.5

Note. IV – April, V – May, VI – June, VII – July, VIII – August.

the Chopin alveograph (Chopin Technologies) traits with the baking of experimental samples of bread. The protein content in grain from the 2023–2025 harvests was determined using the Foss Infratec TM 1241 grain analyzer (Foss Analytical A/S).

Meteorological characteristics of the growing years according to the Selyaninov hydrothermal coefficient (HTC) (www.agrometeo.online/articles/gtk.htm, accessed January 26, 2026) by months of the vegetation period are given in Table 1. Of the three years of research, the most favorable meteorological conditions were in 2023 and 2025. Epiphytotics of leaf rust were observed in all three years of research, with the greatest pathogen development observed in the 2023 and 2025 growing seasons.

The obtained data on lines L6 and L7, recipient and standard cultivars Saratovskaya 68 and Saratovskaya 76 were subjected to a one-way variance analysis with multiple comparisons according to Duncan using the Agros-2.10 breeding and genetic software package.

Results

Cytological stability of L6 and L7 lines

To assess meiotic stability, an integrated indicator called the meiotic index is used. This indicator represents the percentage of normal tetrads relative to the total number of cells studied. Studies have shown that L6 had a meiotic index of 98.2 %, L7 had a meiotic index of 99.0 %, while the recipient cultivar Saratovskaya 68 had a meiotic index of 98.8 %. This indicates that there were no differences between the lines and the recipient cultivar for this indicator. The plants with a meiotic index of 90 % or higher is considered cytologically stable, indicating that both lines are stable. In earlier stages of meiosis, two chromosomes were detected in both lines that were not included in the nuclei in telophase I in an amount of 0.07 %. Among the mononuclear pollen, micropollen was detected in L6 and L7: 0.02 % in L6 and L7, and 0.01 % in Saratovskaya 68.

Phytopathological analysis of lines L6 and L7 for resistance to leaf rust. Identification of the leaf rust resistance gene *Lr51* using DNA markers S30-13L and AGA7-759R

L6 and L7 showed high resistance to *P. triticina* in 2023–2025, both during artificial infection and during natural epiphytotics of the pathogen (Table 2). Considering that plants were at the three-leaf stage during artificial infection with *P. triticina* and field evaluations were conducted during milky or milky-wax ripeness, this suggests a juvenile nature of the resistance gene in the lines L6 and L7. At the same time, the recipient cultivar Saratovskaya 68 and the standard cultivar Saratovskaya 76 were susceptible to the leaf rust pathogen. Results of gene *Lr 51* identification by PCR analysis using DNA markers S30-13L and AGA7-759R in the analyzed lines L6 and L7 showed its presence (see the Figure).

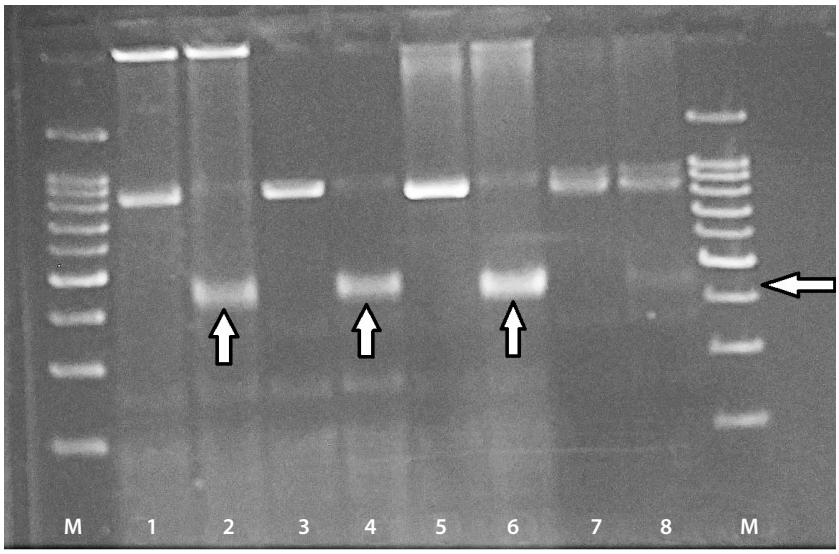
Phenology, grain productivity and bread making quality traits in the lines L6 and L7, recipient cultivar Saratovskaya 68 and standard cultivar Saratovskaya 76

In Table 3 the traits of the germination–heading period, plant height, and lodging resistance in the 2023–2025 growing seasons are given for lines L6, L7, recipient and standard cultivars. During the 2023–2025 growing seasons, the germination–heading period of the lines L6, L7 and the Saratovskaya 68, Saratovskaya 76 cultivars was almost the same

Table 2. Characteristics of resistance of spring bread wheat lines L6 and L7, cultivars Saratovskaya 68 and Saratovskaya 76 to *Puccinia triticina* in the field (natural epiphytotics) and laboratory (artificial infection)

Cultivar, line	Infection type to *P. triticina*					
	artificial infection (laboratory assessment)			natural epiphytotics		
	2023	2024	2025	2023	2024	2025
Saratovskaya 68	3	3	3	3/20	3/10	3/5
L6	0;	0; 1	0; 1	0; 1	0;	0;
L7	0;	0; 1	0; 1	0; 1	0;	0;
Saratovskaya 76	3	3	3	3/20	3/10	3/5

Note. Laboratory assessment at the 3-leaf stage. The assessment was carried out during natural epiphytotics *of P. triticina* in the experimental field of FCAR of the South-East Region, Saratov.



Electrophoregram of amplification and restriction products using primers S30-13L and AGA7-759R, diagnosing the *Lr51* gene.

M – marker of DNA lengths, 100 bp ("Eurogen"). The amplification product with a marker size of 819 bp was determined in line F7-3 *Lr51* (1) and in lines-analogous L6 (3), L7 (5). Tracks 2, 4, 6 are restriction products of PstI amplicons, respectively, F7-3 *Lr51*, L6 and L7. Track 7 is the recipient Saratovskaya 68. Track 8 is the restriction product of the PstI amplicon of the recipient Saratovskaya 68.

and the differences were insignificant. Thus, the translocation T1BS.1BL-1S#F7L-1BL has almost no effect on the germination–heading period. In terms of plant height in 2023 and 2025, the lines L6 and L7 differed insignificantly from the Saratovskaya 68 and Saratovskaya 76 cultivars, but in 2024, line L6 significantly outperformed both cultivars, and in 2025, the differences were between the lines – L7 exceeded L6. On average, for the period 2023–2025, there were no differences in plant height between cultivars (Saratovskaya 68 – 86 cm, Saratovskaya 76 – 85 cm) and lines (L6 – 88 cm, L7 – 89 cm), as well as between the lines themselves. Thus, the translocation T1BS.1BL-1S#F7L-1BL in the Saratovskaya 68 cultivar did not lead to a significant change in plant height. Plant height affects plant resistance to lodging. In our studies, L7 was significantly inferior in this trait to both cultivars and L6 in the 2023 growing season. In 2024, L7 was inferior to the Saratovskaya 76. In 2025, there were no differences between lines and cultivars. On average, for the period 2023–2025, there were no differences for lodging resistance between cultivars (Saratovskaya 68 – 4.0 and Saratovskaya 76 – 4.0) and lines (L6 – 4.0 and L7 – 3.7), or between lines themselves. However, a decrease in lodging resistance was observed in L7. Comparisons of L6, L7 for grain productivity and its elements in the main spike made it possible to identify the influence of the translocation T1BS.1BL-1S#F7L-1BL on these traits (Tables 4 and 5).

It was found that the presence of the translocation T1BS.1BL-1S#F7L-1BL in both lines L6 and L7 during the

Table 3. The period of germination–heading, plant height, resistance to lodging in L6, L7 and the cultivars Saratovskaya 68 and Saratovskaya 76 for the growing seasons of 2023–2025

Cultivar, line	Germination–heading period, days			Plant height, cm			Lodging resistance, points		
	2023	2024	2025	2023	2024	2025	2023	2024	2025
Saratovskaya 68 rec	47	41	45	89.7	68.3	100.0	3.7	4.1	4.1
L6	47	41	44	89.0	75.5	99.0	3.6	4.1	4.2
L7	47	41	45	91.2	73.0	104.0	3.0	4.0	4.2
$LSD_{0.5}$*	NS	NS	NS	NS	5.0	4.0	0.5	NS	NS
Saratovskaya 76 st	47	41	45	90.0	66.0	100.0	3.6	4.3	4.0
$LSD_{0.5}$**	NS	NS	NS	NS	5.2	4.0	0.5	0.2	NS

Note. The least significant difference for the 5 % significance level between L6, L7 and: Saratovskaya 68 (*) and Saratovskaya 76 (**). Here and in Tables 4–6: NS – no difference.

Table 4. The productivity and weight of 1,000 grains of spring bread wheat lines L6, L7 and cultivars Saratovskaya 68, Saratovskaya 76 for the growing seasons 2023–2025

Cultivar, line	Weight of 1,000 grains, g				Grain yield, t/ha			
	2023	2024	2025	average	2023	2024	2025	average
Saratovskaya 68	36.1	32.7	35.5	34.8	3.142	2.238	3.551	2.977
L6	37.0	36.3	34.6	36.0	2.990	2.713	3.250	2.984
L7	37.8	33.6	32.1	34.5	3.244	2.596	3.427	3.022
$LSD_{0.5}$*	NS	3.1	3.0	NS	NS	NS	NS	NS
Saratovskaya 76	38.6	35.4	35.9	36.6	2.776	2.042	3.492	2.770
$LSD_{0.5}$**	NS	NS	3.0	NS	NS	0.501	NS	NS

Note. The least significant difference for the 5 % significance level between L6, L7 and: Saratovskaya 68 (*) and Saratovskaya 76 (**).

Table 5. The elements of the main spike productivity of spring bread wheat lines L6, L7, recipient cultivar Saratovskaya 68 and standard cultivar Saratovskaya 76 on average for the growing seasons 2023–2025

Cultivar, line	Spike length, mm	Number		Spike density	Grain weight per spike, g	Grains for one spikelet, pcs
		spikelets, pcs	grains per spike, pcs			
L6						
Saratovskaya 68	85.97	16.97	42.70	1.87	1.63	2.52
L6	81.53	16.43	40.40	1.90	1.50	2.46
$HCP_{0.5}$*	NS	NS	NS	NS	NS	NS
Saratovskaya76	91.37	16.60	40.30	1.70	1.42	2.40
$LSD_{0.5}$**	NS	NS	NS	0.176	NS	NS
L7						
Saratovskaya 68	85.97	16.97	42.70	1.87	1.63	2.52
L7	85.63	17.27	44.67	1.90	1.73	2.58
$LSD_{0.5}$*	NS	NS	NS	NS	NS	NS
Saratovskaya 76	91.37	16.60	40.3	1.70	1.42	2.40
$LSD_{0.5}$**	NS	NS	NS	0.076	0.252	0.152
L6 and L7						
L6	81.53	16.43	40.4	1.90	1.50	2.46
L7	85.63	17.27	44.67	1.90	1.73	2.58
$LSD_{0.5}$	NS	NS	NS	NS	NS	NS

Note. The least significant difference for the 5 % significance level between the line and: the recipient cultivar Saratovskaya 68 (*) and the standard cultivar Saratovskaya 76 (**).

study years did not significantly affect for grain yield compared to the Saratovskaya 68 (Table 4). However, differences were observed compared to the standard Saratovskaya 76 during the 2024 growing season; the cultivar was significantly inferior to both lines (Table 4). As shown by the hydrothermal coefficients data, drought from strong to weak was observed during the 2024 growing season (Table 1). Thus, there is reason to assume that L6 and L7 with the translocation T1BS.1BL-1S#F7L-1BL are more drought-resistant than the standard Saratovskaya 76, but are of the same level as the recipient Saratovskaya 68. One of the factors that affects grain productivity is the 1,000 grain weight. On average, there were no significant differences in this trait between lines L6, L7 and cultivars Saratovskaya 68 and Saratovskaya 76 over the period 2023–2025, but there were differences in individual years. L6 surpassed the recipient Saratovskaya 68 for 1,000 grain weight in 2024, and L7 was inferior to both Saratovskaya 68 and Saratovskaya 76 in 2025 (Table 4). Analysis of the elements of the main spike productivity revealed that L6 and L7 with the translocation T1BS.1BL-1S#F7L-1BL did not differ significantly from the recipient Saratovskaya 68 for all parameters. Thus, there is reason to assess the effect of the translocation T1BS.1BL-1S#F7L-1BL on the elements of the main spike productivity as neutral. However, significant differences for spike density were found between the standard cultivar Saratovskaya 76 and both L6 and L7. Furthermore, L7 significantly

Table 6. Bread making quality traits for spring bread wheat lines L6, L7, recipient cultivar Saratovskaya 68 and standard cultivar Saratovskaya 76 on average for the growing seasons 2023–2025

Cultivar, line	Protein content, %	Gluten		Alveograph			Bread evaluation indices		
		%	IDK 3, units of device	dough elasticity P, mm	ratio of dough elasticity to extensibility P/L	flour strength W, unit of alveograph	loaf volume V, mL	porosity, point	crumb color
Saratovskaya 68	16.1	30.23	69.4	71.0	0.81	301	712	4.8	white
L6	16.6	31.07	63.9	84.9	1.00	333	597	3.8	
L7	16.3	31.63	65.5	74.5	0.91	320	602	4.3	
$LSD_{0.5}$*	NS	NS	NS	9.1	NS	NS	94	0.5	–
Saratovskaya 76	16.3	31.1	73.9	98.0	1.57	270	707	4.5	white
$LSD_{0.5}$**	NS	NS	6.1	10.1	0.6	35	96	NS	–

Note. The least significant difference for the 5 % significance level between L6, L7 and: the recipient cultivar Saratovskaya 68 (*) and the standard cultivar Saratovskaya 76 (**).

exceeded the standard cultivar for grain weight per spike and grains for one spikelet. There were no significant differences between the L6 and L7 lines for terms of the elements of the main spike productivity (Table 5).

The following results were obtained for bread making quality traits in the studied lines. Grain protein content in L6 and L7 did not differ significantly from either the recipient or standard cultivars. Similarly, no significant differences were found for gluten content or strength compared to the recipient cultivar Saratovskaya 68. However, gluten strength in the lines L6 and L7, as measured by the IDK-3M gluten testing device, was stronger than that of the standard cultivar Saratovskaya 76 (Table 6).

According to the alveograph indices, L6 demonstrated significantly higher dough elasticity (P) compared to the recipient cultivar and the line L7, but L7 did not differ from the Saratovskaya 68 for this parameter. In terms of the elasticity-to-extensibility ratio (P/L) and flour strength (W), the lines L6 and L7 did not differ significantly from the recipient cultivar. However, they significantly reduced the loaf volume, and L6 also reduced the bread porosity rating. The comparison of the L6, L7, and the Saratovskaya 76 cultivar for bread making quality traits revealed greater differences. In terms of elasticity, both lines were inferior to the standard cultivar, while L6 did not differ in terms of the elasticity-to-extensibility ratio, but L7 had a lower value. For flour strength trait, both lines significantly exceeded the Saratovskaya 76, but had a significantly lower loaf volume, and there were no differences in crumb porosity. The translocation T1BS.1BL-1S#F7L-1BL in the lines L6 and L7 did not change the color of the bread crumb; both lines, like the recipient and the standard cultivars, had a white crumb (Table 6).

Discussion

Wild relatives of bread wheat possess many genes of agronomic interest and may be valuable sources of resistance to diseases, insects, and extreme environmental factors. This primarily concerns species closely related to bread wheat, including *Ae. speltoides* Tausch $2n = 14$, genome S. This species belongs to the secondary gene pool of bread wheat (Shneider et al., 2008). Overall, this species is attractive due to its immunity to a number of diseases and its greater capacity for recombination with bread wheat chromosomes. This greater capacity for recombination is due to both the relatives of the S and B genomes and the presence of genes in the S genome that suppress the homologous conjugation gene system (*Ph*) and allow synapsis of homeologous chromosomes. As noted above, 12 genes transferred from this species were registered in the Catalogue of Wheat Gene Symbols, including six genes for resistance to leaf rust, three to stem rust, and three to powdery mildew (grainsgenes.org/GG3/wgc, accessed February 11, 2026). The 1S, 2S, 3S, 5S, 6S, and 7S chromosomes of *Ae. speltoides* were involved in the process of recombinogenesis with the chromosomes of bread wheat. The most of the transferred genes for resistance to pathogens from this species included regions of the 2S chromosome (*Lr35*, *Sr32*, *Sr39*, *Sr47*). From the remaining chromosomes of *Ae. speltoides* there were one or two transfers with resistance genes. Translocations were transferred from chromosome 1S to chromosome 1B: 1BL.1SS (*Pm32*) and 1BS.1BL-1S#F7L-1BL (*Lr51*). Thus, both arms of chromosome 1S were involved in the exchanges (grainsgenes.org/GG3/wgc, accessed February 11, 2026).

In our studies, based on the lines-analogous of spring bread wheat cultivar Saratovskaya 68 with the translocation 1BS.1BL-1S#F7L-1BL with the *Lr51* gene, we studied for cytological stability, determined the effect on morpho-biological and phenological traits, the effectiveness of protection against the leaf rust pathogen, as well as grain productivity and the bread making quality. Unfortunately, we were unable to find reports of similar studies from the sources available to us. Therefore, a comparison of the results of our studies with the results of other studies is not possible.

One factor limiting the practical application of introgression lines is their instability, leading to the rapid loss of alien genetic material. This instability is due to disturbances in the

meiotic cycle of hybrid plants, causing the formation of non-functional gametes (Orlovskaya et al., 2015). Lines with alien translocations obtained by the method of induced homeologous exchanges or spontaneous exchanges between chromosomes of an alien species and chromosomes of common wheat are characterized by greater stability (Sears, 1972; Friebe et al., 2000). The translocation T1BS.1BL-1S#F7L-1BL used by us with the *Lr51* gene in the original F-7-3 line was obtained during crosses (backcrossing) of the cultivar Neepawa with *Ae. speltoides* source F. That is, there is reason to assume a homeological exchange between of the *Ae. speltoides* and bread wheat chromosomes. It is known that *Ae. speltoides* species itself carries both the gene(s) that suppress the action of the *Ph* genes (paired conjugation) and the gametocidal genes that affect microsporogenesis and pollen viability, but the localization of these genes does not affect chromosome 1S (grainsgenes.org/GG3/wgc, accessed February 11, 2026). In this regard, there was reason to expect minor violations of cytological stability in the lines L6 and L7 compared to the recipient cultivar Saratovskaya 68. In general, our study determined the cytological stability in the lines L6 and L7, the meiotic index reached 98.2 and 99.0 %, and 98.8 % in the recipient cultivar Saratovskaya 68.

The *Lr51* gene was highly effective against the Saratov populations of *P. trticina* in the growing seasons of 2023–2025, which coincides with the data of E.I. Gultyaeva for the effectiveness of this gene in the Russian Federation (Gultyaeva et al., 2024). The presence of the translocation T1BS.1BL-1S#F7L-1BL in L6 and L7 did not significantly affect for plant height and lodging resistance either in comparison with the recipient cultivar Saratovskaya 68 or the standard Saratovskaya 76. However, it should be noted that the lodging resistance in L7 decreased in the 2023 and 2024 growing seasons. In the lines-analogous of Saratovskaya 68, the duration of the germination-heading period was at the level of the recipient and the standard cultivars. For grain productivity, the lines with the translocation T1BS.1BL-1S#F7L-1BL did not differ significantly from the recipient cultivar, either in individual years or on average for the period 2023–2025. However, compared with the standard cultivar Saratovskaya 76, the L6 and L7 lines significantly outperformed Saratovskaya 76 in 2024, but there were no differences in 2023 and 2025 and for the period 2023–2025 on average. The detailed analysis of the elements of the main spike productivity on average for 2023–2025 for the lines with the translocation T1BS.1BL-1S#F7L-1BL showed no differences with the recipient cultivar Saratovskaya 68 for all traits. Nevertheless, compared with the standard cultivar Saratovskaya 76, there were significant differences in favor of the lines with the translocation for spike density, and for L7 also in terms of grain weight per spike and grains for one spikelet. The presence of the translocation T1BS.1BL-1S#F7L-1BL in L6 and L7 did not significantly affect for protein content, nor flour and bread indices, except for loaf volume and porosity. Both lines were inferior to the recipient cultivar. By the comparisons with the standard cultivar Saratovskaya 76, the results were mixed. The lines with the translocation were inferior to Saratovskaya 76 for elasticity, the elasticity-to-extensibility ratio, and loaf volume, but surpassed it for flour strength. Based on the above results, M. Helguera's hypothesis (Helguera et al., 2005) on the negative impact of translocation with *Lr 51* gene, associated with its large size, is not confirmed. However, different interactions of the translocation T1BS.1BL-1S#F7L-1BL with different recipient genotypes are possible, which will change the impact on agronomically valuable traits. The different effects were observed in near-isogenic lines of spring bread wheat carrying translocation 7DL-7Ae#1L·7Ae#1S with the gene *Lr29* in the Saratovskaya 68 and Saratovskaya 70 cultivars (Sibikeev et al., 2022).

Conclusion

Overall, the impact of translocation T1BS.1BL-1S#F7L-1BL in the Saratovskaya 68 genotype is assessed as neutral based on cytological stability and the entire range of breeding-valuable traits. Furthermore, this translocation did not reduce grain productivity under the drought conditions of 2024, indicating that its presence does not reduce drought tolerance. The comparisons with the standard cultivar Saratovskaya 76 demonstrated sufficient breeding significance for lines L6 and L7 with translocation T1BS.1BL-1S#F7L-1BL in the Saratovskaya 68 genotype.

References

Abdelbacki A.M.M., Omara R.I., Soliman N.E.K., Najeeb M.A. Molecular markers identification of leaf rust resistant genes Lr19, Lr21, Lr24, Lr47 and Lr51 in selected Egyptian wheat cultivars. *Int J Phytopathol*. 2015;04(02):55-62. doi 10.33687/phytopath.004.02.0873

Adonina I.G., Petrash N.V., Timonova E.M., Khristov Yu.A., Salina E.A. Construction and study of leaf rust-resistant common wheat lines with translocations of *Aegilops speltoides* Tausch. Genetic material. *Russ J Genet*. 2012;48(4):404-409. doi 10.113/S1022795412020020

Baranova O.A. Molecular identification of stem rust resistance genes in new regional wheat varieties. *Plant Protection News*. 2020;103(2):113-118. doi 10.31993/2308-6469-2020-103-2-4936 (in Russian)

Davoyan E.R. Creation of a new, genetically diverse source material for breeding bread wheat based on methods of chromosomal engineering and DNA labeling: Dissertation for the degree of Doctor of Biological Sciences. Krasnodar, 2022 (in Russian)

Dvorak J. Transfer of leaf rust resistance from *Aegilops speltoides* to *Triticum aestivum*. *Can J Genet Cytol*. 1977;19:133-141

Dvorak J., Knott D.R. Chromosome location of two leaf rust resistance genes transferred from *Triticum speltoides* to *T. aestivum. Can J Genet Cytol*. 1980;22:381-389

Dymchenko A.M., Nazarova L.N., Zhemchuzhina A.I. Promising and zoned varieties of winter wheat with different resistance to brown rust. *Selektsiya i Semenovodstvo*. 1990;(5):16-18 (in Russian)

Friebe B., Raupp W.J., Gill B.S. Wheat – alien translocation lines. *Annu Wheat Newslett*. 2000;46. Available: https://graingenes.org/ggpages/awn/46/

Gultyaeva E.I., Sibikeev S.N., Druzhin A.E., Shaydayuk E.L. Enlargement of genetic diversity of spring bread wheat resistance to leaf rust (*Puccinia triticina* Erics.) in Lower Volga region. *Agric Biol*. 2020;55(1):27-44. doi 10.15389/agrobiology.2020.1.27rus (in Russian)

Gultyaeva E., Shaydayuk E., Shreyder E., Kushnirenko I., Shamanin V. Genetic diversity of promising spring wheat accessions from Russia and Kazakhstan for rust resistance. *Plants*. 2024;13(17):2469. doi 10.3390/plants13172469

Gultyaeva E.I., Shaydayuk E.L., Zuev E.V. The potential of modern Russian winter and spring wheat (*Triticum aestivum* L.) varieties for genetic protection against leaf and yellow rust. *Agric Biol*. 2025;60(3):485-502. doi 10.15389/agrobiology.2025.3.485rus (in Russian)

Helguera M., Vanzetti L., Soria M., Khan I.A., Kolmer J., Dubcovsky J. PCR markers for *Triticum speltoides* leaf rust resistance gene *Lr51* and their use to develop isogenic hard red spring wheat lines. *Crop Sci*. 2005;45:728-734. doi 10.2135/cropsci2005.0728

Mains E.B., Jackson H.S. Physiological specialization in the leaf rust of wheat *Puccinia triticina* Erikss. *Phytopathology*. 1926;16: 89-120

McIntosh R.A., Brown G.N. Anticipatory breeding for resistance to rust diseases in wheat. *Ann Rev Phytopatol*. 1997;35:311-326. doi 10.1146/annurev.phyto.35.1.311

Murray M.G., Thompson W.F. Rapid isolation of high molecular weight plant DNA. *Nucleic Acids Res*. 1980;8(19):4321-4325. doi 10.1093/nar/8.19.4321

Orlovskaya O.A., Leonova I.N., Adonina I.G., Salina E.A., Khotyleva L.V., Shumny V.K. Molecular-cytogenetic analysis of triticale and wheat lines with introgressions of the tribe Triticeae species genetic material. *Vavilovskii Zhurnal Genetiki i Selektsii = Vavilov J Genet Breed*. 2015;19(5):552-560. doi 10.18699/VJ15.072 (in Russian)

Peterson R.F., Campbell A.B., Hannah A.E. A diagrammatic scale for estimating rust intensity on leaves and stems of cereals. *Can J Res*. 1948;26(5):496-500. doi 10.1139/cjr48c-033

Schneider A., Molnar I., Molnar-Lang M. Utilisation of *Aegilops* (goatgrass) species to widen the genetic diversity of cultivated wheat. *Euphytica*. 2008;163:1-19. doi 10.1007/s10681-007-9624-y

Sears E.R. Chromosome engineering in wheat. In: Stadler Genetical Symposium. New York; London, 1972;4:23-38

Sibikeev S.N., Gultyaeva E.I., Druzhin A.E., Andreeva L.V. The effect of the 7DL-7Ae#1L·7Ae#1S translocation on the productivity and quality of spring bread wheat grain. *Vavilov J Genet Breed*. 2022;26(6):537-543. doi 10.18699/VJGB-22-65

Conflict of interest. The authors declare no conflict of interest.

Received February 18, 2026. Revised May 7, 2026. Accepted May 8, 2026.

Vavilovskii Zhurnal Genetiki i Selektsii
Vavilov Journal of Genetics and Breeding. 2026;30(6):863-874

doi 10.18699/vjgb-26-88

The ability of FGF21 to ameliorate signs of non-alcoholic fatty liver disease in mice depends on sex and diet

N.Yu. Balybina, E.N. Makarova, T.V. Jakovleva, A.Yu. Kazantseva, N.M. Bazhan

Institute of Cytology and Genetics of the Siberian Branch of the Russian Academy of Sciences, Novosibirsk, Russia
n.yu.balybina@gmail.com

Abstract. Consumption of high-calorie food leads to the development of obesity and non-alcoholic fatty liver disease (NAFLD). The pathogenesis of NAFLD depends on the composition of the diet. Administration of fibroblast growth factor 21 (FGF21) to obese mice improves metabolism and liver condition; however, the dependence of this effect on sex and diet composition has not been studied. Objective: To investigate the influence of sex on liver condition in mice with diet-induced obesity caused by different diets and on the ability of FGF21 to beneficially affect liver function. Obesity was induced in male and female C57BL/6J mice using a high-fat diet (HFD) or a cafeteria diet (DCaf). After obesity development, mice were administered FGF21 (1 mg/kg for 7 days), and the morphofunctional state and gene expression in the liver were assessed. When maintained on an HFD, hepatic steatosis was less severe in females than in males. FGF21 did not affect the lipid droplet area in individuals of either sex but exerted a sex-dependent influence on gene expression: in females, it reduced the expression of glycolysis and lipogenesis genes, preventing lipid accumulation, while in males, it reduced the expression of inflammation, apoptosis, and fibrosis genes, preventing the transition from steatosis to steatohepatitis. When maintained on a DCaf, pronounced steatosis developed in mice of both sexes. FGF21 reduced liver lipid content regardless of sex. However, only in females did FGF21 reduce the expression of the *Cidec* gene involved in lipid droplet formation and increase the number of apoptotic bodies. In males, the effect of FGF21 on lipid accumulation in the liver appeared to be mediated by its action on other tissues. Thus, in obese mice, sex differences in the severity of hepatic steatosis depended on the diet type and were observed only against the background of HFD. Administration of FGF21 led to a reduction in the total area of lipid droplets in the liver in mice of both sexes only against the background of pronounced steatosis induced by the DCaf. The influence of FGF21 on gene expression in the liver was sex-dependent, both against the background of HFD and DCaf.

Key words: non-alcoholic fatty liver disease (NAFLD); steatosis; FGF21; diet; obesity; sex differences; liver

For citation: Balybina N.Yu., Makarova E.N., Jakovleva T.V., Kazantseva A.Yu., Bazhan N.M. The ability of FGF21 to ameliorate signs of non-alcoholic fatty liver disease in mice depends on sex and diet. *Vavilovskii Zhurnal Genetiki i Selektsii = Vavilov J Genet Breed*. 2026;30(6):863-874. doi 10.18699/vjgb-26-88

Funding. The work was carried out with the support of the Russian Science Foundation, project No. 23-15-00093.

Author contributions. Natalya Yu. Balybina – processing of experimental results, writing of the manuscript; Antonina Yu. Kazantseva – conducting experiments, processing of experimental results, editing of the manuscript; Elena N. Makarova – planning of experiments, conducting experiments, editing of the manuscript; Tatiana V. Yakovleva – processing of results, editing of the manuscript; Nadezhda M. Bazhan – conception of the work, planning of experiments, approval of the final version of the publication.

Способность FGF21 снижать выраженность признаков неалкогольной жировой болезни печени у мышей зависит от пола и диеты

Н.Ю. Балыбина, Е.Н. Макарова, Т.В. Яковлева, А.Ю. Казанцева, Н.М. Бажан

Федеральный исследовательский центр Институт цитологии и генетики Сибирского отделения Российской академии наук, Новосибирск, Россия
n.yu.balybina@gmail.com

Аннотация. Потребление высококалорийной пищи вызывает развитие ожирения и неалкогольной жировой болезни печени (НАЖБП). Патогенез НАЖБП зависит от состава диеты. Введение фактора роста фибробластов 21 (FGF21) ожиревшим мышам улучшает метаболизм и состояние печени, однако зависимость этого эффекта от пола и состава диеты еще не изучена. Цель нашего исследования – изучить влияние пола на состояние печени у мышей с алиментарным ожирением, вызванным диетами разного состава, и на способность FGF21 благотворно влиять на метаболическую функцию печени. Ожирение индуцировали у самцов и самок мышей C57BL/6J высокожирной

© Balybina N.Yu., Makarova E.N., Jakovleva T.V., Kazantseva A.Yu., Bazhan N.M., 2026
This work is licensed under a Creative Commons Attribution 4.0 License

диетой (ВЖД) или диетой кафетерия (ДК). После развития ожирения мышам вводили FGF21 (1 мг/кг, 7 дней) и оценивали морфофункциональное состояние печени и экспрессию генов, участвующих в процессах метаболизма жиров и углеводов, воспаления, фиброза и апоптоза в ткани печени. При содержании на ВЖД стеатоз печени у самок был менее выражен, чем у самцов. FGF21 не влиял на площадь липидных капель у особей обоих полов, но оказывал зависящее от пола влияние на экспрессию генов: у самок снижал экспрессию генов гликолиза и липогенеза, препятствуя отложению липидов, а у самцов – генов воспаления, апоптоза и фиброза, предотвращая переход стеатоза в стеатогепатит (воспаление печени). При содержании на ДК у мышей обоих полов развивался выраженный стеатоз. FGF21 снижал содержание липидов в печени независимо от пола. Однако только у самок FGF21 снижал экспрессию гена *Cidec*, участвующего в образовании липидных капель, и повышал количество апоптозных телец. У самцов эффект FGF21 на накопление липидов в печени, по-видимому, опосредован действием на другие ткани: жировую, мышечную и т. д. Таким образом, у мышей с ожирением половые различия в степени выраженности стеатоза печени зависели от типа диеты и проявлялись только на фоне ВЖД. Введение FGF21 приводило к уменьшению общей площади липидных капель в печени у мышей обоих полов только на фоне выраженного стеатоза, вызванного содержанием на ДК. Влияние FGF21 на экспрессию генов в печени зависело от пола как на фоне высокожирной диеты, так и на фоне диеты кафетерия.

Ключевые слова: неалкогольная жировая болезнь печени (НАЖБП); стеатоз; FGF21; диета; ожирение; половые различия; печень

Introduction

Obesity is a disease that leads to the development of a number of metabolic disorders, in particular non-alcoholic fatty liver disease (NAFLD). This disease is characterized by excessive lipid accumulation in the liver and has a progressive course ranging from hepatic steatosis (lipid deposition in hepatocytes) to non-alcoholic steatohepatitis (liver inflammation), fibrosis and cirrhosis (Friedman et al., 2018; Haas et al., 2019). The search for effective NAFLD treatment requires adequate laboratory models that reproduce the disorders occurring in humans.

One of the most common models of obesity and related diseases in mice is high-fat diet (HFD)-induced obesity (Speakman, 2019). On this type of diet, animals obtain 40 to 65 % of their calories from fat (Speakman, 2019). This diet promotes the development of pronounced obesity and associated disorders and is most often used in NAFLD research (Hu et al., 2018). However, in the human population, the main cause of obesity is more often the consumption of a combination of fats and carbohydrates. The corresponding model in laboratory animals is known as the "cafeteria diet" (DCaf) (Buyukdere et al., 2019). In this approach, animals are given a free choice between high-fat (lard, chips, sausages, etc.) and high-carbohydrate food (cookies, biscuits, sweet drinks). It is assumed that the mechanisms of obesity development and associated disorders in animals are more accurately reproduced on a diet close to human diet pattern.

Sex influences the development of obesity. It has been shown that when mice are kept on an HFD, females usually have lower body and liver weight, as well as lower liver triglyceride content, than males (Senthil et al., 2014; Makarova et al., 2021b). The expression of the insulin receptor gene (*InsR*) and genes involved in lipid metabolism (*Ppara*, *Pgc1a*, *Fgf21*, *Acca*, *Accb*, *Fasn*) is higher in females compared to males (Makarova et al., 2021b). However, it is not known whether sex differences in the severity of NAFLD occur under these conditions. For the first time, the present work comprehensively investigates inflammation, fibrosis and apoptosis genes whose expression changes during the development of non-alcoholic fatty liver disease. When mice are kept on a DCaf, females show more pronounced signs of impaired liver morphology and function, including greater accumulation of lipid droplets and triglycerides, and higher expression levels of pro-inflammatory factor genes than males (Gasparin et al., 2018). Based on this, therapeutic approaches to NAFLD treatment may depend on sex and diet type.

One of the promising candidates for NAFLD treatment is fibroblast growth factor 21 (FGF21), a member of the fibroblast growth factor family with a wide range of metabolic functions (Li H. et al., 2013). Administration of exogenous FGF21 alleviates manifestations of hepatic steatosis (Leow et al., 2023), reduces obesity, insulin resistance and blood free fatty acid levels in both rodents and primates (Fisher, Maratos-Flier, 2016; Makarova et al., 2021b; Bazhan et al., 2023). These findings have stimulated the study of FGF21 as a potential therapy for NAFLD and other metabolic disorders.

It has been shown that in mice, the expression of endogenous FGF21 and the effects of recombinant FGF21 on carbohydrate and lipid metabolism depend on the sex of the animal and the etiology of obesity (Makarova et al., 2020, 2021a; Bazhan et al., 2023). Against the background of HFD, FGF21 improves general metabolic parameters in both sexes (Makarova et al., 2021b) and reduces NAFLD signs in males (Keinicke et al., 2020). However, the effect of FGF21 on NAFLD signs in females on HFD has not been studied. When animals are kept on a DCaf, FGF21 reduces blood fatty acid and leptin levels, improves glucose tolerance and increases the expression of genes involved in the regulation of lipid metabolism in the liver only in male mice (Bazhan et al., 2023). It can be assumed that on a DCaf, there is sexual dimorphism in the effects of FGF21 on NAFLD signs. This issue has not been investigated. The aim of this study is to investigate the effect of sex on liver condition in mice with diet-induced obesity caused by diets of different composition, and on the ability of FGF21 to beneficially influence liver metabolic function.

Research methods

Animals. This work is a continuation of experiments assessing the effect of exogenous FGF21 on food choice and metabolic parameters in mice of different sexes with obesity induced by diets of different compositions. The experimental design and diet composition are described in detail in previously published studies (Makarova et al., 2021b; Bazhan et al., 2023). Two experiments were conducted using male and female C57BL/6J mice from the vivarium of the Institute of Cytology and Genetics SB RAS, Novosibirsk.

The experiment on the effect of FGF21 administration on metabolic parameters in mice with obesity induced by a high-fat diet was performed in the SPF vivarium of the Institute of Cytology and Genetics SB RAS. To induce obesity, 12-week-old mice (17 males and 20 females) were given, in addition to standard chow (Ssniff Spezialdiäten GmbH, protein 19 %, fat 3.3 %), high-fat diet pellets in which 60 % of calories come from fat (D12492, Ssniff Spezialdiäten GmbH, protein 24.4 %, fat 34.6 %). Thereafter, animals were kept on a mixture of these diets, with mice obtaining 80–90 % of their energy from the HFD (Makarova et al., 2021b). In this experiment, females gained weight less intensively than males. FGF21 administration was started when male body weight reached 44–46 g and female body weight exceeded 30 g. The age of mice at the start of FGF21 administration ranged from 28 to 38 weeks.

The experiment on the effect of FGF21 administration on metabolic parameters in mice with obesity induced by a cafeteria diet was performed in a conventional vivarium of the Institute of Cytology and Genetics SB RAS (Bazhan et al., 2023). To induce obesity, 10-week-old mice were given, in addition to standard chow (Assortiment Agro, Turakovo, Moscow Region, Russia), lard and sweet butter cookies. Previously, we showed that on such a diet, weight gain rates do not differ between females and males (Bazhan et al., 2023). FGF21 administration was started at the age of 28 weeks, when the average body weight of male mice was 42.13 g (range 36.1–47.5 g) and that of females was 41.6 g (range 37.3–44.2 g).

In each experiment, animals were divided into four groups: males receiving vehicle (phosphate-buffered saline, PBS), males receiving FGF21, females receiving PBS, and females receiving FGF21. Each group contained 5–7 individuals.

For seven days, mice were subcutaneously injected with recombinant mouse FGF21 protein at a dose of 1 mg/kg body weight or an equivalent volume of PBS. The dose was selected based on the results of J. Xu et al., who administered FGF21 at doses of 0.1, 1, and 10 mg/kg and showed that the pharmacological effect of FGF21 begins to manifest at a dose of 1 mg/kg body weight (Xu et al., 2009). At the end of the experiment, one day after the last injection, animals were decapitated. The liver was excised and weighed. Relative liver weight was calculated relative to lean body mass (body weight minus fat mass). For subsequent gene expression analysis, liver samples were frozen in liquid nitrogen. Liver samples for histological analysis were placed in 10 % formalin solution.

Production and purification of mouse recombinant FGF21 protein. Production and purification of mouse recombinant FGF21 were carried out according to a previously published protocol (Makarova et al., 2021b).

Determination of triglyceride levels in the liver. To determine triglyceride levels, liver samples were placed in PBS at a ratio of 8 mL PBS per 1 mg of sample. The sample was then homogenized and centrifuged at low speed (~50g). The supernatant was collected and centrifuged again at the same speed. After the second centrifugation, the supernatant was collected for triglyceride content determination. Triglyceride concentration was measured using an enzymatic colorimetric method with the "Triglycerides-Novo liquid form" kit from Vector-Best (cat. No. B-8323).

Histological analysis of liver structure. To assess the degree of steatosis (lipid accumulation in the liver, as well as macrophage and apoptotic body content), a generally accepted diagnostic approach was used (Yanko et al., 2021; Leow et al., 2023). Liver sections were stained with hematoxylin and eosin according to the standard protocol (Makarova et al., 2021a). F.R.S. Gasparin et al. showed that the non-stained round inclusions detected by hematoxylin-eosin staining are lipid inclusions and that their number correlates with the amount of lipids determined by Sudan III staining (Gasparin et al., 2018).

For histological analysis of liver structure, a Zeiss light microscope (Axioskop 2 plus, Carl Zeiss Microscopy GmbH, Jena, Germany) with a built-in camera was used. For each animal, 10 photographs of liver sections were taken at ×400 magnification. Statistical analysis was performed on averaged data for each animal (n = 5–7). The area of lipid droplets, the number of macrophages and the number of apoptotic bodies were quantified using ImageJ software (National Institutes of Health, Bethesda, MD, USA). Lipid droplets of different sizes were distinguished. Large lipid droplets were those that displaced the nucleus to the cell periphery; medium-sized droplets were closely apposed lipid inclusions that did not displace the nucleus; and small lipid droplets were those located at a distance from each other. The total area occupied by lipids (sum of areas of lipid droplets of different sizes) and the area occupied by lipid droplets of different sizes relative to the total area of the photograph were calculated (Makarova et al., 2021a).

Assessment of mRNA levels of genes. The mRNA levels of genes involved in lipid and carbohydrate metabolism, inflammation, fibrosis and apoptosis were studied by relative quantitation using reverse transcription and real-time PCR (relative quantitation real-time PCR). RNA was isolated from tissue samples using ExtractRNA reagent for total RNA isolation (Eurogen, Moscow, Russia) according to the manufacturer's instructions. Reverse transcription was performed using MMLV reverse transcriptase (Eurogen, Moscow, Russia) and oligo-dT primer according to the manufacturer's protocol. PCR was performed according to the instructions using a ready-made reaction mixture qPCRmix-HS LowROX (Eurogen, Moscow, Russia) and reagents from Applied Biosystems: TaqMan

Gene Expression Assay for the mouse genes Beta-actin, Actb, Mm00607939_s1C. The expression of genes involved in various processes and systems of the liver was examined: glycolysis (Glucokinase, *Gck*, Mm00439129_m1; Pyruvate kinase liver and red blood cell, *Pklr*, Mm00443090_m1); gluconeogenesis (Glucose-6-phosphatase, *G6p*, Mm00839363_m1; Phosphoenolpyruvate carboxykinase 1, *Pck1*, Mm01247058_m1); FGF21 system (Fibroblast growth factor 21, *Fgf21*, Mm00840165_g1; Klotho beta, *Klb*, Mm00473122_m); lipid oxidation (Peroxisome proliferator activated receptor alpha, *Ppara*, Mm0040939_m1; Carnitine palmitoyltransferase 1a, *Cpt1a*, Mm01231183_m1; *P*eroxisome proliferative activated receptor, gamma, coactivator 1 alpha, *Ppargc1a*, Mm01208835_m1); lipid synthesis (Fatty acid synthase, *Fasn*, Mm00662319_m1; Acetyl-coenzyme A carboxylase alpha, *Acca*, Mm01304285_m1; Acetyl-coenzyme A carboxylase beta, *Accb*, Mm01204683_m1; Cell death-inducing DFFA-like effector c, *Cidec*, Mm00617672_m1); inflammation and fibrosis (Tissue inhibitor of metalloproteinase 1, *Timp1*, Mm01341361_m1; Transforming growth factor, beta 1, *Tgfb1*, Mm01178820_m1; CD68 antigen, *Cd68*, Mm03047343_m1; Tumor necrosis factor a, *Tnfa*, Mm00443258_m1; Interleukin 1 beta, *Il1b*, Mm00434228_m1; Nuclear factor, erythroid derived 2, like 2, *Nfe2l2*, Mm00477784_m1; Chemokine (C-C motif) ligand 3, *Ccl3*, Mm00441259_g1); apoptosis (BCL2, apoptosis regulator, *Bcl2*, Hs04986394_s1; BCL2-antagonist/killer 1, *Bak1*, Mm00432045_m1); growth factor (Insulin-like growth factor 1, *Igf1*, Mm00439560_m1). Beta-actin was used as an endogenous control. PCR and fluorescence detection were performed on an Applied Biosystems VIIA 7 real-time PCR system. Relative quantification was performed using the comparative threshold cycle (CT) method ($2^{-\Delta\Delta Ct}$).

Statistical analysis. To analyze the effect of FGF21 on lipid accumulation in the liver, two-way ANOVA with the factors "sex" and "experimental group" (EG) was used. For multiple comparisons, the *post-hoc* Newman–Keuls test was used. Results were considered statistically significant at $p < 0.05$.

Due to heterogeneity of variances, gene expression data were analyzed using the non-parametric Mann–Whitney U test (n = 5–7). Significance was set at $p < 0.05$. Gene expression data are presented as medians, means, maximum and minimum values, as well as the 25–75 % range of values for each parameter.

All analyses were performed using the STATISTICA 6 software package (StatSoft, TIBCO Software Inc., Palo Alto, CA, USA).

Results

High-fat diet experiment. Liver morphology. Figure 1*a* shows a typical histological picture of the liver in obesity: hepatocytes containing large, medium and small lipid droplets, as well as macrophages and apoptotic bodies.

In animals kept on a high-fat diet, signs of steatosis in the liver of females were less pronounced than in males (Fig. 1*b*). Relative liver weight was lower in females than in males (effect of the factor "Sex", $F_{(1.20)} = 7.52$, $p < 0.05$) (Fig. 2*a*). The area of small lipid droplets and liver triglyceride content in PBS-treated females and males did not differ, whereas the total lipid droplet area (effect of "Sex", $F_{(1.20)} = 7.45$, $p < 0.05$) and the area of medium-sized ($F_{(1.20)} = 12.39$, $p < 0.01$) and large ($F_{(1.20)} = 9.93$, $p < 0.01$) droplets were significantly lower in females than in males (Fig. 2*b*, *c*, *e*). However, the number of macrophages (effect of "Sex", $F_{(1.20)} = 39.07$, $p < 0.001$; Newman–Keuls *post-hoc* test, $p < 0.05$) and the number of apoptotic bodies (effect of "Sex", $F_{(1.20)} = 5.02$, $p < 0.05$; Newman–Keuls test, $p < 0.05$) were higher in females than in males, indicating more pronounced inflammation in females compared to males (Fig. 2*d*, *e*).

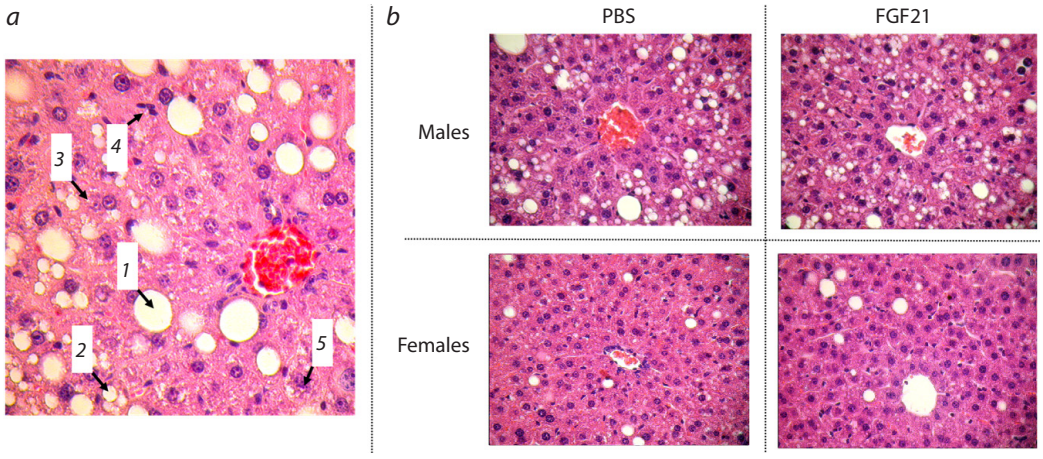


Fig. 1. Representative images: *a* – lipid accumulation in the liver of male and female mice fed a high fat diet and receiving PBS or FGF21; *b* – general liver architecture in obese mice.

Hematoxylin and eosin staining, ×400. 1 – large lipid droplets, 2 – medium lipid droplets, 3 – small lipid droplets, 4 – macrophages, 5 – apoptotic bodies.

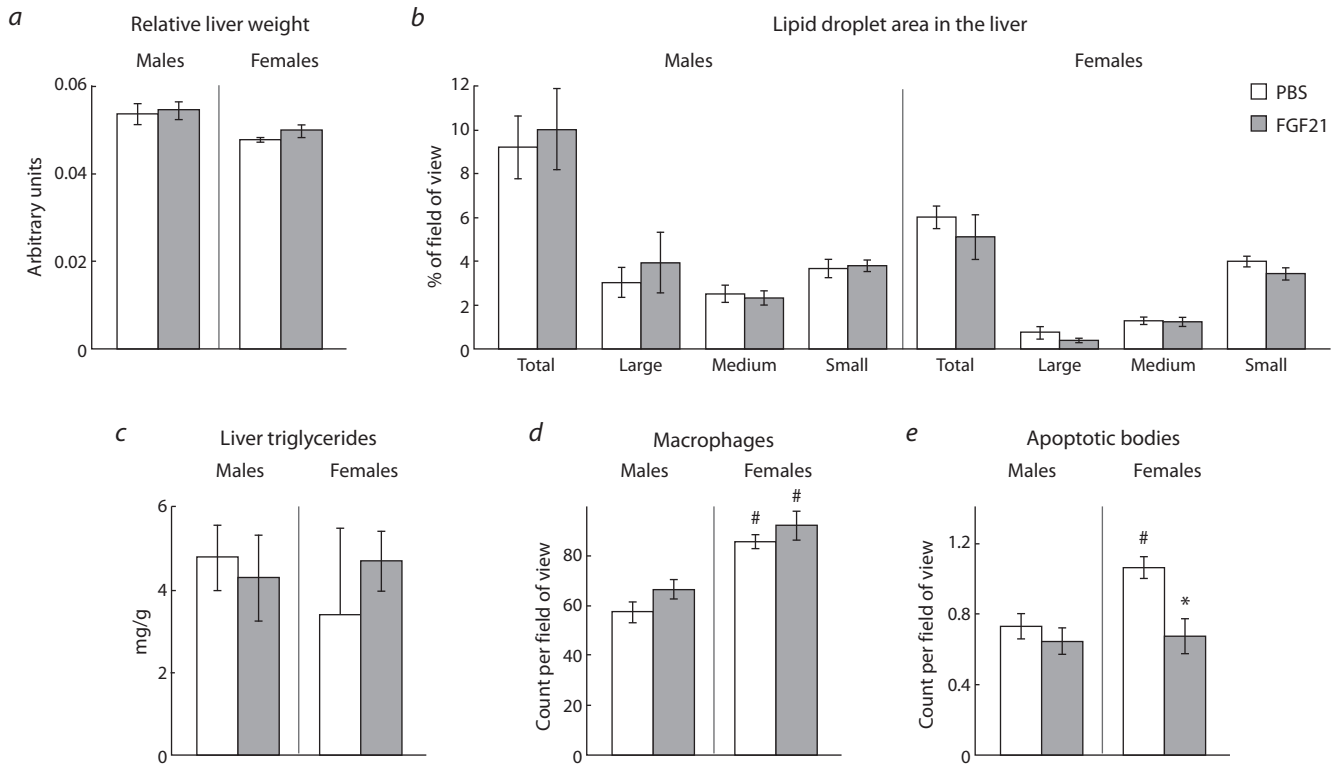


Fig. 2. Relative liver weight (*a*), lipid droplet area (*b*), triglyceride content (*c*), macrophage count (*d*) and apoptotic body count (*e*) in the liver of male and female mice fed a high fat diet and receiving PBS or FGF21.

$p < 0.05$ *vs.* males, *post-hoc* Newman–Keuls test; * $p < 0.05$ *vs.* PBS, *post-hoc* Newman–Keuls test.

FGF21 administration did not affect relative liver weight, triglyceride content, macrophage number or lipid droplet area in the liver, but reduced the number of apoptotic bodies (effect of the factor "EG", $F_{(1.20)} = 8.67$, $p < 0.01$; Newman–Keuls test, $p < 0.05$ for females) in the liver of both sexes (Fig. 2).

Expression of genes involved in lipid and carbohydrate metabolism

In HFD-fed females treated with PBS, the expression levels of *Fgf21* ($p < 0.01$, U = 0.00, n♀ = 5, N♂ = 7), *Acca* ($p < 0.01$, U = 0.00, n♀ = 5, N♂ = 7) and *Ppara* ($p < 0.05$, U = 4.00, n♀ = 5, N♂ = 7) were higher than in males. FGF21 administration reduced the expression of *Gck* ($p < 0.05$, U = 3.00, $n = 5$ for both groups), *Pklr* ($p < 0.05$, U = 2.00, $n = 5$ for both groups) and *Fasn* ($p < 0.05$, U = 2.00, $n = 5$ for both groups) in females and had no effect on the expression of the studied genes in males (Fig. 3).

Expression of genes involved in inflammation, fibrosis and apoptosis

In PBS-treated animals, the expression levels of *Tnfa* ($p < 0.05$, U = 5.00, n♀ = 5, N♂ = 7) and *Nfe2l2* ($p < 0.05$, U = 2.00, n♀ = 5, N♂ = 7) were higher in females than in males. FGF21 administration reduced the expression of *Tgfb1* ($p < 0.05$, U = 6.50, $n = 7$ for both groups), *Nfe2l2* ($p < 0.05$, U = 9.00, $n = 7$ for both groups), *Bak1* ($p < 0.05$, U = 2.00, $n = 7$ for both groups) and *Igf1* ($p < 0.05$, U = 5.00, $n = 7$ for both groups) in males and had no effect on the expression of the studied genes in females (Fig. 4).

Cafeteria diet experiment. Liver morphology. In animals kept on a cafeteria diet, control mice of both sexes showed high lipid content in the liver, with no sex differences in this parameter (Fig. 5 and 6*b*). Relative liver weight and liver triglyceride content did not differ between male and female mice (Fig. 6*a*, *c*). Females had an increased number of macrophages compared to males (effect of the factor "Sex", $F_{(1.14)} = 4.56$, $p < 0.05$) (Fig. 6*d*). The number of apoptotic bodies in controls did not differ between females and males (Fig. 6*e*).

FGF21 administration reduced relative liver weight (effect of "EG", $F_{(1.14)} = 4.94$, $p < 0.05$) and total lipid droplet area in both males and females (effect of "EG", $F_{(1.14)} = 4.68$, $p < 0.05$) (Fig. 6*a*, *b*). FGF21 administration did not affect liver triglyceride content, macrophage number or apoptotic body number in either sex (Fig. 6*c*–*e*).

Expression of genes involved in lipid and carbohydrate metabolism

In obesity induced by the DCaf, only *Cidec* expression was lower in females ($p < 0.05$, U = 3.00, $n = 5$ for both groups) than in males, and FGF21 reduced its expression only in females ($p < 0.01$, U = 0.00, $n = 5$ for both groups) (Fig. 7). No effect of sex or FGF21 was detected on the expression of other studied genes involved in the regulation of lipid and carbohydrate metabolism.

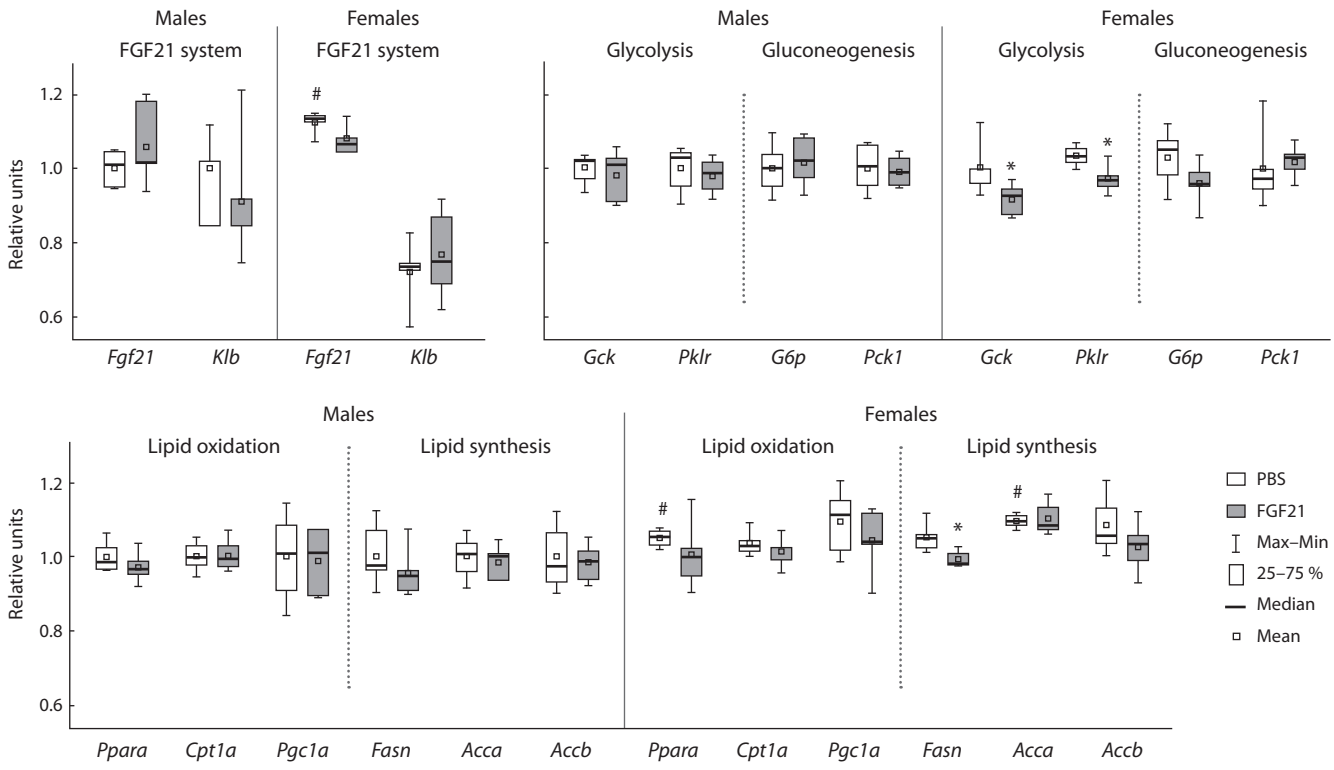


Fig. 3. Relative expression levels of carbohydrate and lipid metabolism genes in the liver of male and female mice fed a high fat diet and receiving PBS or FGF21.

$p < 0.05$ *vs.* males, Mann–Whitney U test; * $p < 0.05$ *vs.* PBS, Mann–Whitney U test.

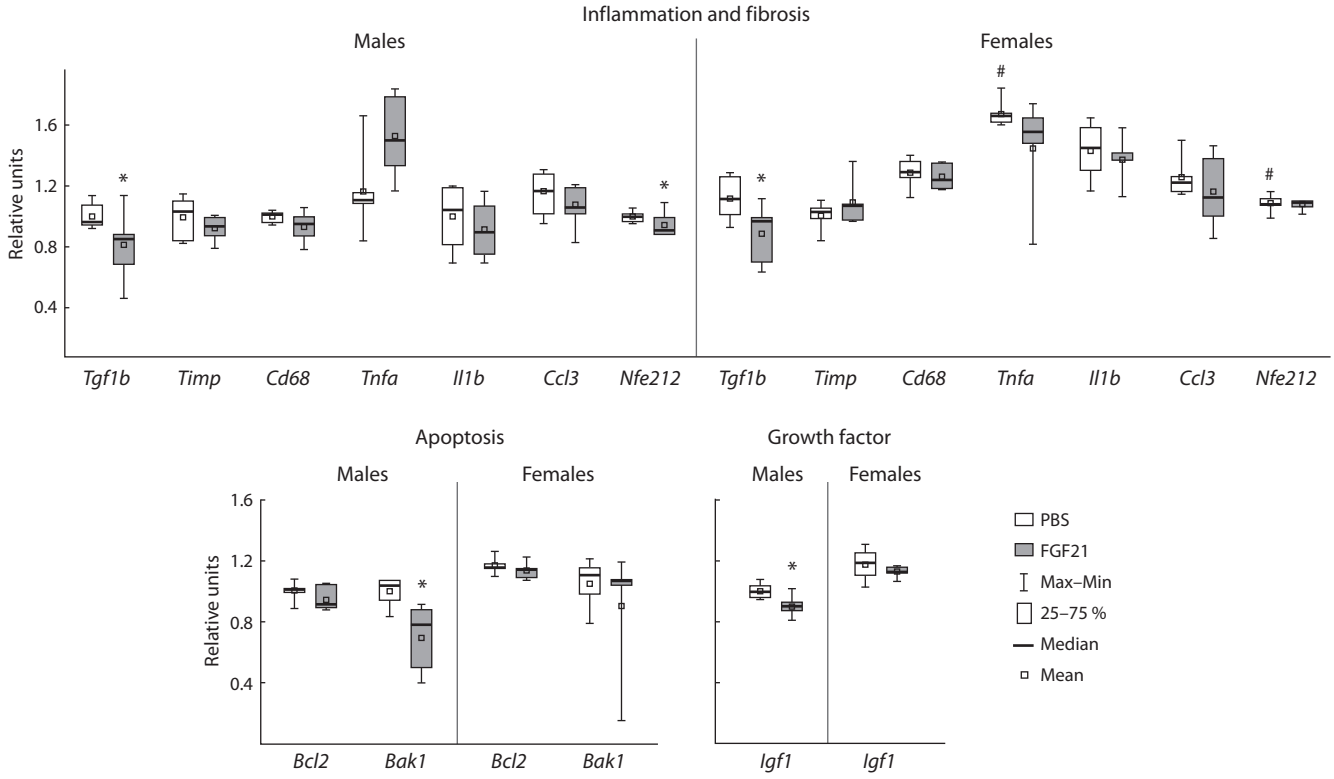


Fig. 4. Relative expression levels of inflammation, fibrosis, apoptosis and insulin like growth factor genes in the liver of male and female mice fed a high fat diet and receiving PBS or FGF21.

$p < 0.05$ *vs.* males, Mann–Whitney U test; * $p < 0.05$ *vs.* PBS, Mann–Whitney U test.

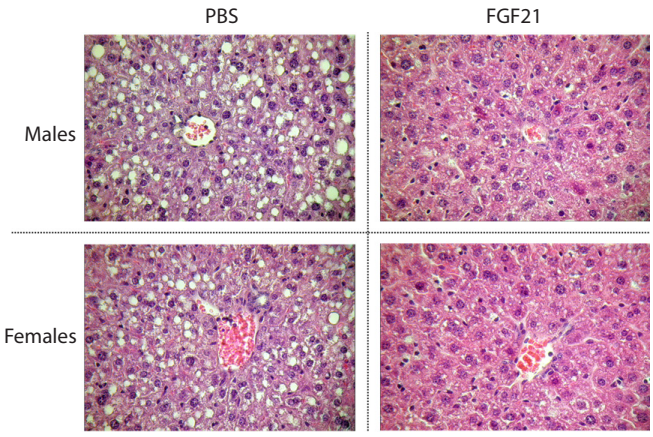


Fig. 5. Representative images. Lipid accumulation in the liver of male and female mice fed a cafeteria diet and receiving PBS or FGF21.

Hematoxylin and eosin staining, ×400.

Expression of genes involved in inflammation, fibrosis and apoptosis

No sex differences were found in the expression levels of inflammation and fibrosis genes in the liver under DCaf-induced obesity, nor any effect of FGF21 administration on the expression of these genes (Fig. 8).

Discussion

In this study, we investigated sex-specific features of steatosis development in diet-induced obesity caused by diets of different composition, as well as the effect of FGF21 on the morphofunctional state of the liver and on the expression of genes involved in carbohydrate and lipid metabolism, inflammation, fibrosis and apoptosis in the liver of male and female mice under different types of obesity.

A high-fat diet is widely used to study the mechanisms of obesity development and potential agents for correcting associated disorders (Li J. et al., 2020). It has previously been shown that HFD consumption promotes the development of obesity and non-alcoholic fatty liver disease in male mice (Lau et al., 2017). In our study, we used a mixed diet: standard chow together with high-fat pellets in which 60 % of calories come from fat. According to S. Hu et al., such nutrition in male mice causes more pronounced disturbances in metabolic parameters, faster obesity development, a significant decrease in insulin sensitivity and greater liver fat deposition compared to diets in which 10 and 45 % of calories come from fat (Hu et al., 2018).

HFD consumption revealed significant sex differences in liver histology. Relative liver weight and the area occupied by lipid droplets were significantly lower in females than in males, indicating less severe steatosis (Fig. 1 and 2). Previously, other authors (Hwang et al., 2010) and ourselves in this experiment (Makarova et al., 2021b) showed that on an HFD, female mice exhibit a lower degree of whole-body obesity, manifested by lower body weight, lower fat mass and lower liver weight compared to males.

Decreased insulin sensitivity promotes lipid deposition in the liver and NAFLD development (Takaki et al., 2013). In the present experiment (Makarova et al., 2021b) and by other authors (Hwang et al., 2010), female mice were shown to be

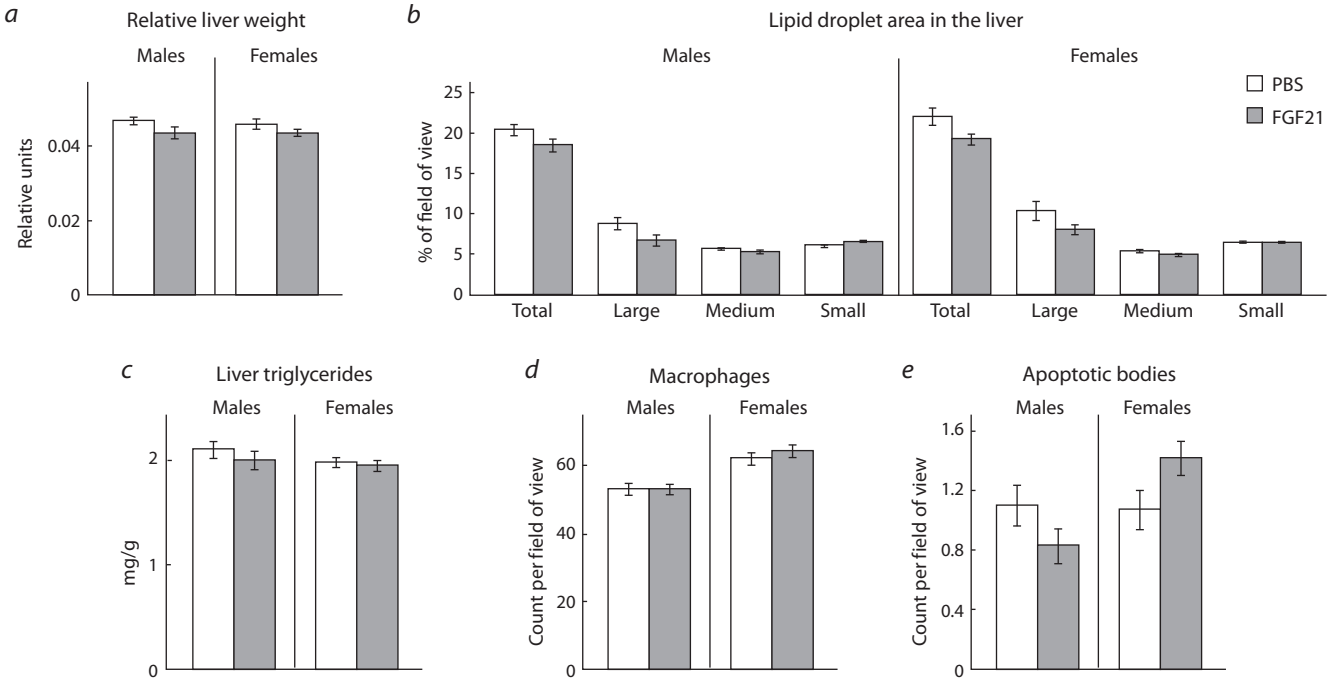


Fig. 6. Relative liver weight (*a*), lipid droplet area (*b*), triglyceride content (*c*), macrophage count (*d*) and apoptotic body count (*e*) in the liver of male and female mice fed a cafeteria diet and receiving PBS or FGF21.

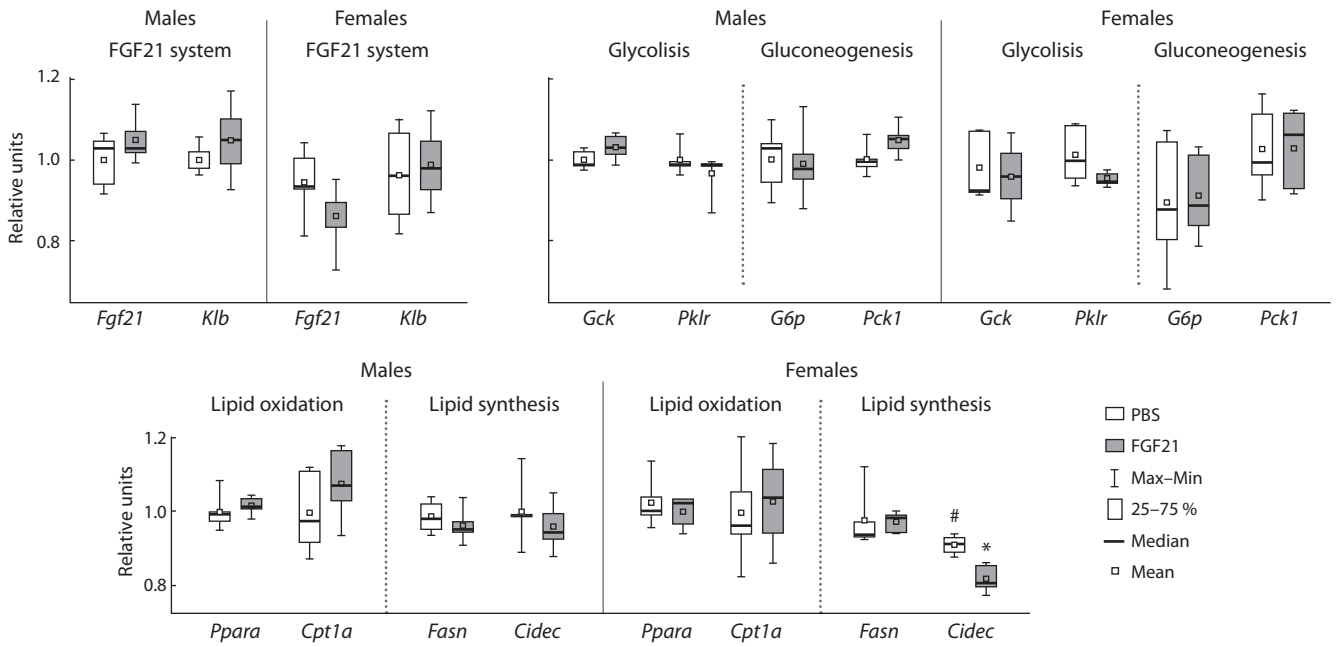


Fig. 7. Relative expression levels of carbohydrate and lipid metabolism genes in the liver of male and female mice fed a cafeteria diet and receiving PBS or FGF21.

$p < 0.05$ *vs.* males, Mann–Whitney U test; * $p < 0.05$ *vs.* PBS, Mann–Whitney U test.

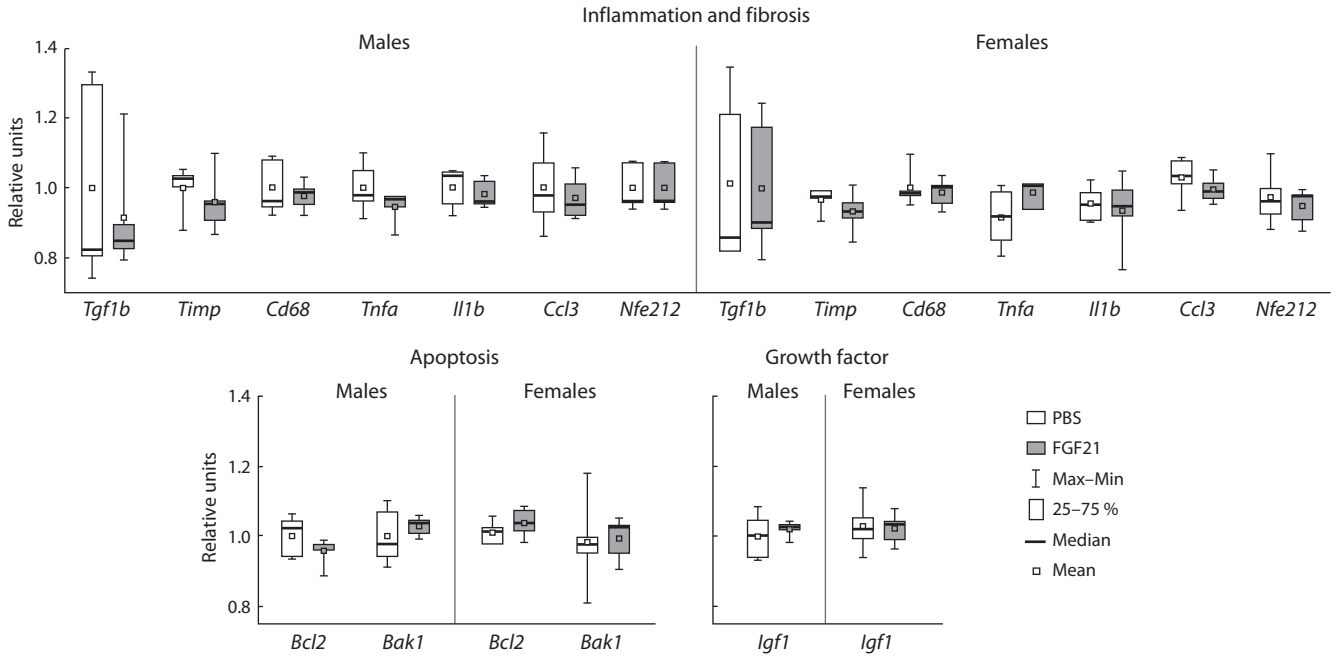


Fig. 8. Relative expression levels of inflammation, fibrosis, apoptosis and insulin like growth factor genes in the liver of male and female mice fed a cafeteria diet and receiving PBS or FGF21.

more insulin-sensitive than males; therefore, the lower lipid accumulation in the liver of females may be a consequence of their higher insulin sensitivity.

The lower lipid accumulation in the liver of females on HFD may also be explained by higher lipid metabolism activity. The expression levels of genes encoding lipogenesis enzymes (*Acca*) and fatty acid oxidation enzymes (*Ppara*) were higher in females (Fig. 3). Females also had increased expression of the *Fgf21* gene in the liver. FGF21 can trigger the expression of genes involved in free fatty acid oxidation, thereby reducing lipid deposition in the liver (Kleiner et al., 2012; Fisher, Maratos-Flier, 2016).

On HFD, females exhibited a higher expression level of the pro-inflammatory factor gene *Tnfa* and a lower expression level of the *Nfe2l2* gene, which encodes a transcription factor that protects cells from oxidative stress by activating genes involved in antioxidant and detoxification reactions (Fig. 4). It has been shown that under prolonged stress, its level may decrease, exacerbating signs of oxidative stress (Ye et al., 2023). These facts indicate that, despite lower fat deposition in the liver, signs of oxidative stress were more pronounced in females than in males.

We observed in HFD-fed females a greater number of macrophages and apoptotic bodies in the liver parenchyma compared to males, both after PBS and FGF21 administration (Fig. 2). Similar changes were observed in genetic melanocortin obesity (Makarova et al., 2021a). Macrophages, in turn, express pro-inflammatory cytokines such as *Il1b*, *Tnfa* and *Il6*, which promote the progression of inflammation and the development of steatohepatitis (Alkhouri et al., 2011).

Thus, we show for the first time that when consuming high-fat food, females demonstrate lower accumulation of lipid droplets in the liver compared to males. However, they show higher expression of the *Tnfa* gene and greater numbers of macrophages and apoptotic bodies, which may indicate a higher degree of inflammation or may represent an adaptive response to high-fat diet consumption in female mice. This question requires further investigation.

When FGF21 was administered to HFD-fed mice, we observed suppression of glycolysis (*Pklr*, *Gck*) and lipogenesis (*Fasn*) gene expression only in females (Fig. 3), which may indicate the activation of adaptive mechanisms protecting the liver from excessive fat deposition. Despite this, no reduction in lipid droplet numbers was found in females. We attribute this to the fact that, according to the literature, the baseline lipid level in females was only slightly elevated compared to normal (Kim et al., 2013), which limited the scope for visible improvement.

In HFD-fed males, which had more severe steatosis than females, FGF21 also did not affect liver lipid content (Fig. 2). The lack of effect may be explained by the fact that FGF21 suppressed *Igf1* gene expression in the liver (Fig. 4) (Boparai et al., 2015). It is known that IGF1 prevents fat accumulation in the liver (Ma, Stanley, 2023). Possibly, the inhibitory effect of FGF21 on *Igf1* expression, observed by us and other researchers, may counteract the direct lipid-lowering action of IGF1.

On HFD, both sexes showed a decrease in the number of apoptotic bodies in the liver in response to FGF21 administration (Fig. 2), and males also showed decreased expression of the pro-apoptotic gene *Bak1* (Fig. 5). Since inflammation is often associated with apoptosis, these changes may indicate reduced liver inflammation (Chen et al., 2018). Moreover, in males, FGF21 reduced the expression of the pro-fibrotic gene *Tgfb1*, which may prevent the development of fibrosis – a characteristic sign of NAFLD progression.

Thus, in obesity induced by a high-fat diet, the effect of FGF21 on liver status depended on the degree of steatosis: when lipid content was low (as in females), the effect was aimed at preventing fat deposition by suppressing glycolysis and lipogenesis gene expression. When steatosis was pronounced (as in males in this study), the effects of FGF21 were directed towards reducing the expression of genes involved in the inflammatory process.

Previously, we and other authors have shown that when excess carbohydrates are added to the diet together with excess fat, females achieve a greater degree of obesity than males (Gasparin et al., 2018; Bazhan et al., 2020). However, in the present study we found that the area of lipid droplets in the liver did not differ between males and females (Fig. 6). The absence of differences in liver lipid accumulation despite greater obesity in females on the DCaf may be related to their relatively lower expression of the *Cidec* gene compared to males (Fig. 7). The product of this gene plays a key role in lipid droplet formation in the liver. It has been shown that animals with reduced *Cidec* expression exhibit a marked reduction in lipid stores in various tissues (Chen et al., 2018).

In obesity induced by the DCaf, females had more macrophages in the liver than males, which may indicate that their liver obesity is complicated by inflammation (Fig. 6). Previously, F.R.S. Gasparin et al. (2018) and A. Spruss et al. (2012) observed more pronounced signs of liver inflammation in females than in males. Thus, in animals kept on a cafeteria diet, no differences were found in the degree of hepatic steatosis, but females showed signs of greater liver inflammation than males.

Administration of FGF21 to DCaf-fed mice led to a decrease in relative liver weight and hepatocyte lipid content in both sexes (Fig. 6). The mechanism of this effect differed: in females, FGF21 suppressed the expression of the *Cidec* gene in the liver, whose product plays a key role in the formation and fusion of lipid droplets (Fig. 7) (Chen et al., 2018). In DCaf-fed males, FGF21 did not affect the expression of liver genes involved in the regulation of lipid metabolism. It can be assumed that in males, the FGF21-induced reduction in lipid droplet area in the liver was related to its action on white adipose tissue, which is the main target organ for FGF21 (Makarova et al., 2021b). Previously, we showed that in male mice with DCaf-induced obesity, FGF21 reduces blood free fatty acid levels (Bazhan et al., 2023). This may reduce fat uptake by the liver and its subsequent deposition as lipid droplets.

Thus, FGF21 had a similar effect on liver lipid content in male and female C57BL/6J mice on a cafeteria diet. However, the mechanisms underlying this effect differed: in females it likely acted through suppression of a lipogenesis gene in the liver, whereas in males it acted through extrahepatic mechanisms.

It is known that sex differences in the metabolic effects of FGF21 depend on the cause of obesity. Thus, on a high-fat diet, FGF21 exerts unidirectional effects in males and females on body weight and fat mass, blood cholesterol, glucose and insulin levels, and on the expression of glycolysis and fatty acid synthesis genes in the liver (Makarova et al., 2021b). In animals kept on a cafeteria diet, the therapeutic effects of

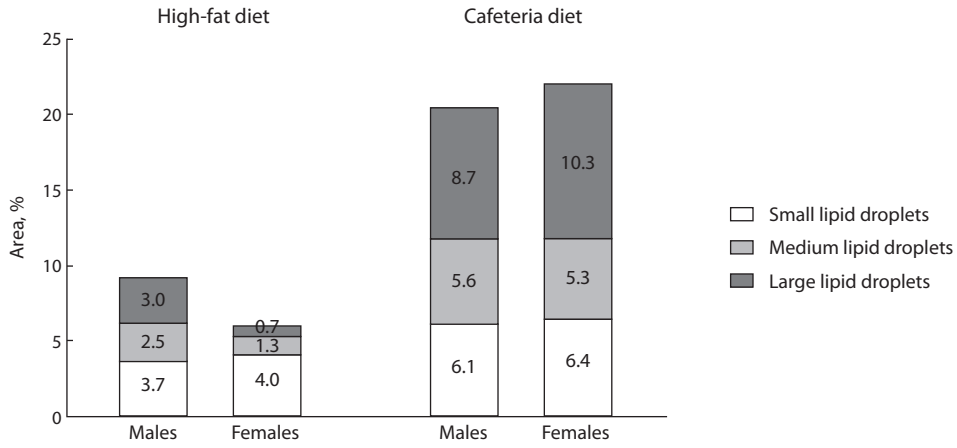


Fig. 9. Percentage of the field of view occupied by small, medium and large lipid droplets (based on images from Figures 1 and 5) in male and female mice fed a high fat diet or a cafeteria diet.

FGF21 administration are more pronounced in males – manifested as reduced plasma fatty acid and leptin levels, improved glucose tolerance, and increased expression of genes involved in insulin signaling and lipid metabolism in the liver (Bazhan et al., 2023).

In the present study, we found that the degree of hepatic steatosis depends on the type of diet offered to the animals. Sex differences in liver lipid accumulation were observed in the HFD model, which was characterized by early stages of hepatic steatosis in mice. On HFD, female mice showed a small amount of small lipid droplets with virtually no large or medium-sized droplets; the total lipid droplet area in females was about 6 % of the field of view, corresponding to a slight increase above the normal level in mice (normal ~5 %) (Leow et al., 2023). In contrast, male mice had lipid droplets of all sizes in the liver, and the total area exceeded 9 % of the field of view, corresponding to the initial stages of the first (mild) stage of hepatic steatosis in mice (Leow et al., 2023) (Fig. 9).

DCaf consumption caused more pronounced accumulation of lipid droplets of various sizes in the liver of both sexes than HFD consumption, with no sex differences in the degree of steatosis. In both males and females, the total lipid droplet area exceeded 20 %, corresponding to a later stage of the first stage of hepatic steatosis (Leow et al., 2023) (Fig. 9).

The differences we observed in liver lipid accumulation between diet types may be due to several factors. The DCaf provides not only fats but also an excess of simple carbohydrates (sugars); consumption of simple carbohydrates activates specific *de novo* lipogenesis pathways, which can operate in parallel with dietary fat assimilation (Sanders, Griffin, 2016). This creates an additional burden on lipid metabolism. Moreover, an excess of carbohydrates in the diet promotes the development of insulin resistance, which in turn leads to fat accumulation in the liver (Takaki et al., 2013). In addition, the DCaf may cause more pronounced oxidative damage to liver cells due to the combination of different types of fats and excess sugars, disrupting lipid utilization processes and promoting steatosis development (Asrih, Jornayvaz, 2013).

The effect of FGF21 on the liver depended on the degree of steatosis. In female mice on HFD, where steatosis was not pronounced, the effect of FGF21 was to prevent lipid accumulation in the liver by reducing the expression of glycolysis and lipogenesis genes. In male mice on the same diet, but with early-stage steatosis, the effect of FGF21 was to suppress the expression of inflammation and fibrogenesis genes. It is known that already at the early stages of NAFLD development, the expression of pro-inflammatory cytokines increases, which contributes to disease aggravation (Asrih, Jornayvaz, 2013). Apparently, the main action of FGF21 in this case is aimed at preventing the development of non-alcoholic steatohepatitis.

At the more advanced stage of hepatic steatosis observed in both male and female mice on DCaf, the effect of FGF21 was directed towards reducing the area of lipids in the liver. However, the mechanism of this effect differed between males and females: in females, a decrease in the expression of the *Cidec* gene, which plays a key role in lipid droplet formation and fusion (Chen et al., 2018), was observed, whereas in males no direct effect of FGF21 on the liver was detected.

Conclusion

The present study revealed sex differences in the development of non-alcoholic fatty liver disease and in the response to FGF21 therapy depending on the type of diet. On a high-fat diet, females displayed less pronounced steatosis, which was associated with higher expression levels of lipid metabolism genes and higher basal *Fgf21* expression. However, judging by the expression of inflammation genes and the number of macrophages and apoptotic bodies in the liver, steatosis in females was accompanied by an enhanced inflammatory response, increasing the risk of steatohepatitis. In contrast, on a cafeteria diet, steatosis was equally pronounced in both sexes, with more pronounced signs of inflammation in females compared to males.

The effects of FGF21 depended on sex and the stage of steatosis: at early stages of steatosis (high-fat diet) in females, judging by *Gck* and *Pklr* expression, it suppressed glycolysis

(both genes belong to glycolysis) and lipogenesis (*Fasn*), preventing lipid accumulation, whereas in males it reduced signs of inflammation and exerted an anti-fibrotic action. At a more advanced stage of steatosis (cafeteria diet), FGF21 reduced liver lipid content in both male and female mice, but by different mechanisms – in females through suppression of *Cidec* gene expression, in males indirectly, apparently through action on adipose tissue. Thus, the therapeutic strategy for using FGF21 in non-alcoholic fatty liver disease requires consideration of the patient's sex, the stage of steatosis and the etiology of obesity.

Ethics approval. The study was conducted according to the guidelines of the Declaration of Helsinki and approved by the Independent Ethics Committee of the Institute of Cytology and Genetics, Siberian Division, Russian Academy of Sciences (Protocol No. 47 dated February 23, 2019, for HFD (high-fat diet), and dated November 8, 2021, for DCaf (cafeteria diet).

References

Alkhouri N., Carter-Kent C., Feldstein A.E. Apoptosis in nonalcoholic fatty liver disease: diagnostic and therapeutic implications. *Expert Rev Gastroenterol Hepatol.* 2011;5(2):201-212. doi 10.1586/egh.11.6

Asrih M., Jornayvaz F.R. Inflammation as a potential link between nonalcoholic fatty liver disease and insulin resistance. *J Endocrinol*. 2013;218(3):R25-R36. doi 10.1530/JOE-13-0201

Bazhan N.M., Iakovleva T.V., Dubinina A.D., Makarova E.N. Impact of sex on the adaptation of adult mice to long consumption of sweet-fat diet. *Vavilov J Genet Breed*. 2020;24(8):844-852. doi 10.18699/VJ20.682

Bazhan N.M., Jakovleva T.V., Kazantseva A.Yu., Kostina N.E., Orlov P.E., Balybina N.Yu., Baranov K.O., Makarova E.N. Studying sex differences in responses to fibroblast growth factor 21 administration in obese mice consuming a sweet-fat diet. *Vavilov J Genet Breed*. 2023;27(4):333-341. doi 10.18699/VJGB-23-40

Boparai R.K., Arum O., Miquet J.G., Masternak M.M., Bartke A., Khardori R.K. Resistance to the beneficial metabolic effects and hepatic antioxidant defense actions of fibroblast growth factor 21 treatment in growth hormone-overexpressing transgenic mice. *Int J Endocrinol*. 2015;2015:282375. doi 10.1155/2015/282375

Buyukdere Y., Gulec A., Akyol A. Cafeteria diet increased adiposity in comparison to high fat diet in young male rats. *PeerJ.* 2019;7:e6656. doi 10.7717/peerj.6656

Chen X.L., Han Y.D., Wang H. Relations of hepatic steatosis with liver functions, inflammations, glucolipid metabolism in chronic hepatitis B patients. *Eur Rev Med Pharmacol Sci.* 2018;22(17):5640-5646. doi 10.26355/eurrev_201809_15830

Fisher F.M., Maratos-Flier E. Understanding the physiology of FGF21. *Annu Rev Physiol.* 2016;78:223-241. doi 10.1146/annurev-physiol-021115-105339

Friedman S.L., Neuschwander-Tetri B.A., Rinella M., Sanyal A.J. Mechanisms of NAFLD development and therapeutic strategies. *Nat Med.* 2018;24(7):908-922. doi 10.1038/s41591-018-0104-9

Gasparin F.R.S., Carreño F.O., Mewes J.M., Gilglioni E.H., Pagadigorria C.L.S., Natali M.R.M., Utsunomiya K.S., Constantin R.P., Ouchida A.T., Curti C., Gaemers I.C., Elferink R.P.J.O., Constantin J., Ishii-Iwamoto E.L. Sex differences in the development of hepatic steatosis in cafeteria diet-induced obesity in young mice. *Biochim Biophys Acta Mol Basis Dis.* 2018;1864(7):2495-2509. doi 10.1016/j.bbadis.2018.04.004

Haas J.T., Vonghia L., Mogilenko D.A., Verrijken A., Molendi-Coste O., Fleury S., Deprince A., … Driessen A., Lefebvre P., Staels B., Francque S., Dombrowicz D. Transcriptional network analysis implicates altered hepatic immune function in NASH development and resolution. *Nat Metab.* 2019;1(6):604-614. doi 10.1038/s42255-019-0076-1

Hu S., Wang L., Yang D., Li L., Togo J., Wu Y., Liu Q., … Mazidi M., Luo L., Wang S., Douglas A., Speakman J.R. Dietary fat, but not protein or carbohydrate, regulates energy intake and causes adiposity in mice. *Cell Metab.* 2018;28(3):415-431.e4. doi 10.1016/j.cmet.2018.06.010

Hwang L.L., Wang C.H., Li T.L., Chang S.D., Lin L.C., Chen C.P., Chen C.T., Liang K.C., Ho I.K., Yang W.S., Chiou L.C. Sex differences in high-fat diet-induced obesity, metabolic alterations and learning, and synaptic plasticity deficits in mice. *Obesity*. 2010;18(3):463-469. doi 10.1038/oby.2009.273

Keinicke H., Sun G., Mentzel C.M.J., Fredholm M., John L.M., Andersen B., Raun K., Kjaergaard M. FGF21 regulates hepatic metabolic pathways to improve steatosis and inflammation. *Endocr Connect.* 2020;9(8):755-768. doi 10.1530/EC-20-0152

Kim H.W., Lee J.E., Cha J.J., Hyun Y.Y., Kim J.E., Lee M.H., Song H.K., Nam D.H., Han J.Y., Han S.Y., Han K.H., Kang Y.S., Cha D.R. Fibroblast growth factor 21 improves insulin resistance and ameliorates renal injury in *db*/*db* mice. *Endocrinology*. 2013;154(9):3366-3376. doi 10.1210/en.2012-2276

Kleiner S., Mepani R.J., Laznik D., Ye L., Jurczak M.J., Jornayvaz F.R., Estall J.L., Chatterjee B.D., Shulman G.I., Spiegelman B.M. Development of insulin resistance in mice lacking PGC-1α in adipose tissues. *Proc Natl Acad Sci USA*. 2012;109(24):9635-9640. doi 10.1073/pnas.1207287109

Lau J.K., Zhang X., Yu J. Animal models of non-alcoholic fatty liver disease: current perspectives and recent advances. *J Pathol*. 2017;241(1):36-44. doi 10.1002/path.4829

Leow W.Q., Chan A.W.H., Mendoza P.G.L., Lo R., Yap K., Kim H. Non-alcoholic fatty liver disease: the pathologist's perspective. *Clin Mol Hepatol*. 2023;29(Suppl):S302-S318. doi 10.3350/cmh.2022.0329

Li H., Zhang J., Jia W. Fibroblast growth factor 21: a novel metabolic regulator from pharmacology to physiology. *Front Med*. 2013;7(1):25-30. doi 10.1007/s11684-013-0244-8

Li J., Wu H., Liu Y., Yang L. High fat diet induced obesity model using four strains of mice: Kunming, C57BL/6, BALB/c and ICR. *Exp Anim*. 2020;69(3):326-335. doi 10.1538/expanim.19-0148

Ma I.L., Stanley T.L. Growth hormone and nonalcoholic fatty liver disease. *Immunometabolism* 2023;5(3):e00030. doi 10.1097/IN9.0000000000000030

Makarova E.N., Yakovleva T.V., Balyibina N.Yu., Baranov K.O., Denisova E.I., Dubinina A.D., Feofanova N.A., Bazhan N.M. Pharmacological effects of fibroblast growth factor 21 are sex-specific in mice with the *lethal yellow* (A^y) mutation. *Vavilov J Genet Breed*. 2020;24(2):200-208. doi 10.18699/VJ20.40-o

Makarova E., Kazantseva A., Dubinina A., Denisova E., Jakovleva T., Balybina N., Bgatova N., Baranov K., Bazhan N. Fibroblast growth factor 21 (FGF21) administration sex-specifically affects blood insulin levels and liver steatosis in obese A^y mice. *Cells*. 2021a;10(12):3440. doi 10.3390/cells10123440

Makarova E., Kazantseva A., Dubinina A., Jakovleva T., Balybina N., Baranov K., Bazhan N. The same metabolic response to FGF21 administration in male and female obese mice is accompanied by sex-specific changes in adipose tissue gene expression. *Int J Mol Sci*. 2021b;22(19):10561. doi 10.3390/ijms221910561

Sanders F.W., Griffin J.L. *De novo* lipogenesis in the liver in health and disease: more than just a shunting yard for glucose. *Biol Rev Camb Philos Soc.* 2016;91(2):452-468. doi 10.1111/brv.12178

Senthil K.S.P., Shen M., Spicer E.G., Goudjo-Ako A.J., Stumph J.D., Zhang J., Shi H. Distinct metabolic effects following short-term exposure of different high-fat diets in male and female mice. *Endocr J.* 2014;61(5):457-470. doi 10.1507/endocrj.EJ13-0455

Speakman J.R. Use of high-fat diets to study rodent obesity as a model of human obesity. *Int J Obes*. 2019;43(8):1491-1492. doi 10.1038/s41366-019-0363-7

Spruss A., Henkel J., Kanuri G., Blank D., Püschel G.P., Bischoff S.C., Bergheim I. Female mice are more susceptible to nonalcoholic fatty liver disease: Sex-specific regulation of the hepatic AMP-activated protein kinase-plasminogen activator inhibitor 1 cascade, but not the hepatic endotoxin response. *Mol Med.* 2012;18(1):1346-1355. doi 10.2119/molmed.2012.00223

Takaki A., Kawai D., Yamamoto K. Multiple hits, including oxidative stress, as pathogenesis and treatment target in non-alcoholic steatohepatitis (NASH). *Int J Mol Sci*. 2013;14(10):20704-20728. doi 10.3390/ijms141020704

Xu J., Stanislaus S., Chinookoswong N., Lau Y.Y., Hager T., Patel J., Ge H., … Hecht R., Li Y.-S., Li Y., Lindberg R., Véniant M.M. Acute glucose-lowering and insulin-sensitizing action of FGF21 in insulin-resistant mouse models – association with liver and adipose tissue effects. *Am J Physiol Endocrinol Metab.* 2009;297(5):E1105-E1114. doi 10.1152/ajpendo.00348.2009

Yanko R.V., Chaka E.G., Zinchenko A.S., Safonov S.L., Levashov M.L. Features of modeling fatty liver disease in rats of different ages based on a high-calorie diet. *Obes Metab*. 2021;18(4):387-397. doi 10.14341/omet12789 (in Russia)

Ye Q., Jiang Y., Wu D., Cai J., Jiang Z., Zhou Z., Liu L., Ling Q., Wang Q., Zhao G. Atractylodin alleviates nonalcoholic fatty liver disease by regulating Nrf2-mediated ferroptosis. *Heliyon.* 2023;9(7):e18321. doi 10.1016/j.heliyon.2023.e18321

Conflict of interest. The authors declare no conflict of interest.
Received November 14, 2025. Revised April 2, 2026. Accepted April 24, 2026.

Vavilovskii Zhurnal Genetiki i Selektsii
Vavilov Journal of Genetics and Breeding. 2026;30(6):875-882

doi 10.18699/vjgb-26-89

Effect of selection for behavior on the blood glucose level in foxes exposed to restriction stress

R.G. Gulevich, S.G. Shikhevich, D.V. Shepeleva, A.V. Kharlamova

Institute of Cytology and Genetics of the Siberian Branch of the Russian Academy of Sciences, Novosibirsk, Russia
gulevich@bionet.nsc.ru

Abstract. Selection of silver foxes for attitude to humans influences the hypothalamus-pituitary-adrenal axis and sympathetic nervous system, which, in turn, are involved in the regulation of carbohydrate metabolism under stress. It has also been shown that heredity affectes carbohydrate metabolism and glucose tolerance. It remains to find out whether the selection for attitude to humans affected carbohydrate metabolism and blood glucose levels in silver foxes. We studied basal blood glucose levels in tame, aggressive, and unselected male and female silver foxes and glucose levels in females exposed to stress. Our results indicate that the basal blood glucose level in tame foxes is significantly lower than in unselected or aggressive ones regardless of sex. In unselected males, this parameter was lower than in aggressive animals. Aggressive foxes showed a sex difference in the basal blood glucose level: it was higher in males than in females. The glucose levels in aggressive females remained higher than in tame ones immediately after 10-min stress and two hours afterwards. Only aggressive females showed an excess blood glucose level over the basal one two hours after stress. The bulk group of foxes demonstrated a negative correlation between blood glucose and behavior score (response to humans) both at rest and after stress. A glucose tolerance test (GTT) was performed to compare the rates of glucose absorption from the bloodstream in silver fox females selected for behavior. Although selection for behavior did not affect glucose tolerance, judging from the area under the GTT curves, aggressive females differed from tame and unselected at the beginning of the test in longer persistence of elevated blood glucose. Thus, the selection of silver foxes for attitude to humans influences blood glucose levels at rest in both sexes and after stress in females.

Key words: selection; behavior; fox; aggressiveness; stress; glucose; tolerance; cortisol; correlation

For citation: Gulevich R.G., Shikhevich S.G., Shepeleva D.V., Kharlamova A.V. Effect of selection for behavior on the blood glucose level in foxes exposed to restriction stress. *Vavilovskii Zhurnal Genetiki i Selektsii = Vavilov J Genet Breed*. 2026; 30(6):875-882. doi 10.18699/vjgb-26-89

Funding. This work was supported by State Budgeted Project FWNR-2026-0032.

Acknowledgements. We are grateful to A.S. Babailova for data collection and preprocessing.

Authors' contributions. G.R.G.: concept, experiment design, manuscript editing, and approval of the final version; Sh.S.G.: data processing, result discussion, and editing of the manuscript; Sh.D.V., experimental work and discussion; Kh.A.V.: experimental work, discussion, and manuscript editing.

Влияние отбора по поведению на уровень глюкозы в крови у серебристо-черных лисиц после рестрикционного стресса

Р.Г. Гулевич, С.Г. Шихевич, Д.В. Шепелева, А.В. Харламова

Федеральный исследовательский центр Институт цитологии и генетики Сибирского отделения Российской академии наук, Новосибирск, Россия
gulevich@bionet.nsc.ru

Аннотация. Известно, что отбор серебристо-черных лисиц по отношению к человеку влияет на гипоталамо-гипофизарно-надпочечниковую (ГГН) и симпатическую нервную системы, которые, в свою очередь, участвуют в регуляции углеводного обмена при стрессе. Наряду с этим показано влияние генетических факторов на углеводный обмен и толерантность к глюкозе. Оставалось неизвестным, влияет ли отбор по отношению к человеку на уровень глюкозы в крови у серебристо-черных лисиц. В данной работе исследовали базальный уровень глюкозы в крови у ручных, агрессивных и неселекционированных самцов и самок серебристо-черных лисиц, а также уровень глюкозы после рестрикционного стресса у самок. Полученные результаты свидетельствуют о достоверно более низком базальном уровне глюкозы в крови у ручных лисиц по сравнению с агрессивными и неселекционированными животными, независимо от пола. Кроме того, у неселекционированных самцов этот

© Gulevich R.G., Shikhevich S.G., Shepeleva D.V., Kharlamova A.V., 2026
This work is licensed under a Creative Commons Attribution 4.0 License

показатель был ниже по сравнению с агрессивными животными. У агрессивных лисиц найдены половые различия по базальному уровню глюкозы в крови: у самцов этот показатель выше, чем у самок. В течение всего исследуемого периода после стресса (через 10 мин и 2 ч) уровень глюкозы в крови у агрессивных самок оставался повышенным по сравнению с ручными. Спустя 2 ч после стресса только у агрессивных самок отмечали более высокий уровень глюкозы по сравнению с исходным уровнем. В суммарной выборке самок лисиц, независимо от поведения до и после стресса, найдена отрицательная корреляция между уровнем глюкозы в крови и баллом поведения, которым оценивали реакцию на человека. Для сравнения скорости поглощения глюкозы из общего кровотока у самок серебристо-черных лисиц, селекционируемых по поведению, проводили глюкозотолерантный тест (ГТТ). В целом, судя по показателям площади под кривыми ГТТ, отбор по поведению не влиял на толерантность к глюкозе, вместе с тем у агрессивных самок, в отличие от ручных и неселекционированных, в начале теста отмечали более продолжительный период повышенного уровня глюкозы в крови. Таким образом, отбор по поведению влияет на уровень глюкозы в крови у серебристо-черных лисиц независимо от пола в состоянии покоя, а у самок – и после стресса.

Ключевые слова: отбор; поведение; лисицы; агрессивность; стресс; глюкоза; глюкозотолерантность; кортизол; корреляция

Introduction

Glucose is the main energy source for the brain. An increased blood glucose level, ensuring stable delivery of the nutrient to the brain, is an important prerequisite for survival at stress (Magomedova, Cummins, 2016). It is known that stress activates the sympathoadrenal and hypothalamic-pituitary-adrenal (HPA) axes. Their signals are involved in the development of stress-induced hyperglycemia (Stover et al., 2002; Barth et al., 2007; Magomedova, Cummins, 2015; Ross et al., 2015). In particular, catecholamines and glucocorticoids can enhance gluconeogenesis (glucose synthesis from non-sugar precursors), glycogenolysis (glycogen conversion to glucose) in the liver, and glucose release from the liver. They also inhibit glucose uptake by cells from the bloodstream.

Hereditary differences in stress-induced hyperglycemia were noted in inbred mouse lines (Harizi et al., 2007). Movement restriction, considered to be psychic stress, was responded by BALB/c mice with the maximum blood corticosterone level, whereas the increase in glucose level was lower than in DBA or C57Bl/6 mice. In contrast, restricted C57Bl/6 mice showed the minimum increase in corticosterone and maximum increase in glucose as compared to DBA and BALB/c.

Blood glucose increase was also observed in Large White pigs after aggressive clashes of two unfamiliar castrated males. In these cases, blood glucose linearly correlated with both aggressiveness and catecholamine (epinephrine and norepinephrine) levels, but the cortisol level did not correlate with aggressiveness (Fernandez et al., 1994).

A study of molecular mechanisms underlying the variation in stress sensitivity and aggressiveness was conducted in pigs of a synthetic line (SYN) obtained from males of one breed and hybrid dams from six commercial parental lines. Associations of DNA markers from ten genes related to the HPA axis were analyzed, as well as several physiological parameters: plasma levels of cortisol, creatine kinase, glucose, and lactate; adrenal weight; and aggressiveness (Muráni et al., 2010). A considerable association between single-nucleotide polymorphism g.233C>T in the *CRH* gene for corticotropin-releasing hormone and the plasma glucose level was revealed.

Low expression of genes involved in glucose metabolism, including glucose transport, gluconeogenesis, and glycolysis, was found in domesticated male pigs (or adapted to captivity for many generations) as compared to wild animals captured early in life. All animals received equal diets (He et al., 2017).

Studies of dogs of various breeds differing in liability to diabetes mellitus point to an influence of hereditary factors on hyperglycemia caused by insulin deficiency (Catchpole et al., 2013). This pancreatic hormone participates in the uptake of glucose from the bloodstream by cells and thereby lowers the blood glucose level. In contrast, small and fancy dog breeds are inclined to hypoglycemia. Its causes are thought to be disturbances in gluconeogenesis and glycogenolysis in the liver and low levels of glucocorticoids, which enhance these processes (Fleisher et al., 2008; Idowu, Heading, 2018).

Experiments on silver foxes selected for aggressive and tolerant attitude to humans may contribute to the understanding of the functional regulation of carbohydrate metabolism in animals with hereditary differences in the stress response of the HPA axis. The experiment modeling domestication, which has been conducted at the Institute of Cytology and Genetics (Novosibirsk) for decades, shows that silver fox selection for tame behavior lowers the HPA axis function as compared to animals selected for aggressive behavior (Bazhan et al., 1974; Oskina, 1996, 2008; Gulevich et al., 2004; Alexandrovich et al., 2023). In addition, the tame foxes show a lower activity of the sympathetic nervous system, as follows

from the lower blood norepinephrine level in comparison to aggressive and unselected animals (Oskina et al., 2008).

The results obtained from Norway rats and American minks selected for tame and aggressive behavior indicate that selection for behavior may alter some carbohydrate metabolism parameters (Albert et al., 2008; Kalinina et al., 2022). Tame male rats demonstrated a decrease in blood glucose level in comparison to aggressive ones (Albert et al. 2008). There is no information on blood glucose in minks selected for behavior, but it has been shown that the activity of alpha amylase in the pancreas, duodenum, and jejunum in tame minks is higher than in aggressive ones. This enzyme degrades starch to di- and trisaccharides in the gastrointestinal tract, and these oligosaccharides are then degraded to glucose, which is absorbed into the bloodstream (Kalinina et al., 2022). The blood glucose level is influenced not only by the pancreatic alpha amylase activity but also by other multidirectional factors.

In addition, the maximum alpha amylase activity in the pancreas was recorded in minks with highest tame behavior scores and the minimum, in most aggressive animals. This correlation appears to be related to the fact that changes in the mink brain caused by selection for behavior, in particular, monoamine levels in the hippocampus (Kulikov et al., 2016), may correspond to behavior scores, and the signals induced by these changes may reach norepinephrine-secreting cells of adrenal medulla via the sympathicoadrenal axis and glucocorticoid-secreting adrenal cortex via the HPA axis. Both norepinephrine and glucocorticoids are involved in the secretory function of the pancreas (Mössner et al., 1989; Nagain-Domaine et al., 1999).

These studies leave open the question whether and how the selection of silver foxes for behavior affects blood glucose levels at rest and after stress.

The goal of the present study is to investigate the effect of selection for behavior on blood glucose levels in tame and aggressive silver foxes at rest and after stress.

Materials and methods

Experiments were conducted with lines of adult silver foxes that had been selected for emotionally positive and aggressive-defensive attitudes to humans for over 60 years, hereafter referred to as tame and aggressive, respectively (Belyaev, 1979; Trut et al., 2004, 2009). A third group included foxes not exposed to deliberate selection for behavior, hereafter unselected.

Experimental animals were kept at the Shared Access Center for Gene Pools of Fur and Farm Animals (ICG, Novosibirsk). Animal behavior was assessed in the glove test. Tame foxes scored +4 to +4.5; aggressive, –2.5 to –3.5; and unselected, –0.75 to +1.

Basal blood glucose levels were measured in mmol/L with a One Touch Basic Plus glucose meter in fox males and females of each group after overnight fasting. One blood drop from the ear tip was loaded onto the test strip. Each group included 12 males and 10 females.

The effects of 10-min restriction stress on blood cortisol and glucose levels were analyzed only in females, whereas males were used in other experiments. Each group included eight naïve females. In the restriction stress experiment, foxes were placed to animal carriers with one side made of wire mesh. To reduce the stress, the restriction was applied for shorter time (10 min) in comparison to earlier studies (20 min) (Oskina, 1996).

Blood samples for cortisol assay were taken from *vena safena* in the morning after overnight fasting. The sampling lasted no more than 2–3 min per animal. Blood was sampled immediately after 10-min stress and 2 h afterwards. After taking the first blood sample, the foxes were placed to their home cages. One week before the experimental stress, blood samples were taken for the basal cortisol level. Blood cortisol was assayed by enzyme immunoassay with a Cortisol-IFA-BEST kit (Vector-Best, Novosibirsk).

One month after blood sampling from *vena safena* and one week before the stress experiment, basal blood glucose was assayed in the same animals with a Satellite glucose meter (ELTA, Moscow) in the morning after overnight fasting. Anothert glucose measurement was done in females immediately after exposure to stress, and the animals were placed to their hame cages. The next measurement was done two hours after stress.

To analyze the rates of glucose uptake from the bloodstream after carbohydrate loading, the glucose tolerance test (GTT) was conducted in the fox groups: five naïve females from each group. Blood glucose levels were recorded after overnight fasting and 10, 20, 40, and 120 min after intravenous administration of 50 % glucose monohydrate (0.5 g/kg).

The statistical evaluation of the results was performed with Statistica 10.0 software (Stat Soft, United States). Data on the basal blood glucose levels in fox males and females from the tame, aggressive, and unselected groups were analyzed by ANOVA for independent measurements followed by Fisher's LSD *post-hoc* test. Data on blood glucose levels in foxes within a particular behavior group in GTT and after stress were analyzed by Student's dependent *t*-test, and foxes from different groups were compared by Student's independent *t*-test.

Results

Figure 1 presents data on the basal glucose level in peripheral blood of tame, aggressive, and unselected foxes of both sexes. Two-way ANOVA shows that selection for behavior influenced the blood glucose level ($F_{2.60} = 16.07$, $p < 0.001$), the sex factor did not ($F_{1.60} = 1.64$, $p > 0.05$), and their interaction was significant ($F_{2.60} = 5.85$, $p < 0.01$). The subsequent *post-hoc* test indicates that glucose levels in tame males were significantly lower than in unselected ($p < 0.05$) or aggressive ($p < 0.001$), and the levels in unselected males were lower than in aggressive ($p < 0.001$). In tame females, as in males, glucose levels were lower than in unselected or aggressive ($p < 0.05$ in both cases). Sex-related differences in glucose levels were recorded only in the aggressive group: males showed higher levels than females ($p < 0.001$).

Figure 2 presents blood cortisol levels in tame, aggressive, and unselected fox females after restriction stress. This parameter was significantly lower in tame foxes than in aggressive or unselected before stress, immediately after stress, and two hours later. In tame foxes, 10-min restriction stress did not affect blood cortisol levels either immediately after stress or two hours after. In unselected and aggressive foxes, stress induced a significant increase in blood cortisol as compared to the respective basal levels ($p < 0.01$, $p < 0.001$, respectively). Two hours after stress, blood cortisol levels were significantly lower than those immediately after stress in unselected ($p < 0.01$) or aggressive ($p < 0.001$) foxes.

Figure 3 illustrates blood glucose levels in tame, aggressive, and unselected female foxes after restriction stress. We see that blood glucose levels in tame females were significantly lower than in aggressive before stress ($p < 0.01$), immediately after stress ($p < 0.05$), or two hours later ($p < 0.001$). Glucose levels in unselected foxes were intermediate between tame and aggressive at all timepoints. The basal glucose level in unselected foxes did not differ from the corresponding levels in tame or aggressive ones, but after stress it was higher than in tame animals ($p < 0.01$) and two hours after stress it was lower than in aggressive ones ($p < 0.001$). Stress did not induce blood glucose changes in tame or unselected foxes throughout the experiment period. In aggressive

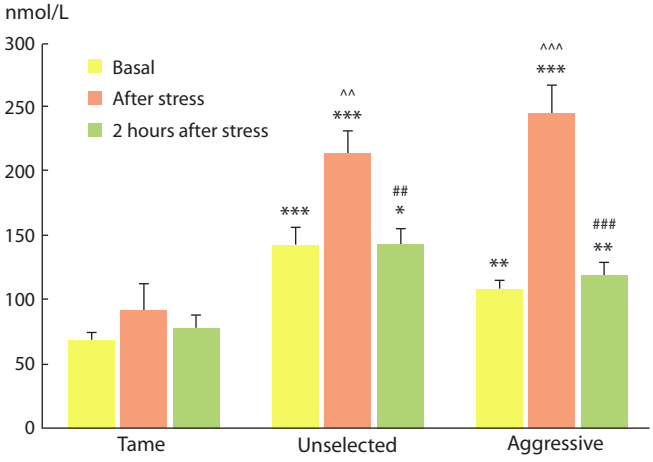


Fig. 2. Blood cortisol levels (nmol/L) in tame, unselected, and aggressive female foxes after stress.

* $p < 0.05$, ** $p < 0.01$, *** $p < 0.001$ as compared to tame females according to independent Student's *t*-test; ^^ $p < 0.01$, ^^^ $p < 0.001$ as compared to the corresponding basal level according to dependent Student's *t*-test; ## $p < 0.01$, ### $p < 0.001$ as compared to the level immediately after stress according to dependent Student's *t*-test.

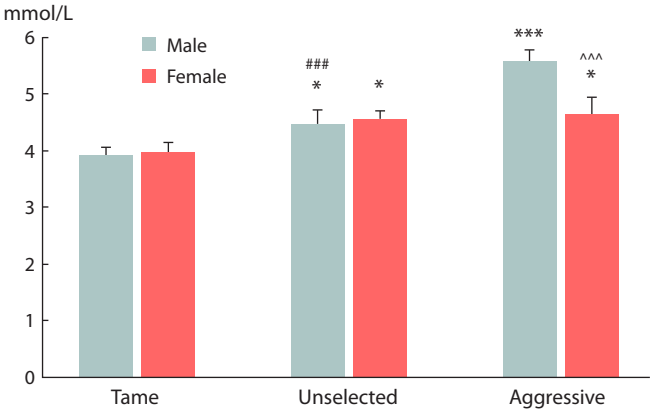


Fig. 1. Basal blood glucose levels in tame, aggressive, and unselected male and female foxes, mmol/L.

* $p < 0.5$, *** $p < 0.001$ compared to tame; ### $p < 0.001$ compared to aggressive; ^^^ $p < 0.001$ compared to corresponding males according to two-way ANOVA followed by *post-hoc* Fisher's LSD test.

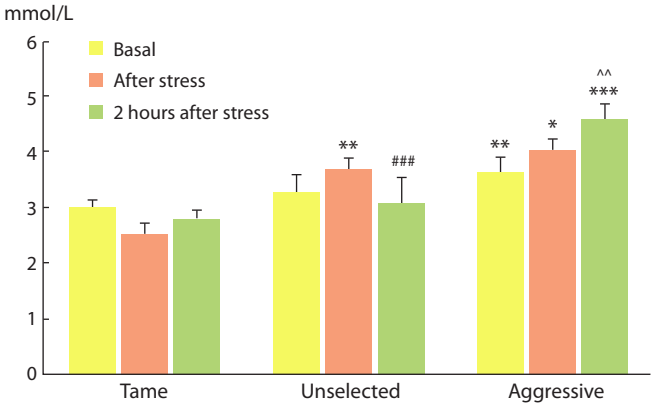


Fig. 3. Blood glucose levels in tame, aggressive, and unselected female foxes after stress, mmol/L.

* $p < 0.05$, ** $p < 0.01$, *** $p < 0.001$ as compared to tame according to independent Student's *t*-test; ^^ $p < 0.01$ as compared to the corresponding basal level according to dependent Student's *t*-test; ### $p < 0.001$ as compared to aggressive according to independent Student's *t*-test.

Correlation coefficients between behavior scores and blood glucose levels before and after stress in all foxes examined regardless of behavior

Tame, aggressive, and unselected silver foxes ($n = 24$)	Before stress	After 10-min stress	Two hours after stress
	–0.56*	–0.58*	–0.75*

Note. Behavior scores in unselected animals are indicated with plus and minus signs; tame, with plus signs; and aggressive, with minus signs.

* Significance level for correlation coefficients $p < 0.05$.

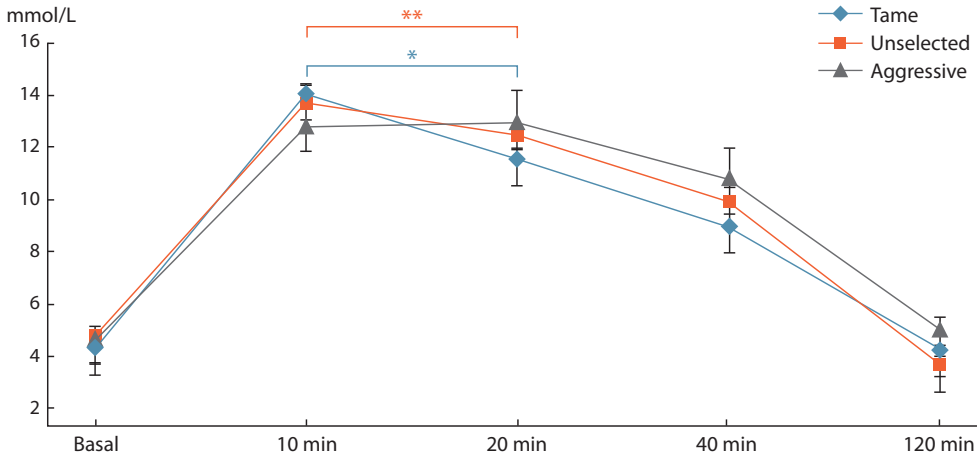


Fig. 4. Blood glucose levels (mmol/L) in tame, unselected, and aggressive female foxes after administration of 50 % glucose monohydrate, 0.5 g/kg (glucose tolerance test).

* $p < 0.05$ and ** $p < 0.01$ – Student's *t*-test for repetitive measurements for comparison of the levels between the 10- and 20-min timepoints.

animals, it increased as compared to the basal level two hours after stress ($p < 0.01$).

The Table presents correlation coefficients between behavior scores and blood glucose levels in the overall group of foxes: tame, aggressive, and unselected. Significant negative correlations were found between blood glucose levels and behavior scores before stress, immediately after stress, and two hours after stress.

We also assessed the correlation between blood glucose and cortisol levels in the same bulk sample. A significant positive correlation (0.51; $n = 22$) was found only at one timepoint: immediately after stress.

Data on blood glucose levels in tame, aggressive, and unselected female foxes in GTT are shown in Figure 4. Ten minutes after glucose monohydrate administration, blood glucose increased significantly in all animals regardless of behavior group: $p < 0.001$ in tame and unselected, $p < 0.01$ in aggressive.

Twenty minutes after test, glucose in tame and unselected foxes was significantly lower than the earlier values ($p < 0.05$ and $p < 0.01$, respectively), but did not decrease in aggressive foxes, remaining elevated; thus, the elevated glucose after glucose monohydrate administration to aggressive foxes persisted longer than in tame or unselected ones. Only 40 min after the glucose monohydrate challenge, the glucose level in aggressive foxes became significantly lower than in the preceding measurements ($p < 0.05$), whereas in tame and aggressive animals the decrease in comparison to preceding values continued ($p < 0.01$ and $p < 0.05$, respectively). Two hours after glucose monohydrate, blood glucose got back to a value close to the basal level in tame and aggressive foxes. In the unselected group, blood glucose at the same timepoint was significantly below the respective basal level ($p < 0.01$) and lower than in the tame or aggressive groups ($p < 0.01$ and $p < 0.05$, respectively).

The areas below the GTT curves did not differ significantly among the tame, unselected, and aggressive groups: 951.5±77.7; 986.8±83.3, and 1,088.1±236.3, respectively. In contrast to the above results, GTT did not reveal significant differences in basal blood glucose levels in tame, aggressive, and unselected female foxes; apparently, because of smaller samples ($n = 5$).

Discussion

Our results demonstrate a lower basal blood glucose level in tame male and female foxes as compared to unselected and aggressive ones (Fig. 1). This observation appears to

be caused by a lower activity of the HPA and sympathetic axes in the first group as compared to the other two, which has been reported by N.M. Bazhan et al. (1974), I.N. Oskina et al. (1985, 2008), and R.G. Gulevich et al. (2004). This study also confirms the lower basal cortisol level in tame females compared to aggressive or unselected ones (Fig. 2).

As mentioned above, glucocorticoids and norepinephrine participate in blood glucose regulation by intensifying gluconeogenesis (glucose synthesis from nonsugar precursors), glycogenolysis (glycogen breakdown to glucose) in the liver, and glucose release from the liver and also by inhibiting glucose uptake by cells from the bloodstream (Stover et al., 2002; Barth et al., 2007; Magomedova, Cummins, 2015; Ross et al., 2015). Studies on Norway male rats selected for behavior have shown that tame animals differed from aggressive in lower levels of blood corticosterone and glucose, which is consistent with data for foxes (Plyusnina, Oskina, 1997; Albert et al., 2008).

A lowered expression of genes involved in glucose metabolism, glucose transport, gluconeogenesis, and glycolylis has been found in domestic pigs as compared to wild ones captured early in life in spite of equal diets (He et al., 2017). Probably, fox selection for domestic and aggressive behavior influences the same glucose metabolism processes, so that blood glucose levels in tame foxes are lower than in aggressive ones.

The blood glucose levels measured in silver foxes in our study were close to those reported for dogs (3.3–6.2 mmol/L) by O. Idowu and K. Heading (2018). The gender difference in basal blood glucose levels found in aggressive foxes (higher values in males than in females) (Fig. 1) agrees with the results obtained on mice by H. Harizi et al. (2007), who presume that this sex dimorphism is due to the involvement of androgens in insulin resistance induction. Regrettably, the results on blood glucose in Norway rats selected for behavior include only males (Albert et al., 2008).

Restriction stress did not affect the cortisol or glucose levels in the blood of tame foxes, which showed a lower response to stress, at any timepoint: immediately after stress and two hours later. Blood cortisol levels in unselected and aggressive foxes increased significantly immediately after stress. Blood glucose levels did not change in unselected foxes but increased two hours after stress in aggressive ones, characterized by a stronger stress response.

In a study by P.D. Miles et al. (1991), i.c.v. carbachol (acetylcholine analog) injections to dogs raised the levels of catecholamines and cortisol, thereby mimicking the effect of stress, and enhanced not only glucose production but also its absorption. As a result, the glucose level increased slightly but statistically significantly no sooner than 15 min after the injection.

Thus, it is reasonable to suppose that the increase in blood glucose in stressed unselected and aggressive foxes occurred slightly later than after 10 min. The increase in blood glucose recorded in aggressive foxes two hours after stress as compared to the basal value could be caused by long-term intense production of glucose and/or its release to blood combined with slower absorption from the bloodstream.

The negative correlation between blood glucose before and after stress, on the one side, and behavior score, on the other side, found in the bulk fox sample regardless of behavior (see the Table) is consistent with data on the correlation between blood glucose and aggressiveness in pigs after a clash between two unfamiliar males (Fernandez et al., 1994). The difference in the sign of correlation between foxes and pigs (negative in the former and positive in the latter) may be related to the fact that the behavior of the most aggressive foxes was marked with the minimum score and of the tamest, the maximum, as opposed to pigs. To put it simply, the higher is aggressiveness, the higher is the blood glucose level, both in foxes and pigs.

The same study on pigs demonstrated a correlation between the levels of glucose and catecholamines (epinephrine and norepinephrine) in blood. We have mentioned that the blood levels of norepinephrine in tame foxes is lower than in aggressive or unselected (Oskina et al., 2008).

The detected correlation between behavior scores and blood glucose levels in foxes is likely to be related to the assumption that the changes in the fox brain induced by selection for behavior, in particular, levels of tyrosine hydroxylase (enzyme involved in catecholamine production) and serotonin (Dygalo et al., 1988; Popova, 2017) correspond to behavior scores and the signals from such changes come to cells of the adrenal medulla, which secrete norepinephrine, via the sympathoadrenal axis and to the adrenal cortex, which secretes glucocorticoids, via the HPA axis. In turn, both norepinephrine and glucocorticoids participate in the regulation of gluconeogenesis in the liver, glucose release from the liver, and glucose uptake by cells from the bloodstream (Stover et al., 2002; Barth et al., 2007; Magomedova, Cummins, 2015; Ross et al., 2015).

The area under the GTT curve shows that the rate of glucose disposal after carbohydrate challenge did not differ among tame, aggressive, and unselected foxes. However, soon after glucose monohydrate administration to aggressive foxes, we noted a longer period of elevated

blood glucose level than in tame or unselected animals, as it remained elevated after 20 min, whereas in tame and unselected foxes it decreased (Fig. 4).

The blood glucose level in tame and aggressive foxes returned to the basal level two hours after glucose monohydrate administration, whereas this parameter in unselected foxes remained significantly lower than the basal level and corresponding levels in tame or aggressive ones. This observation may be indicative of a faster glucose uptake from the bloodstream in unselected animals in this time interval. A slight hypoglycemia three hours after oral glucose administration has also been reported in dogs: the maximum values are recorded after 30–60 min, and the return to the basal level, 2 h after the challenge (Kaneko, 1997).

Conclusion

The selection of silver foxes for attitude to humans affects the basal blood glucose level regardless of sex, which may be associated with changes in the activity of the sympathetic and HPA axes in the selection. Tame male and female foxes showed lower blood glucose levels than aggressive or unselected ones.

The stress conditions did not influence blood glucose in tame and unselected female foxes, whereas aggressive animals demonstrated a delayed response, as glucose levels rose only two hours after stress. Although the glucose tolerance estimated from the area under the GTT curve did not change in selection for behavior, a longer time interval of elevated blood glucose was noted at the early step of GTT in aggressive females than in tame or unselected.

Compliance with ethical standards. Experiments were conducted in accordance with the Guidelines on the work with laboratory predator mammals (GOST 33217-2014) and European bioethical standards (Directive 2010/63/EU).

References

Albert F.W., Shchepina O., Winter C., Römpler H., Teupser D., Palme R., Ceglarek U., … Thiery J., Morgenstern R., Plyusnina I.Z., Schöneberg T., Pääbo S. Phenotypic differences in behavior, physiology and neurochemistry between rats selected for tameness and for defensive aggression towards humans. *Horm Behav.* 2008;53(3):413-421. doi 10.1016/j.yhbeh.2007.11.010

Alexandrovich Yu.V., Antonov E.V., Shikhevich S.G., Kharlamova A.V., Meister L.V., Makovka Y.V., Shepeleva D.V., Gulevich R.G., Herbeck Yu.E. The expression profile of genes associated with behavior, stress, and adult neurogenesis along the hippocampal dorsoventral axis in tame and aggressive foxes. *Vavilovskii Zhurnal Genetiki i Selektsii = Vavilov J Genet Breed*. 2023;27(6):651-661. doi 10.18699/VJGB-23-76

Barth E., Albuszies G., Baumgart K., Matejovic M., Wachter U., Vogt J., Radermacher P., Calzia E. Glucose metabolism and catecholamines. *Crit Care Med.* 2007;35(9 Suppl):S508-S518. doi 10.1097/01.CCM.0000278047.06965.20

Bazhan N.M., Krass P.M., Kolpakov M.G., Trut L.N. Change in the secretory activity of the adrenal cortex in silver foxes in the process of domestication. *Doklady Akademii Nauk SSSR = Proceedings of the Academy of Sciences of USSR.* 1974;216(4):922-924 (in Russian)

Belyaev D.K. Destabilizing selection as a factor in domestication. *J Hered*. 1979;70:301-308

Catchpole B., Adams J.P., Holder A.L., Short A.D., Ollier W.E.R., Kennedy L.J. Genetics of canine diabetes mellitus: are the diabetes susceptibility genes identified in humans involved in breed susceptibility to diabetes mellitus in dogs? *Vet J*. 2013;195(2):139-147. doi 10.1016/j.tvjl.2012.11.013

Dygalo N.N., Bykova T.S., Naumenko E.V. Brain tyrosine hydroxylase activity in behavior-selected silver foxes. *Journal of Evolutionary Biochemistry and Physiology*.1988;24(4):503-508 (in Russian)

Fernandez X., Meunier-Salaün M.-C., Mormede P. Agonistic behavior, plasma stress hormones, and metabolites in response to dyadic encounters in domestic pigs: interrelationships and effect of dominance status. *Physiol Behav*. 1994;56(5):841-847. doi 10.1016/0031-9384(94)90313-1

Fleischer S., Sharkey M., Mealey K., Ostrander E.A., Martinez M. Pharmacogenetic and metabolic differences between dog breeds: their impact on canine medicine and the use of the dog as a preclinical animal model. *AAPS J.* 2008:10(1):110-119. doi 10.1208/s12248-008-9011-1

Gulevich R.G., Oskina I.N., Shikhevich S.G., Fedorova E.V., Trut L.N. Effect of selection for behavior on pituitary-adrenal axis and proopiomelanocortin gene expression on silver foxes (*Vulpes vulpes*). *Physiol Behav*. 2004;82(2-3):513-518. doi 10.1016/j.physbeh.2004.04.062

Harizi H., Homo-Delarche F., Amrani A., Coulaud J., Mormède P. Marked genetic differences in the regulation of blood glucose under immune and restraint stress in mice reveals a wide range of corticosensitivity. *J Neuroimmunol.* 2007;189(1-2):59-68. doi 10.1016/j.jneuroim.2007.06.019

He D., Ma J., Long K., Wang X., Li X., Jiang A., Li M. Differential expression of genes related to glucose metabolism in domesticated pigs and wild boar. *Biosci Biotechnol Biochem.* 2017;81(8):1478-1483. doi 10.1080/09168451.2017.1322893

Idowu O., Heading K. Hypoglycemia in dogs: causes, management, and diagnosis. *Can Vet J*. 2018;59(6):642-649

Kalinina S.N., Ilyukha V.A., Trapezov O.V., Morozov A.V., Trapezova L.I., Nekrasova M.A., Stepanova M.A., Sysoeva E.A. Activity of digestive enzymes in the American mink (*Neovison vison*) selected for tameness and defensive aggression toward humans. *J Evol Biochem Physiol.* 2022;58(1):64-72. doi 10.1134/S0022093022010069

Kaneko J.J. Carbohydrate metabolism and its diseases. In: Clinical Biochemistry of Domestic Animals. Academic Press, 1997;45-81. doi 10.1016/B978-012396305-5/50004-X

Kulikov A.V., Bazhenova E.Yu., Kulikova E.A., Fursenko D.V., Trapezova L.I., Terenina E.E., Mormeded R., Popova N.K., Trapezov O.V. Interplay between aggression, brain monoamines and fur color mutation in the American mink. *Genes Brain Behav*. 2016;15(8):733-740. doi 10.1111/gbb.12313

Magomedova L., Cummins C.L. Glucocorticoids and metabolic control. In: Herzig S. (Ed.) Metabolic Control. Handbook of Experimental Pharmacology. Vol. 233. Springer, 2015;73-93. doi 10.1007/164_2015_1

Miles P.D., Yamatani K., Lickley H.L., Vranic M. Mechanism of glucoregulatory responses to stress and their deficiency in diabetes. *Proc Natl Acad Sci USA.* 1991;88(4):1296-1300. doi 10.1073/pnas.88.4.1296

Mössner J., Böhm S., Fischbach W. Role of glucocorticosteroids in the regulation of pancreatic amylase synthesis. *Pancreas*. 1989;4(2):194-203. doi 10.1097/00006676-198904000-00008

Muráni E., Ponsuksili S., D'Eath R.B., Turner S.P., Kurt E., Evans G., Thölking L., Klont R., Foury A., Mormède P., Wimmers K. Association of HPA axis-related genetic variation with stress reactivity and aggressive behaviour in pigs. *BMC Genet*. 2010;11:74. doi 10.1186/1471-2156-11-74

Nagain-Domaine C., Presset O., Chariot J., Roze C. Modulation of external pancreatic secretion by endogenous norepinephrine: study with a norepinephrine uptake blocker in the rat. *Pancreas*. 1999;18:300-307. doi 10.1097/00006676-199904000-00012

Oskina I.N., Trut L.N. Age-related changes in blood corticosteroid levels in foxes of different behaviors. *Doklady Akademii Nauk SSSR = Proceedings of the Academy of Sciences of USSR*. 1985;281(3):1010-1014 (in Russian)

Oskina I.N. Analysis of the functional state of the pituitary-adrenal axis during posnatal development of domesticated silver foxes (*Vulpes vulpes*). *Scientifur.* 1996;20(2):159-167

Oskina I.N., Herbeck Yu.E., Shikhevich S.G., Plyusnina I.Z., Gulevich R.G. Alterations in the hypothalamus-pituitary-adrenal and immune systems during selection of animals for tame behavior. *Informatsionnyy Vestnik VOGiS = The Herald of Vavilov Society for Geneticists and Breeders.* 2008;12(1/2):39-49 (in Russian)

Plyusnina I.Z., Oskina I.N. Behavioral and adrenocortical responses to open-field test in rats selected for reduced aggressiveness towards humans. *Physiol Behav*. 1997;61(3):381-385. doi 10.1016/s0031-9384(96)00445-3

Popova N.K. The domestication and the brain: forty years after. *Vavilovskii Zhurnal Genetiki i Selektsii =Vavilov J Genet Breed*. 2017;21(4):414-420. doi 10.18699/VJ17.259 (in Russian)

Ross A.P., Darling J.N., Parent M.B. Excess intake of fat and sugar potentiates epinephrine-induced hyperglycemia in male rats. *J Diabetes Complications.* 2015;29(3):329-337. doi 10.1016/j.jdiacomp.2014.12.017

Stover J.F., Sakowitz O.W., Thomale U.W., Kroppenstedt S.N., Unterberg A.W. Norepinephrine-induced hyperglycemia does not increase cortical lactate in brain-injured rats. *Intensive Care Med*. 2002;28(10):1491-1497. doi 10.1007/s00134-002-1431-2

Trut L.N., Plyusnina I.Z., Oskina I.N. An experiment on fox domestication and debatable issues of evolution of the dog. *Russ J Genet*. 2004;40:644-655. doi 10.1023/B:RUGE.0000033312.92773.c1

Trut L., Oskina I., Kharlamova A. Animal evolution during domestication: the domesticated fox as a model. *BioEssays*. 2009;31(3):349-360. doi 10.1002/bies.200800070

Conflict of interest. The authors declare no conflict of interest.

Received December 5, 2025. Revised April 29, 2026. Accepted May 4, 2026.

Vavilovskii Zhurnal Genetiki i Selektsii
Vavilov Journal of Genetics and Breeding. 2026;30(6):883-898

doi 10.18699/vjgb-26-90

Whole genome sequencing identifies genetic variants associated with senescence-accelerated phenotype of OXYS rats

V.M. Petrova [1], M.S. Protasova [1, 2], A.D. Manakhov [1, 2], N.A. Stefanova [3], N.G. Kolosova [3], E.I. Rogaev [4]

[1] Sirius University of Science and Technology, Sirius Federal Territory, Krasnodar region, Russia
[2] Vavilov Institute of General Genetics of the Russian Academy of Sciences, Moscow, Russia
[3] Institute of Cytology and Genetics of the Siberian Branch of the Russian Academy of Sciences, Novosibirsk, Russia
[4] UMass Chan Medical School, Department of Psychiatry, Shrewsbury, United States
petrova.vm@talantiuspeh.ru; evivrecc@gmail.com

Abstract. Age is the primary risk factor for age-related diseases, the early onset of which manifests as premature aging, whereas delayed development forms the basis for healthy aging and longevity. Adverse genetic variants contribute to premature aging and its diverse manifestations, including increased multimorbidity. Identifying the genetic underpinnings of premature aging and developing preventive approaches are essential to extending the human healthspan, which requires fundamental research using animal models. In this study, we performed whole-genome sequencing (coverage depth >25×) of OXYS rats – a unique model of premature aging characterized by the early onset of geriatric disorders, including cataracts, AMD-like retinopathy, Alzheimer's disease-like pathology, osteoporosis, sarcopenia, and hypertrophic cardiomyopathy – using the parental Wistar/Icgn rat strain as a control. The screening for single-nucleotide variants (SNVs), short insertions/deletions (indels), and copy number variations (CNVs) and comparative genomic analysis revealed genetic variants unique to OXYS rats that are absent in other rat strains. Specifically, we identified a large deletion in the *Fat1* enhancer, deletions in the promoter regions of *Abcf1* and *Gsta6*, and missense variants in *Cic*, *Akap6*, *Nqo2*, *Cerkl*, *Bfsp1*, and *Cmya5* that lead to amino acid substitutions in highly conserved protein regions. Bioinformatic analysis suggested that these variants may contribute to the key features of premature aging in OXYS rats. Notably, deletions in the *Fat1* enhancer and *Gsta6* promoter, alongside missense substitutions in *Cic*, *Akap6*, and *Nqo2*, may drive early neurodegeneration and cognitive deficits by disrupting neurogenesis, reducing neuronal survival, and impairing antioxidant defense. The deletion in the *Abcf1* promoter and the missense variants in *Cerkl* may induce retinopathy features by disrupting retinal homeostasis and weakening the protection of photoreceptors and retinal pigment epithelium (RPE) cells against oxidative stress and apoptosis. Furthermore, the missense substitution in *Bfsp1* likely contributes to early cataract development by reducing the stability of lens intermediate filaments. Finally, missense variants in *Cmya5* and *Akap6* may promote sarcopenia and cardiomyopathy via the destabilization of myofibrils in skeletal muscles and cardiomyocytes (*Cmya5*) and through impaired skeletal muscle regeneration and structural disorganization of cardiomyocytes (*Akap6*).

Key words: premature aging; age-associated diseases; OXYS rat strain; whole genome sequencing; genetic variants; copy number variations

For citation: Petrova V.M., Protasova M.S., Manakhov A.D., Stefanova N.A., Kolosova N.G., Rogaev E.I. Whole genome sequencing identifies genetic variants associated with senescence-accelerated phenotype of OXYS rats. *Vavilovskii Zhurnal Genetiki i Selektsii = Vavilov J Genet Breed*. 2026;30(6):883-898. doi 10.18699/vjgb-26-90

Funding. This work was supported by State Program "Scientific and Technological Development of the Sirius Federal Territory", Agreement 18-03 of September 10, 2024, project IMB-BFT-2403 (Protasova M.S.).

Полногеномное исследование генетических детерминант преждевременного старения крыс OXYS

В.М. Петрова [1], М.С. Протасова [1, 2], А.Д. Манахов [1, 2], Н.А. Стефанова [3], Н.Г. Колосова [3], Е.И. Рогаев [4]

[1] Научно-технологический университет «Сириус», федеральная территория «Сириус», Краснодарский край, Россия
[2] Институт общей генетики им. Н.И. Вавилова Российской академии наук, Москва, Россия
[3] Федеральный исследовательский центр Институт цитологии и генетики Сибирского отделения Российской академии наук, Новосибирск, Россия
[4] Медицинская школа Чан Массачусетского университета, департамент психиатрии, Шрусбери, США
petrova.vm@talantiuspeh.ru; evivrecc@gmail.com

Аннотация. Возраст – основной фактор риска ассоциированных со старением заболеваний, раннее развитие которых лежит в основе преждевременного старения, а более позднее – обеспечивает долголетие. Неблагоприятные генетические варианты способствуют преждевременному старению и его множественным

© Petrova V.M., Protasova M.S., Manakhov A.D., Stefanova N.A., Kolosova N.G., Rogaev E.I., 2026
This work is licensed under a Creative Commons Attribution 4.0 License

проявлениям – увеличению числа коморбидных состояний. Установление предпосылок преждевременного старения и разработка подходов к его профилактике – основной резерв увеличения здорового периода жизни людей, что обусловливает необходимость в фундаментальных исследованиях на моделях животных. Нами проведено полногеномное секвенирование (с глубиной покрытия >25×) крыс линии OXYS – модели преждевременного старения, которое сопровождается ранним развитием комплекса гериатрических заболеваний: катаракты, ретинопатии, аналогичной возрастной макулярной дегенерации (ВМД), признаков болезни Альцгеймера (БА), остеопороза, саркопении и гипертрофической кардиомиопатии (контроль – родительская линия крыс Wistar/Icgn). Поиск однонуклеотидных вариантов, инсерций-делеций (инделов) и вариаций числа копий геномных регионов (CNV) и сравнительный геномный анализ выявили генетические варианты, уникальные для крыс OXYS и не встречающиеся среди других линий крыс. Обнаружены: крупная делеция в энхансере гена *Fat1*; делеции в промоторных регионах генов *Abcf1* и *Gsta6*; а также миссенс-варианты в генах *Cic*, *Akap6*, *Nqo2*, *Cerkl*, *Bfsp1* и *Cmya5*, приводящие к аминокислотным заменам в высококонсервативных регионах белков. Проведенный биоинформатический анализ показал, что данные варианты, вероятно, вносят вклад в развитие ключевых проявлений преждевременного старения у линии крыс OXYS. А именно: делеции в энхансере *Fat1* и промоторе *Gsta6*, а также миссенс-замены в *Cic*, *Akap6* и *Nqo2* могут способствовать ранней нейродегенерации и когнитивному дефициту, нарушая нейрогенез, снижая выживаемость нейронов и их антиоксидантную защиту; делеция в промоторной области *Abcf1* и миссенс-варианты в *Cerkl* могут приводить к возникновению признаков ВМД, нарушая гомеостаз сетчатки и ослабляя защиту фоторецепторов и клеток пигментного эпителия сетчатки (РПЭ) от окислительного стресса и апоптоза соответственно, а миссенс-замена в *Bfsp1* – к раннему развитию катаракты через снижение стабильности промежуточных филаментов хрусталика. Миссенс-варианты в *Cmya5* и *Akap6* могут способствовать развитию саркопении и кардиомиопатии: замена в *Cmya5* – за счет дестабилизации миофибрилл в кардиомиоцитах и скелетных мышцах, а замена в *Akap6* – за счет нарушения регенерации скелетных мышц и структурной организации кардиомиоцитов.

Ключевые слова: преждевременное старение; возраст-ассоциированные заболевания; линия крыс OXYS; полногеномное секвенирование; генетические варианты; вариации числа копий геномных регионов

Introduction

Age-related diseases are a natural consequence of the aging process. Their onset at an earlier age is a hallmark of premature aging, whereas their delayed manifestation forms the basis of healthy aging and longevity. Advances in the treatment of age-related diseases have led to a steady increase in life expectancy over the last few decades, while the healthy lifespan is increasing at a noticeably slower rate. Currently, over 60 % of individuals aged 65 and older suffer from multimorbidity rather than a single geriatric disorder (Figueira et al., 2016), the variety and age of onset of which are determined by genetic and environmental factors, quality of life, and access to healthcare. In this context, identifying the molecular and genetic underpinnings of premature aging and developing reliable methods for its prevention are fundamental to extending the human healthspan.

Research in this field requires fundamental studies using biological models. One of them is the OXYS rat strain (Institute of Cytology and Genetics, Siberian Branch of the Russian Academy of Sciences, hereafter ICG SB RAS), a model of premature aging characterized by the early development of a complex of geriatric diseases (Kolosova et al., 2014). The strain was bred in the 1970s by selecting Wistar/Icgn rats for early spontaneous cataracts. In the first five generations, cataract development was induced by galactose loading; subsequently, selection was carried out for early spontaneous cataracts, with which the animals inherited the premature aging syndrome.

Against a background of moderately elevated blood pressure, OXYS rats spontaneously develop cataracts, hypertrophic cardiomyopathy, sarcopenia, osteoporosis, and a retinopathy similar to human age-related macular degeneration (Kolosova et al., 2014). OXYS rats also develop all the key pathogenetic and "clinical" features of Alzheimer's disease (AD) in the absence of mutations in the genes (*App*, *Psen1*, and *Psen2*) specific to the familial form of AD. Thus, the strain can be considered a model of the most common (>95 %) sporadic form of this disease (Stefanova et al., 2014). The development of these manifestations of premature aging could be linked to oxidative stress, an imbalance in the systems responsible for the generation and detoxification of reactive oxygen species (ROS). However, elevated levels of oxidative damage to lipids, proteins, and DNA are recorded in tissues of OXYS rats later than signs of premature aging become apparent (Kolosova et al., 2006). Mitochondrial dysfunction, initially identified in the liver (Kolosova et al., 2001) and subsequently in muscles (Vays et al., 2014), the heart muscle (El'darov et al., 2015), brain structures (Tyumentsev et al., 2018), and the retina (Zhdankina et al., 2023), is considered the most likely cause of premature aging in OXYS rats. The link between mitochondrial dysfunction and premature aging in OXYS rats is also supported by the presence of single-nucleotide variants (SNVs) that can cause abnormalities in protein structure and/or function and influence the development of the OXYS phenotype (Devyatkin et al., 2020a, b).

The aim of this study is to identify genetic variants of various types – SNVs, short insertions/deletions (indels), and copy number variations (CNVs) – that may be associated with the development of the premature aging phenotype in OXYS rats.

Materials and methods

Animals. The study was performed on male rats of the OXYS strain (n = 3) and the Wistar/Icgn parental strain (n = 3) provided by the Center for Genetic Resources of Laboratory Animals at ICG SB RAS. The animals were kept under standard laboratory conditions (22 ± 2 °C and a 12-hour light/dark cycle) in cages (57 × 36 × 20 cm). Animals had *ad libitum* access to water and standard pelleted chow (BioPro, Russia).

Animal housing (including appropriate facilities, qualified personnel, and necessary documentation) and all animal experiments were conducted in accordance with the ethical guidelines for the use of animals in research supported by the Russian Science Foundation. The study also complied with Directive 2010/63/EU of the European Parliament and Council of the European Union of September 22, 2010, and was approved by the Bioethics Committee of ICG SB RAS (Protocol No. 85/1 of June 18, 2021).

Tissue collection. Animals were euthanized using carbon dioxide asphyxiation followed by decapitation for tissue harvesting. Cerebellar tissue fragments (30 mg) were collected from 3-month-old OXYS (n = 3) and Wistar/Icgn (n = 3) rats into 1.5 mL tubes. The samples were immediately frozen in liquid nitrogen and stored at –80 °C.

DNA extraction. Genomic DNA was extracted using the QIAamp DNA Mini Kit (Qiagen, Germany). DNA quality and quantity were assessed using a NanoDrop OneC microvolume UV-Vis spectrophotometer (Thermo Fisher Scientific, USA) and a Qubit 4 fluorometer (Thermo Fisher Scientific, USA).

Library preparation and whole-genome sequencing. Whole-genome libraries were prepared using the TruSeq DNA PCR-Free Kit (Illumina, USA). Library quality was assessed using a TapeStation 4150 automated electrophoresis platform (Agilent Technologies, USA), and library molarity was determined by quantitative PCR using the KAPA Library Quantification Kit (Roche Sequencing Solutions, USA). Paired-end sequencing (2 × 151 bp) was performed on a NovaSeq 6000 system (Illumina, USA).

Sequencing data processing. The quality of the obtained reads was assessed using FastQC v0.11.9 (Andrews, 2010). Adapter removal and quality filtering were performed using AdapterRemoval v2.3.3 with the parameters --minquality 20, --trimqualities, and --minlength 50 (Schubert et al., 2016). After preprocessing, the reads were mapped to the mRatBN7.2 *Rattus norvegicus* genome assembly using the BWA-MEM algorithm from BWA v0.7.17 (Li H., Durbin, 2009). Read duplicates were marked using MarkDuplicates from Picard v2.26.11 (Broad Institute, 2022). Alignment quality was assessed using SAMtools v1.9 (Li H. et al., 2009). Sequencing coverage was estimated using the CollectWgsMetrics tool from Picard v2.26.11 (Broad Institute, 2022).

Identification, annotation and filtering of SNVs and indels. The positions and genotypes of SNVs and indels were identified using HaplotypeCaller from GATK v4.2.2.0 (McKenna et al., 2010). Principal component analysis (PCA) was performed using PLINK v1.9 (Purcell et al., 2007) and visualized in RStudio (R version 4.3.2) using the tidyverse and ggplot2 packages (Wickham, 2016; Wickham et al., 2019). Genotype filtering was performed using a custom Python script. The script accepted a VCF file as input to select variants with a minimum coverage of 10×, homozygous for the alternative allele in all samples of the case group (OXYS) and absent in the homozygous state from the control group (Wistar/Icgn).

The Ensembl Variant Effect Predictor (VEP) version 113 (McLaren et al., 2016) was used for the annotation and classification of each SNV and indel. The SNV and indel genotypes of OXYS rats were compared with those of 146 rat strains from the Rat Genome Database (RGD) (de la Cruz et al., 2004) using BCFtools v1.15 (Danecek et al., 2021). All selected genetic variants were manually inspected using the Integrative Genomics Viewer (IGV) (Robinson et al., 2011). Analysis of amino acid substitutions was performed for canonical gene transcripts according to the Ensembl version 115 annotation (Dyer et al., 2025). The conservation of amino acid residues was assessed based on multiple alignments of orthologs from placental mammals (Table S1 in Supplementary Materials)[1], rodents, and related species (Table S2), retrieved from the Ensembl database version 115 (Dyer et al., 2025). A search for paralogs was also conducted in the Ensembl database version 115 (Dyer et al., 2025). Multiple alignments were visualized using UGENE v45.0 software (Okonechnikov et al., 2012). Protein structure prediction and visualization were performed in AlphaFold 3 (Abramson et al., 2024).

CNV detection, annotation and selection. CNV detection was performed using CNVpytor v1.3.1 with a 100-bp bin size as recommended for 20–30× coverage (Abyzov et al., 2011; Suvakov et al., 2021). Smoove v0.2.8 (Pedersen et al., 2020) was used to refine CNV coordinates and genotype the samples. For subsequent annotation, CNVs in regions with low mapping quality were filtered out. Genotypes were filtered using BCFtools v1.15 (Danecek et al., 2021). CNV annotation was performed by intersecting the coordinates with the genomic features of the mRatBN7.2 *Rattus norvegicus* assembly using the intersect command from BEDTools v2.30.0 (Quinlan, Hall, 2010). BEDTools v2.30.0 was also used to intersect CNV coordinates with H3K27ac enrichment peaks generated by MACS2 v2.2.6 (Zhang et al., 2008). CNV visualization was performed using IGV (Robinson et al., 2011).

A schematic description of the bioinformatics analysis is presented in Figure 1.

Results

Principal component analysis (PCA)

The genome coverage depth for each OXYS and Wistar/Icgn rat sample is presented in Table S3. The mean coverage depth was 32.36× for OXYS and 28.88× for Wistar/Icgn rats. A total

[1] Tables S1–S5, Figures S1–S25 and List S1 are available at: https://vavilov.elpub.ru/jour/manager/files/Suppl_Petrova_Engl_30_6.pdf

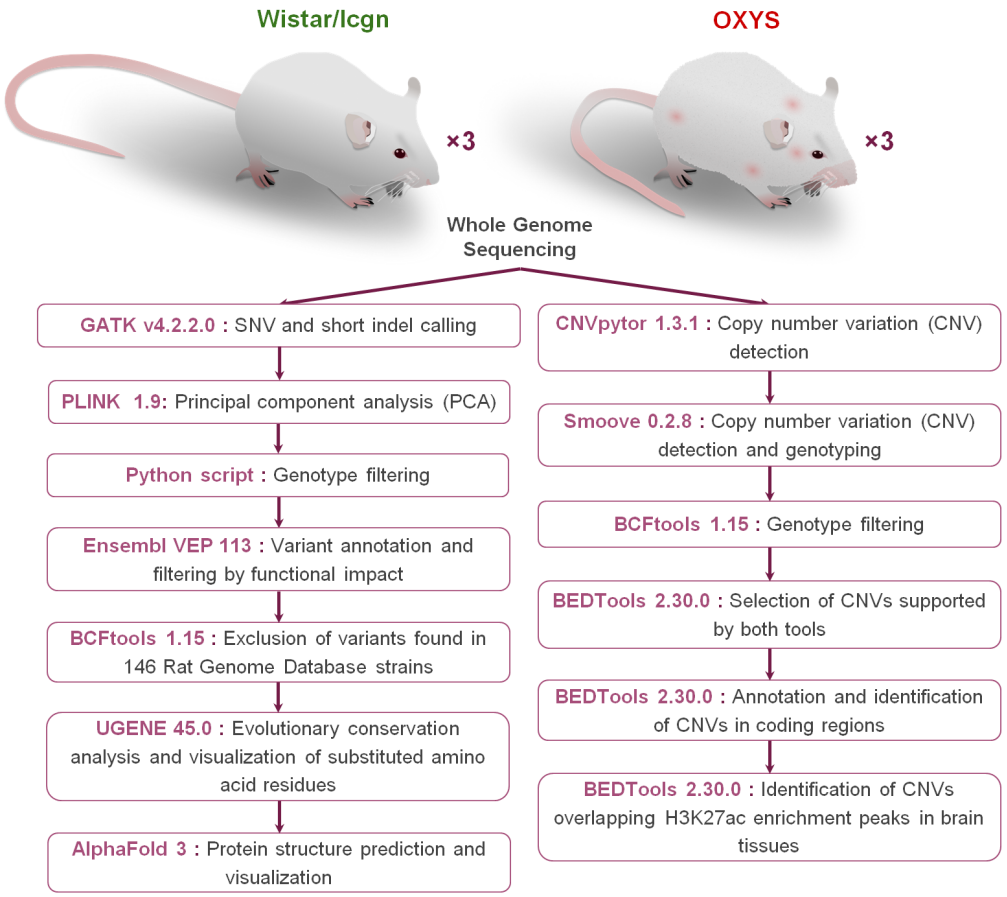


Fig. 1. Bioinformatics pipeline for genome analysis of Wistar/Icgn and OXYS rats.

of 12,412,404 genetic variants differing from the mRatBN7.2 *Rattus norvegicus* reference assembly were identified in the genomes of OXYS and Wistar/Icgn rats.

The genotypes of the OXYS and Wistar/Icgn rats were subjected to PCA. The two-dimensional plot shows the first (PC1) and second (PC2) principal components, which together account for 79.1 % of the total variance (Fig. 2). The plot demonstrates that the OXYS and Wistar/Icgn samples, as expected, form distinct clusters. Notably, the OXYS rat cluster (marked in red) is tightly grouped, pointing to a genetic homogeneity characteristic of inbred strains.

Analysis of SNVs and indels

Since the OXYS rat strain is inbred, the genetic variants determining its specific phenotype were expected to be homozygous in all individuals. Out of 12,009,286 chromosomal variants, we selected 1,363,823 positions where all three OXYS rats were homozygous for the alternative allele (with a coverage depth of ≥10×), while no individuals from the control Wistar/Icgn strain carried this allele in a homozygous state. Variants leading to predicted high-impact functional disruptions in canonical gene transcripts were then selected according to the Sequence Ontology classification (Eilbeck et al., 2005).

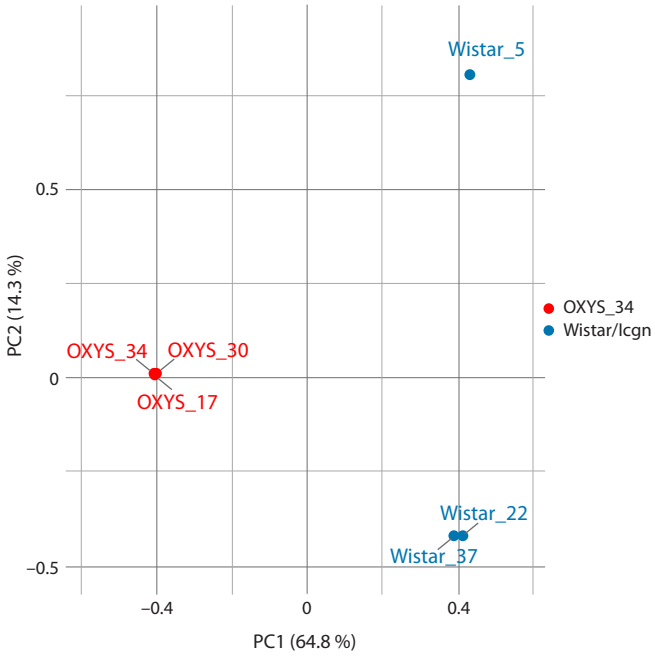


Fig. 2. Principal component analysis (PCA) performed using PLINK v1.9 based on the genotypes of OXYS (red circles) and Wistar/Icgn (blue circles) rats.

Specifically, 78 variants were identified as causing premature translation termination, loss of gene function, or triggering nonsense-mediated mRNA decay. Additionally, 423 missense variants predicted as damaging by the SIFT algorithm and leading to amino acid substitutions in the translated proteins were selected. By comparing the SNV and indel genotypes of OXYS rats with the genotypes of 146 rat strains (List S1) from RGD (de la Cruz, 2004), we identified 33 high-impact variants and 87 damaging missense variants that were completely absent from all other strains.

From this pool of genetic variants unique to OXYS rats, we prioritized variants in genes involved in key pathways related to aging and age-related pathologies, such as mitochondrial dysfunction, oxidative stress, neurodegeneration, cognitive and visual impairment, sarcopenia, and lipid metabolism disorders. Each candidate variant was verified by visual inspection of alignments using IGV and by analyzing the evolutionary conservation of the affected amino acid residues. Variants in regions with poor mapping quality, alignment artifacts, or low conservation were rejected. As a result, the following candidate genes were selected: *Abca1*, *Apob*, *Cic*, *Nqo2*, *Akap6*, *Cmya5*, *Cerkl*, and *Bfsp1*, whose functional impairments may underlie the premature aging phenotype of OXYS rats. The variants identified in these candidate genes are summarized in Table 1, visualized using IGV (Fig. S1), and shown in the transcript models (Fig. S2).

Lipid metabolism disorders. The *Apob* and *Abca1* genes are involved in lipid metabolism. *Abca1* is predominantly expressed in rat adipose tissue and liver, as well as in various immune cell types (Wu et al., 2009; RatGTEx Consortium, 2021). The *Abca1* gene product plays a key role in transporting cholesterol and phospholipids across the cell membrane, which is essential for high-density lipoprotein (HDL) formation in the liver (Oram, 2003; Ghanbari-Niaki et al., 2007). The V695L amino acid substitution is located in one of the transmembrane domains of Abca1, which is enriched in hydrophobic amino acid residues (Fig. 3*A* and Fig. S3). Valine (V) is present at the homologous position in most of its orthologs among placental mammals and rodents; however, leucine (L) was identified in the Arctic ground squirrel (*Urocitellus parryii*) (Fig. S4*A*). Other hydrophobic amino acids can also be found at this position. Examples are methionine (M) in birds, including the chicken (*Gallus gallus*) and the golden eagle (*Aquila chrysaetos*), and isoleucine (I) in fish, such as the Atlantic salmon (*Salmo salar*) (Fig. 3*A*). Furthermore, Abca1 has 15 ancient paralogs, which, in addition to valine (V), contain other hydrophobic amino acids at the homologous position, including isoleucine (I), alanine (A), methionine (M), and leucine (L) (Fig. S5). Taken together, these data indicate that the V695L substitution is likely compatible with the structural integrity and function of the protein.

The *Apob* gene encodes two isoforms of apolipoprotein B: ApoB-100, a structural protein of low-density lipoprotein (LDL) synthesized in the liver, and ApoB-48, a component

Table 1. Genomic coordinates and genotypes of unique OXYS missense variants identified in candidate genes across all analyzed samples (0 – reference allele, 1 – alternative allele)

Genomic coordinates	Reference allele	Alternative allele	Gene	Transcript consequence	Amino acid substitution	OXYS 17	OXYS 30	OXYS 34	Wistar 5	Wistar 22	Wistar 37
1:80,874,547	G	A	*Cic*	ENSRNOT00000101741.1:c.4235G>A	ENSRNOP00000094181.1:p.Cys1412Tyr	1/1	1/1	1/1	0/0	0/0	0/0
2:24,306,965	T	A	*Cmya5*	ENSRNOT00000073710.4:c.11011A>T	ENSRNOP00000064514.2:p.Arg3671Trp	1/1	1/1	1/1	0/0	0/1	0/1
3:64,239,860	C	A	*Cerkl*	ENSRNOT00000057878.6:c.1345G>T	ENSRNOP00000054687.5:p.Val449Leu	1/1	1/1	1/1	0/0	0/0	0/0
3:64,239,861	A	C	*Cerkl*	ENSRNOT00000057878.6:c.1344T>G	ENSRNOP00000054687.5:p.Phe448Leu	1/1	1/1	1/1	0/0	0/0	0/0
3:131,199,280	C	T	*Bfsp1*	ENSRNOT00000007727.6:c.827G>A	ENSRNOP00000007727.4:p.Arg276Gln	1/1	1/1	1/1	0/0	0/1	0/0
5:67,724,612	C	G	*Abca1*	ENSRNOT00000110113.1:c.2083G>C	ENSRNOP00000078596.1:p.Val695Leu	1/1	1/1	1/1	0/0	0/0	0/0
6:30,878,853	C	T	*Apob*	ENSRNOT00000046811.5:c.10237C>T	ENSRNOP00000039779.2:p.Leu3413Phe	1/1	1/1	1/1	0/0	0/0	0/0
6:70,399,863	C	T	*Akap6*	ENSRNOT00000006562.4:c.2443C>T	ENSRNOP00000006562.2:p.Arg815Trp	1/1	1/1	1/1	0/0	0/0	0/0
17:30,913,758	C	T	*Nqo2*	ENSRNOT00000024141.6:c.370G>A	ENSRNOP00000024141.5:p.Gly124Arg	1/1	1/1	1/1	0/0	0/0	0/0

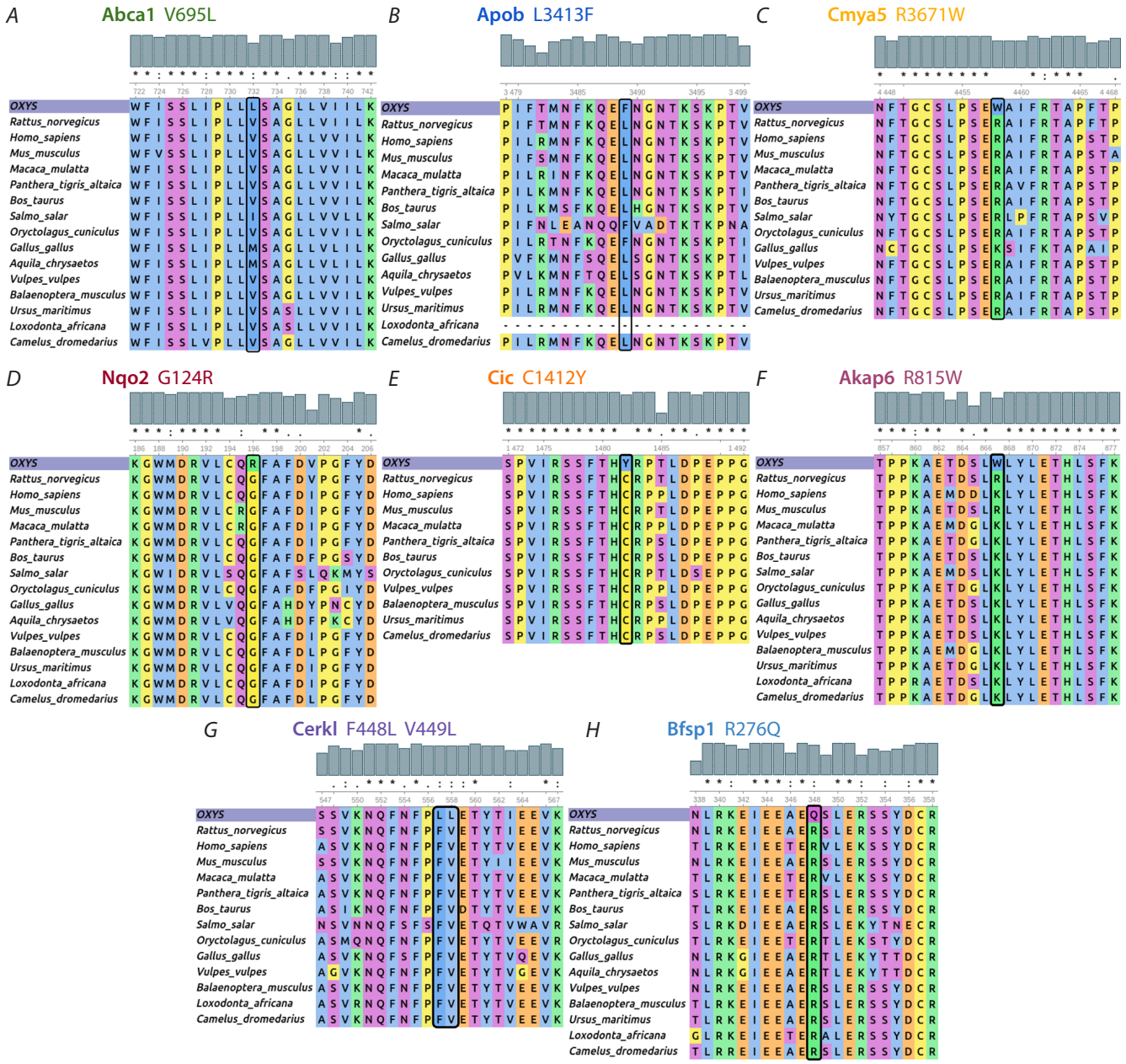


Fig. 3. Amino acid substitutions in OXYS rat proteins (top of each panel) and the homologous position (indicated by a black box) across orthologous proteins from various animal species, including the brown rat (*Rattus_norvegicus*), human (*Homo_sapiens*), house mouse (*Mus_musculus*), rhesus macaque (*Macaca_mulatta*), Amur tiger (*Panthera_tigris_altaica*), cattle (*Bos_taurus*), Atlantic salmon (*Salmo_salar*), European rabbit (*Oryctolagus_cuniculus*), chicken (*Gallus_gallus*), golden eagle (*Aquila_chrysaetos*), red fox (*Vulpes_vulpes*), blue whale (*Balaenoptera_musculus*), polar bear (*Ursus_maritimus*), African bush elephant (*Loxodonta_africana*), and dromedary camel (*Camelus_dromedarius*).

Amino acids are colored by chemical properties: polar uncharged (S, T, N, Q) in purple; hydrophobic (A, V, I, L, M, F, Y, W) in blue; positively charged (R, H, K) in green; negatively charged (D, E) in orange; and special cases (C, G, P) in yellow. The evolutionary conservation track is located above the sequences as a bar chart representing the degree of conservation. Images were generated using UGENE v45.0 software (Okonechnikov et al., 2012).

of chylomicrons produced by small intestinal cells. ApoB-100 is involved in the synthesis and secretion of very-low-density lipoprotein (VLDL), the precursor of LDL required for the transport of endogenous triglycerides and cholesterol into the bloodstream (Davidson, Shelness, 2000). Furthermore, ApoB-100 serves as a ligand for LDL receptors on hepatocytes, mediating the uptake and clearance of ApoB-containing particles by the liver (Davidson, Shelness, 2000). The *Apob* gene has no paralogs. The identified amino acid substitution L3413F is located within the heparin-binding domain of ApoB-100, which mediates the binding of LDL particles to glycosaminoglycan-rich proteoglycans of the extracel-

lular matrix (Flood et al., 2004) (Fig. 3*B* and Fig. S6). While leucine (L) is present at the homologous position in most rodents and mammals, phenylalanine (F) was found at this position in the European rabbit (*Oryctolagus cuniculus*) and the Atlantic salmon (*S. salar*) (Fig. 3*B* and Fig. S4*B*). Since both amino acids are hydrophobic and phenylalanine occurs at the homologous position in evolutionarily distant species without causing a loss of viability, it can be concluded that the L3413F substitution does not disrupt protein function significantly. However, because phenylalanine possesses a bulky aromatic side chain, its potential impact on the local conformation of the domain or the efficiency of interaction with extracellular matrix proteoglycans cannot be entirely ruled out. Therefore, this substitution likely represents a variant with low functional impact.

Skeletal and cardiac muscle dysfunctions. The *Cmya5* gene encodes a large protein highly expressed in skeletal muscles and the heart, where it is involved in structural organization of sarcomeres in cardiomyocytes and skeletal muscle fibers (Wu et al., 2009; Lu et al., 2022). The identified missense variant results in an R3671W substitution within the Fibronectin type-III 1 domain (FN3-1) of Cmya5, which mediates interactions with titin M-domains and stabilizes the sarcomere (Sarparanta, 2008; Sarparanta et al., 2010) (Fig. 3*C* and Fig. 4*A*). Arginine (R) at this position is highly conserved across evolutionarily distant animal species, as well as among rodents (Fig. 3*C* and Fig. S4*C*). Lysine (K), which carries a positive charge similar to arginine, is found only in the chicken (*G. gallus*). The Cmya5 protein has three evolutionarily ancient paralogs: Fsd1, Fsd2, and Fsd1l. One of these, Fsd2, is expressed in muscle tissue, but it performs different functions. The substitution of positively charged arginine for hydrophobic aromatic tryptophan at position 3671 (R3671W) is located within a β-sheet of the Cmya5 FN3-1 domain. This mutation disrupts local interactions with neighboring amino acid residues, presumably impairing domain folding and, as a consequence, its interactions with other proteins (Fig. 4*A*).

Neurodegeneration and cognitive decline. The *Nqo2* gene encodes the flavin-dependent protein Nqo2, which is structurally homologous to Nqo1 quinone dehydrogenase but differs significantly in cofactor specificity. Nqo2 binds the physiological cofactor NAD(P)H extremely inefficiently and likely functions primarily as a regulatory rather than a catalytic protein (Islam, Shilton, 2025). *Nqo2* is highly expressed in the kidney and liver (Wu et al., 2009; RatGTEx Consortium, 2021). The missense variant detected in OXYS rats results in a G124R substitution at a position highly conserved across evolutionarily distant animals, rodents, and related species (Fig. 3*D* and Fig. S4*D*). This substitution is located near the FDV (phenylalanine-aspartic acid-valine) substrate-binding

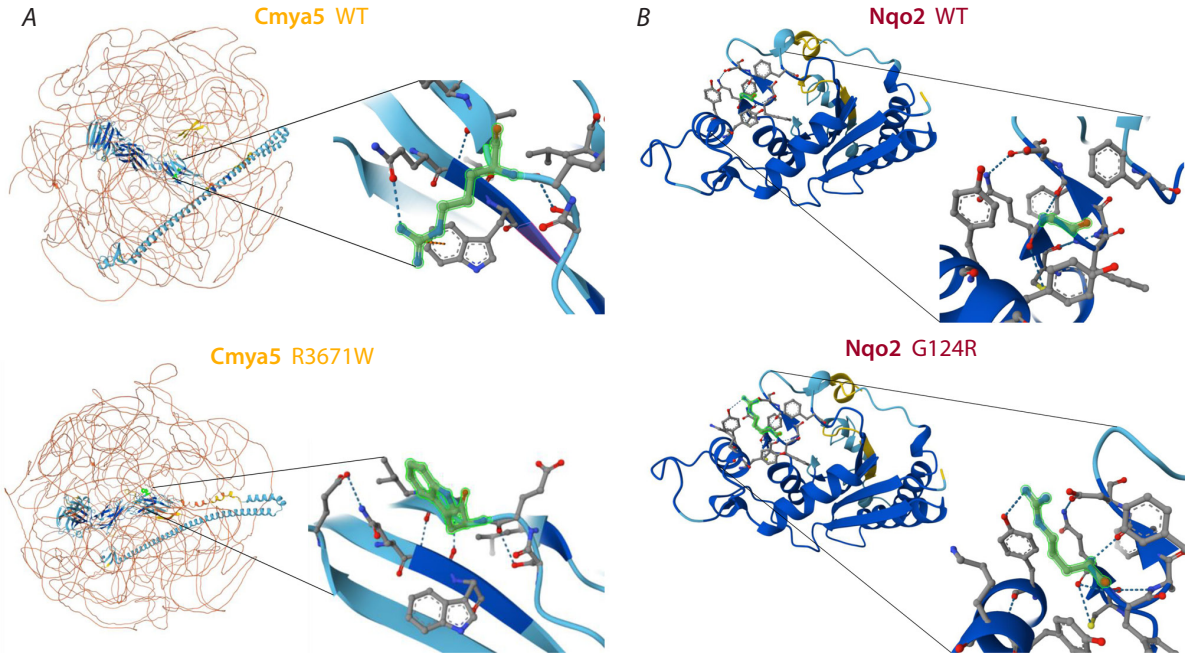


Fig. 4. Protein structures predicted using AlphaFold 3 (Abramson et al., 2024). *A* – Cmya5 (wild-type, WT (3671R); and with the OXYS rat substitution, R3671W). The inset shows a magnified view of the FN3-1 domain harboring the substitution. The amino acid residue at position 3671 is highlighted in green; *B* – Nqo2 (wild-type, WT (124G); and with the OXYS rat substitution, G124R). The inset shows a magnified view of the substitution site. The amino acid residue at position 124 is highlighted in green.

The color coding reflects the local confidence of the structure prediction (pLDDT): blue (90–100) indicates very high, light blue (70–89) indicates confident, yellow (50–69) indicates low, and orange (<50) indicates very low. Regions with pLDDT < 50 likely represent intrinsically disordered protein regions (IDRs).

site at positions 127–129 (Fig. 4*B*). *Nqo2* has two paralogs: a predicted gene, *AABR07044714*, which arose in rats, and the evolutionarily more ancient *Nqo1*, which encodes an enzyme responsible for quinone reduction. The substitution of a small glycine for a bulky, positively charged arginine disrupts local interactions within the protein and may affect protein–protein interactions, ligand affinity, and the redox-dependent regulatory function of Nqo2 (Fig. 4*B*).

The *Cic* gene encodes the Capicua transcriptional repressor, with its highest expression observed in nervous tissue (RatGTEx Consortium, 2021). It plays a crucial role in neurogenesis and acts as a suppressor for various tumor types (Wong, Yip, 2020; Hourigan et al., 2021). The C1412Y substitution identified in OXYS rats is located within a highly conserved region of the protein, which, however, lacks an ordered domain structure and is predicted with low confidence (pLDDT < 50) (Fig. 3*E* and Fig. S7). All analyzed orthologs possess a cysteine (C) residue at the homologous position (Fig. 3*E* and Fig. S4*E*). Cic has only one ancient paralog, Bbx, which performs distinct functions and lacks the homologous region. Since the C1412Y substitution occurs within a highly conserved region of the protein and its functional compensation by the Bbx paralog is impossible, this variant may impair the functional activity of the Cic protein despite its location within a structurally disordered region.

The *Akap6* gene encodes an adapter protein that anchors signaling complexes to the nuclear envelope and sarcoplasmic reticulum (Dodge-Kafka et al., 2005; Vergarajauregui et al., 2020). In rats, it is expressed primarily in the heart, skeletal muscle, and brain, including the hippocampus and cerebral cortex (Wu et al., 2009; RatGTEx Consortium, 2021). The identified R815W substitution is located within the Spectrin 1 repeat domain (SR1) of Akap6, which is critical for protein–protein interactions (Vergarajauregui et al., 2020) (Fig. 3*F* and Fig. S8). The Akap6 protein has one paralog, Cep68, which lacks the homologous region. It does not perform similar adapter functions. Analysis of multiple ortholog alignments demonstrates that position 815 is strictly conserved in charge. Either arginine (R) or lysine (K) – both positively charged amino acid residues – is present at the homologous position across all analyzed animal species (Fig. 3*F* and Fig. S4*F*). Thus, the R815W substitution is nonconservative: a positively charged polar arginine is replaced by a bulky hydrophobic tryptophan residue containing an aromatic ring, which may disrupt protein–protein interactions mediated via the SR1 domain.

Visual impairments. The *Cerkl* gene is involved in regulating autophagy, mitochondrial dynamics, and metabolism. It plays a key role in protecting the photoreceptors, and retinal pigment epithelial (RPE) cells against oxidative stress and apoptosis (Mirra et al., 2021). Two consecutive amino acid substitutions, F448L and V449L, identified in Cerkl are located within the disordered C-terminal region of the protein, which is enriched in hydrophobic amino acid residues (Fig. 3*G* and Fig. S9). Phenylalanine (F) at position 448 is strictly conserved among all analyzed orthologs (Fig. 3*G* and Fig. S4*G*). However, valine (V) at position 449 tolerates a replacement with another hydrophobic amino acid, isoleucine (I), in rodents (Fig. S4*G*). The Cerkl protein has four evolutionarily ancient paralogs (Cerk, Sphk1, Sphk2, and Agk); however, unlike Cerkl, they function as active lipid kinases and utilize different regulatory mechanisms. Nevertheless, because both substitutions are located within a region enriched in hydrophobic residues, their impact on the structure and function of the Cerkl protein may be minimal.

In the *Bfsp1* gene, which encodes a structural protein of lens intermediate filaments, the missense substitution leading to R276Q was identified within one of the α-helical domains of the rod region (Fig. 3*H* and Fig. S10). This region ensures filament polymerization and interaction with the Bfsp2 protein to form the cytoskeleton of lens fibers (Perng et al., 2007). Arginine (R) at position 276 is highly conserved among the analyzed orthologs (Fig. 3*H* and Fig. S4*H*). However, in the Chinese hamster (*Cricetulus griseus*), tryptophan (W) is present at the homologous position (Fig. S4*H*). The *Bfsp1* gene has no paralogs, which points that its function is unique. Despite the overall preservation of the protein structure, the loss of positive charge due to the glutamine-for-arginine-substitution in the center of one of the rod region domains may disrupt intermediate filament assembly in the lens.

Visualization of the tissue-specific expression for each of the aforementioned genes in rats is presented in Figures S11–S18.

Mitochondrial dysfunction. The premature aging phenotype of OXYS rats is considered to be associated with mitochondrial dysfunction (Tyumentsev et al., 2018). Consequently, variants in genes associated with the mitochondrial function were selected from the pool of missense substitutions and high-impact functional variants distinguishing OXYS rats from Wistar/Icgn. Missense substitutions predicted to be damaging by the SIFT algorithm were detected in the *Mrps30*, *Decr1*, *Mecr*, *Ptcd1*, and *Afg3l1* genes (Table S4). The analysis of the prevalence of these genetic variants across 146 rat strains (List S1) showed that they occurred with high frequency among other strains, including healthy ones (Table S5). Therefore, they likely do not contribute significantly to the development of structural and functional disorders in the mitochondria of OXYS rats.

Copy number variation (CNV) analysis

To improve the accuracy of CNV detection and breakpoint identification, two software tools employing different approaches were utilized: CNVpytor (based on a read depth algorithm) and Smoove (based on split-read and discordant paired-end read algorithms). The majority of CNVs present in the OXYS rat genomes and absent from the control Wistar/Icgn strain were located within noncoding regions, specifically intergenic regions and introns. Following the selection of functionally significant CNVs (overlapping coding or regulatory regions), only deletions remained. No other structural variation types were detected within functionally significant regions.

CNVs in coding regions. Some of the CNVs identified in the OXYS rat genomes affected coding regions, specifically the exons of the *LOC100911093*, *Ybx1l1*, *Gsta6*, and *Mettl24* genes (Table 2). The *LOC100911093* and *Ybx1l1* genes were found to be completely deleted (Fig. 5). *LOC100911093* presumably encodes mitochondrial CCA-tRNA nucleotidyltransferase and has one paralog in rats, *Trnt1*, which shares 99.54 % sequence identity and performs the same function within both the cytoplasm and mitochondria. *Ybx1l1* is predicted to bind nucleic acids and participate in the regulation of gene expression. *Ybx1l1* has six paralogs, including *Ybx1*, which exhibits high sequence identity (94.48 %) to *Ybx1l1*. Its human ortholog, *YBX1*, is known to be involved in DNA repair under oxidative stress (Zheng et al., 2025). Both *LOC100911093* and *Ybx1l1* remain poorly characterized in rats, which hampers the assessment of the functional consequences of their loss. However, the presence of highly identical paralogs (*Trnt1* and *Ybx1*) suggests a potential for partial functional compensation.

The first exons of both the *Gsta6* and *Mettl24* genes fall within the deletion regions. The enzyme encoded by the *Gsta6* gene belongs to the alpha glutathione S-transferase family and participates in the metabolism of glutathione, an antioxidant that plays a key role in neutralizing free radicals and maintaining cellular redox homeostasis (Forman et al., 2009). This gene remains poorly characterized and has 19 paralogs, five of which also belong to the alpha glutathione S-transferase family, potentially providing partial functional compensation for a possible dysregulation of *Gsta6*. *Mettl24* encodes an enzyme with predicted methyltransferase activity but has been poorly characterized in rats. Its human ortholog, *METTL24*, is implicated in immune functions and associated with kidney renal clear cell carcinoma (KIRC) (Jiang et al., 2022). The *Mettl24* gene has two ancient paralogs, *Scara3* and *Cthrc1*, which share low sequence identity with the query gene (7.76 and 16.97 %, respectively) and are not functionally related to methyltransferases.

CNVs in regulatory genomic regions. H3K27ac is an epigenetic modification (acetylation) of lysine 27 in the N-terminal region of the DNA packaging protein histone H3. The enrichment of a genomic region in this epigenetic mark indicates the location of active regulatory elements, such as promoters and enhancers. It has been shown that the development of AD traits in OXYS rats, as in humans, is associated with neurodegenerative changes primarily in the hippocampus and prefrontal cortex (Stefanova et al., 2014). Therefore, we investigated whether the CNVs identified in the OXYS rat genomes fall within regions of active regulatory elements in the ventral hippocampus, dorsal hippocampus, and prefrontal cortex.

Table 2. Genomic coordinates and genotypes of deletions affecting the coding regions (exons) of genes across all analyzed samples (0 – reference allele, 1 – deletion)

Genomic coordinates	Length, bp	Gene	OXYS 17	OXYS 30	OXYS 34	Wistar 5	Wistar 22	Wistar 37
1:170,720,408–170,722,750	2,342	*LOC100911093*	1/1	1/1	1/1	0/0	0/1	0/1
1:171,304,588–171,306,097	1,509	*Ybx1l1*	1/1	1/1	1/1	0/0	0/1	0/1
9:23,797,233–23,803,955	6,722	*Gsta6*	1/1	1/1	1/1	0/0	0/0	0/1
20:44,142,209–44,146,664	4,455	*Mettl24*	1/1	1/1	1/1	0/0	0/0	0/0

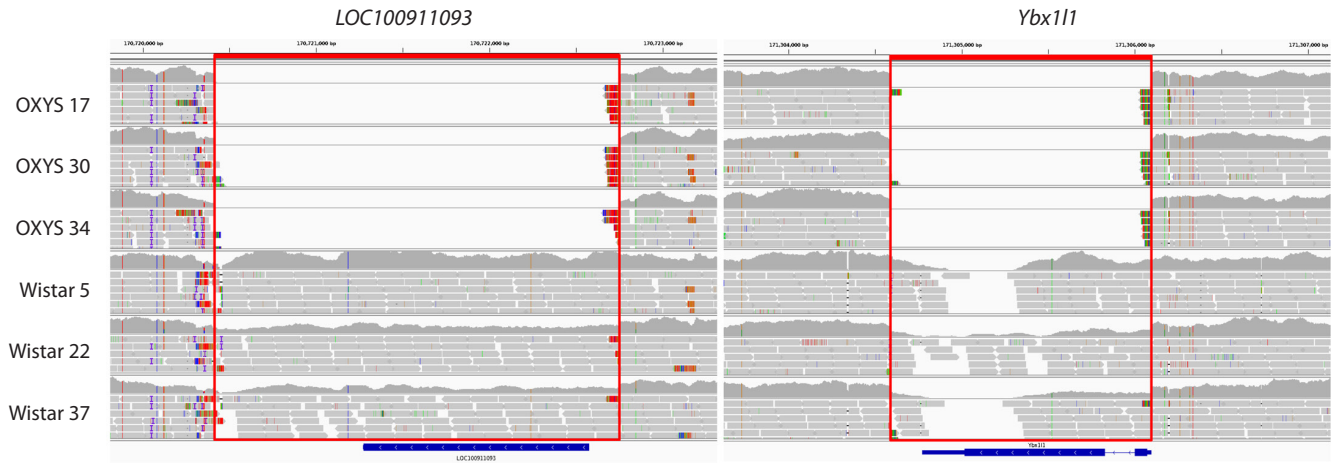


Fig. 5. Deleted *LOC100911093* and *Ybx1l1* genes in the OXYS rat genomes.
Scale bar: 3,500 bp. Red boxes indicate the deletion boundaries. Images were generated using IGV (Robinson et al., 2011).

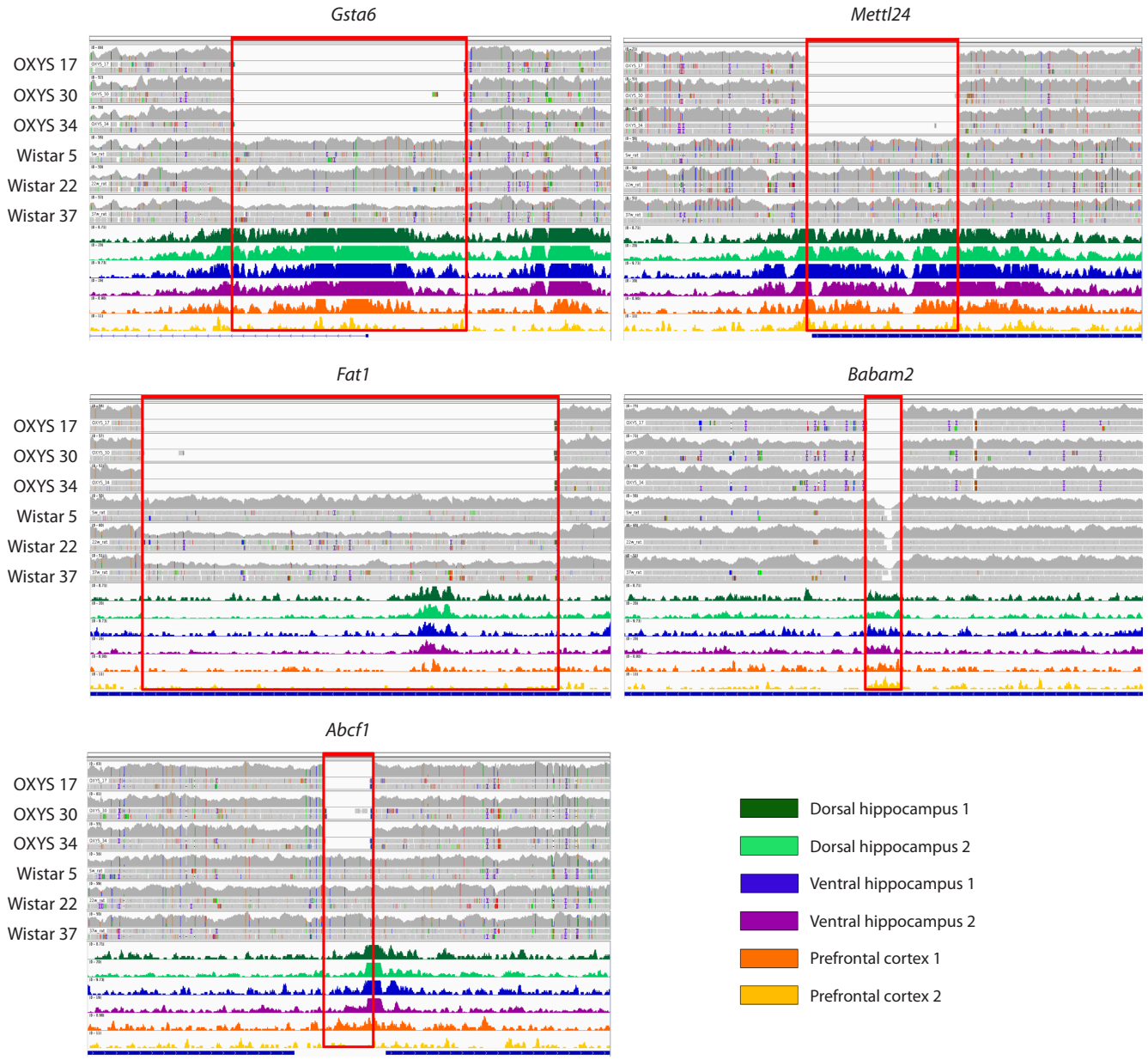


Fig. 6. Deletions within the *Gsta6*, *Mettl24*, *Fat1*, *Babam2*, and *Abcf1* genes overlapping H3K27ac enrichment peaks within the prefrontal cortex, dorsal hippocampus, and ventral hippocampus of *Rattus norvegicus*.

Scale bar: 15 kb. Red boxes indicate the deletion boundaries. Images were generated using IGV (Robinson et al., 2011).

By using ChIP-seq data from the respective brain regions of control Long-Evans outbred rats (Rayan et al., 2022), the coordinates of enriched peaks for the H3K27ac histone mark were obtained and found to intersect with the coordinates of the unique OXYS CNVs. Deletions within the *Gsta6*, *Mettl24*, *Fat1*, and *Babam2* genes, as well as upstream of the *Abcf1* gene, overlap with H3K27ac-enriched regions (Table 3 and Fig. 6). The above-described deletions within the *Gsta6* and *Mettl24* genes are located in their putative promoter regions, and they affect the first exon. The deletions within *Fat1* and *Babam2* are located within introns and are likely to disrupt their active enhancers. The *Fat1* gene encodes a protein from the atypical cadherin family, which is involved in cell–cell adhesion, muscle and neuronal development, and the positive regulation of the migration of various cell types, including neurons, fibroblasts, astrocytic precursors, and vascular smooth muscle cells (Riascos-Bernal et al., 2023; Helmbacher, 2018). *Fat1* has seven paralogs, three of which also belong to the atypical cadherin family. The *Babam2* gene encodes an adapter protein that is a component of the BRCA1-A and BRISC complexes. It plays an important role in double-stranded DNA break repair, cell cycle maintenance, and the prevention of cellular senescence (Chung et al., 2020), while also inhibiting the mitochondrial apoptotic pathway (Li Q. et al., 2004). The

Table 3. Genomic coordinates and genotypes of deletions overlapping H3K27ac enrichment peaks within the prefrontal cortex, dorsal hippocampus, and ventral hippocampus of *Rattus norvegicus* across all analyzed samples (0 – reference allele, 1 – deletion)

Genomic coordinates	Length, bp	Gene	OXYS 17	OXYS 30	OXYS 34	Wistar 5	Wistar 22	Wistar 37
9:23,797,233–23,803,955	6,722	*Gsta6*	1/1	1/1	1/1	0/0	0/0	0/1
20:44,142,209–44,146,664	4,455	*Mettl24*	1/1	1/1	1/1	0/0	0/0	0/0
16:47,224,153–47,236,087	11,934	*Fat1*	1/1	1/1	1/1	0/0	0/1	0/1
6:24,707,559–24,708,619	1,060	*Babam2*	1/1	1/1	1/1	0/0	0/0	0/0
20:2,800,714–2,802,114	1,400	*Abcf1*	1/1	1/1	1/1	0/0	0/0	0/0

absence of paralogs for the *Babam2* gene precludes genetic compensation for potential dysregulation caused by the deletion within the enhancer region. Furthermore, the deletion upstream of the *Abcf1* gene may affect its active promoter. The *Abcf1* gene product is a member of the ATP-binding cassette (ABC) protein superfamily. It participates in the initiation and elongation of translation process and regulates the innate immune response (Wilcox et al., 2017). Both *Abcf1* paralogs belong to the same ABC protein subfamily F.

Our analysis indicates that the deletions identified in OXYS rats lead to the loss of gene regulatory regions. The *Gsta6* and *Mettl24* genes may be the most significantly affected, with deletions located in the most heavily H3K27ac-enriched regions that correspond to the active promoters of these genes.

Visualization of the tissue-specific expression for each of the aforementioned genes in rats is presented in Figures S19–S25.

Discussion

The aim of this study was to identify genetic variants in OXYS rats that might contribute to the premature aging phenotype, which is accompanied by the development of various age-associated pathologies.

Cognitive impairment and neurodegeneration

Variants detected within the *Fat1*, *Cic*, *Akap6*, *Gsta6*, and *Nqo2* genes may be associated with the early development of neurodegenerative changes and cognitive decline in OXYS rats. A large deletion was identified in the noncoding region of the *Fat1* gene, likely disrupting its active enhancer. In vertebrates, including rats, *Fat1* is expressed in both the developing and adult brain, with high expression observed in regions involved in neurogenesis (Peng et al., 2021). Its product, FAT1, is involved in early stages of neuronal differentiation. It controls axon growth via the Hippo signaling pathway and promotes terminal cell differentiation by inhibiting cell proliferation (Ahmed et al., 2015; Peng et al., 2021). Thus, the identified deletion may reduce *Fat1* expression in hippocampal neurogenesis zones, thereby disrupting the regulation of synaptic plasticity and neuronal migration, which could exacerbate the cognitive decline observed in OXYS rats.

The CIC (Capicua) protein is a key effector of the RTK/RAS/MAPK signaling pathway, regulating the balance of proliferation and differentiation of neuronal progenitors in the hippocampus (Hourigan et al., 2021). It also acts as a tumor suppressor by repressing the transcription of ETS-family oncogenes (Wong, Yip, 2020) and forms a complex with the Ataxin-1 protein, which is associated with the development of the neurodegenerative pathology spinocerebellar ataxia type 1 (SCA1) (Rousseaux et al., 2018). Pathogenic variants within *CIC* have been described in human oligodendrogliomas, where its inactivation stimulates glial cell proliferation through the activation of *ETV1/4/5* oncogenes (Yip et al., 2012). Impairment of the repressor function of CIC in the mouse hippocampus leads to a reduction in the pool of neuronal progenitors, alongside the disruption of their differentiation, migration, and dendritic development (Hourigan et al., 2021). Therefore, it can be hypothesized that the *Cic* missense variant found in OXYS rats contributes to the delay in brain maturation observed in this strain during the early postnatal period, which is associated with an altered balance of neural precursor proliferation and differentiation (Rudnitskaya et al., 2020).

The R815W substitution within the SR1 domain of Akap6 was previously described in a study of SNV transcriptome data from the hippocampus and prefrontal cortex of OXYS rats as associated with cognitive impairment (Devyatkin et al., 2020b). The spectrin repeats of AKAP6 are involved in binding to nuclear envelope proteins (nesprin-1α) and components of the microtubule-organizing center (pericentrin, AKAP9), and can also mediate the anchoring of signaling molecules such as calcineurin and NFATc4 (Mackiewicz et al., 2024). Disruption of the structural integrity of AKAP6 spectrin repeats may destabilize its anchoring to the nuclear envelope and the organization of perinuclear signaling complexes. This, in turn, may weaken pro-survival signaling from BDNF receptors to transcriptional targets (e. g., via the calcineurin-NFATc4 pathway), thereby increasing the vulnerability of neurons to stress and degeneration (Mackiewicz et al., 2024). Recent studies have demonstrated that AKAP6 plays a key role in neurotrophin-mediated survival of retinal ganglion cells (Tomczak et al., 2024). Furthermore, genome-wide association

studies have linked polymorphisms within the *AKAP6* locus to impairments in episodic memory, perceptual speed, and other cognitive functions in older adults (Andrews et al., 2017). The location of R815W within the functionally significant SR1 domain and the evolutionary conservation of positive charge at the homologous position in AKAP6 orthologs suggest that this variant may contribute to the development of cognitive decline in OXYS rats.

A decrease in *Gsta6* (a member of the alpha glutathione S-transferase family) expression compared to control Wistar/Icgn rats – previously detected in the prefrontal cortex, hippocampus, and retina of OXYS rats during postnatal brain development (Telegina et al., 2015; Stefanova, Kolosova, 2023) – may be caused by the deletion identified within the putative active promoter of this gene. The reduced *Gsta6* expression may impair glutathione-dependent free radical scavenging, thereby weakening the antioxidant defense of neurons and photoreceptors.

Similarly, a missense substitution within the *Nqo2* gene was previously described in a study of SNV transcriptome data from the hippocampus and prefrontal cortex of OXYS rats and characterized as potentially associated with neurodegeneration and AD development (Devyatkin et al., 2020b). *NQO2* expression in the brain is recorded in areas critical for cognitive function, including the hippocampus and cortex, and it increases with age and AD progression (Janda et al., 2024). The role of NQO2 in learning and memory consolidation may be linked to its involvement in cellular metabolism and ROS production, including mitochondrial ROS (Islam, Shilton, 2025). Recent data also point to the involvement of NQO2 in the regulation of oxidative stress, inflammation, autophagy, and apoptosis, as well as to its ability to interact with a number of bioactive compounds, including certain anticancer drugs (Janda et al., 2024; Islam, Shilton, 2025). Thus, the identified genetic variants within *Gsta6* and *Nqo2* may contribute to the development of early neurodegenerative changes in the brain structures and retina of OXYS rats, which represent hallmarks of AD and AMD-like retinopathy.

It has been demonstrated that the frontal cortex and hippocampus of OXYS rats exhibit elevated levels of oxidative DNA damage (8-oxoguanine) compared to the parental Wistar/Icgn strain (Sattarova et al., 2013). The deletion identified within the *Babam2* regulatory region is of interest as a potential factor contributing to genomic instability. Although there is no direct evidence of DNA double-strand break accumulation in OXYS rats, the reduced expression of repair genes may exacerbate the consequences of oxidative damage in the brain. Importantly, the antiapoptotic function of BABAM2 is mediated through the inhibition of the mitochondrial apoptotic cascade (Li Q. et al., 2004). Given that mitochondrial dysfunction and the dysregulation of apoptosis are early hallmarks of the OXYS phenotype (Stefanova et al., 2014), a reduced expression of *Babam2* in the hippocampus and prefrontal cortex – driven by the detected deletion within the enhancer region – may increase the sensitivity of neurons to stress-induced death.

Ophthalmological pathologies: retinopathy and cataracts

Clinical manifestations of retinopathy, resembling the dry form of age-related macular degeneration (AMD) in humans, appear in OXYS rats at the age of 3–4 months. They are accompanied by structural and functional changes in RPE cells and impaired choroidal microcirculation (Markovets et al., 2010). Pathological changes within the retina progress against the background of increased accumulation of beta-amyloid and lipofuscin in RPE cells, altered morphology, and reactive gliosis, ultimately leading to the complete loss of photoreceptors by 24 months of age (Markovets et al., 2010; Zhdankina et al., 2023). Several genetic variants identified in this study potentially contribute to the development of this pathology. These include a deletion within the putative promoter region of the *Abcf1* gene, which plays a crucial role in retinal homeostasis by regulating the phagocytosis of photoreceptor outer segments by RPE cells (Guo et al., 2015). The detected deletion may reduce *Abcf1* expression, thereby contributing to the development of AMD-like features in OXYS rats.

The *Cerkl* gene is a key protector of photoreceptors and RPE cells against oxidative stress and apoptosis (Mirra et al., 2021). It is expressed predominantly within the cerebellum, hippocampus, cerebral cortex, and retina, playing a crucial role in the function of the latter (García-Arroyo et al., 2021, 2022). Mutations within *CERKL* cause retinal dystrophies characterized by the progressive degeneration of retinal neurons, ultimately leading to vision loss (Tuson et al., 2004; Aleman et al., 2009; Sen et al., 2020). Two consecutive substitutions, F448L and V449L, within the C-terminal region of the Cerkl protein likely do not significantly impair its function because they are conservative (hydrophobic amino acid residues are replaced by hydrophobic ones). However, their potential role in the development of early neurodegenerative changes in the OXYS rat retina cannot be entirely ruled out.

The R276Q substitution within Bfsp1 may accelerate lens degeneration by reducing the mechanical stability of lens intermediate filaments. Dysfunction of BFSP1 is associated with the development of senile cataracts in humans (Song et al., 2009). A charge-depleting amino acid substitution within BFSP1 (D348N) has been reported to cause congenital cataracts in humans (Wang et al., 2023). *Bfsp1*-knockout mice develop progressive cataracts accompanied by a loss of lens optical properties (Song et al., 2009). Therefore, it can be hypothesized that the R276Q substitution, resulting in the loss of the positive amino acid charge, disrupts the assembly of intermediate filaments and may contribute to the early development of cataracts in OXYS rats – a trait linked to the inheritance of premature aging syndrome, for which these animals were originally selected (Kolosova et al., 2014).

Muscle pathologies: sarcopenia and cardiomyopathy

The R815W substitution within the SR1 domain of Akap6 may also contribute to the development of muscle pathologies. AKAP6 has been shown to play a key role in skeletal muscle regeneration by interacting with myogenin, and its inhibition leads to impaired muscle fiber formation and decreased motor activity in mice (Lee et al., 2015). Furthermore, via its spectrin repeats, AKAP6 functions as an adapter protein in cardiomyocytes, linking the nuclear membrane to the microtubule-organizing center, which is critical for normal cardiac function (Vergarajauregui et al., 2020).

The R3671W substitution within Cmya5 is located within the FN3-1 domain. It disrupts intradomain interactions with other amino acid residues, potentially weakening interactions with titin and destabilizing sarcomeres in both skeletal and cardiac muscle tissues (Sarparanta, 2008; Sarparanta et al., 2010). Disruption of the structural integrity of myofibrils may contribute to the development of sarcopenia and hypertrophic cardiomyopathy, both of which are characteristic of OXYS rats (Vays et al., 2014; Muraleva et al., 2017; Lu et al., 2022).

Lipid metabolism disorders

Lipid metabolism disorders are known to significantly contribute to the pathogenesis of AD (Di Paolo, Kim, 2011). The conformation of ApoB-100 in the heparin-binding domain determines the efficiency of the interaction between LDL particles and extracellular matrix proteoglycans in the vascular subendothelial layer. Low-density lipoprotein particles undergo modifications, such as aggregation and oxidation, which trigger inflammatory cascades and enhance atherogenesis (Öörni, Lorey, 2025). The L3413F substitution within this domain of ApoB in OXYS rats could alter this function, potentially contributing to dyslipidemia, systemic oxidative stress, and AD progression. However, based on the analysis of amino acid conservation and protein structure prediction, we assess its effect as minor. It is known that during the period of active manifestation of AD symptoms, dyslipidemia and oxidative stress are not detected in OXYS rats, and blood cholesterol levels are even reduced (Tikhonova et al., 2014). Nonetheless, vascular dysfunction has been shown to significantly contribute to the development of AD (Stefanova et al., 2018), AMD (Zhdankina et al., 2023), and hypertrophic cardiomyopathy (Muraleva et al., 2017) in OXYS rats. The identified V695L substitution within Abca1 is likely functionally insignificant, as it is located within the hydrophobic transmembrane domain and does not disrupt its structure. Nevertheless, it should be noted that ABCA1 plays a key role not only in brain lipid metabolism but also in beta-amyloid clearance, and its genetic variations significantly contribute to AD development (Holstege et al., 2022).

Conclusion

Whole-genome sequencing with high coverage (>25×) performed on three OXYS rats and three Wistar/Icgn control rats detected genetic variants fixed in the homozygous state in the OXYS strain. Based on comparative analysis, we identified unique variants, absent from other rat strains, which may contribute to the premature aging phenotype and the early onset of age-associated pathologies in OXYS rats. Regarding neurodegeneration, the potentially pathogenic variants include the large deletion within the *Fat1* enhancer, leading to the dysregulation of gene expression during neurogenesis; the missense substitution within *Cic*, potentially disrupting the balance of neural progenitor proliferation and differentiation; variants within *Akap6* and *Nqo2* associated with cognitive impairment; and the deletion within the *Gsta6* promoter that may weaken the antioxidant defense in the brain. Furthermore, the early development of retinopathy may be driven by the deletion within the *Abcf1* promoter region, which destabilizes retinal homeostasis, alongside the missense substitutions within *Cerkl*, potentially reducing the protection of photoreceptors and RPE cells against oxidative stress. The missense substitution within *Bfsp1* may impair intermediate filament assembly, leading to cataract development. Finally, the pathogenesis of cardiomyopathy and sarcopenia is likely linked to the missense variant within *Cmya5*, which impairs myofibril stabilization, and the missense variant within *Akap6*, which may affect skeletal muscle regeneration and the structural organization of cardiomyocytes. The identified candidate alleles provide a firm basis for future functional analyses and further study of the molecular mechanisms underlying premature aging in OXYS rats.

References

Abramson J., Adler J., Dunger J., Evans R., Green T., Pritzel A., Ronneberger O., … Bapst V., Kohli P., Jaderberg M., Hassabis D., Jumper J.M. Accurate structure prediction of biomolecular interactions with AlphaFold 3. *Nature.* 2024;630(8016):493-500. doi 10.1038/s41586-024-07487-w

Abyzov A., Urban A.E., Snyder M., Gerstein M. CNVnator: an approach to discover, genotype, and characterize typical and atypical CNVs from family and population genome sequencing. *Genome Res.* 2011;21(6):974-984. doi 10.1101/gr.114876.110

Ahmed A.F., De Bock C.E., Lincz L.F., Pundavela J., Zouikr I., Sontag E., Hondermarck H., Thorne R.F. FAT1 cadherin acts upstream of Hippo signalling through TAZ to regulate neuronal differentiation. *Cell Mol Life Sci.* 2015;72(23):4653-4669. doi 10.1007/s00018-015-1955-6

Aleman T.S., Soumittra N., Cideciyan A.V., Sumaroka A.M., Ramprasad V.L., Herrera W., Windsor E.A.M., … Inglehearn C.F., Kumaramanickavel G., Stone E.M., Fishman G.A., Jacobson S.G. *CERKL* mutations cause an autosomal recessive cone-rod dystrophy with inner retinopathy. *Invest Ophthalmol Vis Sci.* 2009;50(12):5944. doi 10.1167/iovs.09-3982

Andrews S. FastQC: a quality control tool for high throughput sequence data. Version 0.11.9. 2010. Available at: https://www.bioinformatics.babraham.ac.uk/projects/fastqc/ (Accessed 12.25.25)

Andrews S.J., Das D., Anstey K.J., Easteal S. Association of *AKAP6* and *MIR2113* with cognitive performance in a population-based sample of older adults. *Genes Brain Behav.* 2017;16(4):410-418. doi 10.1111/gbb.12368

Broad Institute. Picard Toolkit. Version 2.26.11. 2022. Available at: https://broadinstitute.github.io/picard/ (Accessed 12.25.25)

Chung C.Y.T., Lo P.H.Y., Lee K.K.H. Babam2 regulates cell cycle progression and pluripotency in mouse embryonic stem cells as revealed by induced DNA damage. *Biomedicines*. 2020;8(10):397. doi 10.3390/biomedicines8100397

Danecek P., Bonfield J.K., Liddle J., Marshall J., Ohan V., Pollard M.O., Whitwham A., Keane T., McCarthy S.A., Davies R.M., Li H. Twelve years of SAMtools and BCFtools. *GigaScience*. 2021;10(2):giab008. doi 10.1093/gigascience/giab008

Davidson N.O., Shelness G.S. Apolipoprotein B: mRNA editing, lipoprotein assembly, and presecretory degradation. *Annu Rev Nutr.* 2000;20(1):169-193. doi 10.1146/annurev.nutr.20.1.169

de la Cruz N., Bromberg S., Pasko D., Shimoyama M., Twigger S., Chen J., Chen C.F., … Zuniga-Meyer A., Zhao L., Kwitek A., Tonellato P., Jacob H. The Rat Genome Database (RGD): developments towards a phenome database. *Nucleic Acids Res*. 2004;33(D1): D485-D491. doi 10.1093/nar/gki050

Devyatkin V.A., Muraleva N.A., Kolosova N.G. Identification of single-nucleotide polymorphisms in mitochondria-associated genes capable of affecting the development of hypertrophic cardiomyopathy in senescence-accelerated OXYS rats. *Adv Gerontol*. 2020a;10(2):121-127. doi 10.1134/S2079057020020058

Devyatkin V.A., Redina O.E., Kolosova N.G., Muraleva N.A. Single-nucleotide polymorphisms associated with the senescence-accelerated phenotype of OXYS rats: a focus on Alzheimer's disease-like and age-related-macular-degeneration-like pathologies. *J Alzheimer's Dis*. 2020b;73(3):1167-1183. doi 10.3233/JAD-190956

Di Paolo G., Kim T.-W. Linking lipids to Alzheimer's disease: cholesterol and beyond. *Nat Rev Neurosci.* 2011;12(5):284-296. doi 10.1038/nrn3012

Dodge-Kafka K.L., Soughayer J., Pare G.C., Carlisle Michel J.J., Langeberg L.K., Kapiloff M.S., Scott J.D. The protein kinase A anchoring protein mAKAP coordinates two integrated cAMP effector pathways. *Nature.* 2005;437(7058):574-578. doi 10.1038/nature03966

Dyer S.C., Austine-Orimoloye O., Azov A.G., Barba M., Barnes I., Barrera-Enriquez V.P., Becker A., … Finn R.D., Freeberg M.A., Harrison P.W., Martin F.J., Yates A.D. Ensembl 2025. *Nucleic Acids Res*. 2025;53(D1):D948-D957. doi 10.1093/nar/gkae1071

Eilbeck K., Lewis S.E., Mungall C.J., Yandell M., Stein L., Durbin R., Ashburner M. The Sequence Ontology: a tool for the unification of genome annotations. *Genome Biol*. 2005;6(5):R44. doi 10.1186/gb-2005-6-5-r44

El'darov Ch.M., Vays V.B., Vangeli I.M., Kolosova N.G., Bakeeva L.E. Morphometric examination of mitochondrial ultrastructure in aging cardiomyocytes. *Biochemistry* (*Moscow*). 2015;80(5):604-609. doi 10.1134/S0006297915050132

Figueira I., Fernandes A., Mladenovic Djordjevic A., Lopez-Contreras A., Henriques C.M., Selman C., Ferreiro E., Gonos E.S., Trejo J.L., Misra J., Rasmussen L.J., Xapelli S., Ellam T., Bellantuono I. Interventions for age-related diseases: shifting the paradigm. *Mech Ageing Dev*. 2016;160:69-92. doi 10.1016/j.mad.2016.09.009

Flood C., Gustafsson M., Pitas R.E., Arnaboldi L., Walzem R.L., Borén J. Molecular mechanism for changes in proteoglycan binding on compositional changes of the core and the surface of low-density lipoprotein-containing human apolipoprotein B100. *Arterioscler Thromb Vasc Biol.* 2004;24(3):493-500. doi 10.1161/01.ATV.0000117174.19078.85

Forman H.J., Zhang H., Rinna A. Glutathione: overview of its protective roles, measurement, and biosynthesis. *Mol Aspects Med*. 2009; 30(1-2):1-12. doi 10.1016/j.mam.2008.08.006

García-Arroyo R., Gavaldà-Navarro A., Villarroya F., Marfany G., Mirra S. Overexpression of CERKL protects retinal pigment epithelium mitochondria from oxidative stress effects. *Antioxidants*. 2021; 10(12):2018. doi 10.3390/antiox10122018

García-Arroyo R., Marfany G., Mirra S. *CERKL*, a retinal dystrophy gene, regulates mitochondrial transport and dynamics in hippocampal neurons. *Int J Mol Sci*. 2022;23(19):11593. doi 10.3390/ijms231911593

Ghanbari-Niaki A., Khabazian B.M., Hossaini-Kakhak S.A., Rahbarizadeh F., Hedayati M. Treadmill exercise enhances ABCA1 expression in rat liver. *Biochem Biophys Res Commun*. 2007;361(4):841-846. doi 10.1016/j.bbrc.2007.07.100

Guo F., Ding Y., Caberoy N., Alvarado G., Wang F., Chen R., Li W. ABCF1 extrinsically regulates retinal pigment epithelial cell phagocytosis. *Mol Biol Cell*. 2015;26(12):2311-2320. doi 10.1091/mbc.E14-09-1343

Helmbacher F. Tissue-specific activities of the Fat1 cadherin cooperate to control neuromuscular morphogenesis. *PLoS Biol*. 2018;16(5): e2004734. doi 10.1371/journal.pbio.2004734

Holstege H., Hulsman M., Charbonnier C., Grenier-Boley B., Quenez O., Grozeva D., van Rooij J.G.J., … van Duijn C.M., Williams J., Nicolas G., Bellenguez C., Lambert J.C. Exome sequencing identifies rare damaging variants in ATP8B4 and ABCA1 as risk factors for Alzheimer's disease. *Nat Genet.* 2022;54(12):1786-1794. doi 10.1038/s41588-022-01208-7

Hourigan B., Balay S.D., Yee G., Sharma S., Tan Q. Capicua regulates the development of adult-born neurons in the hippocampus. *Sci Rep*. 2021;11(1):11725. doi 10.1038/s41598-021-91168-5

Islam F., Shilton B.H. Insights into the cellular function and mechanism of action of quinone reductase 2 (NQO2). *Biochem J.* 2025;482(6): 309-324. doi 10.1042/BCJ20240103

Janda E., Boutin J.A., De Lorenzo C., Arbitrio M. Polymorphisms and pharmacogenomics of NQO2: the past and the future. *Genes*. 2024; 15(1):87. doi 10.3390/genes15010087

Jiang Z., Zhang W., Zeng Z., Tang D., Li C., Cai W., Chen Y., Li Y., Jin Q., Zhang X., Yin L., Liu X., Xu Y., Dai Y. A comprehensive investigation discovered the novel methyltransferase METTL24 as one presumably prognostic gene for kidney renal clear cell carcinoma potentially modulating tumor immune microenvironment. *Front Immunol.* 2022;13:926461. doi 10.3389/fimmu.2022.926461

Kolosova N.G., Aidagulova S.V., Nepomnyashchikh G.I., Shabalina I.G., Shalbueva N.I. Dynamics of structural and functional changes in hepatocyte mitochondria of senescence-accelerated OXYS rats. *Bull Exp Biol Med*. 2001;132(2):814-819. doi 10.1023/a:1013014919721

Kolosova N.G., Shcheglova T.V., Sergeeva S.V., Loskutova L.V. Long-term antioxidant supplementation attenuates oxidative stress markers and cognitive deficits in senescent-accelerated OXYS rats. *Neurobiol Aging*. 2006;27(9):1289-1297. doi 10.1016/j.neurobiolaging.2005.07.022

Kolosova N.G., Stefanova N.A., Korbolina E.E., Fursova A.Zh., Kozhevnikova O.S. Senescence-accelerated OXYS rats: a genetic model of premature aging and age-related diseases. *Adv Gerontol*. 2014;4(4):294-298. doi 10.1134/S2079057014040146

Lee S.W., Won J.Y., Yang J., Lee J., Kim S.Y., Lee E.J., Kim H.S. AKAP6 inhibition impairs myoblast differentiation and muscle regeneration: positive loop between AKAP6 and myogenin. *Sci Rep*. 2015;5:16523. doi 10.1038/srep16523

Li H., Durbin R. Fast and accurate short read alignment with Burrows–Wheeler transform. *Bioinformatics*. 2009;25(14):1754-1760. doi 10.1093/bioinformatics/btp324

Li H., Handsaker B., Wysoker A., Fennell T., Ruan J., Homer N., Marth G., Abecasis G., Durbin R.; 1000 Genome Project Data Processing Subgroup. The Sequence Alignment/Map format and SAMtools. *Bioinformatics*. 2009;25(16):2078-2079. doi 10.1093/bioinformatics/btp352

Li Q., Ching A.K.-K., Chan B.C.-L., Chow S.K.-Y., Lim P.-L., Ho T.C.-Y., Ip W.-K., Wong C.-K., Lam C.W.-K., Lee K.K.-H., Chan J.Y.-H., Chui Y.-L. A death receptor-associated anti-apoptotic protein, BRE, inhibits mitochondrial apoptotic pathway. *J Biol Chem*. 2004;279(50):52106-52116. doi 10.1074/jbc.M408678200

Lu F., Ma Q., Xie W., Liou C.L., Zhang D., Sweat M.E., Jardin B.D., Naya F.J., Guo Y., Cheng H., Pu W.T. CMYA5 establishes cardiac dyad architecture and positioning. *Nat Commun*. 2022;13(1):2185. doi 10.1038/s41467-022-29902-4

Mackiewicz J., Tomczak J., Lisek M., Guo F., Boczek T. AKAP6 controls NFATc4 activity for BDNF-mediated neuroprotection. *Mol Brain.* 2024;17(1):85. doi 10.1186/s13041-024-01157-8

Markovets A.M., Saprunova V.B., Zhdankina A.A., Fursova A.Zh., Bakeeva L.E., Kolosova N.G. Alterations of retinal pigment epithelium cause AMD-like retinopathy in senescence-accelerated OXYS rats. *Aging*. 2010;3(1):44-54. doi 10.18632/aging.100243

McKenna A., Hanna M., Banks E., Sivachenko A., Cibulskis K., Kernytsky A., Garimella K., Altshuler D., Gabriel S., Daly M., DePristo M.A. The Genome Analysis Toolkit: a MapReduce framework for analyzing next-generation DNA sequencing data. *Genome Res.* 2010;20(9):1297-1303. doi 10.1101/gr.107524.110

McLaren W., Gil L., Hunt S.E., Riat H.S., Ritchie G.R.S., Thormann A., Flicek P., Cunningham F. The Ensembl Variant Effect Predictor. *Genome Biol*. 2016;17(1):122. doi 10.1186/s13059-016-0974-4

Mirra S., García-Arroyo R., B. Domènech E., Gavaldà-Navarro A., Herrera-Úbeda C., Oliva C., Garcia-Fernàndez J., Artuch R., Villarroya F., Marfany G. *CERKL*, a retinal dystrophy gene, regulates mitochondrial function and dynamics in the mammalian retina. *Neurobiol Dis*. 2021;156:105405. doi 10.1016/j.nbd.2021.105405

Muraleva N.A., Devyatkin V.A., Kolosova N.G. Phosphorylation of αB-crystallin in the myocardium: analysis of relations with aging and cardiomyopathy. *Exp Gerontol*. 2017;95:26-33. doi 10.1016/j.exger.2017.05.009

Okonechnikov K., Golosova O., Fursov M.; UGENE team. Unipro UGENE: a unified bioinformatics toolkit. *Bioinformatics*. 2012;28(8):1166-1167. doi 10.1093/bioinformatics/bts091

Öörni K., Lorey M.B. Beyond cholesterol: linking the conformation of apolipoprotein B to atherogenesis. *Curr Opin Lipidol*. 2025;36(5):226-231. doi 10.1097/MOL.0000000000000997

Oram J.F. HDL apolipoproteins and ABCA1: partners in the removal of excess cellular cholesterol. *Arterioscler Thromb Vasc Biol*. 2003;23(5):720-727. doi 10.1161/01.ATV.0000054662.44688.9A

Pedersen B.S., Layer R., Quinlan A.R. smoove: structural-variant calling and genotyping with existing tools. 2020. Available at: https://github.com/brentp/smoove (Accessed 12.25.25)

Peng Z., Gong Y., Liang X. Role of FAT1 in health and disease. *Oncol Lett*. 2021;21(5):398. doi 10.3892/ol.2021.12659

Perng M.-D., Zhang Q., Quinlan R.A. Insights into the beaded filament of the eye lens. *Exp Cell Res*. 2007;313(10):2180-2188. doi 10.1016/j.yexcr.2007.04.005

Purcell S., Neale B., Todd-Brown K., Thomas L., Ferreira M.A.R., Bender D., Maller J., Sklar P., de Bakker P.I.W., Daly M.J., Sham P.C. PLINK: a tool set for whole-genome association and population-based linkage analyses. *Am J Hum Genet*. 2007;81(3):559-575. doi 10.1086/519795

Quinlan A.R., Hall I.M. BEDTools: a flexible suite of utilities for comparing genomic features. *Bioinformatics*. 2010;26(6):841-842. doi 10.1093/bioinformatics/btq033

RatGTEx Consortium. RatGTEx Portal, version 4. UC San Diego. 2021. Available at: https://ratgtex.org, RRID:SCR_022145 (Accessed 12.25.25)

Rayan N.A., Kumar V., Aow J., Rastegar N., Lim M.G.L., O'Toole N., Aliwarga E., … Anacker C., Hen R., Parent C., Meaney M.J., Prabhakar S. Integrative multi-omics landscape of fluoxetine action across 27 brain regions reveals global increase in energy metabolism and region-specific chromatin remodelling. *Mol Psychiatry*. 2022;27(11):4510-4525. doi 10.1038/s41380-022-01725-1

Riascos-Bernal D.F., Ressa G., Korrapati A., Sibinga N.E.S. The FAT1 cadherin drives vascular smooth muscle cell migration. *Cells*. 2023;12(12):1621. doi 10.3390/cells12121621

Robinson J.T., Thorvaldsdóttir H., Winckler W., Guttman M., Lander E.S., Getz G., Mesirov J.P. Integrative genomics viewer. *Nat Biotechnol*. 2011;29(1):24-26. doi 10.1038/nbt.1754

Rousseaux M.W., Tschumperlin T., Lu H.C., Lackey E.P., Bondar V.V., Wan Y.W., Tan Q., Adamski C.J., Friedrich J., Twede H., Clark G.D., Zoghbi H.Y. ATXN1-CIC complex is the primary driver of cerebellar pathology in spinocerebellar ataxia type 1 through a gain-of-function mechanism. *Neuron*. 2018;97(6):1235-1243.e5. doi 10.1016/j.neuron.2018.02.013

Rudnitskaya E.A., Kozlova T.A., Burnyasheva A.O., Tarasova A.E., Pankova T.M., Starostina M.V., Stefanova N.A., Kolosova N.G. Features of postnatal hippocampal development in a rat model of sporadic Alzheimer's disease. *Front Neurosci.* 2020;14:533. doi 10.3389/fnins.2020.00533

Sarparanta J. Biology of myospryn: what's known? *J Muscle Res Cell Motil*. 2008;29(6-8):177-180. doi 10.1007/s10974-008-9165-6

Sarparanta J., Blandin G., Charton K., Vihola A., Marchand S., Milic A., Hackman P., Ehler E., Richard I., Udd B. Interactions with M-band titin and calpain 3 link myospryn (CMYA5) to tibial and limb-girdle muscular dystrophies. *J Biol Chem.* 2010;285(39):30304-30315. doi 10.1074/jbc.M110.108720

Sattarova E.A., Sinitsyna O.I., Vasyunina E.A., Duzhak A.B., Kolosova N.G., Zharkov D.O., Nevinsky G.A. Age-dependent guanine oxidation in DNA of different brain regions of Wistar rats and prematurely aging OXYS rats. *Biochim Biophys Acta.* 2013;1830(6):3542-3552. doi 10.1016/j.bbagen.2013.01.027

Schubert M., Lindgreen S., Orlando L. AdapterRemoval v2: rapid adapter trimming, identification, and read merging. *BMC Res Notes*. 2016;9(1):88. doi 10.1186/s13104-016-1900-2

Sen P., Maitra P., Natarajan S., Sripriya S., Mathavan S., Bhende M., Manchegowda P.T. CERKL mutation causing retinitis pigmentosa(RP) in Indian population – a genotype and phenotype correlation study. *Ophthalmic Genet*. 2020;41(6):570-578. doi 10.1080/13816810.2020.1814347

Song S., Landsbury A., Dahm R., Liu Y., Zhang Q., Quinlan R.A. Functions of the intermediate filament cytoskeleton in the eye lens. *J Clin Invest.* 2009;119(7):1837-1848. doi 10.1172/JCI38277

Stefanova N.A., Kolosova N.G. The rat brain transcriptome: from infancy to aging and sporadic Alzheimer's disease-like pathology. *Int J Mol Sci*. 2023;24(2):1462. doi 10.3390/ijms24021462

Stefanova N., Kozhevnikova O., Vitovtov A., Maksimova K., Logvinov S., Rudnitskaya E., Korbolina E., Muraleva N., Kolosova N. Senescence-accelerated OXYS rats: a model of age-related cognitive decline with relevance to abnormalities in Alzheimer disease. *Cell Cycle*. 2014;13(6):898-909. doi 10.4161/cc.28255

Stefanova N.A., Maksimova K.Y., Rudnitskaya E.A., Muraleva N.A., Kolosova N.G. Association of cerebrovascular dysfunction with the development of Alzheimer's disease-like pathology in OXYS rats. *BMC Genomics.* 2018;19(Suppl.3):75. doi 10.1186/s12864-018-4480-9

Suvakov M., Panda A., Diesh C., Holmes I., Abyzov A. CNVpytor: a tool for copy number variation detection and analysis from read depth and allele imbalance in whole-genome sequencing. *GigaScience*. 2021;10(11):giab074. doi 10.1093/gigascience/giab074

Telegina D.V., Korbolina E.E., Ershov N.I., Kolosova N.G., Kozhevnikova O.S. Identification of functional networks associated with cell death in the retina of OXYS rats during the development of retinopathy. *Cell Cycle*. 2015;14(22):3544-3556. doi 10.1080/15384101.2015.1080399

Tikhonova M.A., Yu C.H., Kolosova N.G., Gerlinskaya L.A., Maslennikova S.O., Yudina A.V., Loskutov Y.V., Aftanas L.I. Comparison of behavioral and biochemical deficits in rats with hereditary defined or D-galactose-induced accelerated senescence: evaluating the protective effects of diosgenin. *Pharmacol Biochem Behav.* 2014;120:7-16. doi 10.1016/j.pbb.2014.01.012

Tomczak J., Mackiewicz J., Lisek M., Kaluza A., Boczek T. Exploring AKAPs in visual signaling. *Front Mol Neurosci.* 2024;17:1412407. doi 10.3389/fnmol.2024.1412407

Tuson M., Marfany G., Gonzàlez-Duarte R. Mutation of CERKL, a novel human ceramide kinase gene, causes autosomal recessive retinitis pigmentosa (RP26). *Am J Hum Genet*. 2004;74(1):128-138. doi 10.1086/381055

Tyumentsev M.A., Stefanova N.A., Muraleva N.A., Rumyantseva Y.V., Kiseleva E., Vavilin V.A., Kolosova N.G. Mitochondrial dysfunction as a predictor and driver of Alzheimer's disease-like pathology in OXYS rats. *J Alzheimer's Dis*. 2018;63(3):1075-1088. doi 10.3233/JAD-180065

Vays V.B., Eldarov C.M., Vangely I.M., Kolosova N.G., Bakeeva L.E., Skulachev V.P. Antioxidant SkQ1 delays sarcopenia-associated damage of mitochondrial ultrastructure. *Aging*. 2014;6(2):140-148. doi 10.18632/aging.100636

Vergarajauregui S., Becker R., Steffen U., Sharkova M., Esser T., Petzold J., Billing F., Kapiloff M.S., Schett G., Thievessen I., Engel F.B. AKAP6 orchestrates the nuclear envelope microtubule-organizing center by linking Golgi and nucleus via AKAP9. *eLife.* 2020;9:e61669. doi 10.7554/elife.61669

Wang H., Ouyang G., Zhu Y. D348N mutation of BFSP1 gene in congenital cataract: it does matter. *Cell Biochem Biophys.* 2023;81(4):757-763. doi 10.1007/s12013-023-01169-6

Wickham H. ggplot2. Use R! Springer Cham, 2016. doi 10.1007/978-3-319-24277-4

Wickham H., Averick M., Bryan J., Chang W., McGowan L., François R., Grolemund G., … Takahashi K., Vaughan D., Wilke C., Woo K., Yutani H. Welcome to the Tidyverse. *J Open Source Software*. 2019;4(43):1686. doi 10.21105/joss.01686

Wilcox S.M., Arora H., Munro L., Xin J., Fenninger F., Johnson L.A., Pfeifer C.G., Choi K.B., Hou J., Hoodless P.A., Jefferies W.A. The role of the innate immune response regulatory gene ABCF1 in mammalian embryogenesis and development. *PLoS One*. 2017;12(5):e0175918. doi 10.1371/journal.pone.0175918

Wong D., Yip S. Making heads or tails – the emergence of *capicua* (*CIC*) as an important multifunctional tumour suppressor. *J Pathol*. 2020;250(5):532-540. doi 10.1002/path.5400

Wu C., Orozco C., Boyer J., Leglise M., Goodale J., Batalov S., Hodge C.L., Haase J., Janes J., Huss J.W. 3rd, Su A.I. BioGPS: an extensible and customizable portal for querying and organizing gene annotation resources. *Genome Biol.* 2009;10(11):R130. doi 10.1186/gb-2009-10-11-r130

Yip S., Butterfield Y.S., Morozova O., Chittaranjan S., Blough M.D., An J., Birol I., … Jones S.J., Morin G.B., Chan J.A., Cairncross J.G., Marra M.A. Concurrent *CIC* mutations, *IDH* mutations, and 1p/19q loss distinguish oligodendrogliomas from other cancers. *J Pathol*. 2012;226(1):7-16. doi 10.1002/path.2995

Zhang Y., Liu T., Meyer C.A., Eeckhoute J., Johnson D.S., Bernstein B.E., Nusbaum C., Myers R.M., Brown M., Li W., Liu X.S. Model-based analysis of ChIP-Seq (MACS). *Genome Biol*. 2008;9(9):R137. doi 10.1186/gb-2008-9-9-r137

Zhdankina A.A., Tikhonov D.I., Logvinov S.V., Plotnikov M.B., Khlebnikov A.I., Kolosova N.G. Suppression of age-related macular degeneration-like pathology by c-Jun N-terminal kinase inhibitor IQ-1S. *Biomedicines*. 2023;11(2):395. doi 10.3390/biomedicines11020395

Zheng X., Kong W., Dai X., You C. YBX1 modulates 8-oxoguanine recognition and repair in DNA. *ACS Chem Biol*. 2025;20(2):433-442. doi 10.1021/acschembio.4c00831

Conflict of interest. The authors declare no conflict of interest.

Received December 25, 2025. Revised May 28, 2026. Accepted May 29, 2026.

ANIMAL GENETICS
Original article

Vavilovskii Zhurnal Genetiki i Selektsii
Vavilov Journal of Genetics and Breeding. 2026;30(6):899-907

doi 10.18699/vjgb-26-91

Epigenetic regulation of the transcriptional activity of genes mediating the neuroprotective activity of ceftriaxone in the brain in a rat model of sporadic Alzheimer disease: the involvement of histone deacetylase 1

A.A. Bashirzade [1], M.A. Tikhonova [1] ✉, V.M. Belichenko[1], L.A. Fedoseeva [1, 2], M.D. Belyaev[2], T.-Y. Renn [3], H.-M. Chang [3], N.G. Kolosova [2], N.D. Belyaev[1], T.G. Amstislavskaya [1]

[1] Scientific Research Institute of Neurosciences and Medicine, Novosibirsk, Russia
[2] Institute of Cytology and Genetics of the Siberian Branch of the Russian Academy of Sciences, Novosibirsk, Russia
[3] Taipei Medical University, Taipei, Taiwan
✉ tikhonovama@neuronm.ru

Abstract. Histone deacetylases (HDACs) are enzymes that provide transcriptional repression, while HDAC inhibitors are considered to be potential drugs in the treatment of Alzheimer disease (AD). Earlier we found that ceftriaxone (CEF), an antibiotic with neuroprotective activity, augmented mRNA levels of *Ide* and *Mme*, encoding enzymes involved in the catabolism of amyloid beta in the amygdala of OXYS rats, a model of sporadic AD. On the other hand, disturbances of neurotrophic factors (BDNF in particular) play an important role in AD pathogenesis. Moreover, HDACs of class I (HDAC1) are involved in the regulation of *Bdnf* transcriptional activity. The study was aimed to assess the effects of CEF on HDAC1 enrichment at *Mme*, *Ide*, and *Bdnf* gene promoters in the amygdala of OXYS rats and on *Bdnf* mRNA levels in the amygdala of OXYS and Wistar rats. Chromatin immunoprecipitation and qPCR were utilized for epigenetic analysis and assay of *Bdnf* mRNA levels, respectively. Neither significant HDAC1 enrichment, nor its alteration under CEF treatment at the *Mme* or *Ide* promoters were found, whereas CEF attenuated HDAC1 binding at *Bdnf* promoter IV. This is a novel mechanism of transcription regulation by CEF in the brain, which may be involved in its neuroprotective activity. In 5-month-old OXYS rats, it seems to play a minor role, as CEF did not change *Bdnf* transcript 5 (containing exons IV and IX) levels. We were first to demonstrate the transcript-specific regulation of *Bdnf* transcription by CEF. CEF significantly increased the levels of *Bdnf* transcript 6 (containing exons VII, VIII, and IX). The results of our study can be taken into account in AD treatment.

Key words: Alzheimer's disease; histone deacetylase; ceftriaxone; neuroprotection; amyloid metabolism; BDNF

For citation: Bashirzade A.A., Tikhonova M.A., Belichenko V.M., Fedoseeva L.A., Belyaev M.D., Renn T.-Y., Chang H.-M., Kolosova N.G., Belyaev N.D., Amstislavskaya T.G. Epigenetic regulation of the transcriptional activity of genes mediating the neuroprotective activity of ceftriaxone in the brain in a rat model of sporadic Alzheimer disease: the involvement of histone deacetylase 1. *Vavilovskii Zhurnal Genetiki i Selektsii = Vavilov J Genet Breed*. 2026;30(6):899-907. doi 10.18699/vjgb-26-91

Funding. The study was supported by budgetary funding for basic research of the Scientific Research Institute of Neurosciences and Medicine (projects 122042700001-9, 126020316369-9).

Acknowledgements. We are grateful to Ekaterina E. Pisareva, Alla S. Avdeeva, and Inna Lytkina (née Yarantseva) for technical assistance in total RNA extraction and reverse transcription procedures for qPCR analysis of mRNA levels.

Эпигенетическая регуляция транскрипционной активности генов, связанных с нейропротекторным действием цефтриаксона, в головном мозге у крыс на модели спорадической болезни Альцгеймера: участие гистоновой деацетилазы 1

А.А. Баширзаде [1], М.А. Тихонова [1] ✉, В.М. Беличенко[1], Л.А. Федосеева [1, 2], М.Д. Беляев[2], Т.-И. Ренн [3], Х.-М. Чан [3], Н.Г. Колосова [2], Н.Д. Беляев[1], Т.Г. Амстиславская [1]

[1] Научно-исследовательский институт нейронаук и медицины, Новосибирск, Россия
[2] Федеральный исследовательский центр Институт цитологии и генетики Сибирского отделения Российской академии наук, Новосибирск, Россия
[3] Тайбэйский медицинский университет, Тайбэй, Тайвань
✉ tikhonovama@neuronm.ru

© Bashirzade A.A., Tikhonova M.A., Belichenko V.M., Fedoseeva L.A., Belyaev M.D., Renn T.-Y., Chang H.-M., Kolosova N.G., Belyaev N.D., Amstislavskaya T.G., 2026
This work is licensed under a Creative Commons Attribution 4.0 License

Аннотация. Гистоновые деацетилазы (HDAC) – это ферменты, обеспечивающие подавление транскрипции генов, а ингибиторы HDAC рассматриваются как потенциальные лекарственные средства для лечения болезни Альцгеймера (БА). Ранее мы обнаружили, что цефтриаксон, антибиотик с нейропротекторной активностью, повышает уровни мРНК генов *Ide* и *Mme*, кодирующих ферменты, которые участвуют в катаболизме амилоида-бета, в миндалине мозга у крыс линии OXYS, модели спорадической БА. С другой стороны, нарушения нейротрофических факторов (в частности, BDNF) играют важную роль в патогенезе БА. Более того, HDAC класса I (HDAC1) участвуют в регуляции транскрипционной активности *Bdnf*. Целью данного исследования было оценить влияние цефтриаксона на обогащение HDAC1 в промоторах генов *Mme*, *Ide* и *Bdnf* в миндалине у крыс OXYS и на уровни мРНК *Bdnf* в миндалине крыс OXYS и Вистар. Для эпигенетического анализа и определения уровней мРНК *Bdnf* использовали хроматин-иммунопреципитацию и количественную ПЦР, соответственно. Не выявлено значимого обогащения HDAC1 или его изменений под действием цефтриаксона в промоторах *Mme* и *Ide*. В то же время цефтриаксон ослаблял связывание HDAC1 с промотором IV *Bdnf*. Это новый механизм регуляции транскрипции в головном мозге цефтриаксоном, который может быть задействован в его нейропротекторной активности. У 5-месячных крыс OXYS он, по-видимому, играет минорную роль, поскольку цефтриаксон не изменял уровни транскрипта 5 *Bdnf*, содержащего экзоны IV и IX. Мы также впервые продемонстрировали транскрипт-специфическую регуляцию транскрипции *Bdnf* с помощью цефтриаксона. Цефтриаксон значительно повысил уровни транскрипта 6 *Bdnf*, содержащего экзоны VII, VIII и IX. Результаты исследования могут быть учтены при терапии БА.

Ключевые слова: болезнь Альцгеймера; гистоновая деацетилаза; цефтриаксон; нейропротекция; метаболизм амилоида; BDNF

Introduction

Alzheimer's disease (AD) is an incurable multifactorial neurodegenerative disorder characterized by a progressive cognitive decline induced by the accumulation of amyloid beta (Aβ) in the brain, which triggers synaptic plasticity dysfunction, neuronal deficits, and memory loss. Most of the current AD therapies do not stop the disease progression and provide only temporary symptomatic relief. Hence, the development of new treatment strategies that target the key pathogenetic factors in AD development is needed.

Epigenetic factors are considered to make a significant contribution to AD development. Many studies have demonstrated the involvement of different epigenetic mechanisms in the pathogenesis of neurodegeneration in AD (Nikolac Perkovic et al., 2021). Most often, this concerns DNA methylation/demethylation (Poon et al., 2020), posttranslational modifications of histones (Ramazi et al., 2020), and regulation by various forms of noncoding RNAs (Idda et al., 2018). Acetylation/deacetylation of histones at lysine is one of the most common and studied mechanisms of chromatin compaction (Shvedunova, Akhtar, 2022). It is regulated by two types of enzymes: histone acetyltransferases and histone deacetylases (HDACs). HDACs are enzymes that remove acetyl groups from lysine residues in the amino terminal tails of histone proteins. The resulting chromatin compaction, in turn, causes transcriptional and translational repression (Sada et al., 2020). HDAC inhibitors are considered potential drugs in AD treatment (Bondarev et al., 2021).

Increasing the expression and/or enzymatic activity of proteins involved in Aβ cleavage has long been considered a promising targeted approach in AD treatment (Zhang et al., 2023). Neprilysin or membrane metalloendopeptidase (MME), being the major amyloid-degrading enzyme in the brain, plays a significant role in AD pathogenesis, in particular, in the late onset sporadic form (Nalivaeva et al., 2020). Regulation of MME expression by HDACs has been revealed in cell cultures. In SH-SY5Y cells, the endopeptidase promoter interacts with HDAC1 and lacks typical histone acetylation marks, such as H4K16 and H4K8. In human HUVEC cells, 15-fold enrichment of *MME* promoters in HDAC1 has been observed (Belyaev et al., 2009).

Another metallopeptidase, insulinase, also known as insulin-degrading enzyme (IDE), together with MME is one of the main enzymes that participate in the extra- and intracellular degradation of Aβ (Kurochkin et al., 2018). Enrichment of the *IDE* gene promoter in HDACs of class I (but not class III) was significantly reduced in the cell culture of neuron-like SH-SY5Y cells overexpressing APP751 and APP770 (Nalivaeva et al., 2016).

Abbreviations
Aβ, amyloid-beta;
AD, Alzheimer's disease;
AICD, APP intracellular domain;
APP, amyloid precursor protein;
BDNF, Brain-Derived Neurotrophic Factor;
BDNF/*Bdnf*, gene for BDNF;
CA, cornu Ammonis of the hippocampus;
CEF, ceftriaxone;
ChIP, chromatin immunoprecipitation;
FP, forward primers;
Gapdh, gene encoding glyceraldehyde 3-phosphate dehydrogenase;
HDAC, histone deacetylase;
Hprt1, gene encoding hypoxanthine phosphoribosyltransferase 1;
IDE, Insulin-degrading enzyme;
IDE/*Ide*, gene for IDE;
MME, membrane metalloendopeptidase;
MME/*Mme*, gene for MME; NFκB, nuclear factor kappa B;
NMDA receptor, N-methyl-D-aspartate receptor;
qPCR, quantitative real-time PCR;
RP, reverse primers;
TSS, Transcription Start Site;
tr.var., transcript variant

Ceftriaxone (CEF) is a third-generation cephalosporin antibiotic with neuroprotective activity. The drug is extensively applied in preclinical studies on models of neurological disorders. The studies have revealed beneficial effects of CEF in AD-like pathology (Zumkehr et al., 2015; Hefendehl et al., 2016; Tikhonova et al., 2017, 2021). Moreover, long-term treatment with CEF, even over several months, is found to be safe in laboratory rodents (Ratti et al., 2015) and in humans in clinical trials on CEF as a neuroprotective agent in amyotrophic lateral sclerosis (Cudkowicz et al., 2014) or Parkinson's disease dementia[1]. Suppression of glutamate-induced excitotoxicity was long regarded as the main neuroprotective effect of CEF. However, additional mechanisms of its neuroprotective effects such as an activity targeted at the proteostasis network or pathological aggregation of proteins are suspected (Kumari, Deshmukh, 2021). Indeed, our group has shown that CEF attenuates Aβ load in the brains of mice with Aβ-induced AD-like pathology (Tikhonova et al., 2021). Moreover, CEF changes the transcriptional activity of genes encoding enzymes involved in the catabolism of Aβ. In OXYS rats, which are a model of accelerated senescence and sporadic AD (Stefanova et al., 2014), administration of CEF resulted in the restoration of cognitive and neuronal deficits (Tikhonova et al., 2017) associated with an increase in the mRNA levels of *Ide* and *Mme* in the amygdala (Rasero et al., 2017) but not in the hippocampus or frontal cortex (Tikhonova et al., 2018). Amygdala is a brain structure that is closely associated with learning and memory function and is involved in the pathogenesis of AD since the early stages of disease progression. However, the mechanisms of the effect of CEF on the transcriptional activity of endopeptidases remain unknown. Here, we checked whether CEF might influence the expression of genes encoding MME and IDE through the epigenetic regulation of HDAC1 enrichment of the gene promoters.

The search for means enhancing the clearance of intracellular amyloid oligomers using a system of degrading enzymes is not the only direction being developed for AD therapy. There are other approaches, in particular, those related to increasing neuroprotection and neurotrophic function in brain structures. BDNF is the most abundant neurotrophic factor in the central nervous system. It supports the processes of neurogenesis and neuroplasticity and it is involved in learning and memory processes. According to the results of meta-analyses, patients with AD have decreased BDNF levels in the blood and brain (Du et al., 2018; Ng et al., 2019). Moreover, CEF restores the reduced BDNF levels in the striatum of rats in the MPTP-induced model of Parkinson's disease (Kaur, Prakash, 2017). Earlier we found that alterations in neurotrophic balance indicating increased apoptosis precede the development of AD-like pathology in OXYS rats. Rapid progression of AD-like pathology in OXYS rats is accompanied by the suppression of activity of the neurotrophin system (Rudnitskaya et al., 2017). Hence, we assumed a modulating effect of CEF on the transcriptional activity of *Bdnf* in the brain of OXYS rats. On the other hand, previous studies revealed that the modulation of the transcriptional activity of *Bdnf* was associated with alterations in HDAC1 binding at the *Bdnf*-IV promoter in the hippocampus of early-life iron-deficient rats (Tran et al., 2015).

Thus, this study was aimed to assess the effect of CEF on the mRNA levels of *Bdnf* in the amygdala of OXYS and Wistar rats and to evaluate the involvement of enrichment of the gene promoters in HDACs of class I (HDAC1) in the CEF effects on the expression of *Mme*, *Ide*, and *Bdnf* genes in the amygdala of OXYS rats.

Materials and methods

Experimental procedures involving animals. The experiment was performed with 14-week-old male OXYS rats developed at the Federal Research Center Institute of Cytology and Genetics, Siberian Branch of the Russian Academy of Sciences, Novosibirsk, Russia, and male Wistar rats of the control parental strain of the same age. The animals were kept in cages (40 × 60 × 20 cm), five rats in each, with free access to standard chow for laboratory rats and water under standard conditions: a natural light–dark cycle 16 h light : 8 h dark, temperature 18–22 °C, relative humidity 50–60 %. The animals were divided into four experimental groups: OXYS Control, OXYS CEF, Wistar Control, and Wistar CEF. The Control groups were administered saline intraperitoneally (i.p.) while the CEF groups were treated with CEF i.p. at a daily dose of 100 mg/kg. Rats received 36 daily i.p. injections of CEF or saline according to the previously described design in the study of the effect of CEF on the expression of genes related to the system of Aβ metabolism in the brain (Tikhonova et al., 2018). The rationale behind the CEF dosage – 100 mg/(kg·day) – and treatment duration adopted in the current study was based on our previous studies showing neuroprotective effects of CEF in correcting the behavioral and neuronal deficits in OXYS rats (Tikhonova et al., 2017) and the modulating effect of CEF on the expression of *Mme* and *Ide* in the amygdala of OXYS rats (Tikhonova et al., 2018). On day 37 the rats were sacrificed by exposure to CO_2 and decapitation. Immediately upon sacrifice, the amygdalae were rapidly dissected on ice, frozen in liquid nitrogen, and stored at −70 °C until further analysis.

The study of gene promoter enrichment in HDAC1 was performed in biosamples of the amygdala of rats from the OXYS Control (n = 5) and OXYS CEF (n = 5) groups, as we had not revealed significant effects of CEF treatment on the mRNA levels of *Ide* and *Mme* in Wistar rats (Tikhonova et al., 2018). The *Bdnf* transcriptional activity was assessed by mRNA levels in biosamples of the amygdala in rats of the OXYS Control (n = 8), OXYS CEF (n = 10), Wistar Control (n = 8), and Wistar CEF (n = 10) groups.

Chromatin immunoprecipitation (ChIP). The ChIP procedure was performed according to the previously published protocol (Zuccato et al., 2007) with minor modifications. Amygdala tissue was crushed into small pieces in a mortar with liquid nitrogen using a ceramic pestle. Next, the tissue mass was immersed in 1 % formaldehyde solution in PBS to fix DNA and proteins and intensively mixed for 10 min at 4 °C. Fixation was stopped by adding 1.25 M glycine solution. Then the samples were washed three times with cooled

[1] National Library of Medicine. To assess the efficacy and safety of ceftriaxone in patients with mild to moderate Parkinson's disease dementia. ClinicalTrials.gov ID NCT03413384. https://clinicaltrials.gov/ct2/show/NCT03413384 (Accessed March, 11, 2026).

Table 1. Primers for the promoters of target genes

Gene symbol	Sequence	T_1, °C	T_2, °C	T_3, °C
Mme (promoter I)	F: 5′-GGACCTGAGAATGTGGGGA-3′ R: 5′-GGCTGCAGGAAGCTATGAAAA-3′	60–64	84	87
Ide (promoter I)	F: 5′-GAAATGTCCTTACTCCCCCA-3′ R: 5′-CACAAAGCGGTAGGTCCC-3′	61–63	89	92.5
Bdnf (promoter IV)	F: 5′-GATGAAAGGTTTGGCTTCTGTG-3′ R: 5′-TCGGTGAATGGGAAAGTGG-3′	55	78	82.5

Note. T_1: annealing temperature; T_2: temperature at fluorescence signal acquisition; T_3: product melting temperature.

PBS solution and immersed in 1 mL of lysis buffer (10 mM Tris-HCl, pH 8.0, 140 mM NaCl, 1 mM EDTA, 1 % Triton X-100, 0.1 % deoxycholate, 1 mM PMSF). The samples were homogenized by passing through a 21G syringe needle. Ultrasonic treatment (sonication) of samples was performed using a Sonopuls mini20 sonicator (Bandelin, Germany) with a power of 20 W in a volume of 1 mL. Sonication mode used: eight times for 30 s with 2-min intervals. The DNA fragments obtained under these conditions were 500–1000 bp long. Then the samples were divided into three unequal parts: 10 % of the volume was allocated for input (i. e. DNA fragments with ligated protein, not treated with immune antibodies) and two equal parts, one for the interaction with specific antibodies against HDAC1 (Catalog # PA1-860, Invitrogen, Thermo Fisher Scientific, United States) and the other for the interaction with control nonimmune antibodies IgG (Catalog # 02-6102, Invitrogen, Thermo Fisher Scientific, United States). The input was stored at –20 °C until the stage of de-cross-linking the DNA and protein fractions. The ratio of antibody volume to sample volume was 1:500. The samples with antibodies were incubated at 4 °C overnight.

Protein G Sepharose (Catalog # ab193259, Abcam, UK) was incubated with 5 % BSA overnight. BSA-blocked Sepharose was added to the samples immediately after incubation with antibodies and intensively mixed in a shaker for 1 h at 4 °C. Sepharose samples were sequentially washed with solutions containing increasing concentrations of salts and nonionic detergents. The first wash solution consisted of lysis buffer (10 mM Tris HCl, pH 8.0, 140 mM NaCl, 1 mM EDTA, 1 % Triton X-100, 0.1 % deoxycholate, 1 mM PMSF). The second wash solution consisted of 10 mM Tris HCl, pH 8.0, 250 mM LiCl, 0.5 % Triton X-100, 0.5 % sodium deoxycholate, 1 mM EDTA. Sepharose beads were washed with 1 % SDS in 0.1 M $NaHCO_3$.

Bound DNA and protein fractions including inputs were de-cross-linked by adding 5M NaCl and incubating at 65 °C overnight. The samples were then treated with proteinase K in the buffer containing 0.1 M Tris-HCl, pH 8.0, 50 mM EDTA, and 10 % SDS at 50°C for 1 h. DNA was isolated by phenol-chloroform extraction, precipitated with two volumes of 95 % ethanol, and washed twice with 70 % ethanol. The remaining alcohol was evaporated in a thermostat. The precipitate was dissolved in 22 μL of TE buffer (0.01 M Tris + 0.001 M EDTA, pH 8.0). The amount of isolated DNA was measured in a Nanodrop 2000C spectrophotometer (Thermo Fisher Scientific, United States).

To assess the enrichment of the promoter regions of the *Mme*, *Ide*, and *Bdnf* genes, semiquantitative real-time PCR was performed using a CFX96 Touch amplifier (Bio-Rad, United States) with the SYBR Green fluorescent dye. Sequences of specific primers for the promoters of the target genes (*Mme*, *Ide*, and *Bdnf*) were selected using Primer 3 (NCBI) (Table 1). The specificity of the primers was checked using the Primer-BLAST online software[2]. For *Bdnf*, we studied promoter IV as previous studies revealed the involvement of HDAC1 binding at the *Bdnf*-IV promoter in the modulation of the transcriptional activity of *Bdnf* (Tran et al., 2015). Loci that are homologous to primer sequences in the promoter region of the studied genes are shown in Figures 3*a*, 4*a*, and 5*a*.

The obtained amplicons homologous to the fragments of the specified promoters of the target genes in the samples treated with specific antibodies against HDAC1 or control non-immune IgG antibodies and inputs were loaded onto 1 % agarose gel containing ethidium bromide (1 mg/mL). Electrophoresis was performed in a horizontal chamber with 1x TAE buffer at 130 V for 40 min (PowerPac HC, BioRad, United States). The samples were visualized using the Molecular Imager® Gel Doc™ XR System (BioRad, United States). The DNA markers Step100 Long (Catalog # S-8055, Biolabmix, Novosibirsk, Russia) and Step50 plus (Catalog # S-8103, Biolabmix, Novosibirsk, Russia) were used for assessing DNA length.

The enrichment of the promoter regions in HDAC1 was calculated using Percent Input Method[3]. The mean Ct was calculated for each antibody type and input ($n = 5$). The adjusted mean Ct for the input (10 % of total DNA) was calculated as the difference between the mean Ct for the inputs and the binary logarithm of the dilution factor of 10 ($\log_2 10$). For target and non-immune antibodies, the percentage of input was calculated as $100*2^{\Delta Ct}$, where ΔCt is the difference between the adjusted mean Ct for the input and the mean Ct for samples treated with target/non-immune antibodies.

Analysis of mRNA levels of Bdnf transcript variants using qPCR. To analyze the transcriptional activity of the *Bdnf* gene under the conditions of our experiment, we used two pairs of primers that allowed us to study the expression of two different transcript variants. Despite the final protein product being selfsame, there are 10 validated transcripts of

[2] National Library of Medicine. Primer-BLAST. https://www.ncbi.nlm.nih.gov/tools/primer-blast/ (Accessed October, 20, 2025).
[3] Thermo Fisher Scientific Inc. ChIP Analysis. https://www.thermofisher.com/ru/ru/home/life-science/epigenetics-noncoding-rna-research/chromatin-remodeling/chromatin-immunoprecipitation-chip/chip-analysis.html (Accessed October, 20, 2025).

Table 2. Primers used in qPCR analysis for target and reference genes

Gene symbol	Sequence	Amplicon size, bp	Annealing T, °C
	Target genes		
Bdnf-tr.var.5	F: 5′-AGTACATATCGGCCACCAAA-3′ R: 5′-ATGGTCATCACTCTTCTCACC-3′	178	62
Bdnf-tr.var.6	F: 5′-GTATCCGACCCTCTCTGTCC-3′ R: 5′-CAGCAATCGTTTGTTCAGCTCC-3′	135	56
	Reference genes		
Hprt1	F: 5′-CATTGTGGCCCTCTGTGTG-3′ R: 5′-AACTTTTATGTCCCCCGTTGA-3′	166	60
Gapdh	F: 5′-GTGCCAGCCTCGTCTCATA-3′ R: 5′-TCGTTGATGGCAACAATGTCC-3′	123	65

the rat *Bdnf* gene[4] which are involved in different functions (Baj et al., 2011). Here, we studied the levels of transcript variant 5 (*Bdnf*-tr.var.5; NM_001270633.1) and transcript variant 6 (*Bdnf*-tr.var.6; NM_001270634.1). *Bdnf*-tr.var.5 contains exons IV and IX and is the only transcript specific for exon IV (and its associated promoter region) among all *Bdnf* transcripts. *Bdnf*-tr.var.6 contains exons VII, VIII, and IX and is transcribed starting from exon VII – but not the exon IV-associated promoter region; its levels were assessed to evaluate transcript-specific effects of CEF. The primers were mapped onto the gene regions homologous to the transcript variants of interest using the UCSC Santa Cruz Genome Browser[5]. The specific *Bdnf* primers for the analysis of mRNA levels of *Bdnf*-tr.var.5 and *Bdnf*-tr.var.6 as well as the reference genes *Gapdh* and *Hprt1* were chosen using the Primer-BLAST online software[6].

Extraction of total RNA from fresh-frozen rat amygdala samples was performed using RNeasy Minikit in accordance with the manufacturer's recommendations (Qiagen, Germany). Residual genomic DNA was removed using DNase I (Promega, United States). The reverse transcriptase reaction was carried out as in (Tikhonova et al., 2018) with 160 units of reverse transcriptase (Biosan, Russia) and 1× RT Buffer (Biosan, Russia). The temperature regime of reverse transcription included three steps: 25 °C for 5 min, 42 °C for 30 min, and 95 °C for 5 min.

The mRNA levels of target and reference genes were measured by qPCR according to a previously published protocol (Belichenko et al., 2023). The reaction was carried out in a LightCycler-480 II thermocycler (Roche, Switzerland) in master mix from a BioMaster HS-qPCR SYBR Blue (2 ×) reagent kit (BIOLABMIX, Novosibirsk, Russia) with forward and reverse specific primers (150 nM each; BIOSSET Ltd., Novosibirsk, Russia; Table 2), and a cDNA template.

All samples were analyzed in triplicate. The relative concentration of a tested cDNA was determined by the standard-curve quantitation method (Ginzinger, 2002) using the LightCycler 480 Software (Release 1.5.1) and calibration curves derived from the dilutions of a standard cDNA. The standard cDNA solution for plotting the calibration curves was prepared by mixing aliquots from each synthesized cDNA sample. The expression value for a target gene was next normalized to the geometric mean mRNA levels of the two reference genes (*Hprt1* and *Gapdh*).

Statistical analysis. All results were presented as mean ± SEM. STATISTICA 10.0 software (StatSoft, Tulsa, OK, United States) was used to perform all the statistical analyses. The normality of the data distribution was determined by the Shapiro–Wilk *W* test. To compare the enrichment of gene promoters in HDAC1, paired Student's *t* test for dependent samples and Student's *t* test for independent samples (in Welch's modification) were used. Statistical evaluation of the *Bdnf*-tr.var.5 and *Bdnf*-tr.var.6 transcriptional data was performed by two-way analysis of variance (ANOVA) followed by Bonferroni's post hoc test. Independent variables for the two-way ANOVA were *genotype* (Wistar or OXYS strain) and *treatment* (saline or CEF). The level of significance was defined as $p < 0.05$ in all experiments reported here. The tendency level was accepted to be $0.05 < p < 0.2$.

Results

Analysis of the levels of Bdnf transcript variants in the amygdala of OXYS and Wistar rats. The levels of mRNA species for *Bdnf*-tr.var.-5 (the only *Bdnf* transcript containing exon IV) in the amygdala are summarized in Figure 1. According to two-way ANOVA, there was no significant effect of the *Treatment* factor [$F(1, 32) = 1.245$, $p = 0.274$] but there was a tendency toward influence of the interaction between the factors of *Treatment* and *Genotype* [$F(1, 32) = 2.565$, $p = 0.120$] on the mRNA levels of *Bdnf*-tr.var.-5 in the amygdala of the rats. The abundance of mRNA species for *Bdnf*-tr.var.-6 (*Bdnf* transcript containing exons VII, VIII, and IX) in the amygdala is summarized in Figure 2. According to two-way ANOVA, the *Treatment* factor significantly influenced the mRNA levels of *Bdnf*-tr.var.-6 in the amygdala of the rats [$F(1, 29) = 4.526$, $p < 0.05$].

Analysis of the enrichment of gene promoters in HDAC1 in the amygdala of OXYS rats. In the analysis of the promoter region of *Mme* gene, the enrichment values for the target antibody against HDAC1 did not differ from the background values for the control IgG antibody according

[4] National Library of Medicine. NCBI_Gene_Bdnf brain-derived neurotrophic factor [Rattus norvegicus (Norway rat)]. https://www.ncbi.nlm.nih.gov/gene/24225 (Accessed March, 20, 2026).

[5] Santa Cruz Genome Browser. 2025. http://genome.ucsc.edu/index.html (Accessed October, 20, 2025).

[6] National Library of Medicine. Primer-BLAST. https://www.ncbi.nlm.nih.gov/tools/primer-blast/ (Accessed October, 20, 2025).

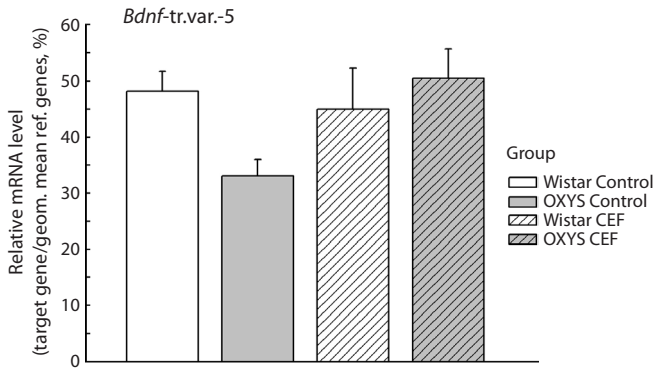


Fig. 1. Effects of CEF on *Bdnf*-tr.var.-5 mRNA levels in the amygdala of OXYS and Wistar rats.

Data are presented as a ratio (%) of target transcript mRNA levels to the geometric mean of *Gapdh* and *Hprt1* mRNA levels. The data are expressed as the mean ± SEM of the values obtained in an independent group of animals (n = 4 to 10 per group).

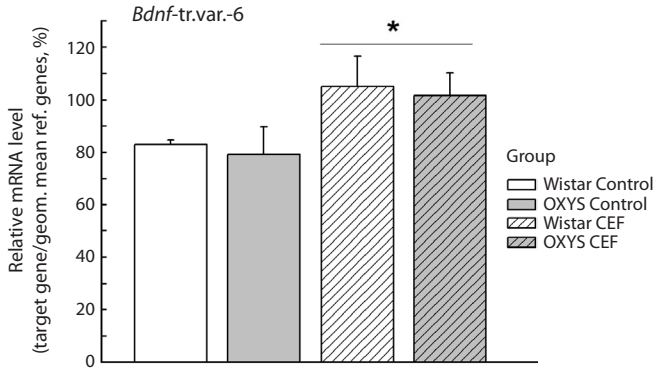


Fig. 2. Effects of CEF on *Bdnf*-tr.var.-6 mRNA levels in the amygdala of OXYS and Wistar rats.

The data are presented as a ratio (%) of target transcript mRNA levels to the geometric mean of *Gapdh* and *Hprt1* mRNA levels. The data are expressed as the mean ± SEM of the values obtained in an independent group of animals (n = 5 to 10 per group). Statistically significant differences: * $p < 0.05$ vs. Control (saline-treated) groups.

to the t test for independent samples in the Control group ($t(8) = 1.35$, $p > 0.05$) or in the group of CEF-treated OXYS rats ($t(8) = 0.36$, $p > 0.05$) (Fig. 3). Enrichment of the *Ide* promoter also did not differ from the background level in either control ($t(8) = 0.84$, $p > 0.05$) or CEF-treated group ($t(8) = 0.2$, $p > 0.05$) (Fig. 4).

We also focused on *Bdnf* promoter IV. According to previous reports, it is regulated by HDAC1 (Tran et al., 2015) and, accordingly, should be enriched in this protein. Indeed, the enrichment in HDAC1 in the Control group exceeded the background level by a factor of 8 ($t(8) = 7.12$, $p < 0.001$). In the CEF-treated group, it was also significantly augmented ($t(8) = 2.79$, $p < 0.05$), which motivated us to perform an intergroup comparison for target antibodies against HDAC1. The precipitation rates of the target DNA regions differed significantly between the groups ($t(8) = 4.31$, $p < 0.01$). Hence, we infer that CEF affects the degree of HDAC1 enrichment in the *Bdnf* promoter IV in OXYS rats (Fig. 5).

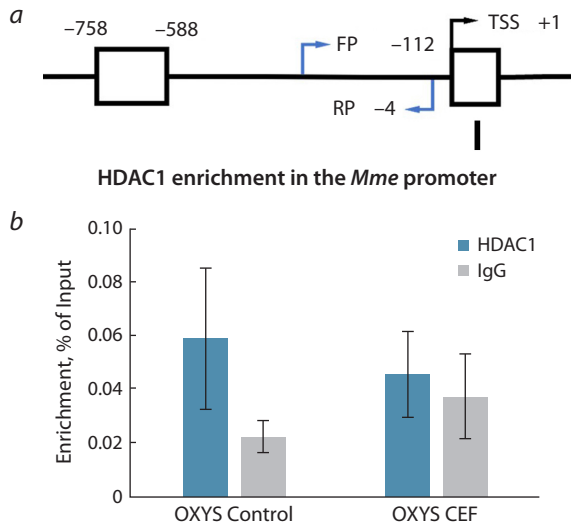


Fig. 3. Effects of CEF on rhe enrichment of the *Mme* promoter in HDAC1 in the amygdala of OXYS rats.

(*a*) Loci that are homologous to primer sequences in the promoter region of the *Mme* gene are shown. (*b*) Quantitative results of enrichment in HDAC1 in the promoter region of the gene.

Here and in Figures 4 and 5: TSS – Transcription Start Site; FP and RP – Forward and Reverse Primers. The distances (base pairs) from TSS are indicated. Data are expressed as the mean ± SEM of the values obtained in an independent group of animals (n = 5 per group).

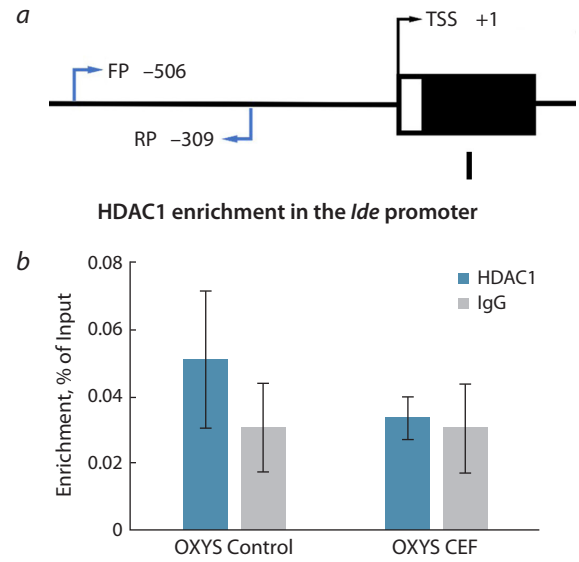


Fig. 4. Effects of CEF on enrichment in HDAC1 in the *Ide* promoter in the amygdala of OXYS rats.

(*a*) The annealing sites for the primers in the promoter region of the *Ide* gene are shown. (*b*) Quantitative results of enrichment in HDAC1 in the promoter region of the gene.

Discussion

It has been reported that CEF significantly affects *BDNF* expression in the brain. Moreover, CEF exerts a modulating effect on BDNF: it can augment (Kaur, Prakash, 2017; Gao et al., 2024; Cini et al., 2025) or attenuate (Alhaddad et al., 2020; Hammad et al., 2021) its increased levels in different models

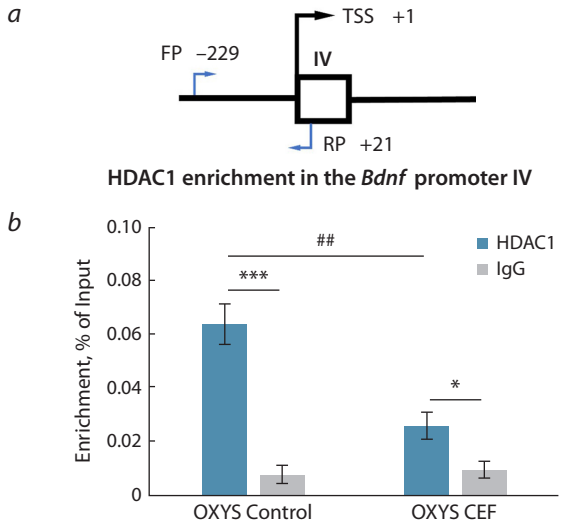


Fig. 5. Effects of CEF on enrichment in HDAC1 in the *Bdnf* promoter IV in the amygdala of OXYS rats.

(*a*) The annealing sites for the primers in the promoter region of the *Bdnf* exon IV are shown. (*b*) Quantitative results of enrichment in HDAC1 in the promoter region of the gene. Statistically significant differences: $^{*}p < 0.05$, $^{***}p < 0.001$ vs. corresponding IgG-treated samples; $^{\#\#}p < 0.01$ vs. OXYS Control samples treated with antibodies against HDAC1.

of neuropathology. Typically, studies of *BDNF* expression address the levels of the protein-coding exon IX or mature protein. Here, we are the first to demonstrate the transcript-specific regulation of *BDNF* transcription by CEF. CEF significantly increased the levels of *Bdnf*-tr.var.-6 (containing exons VII, VIII, and IX) but not of *Bdnf*-tr.var.-5 (containing exons IV and IX) in the amygdala of OXYS rats. Noteworthy, despite the same final protein product, there are 10 validated transcripts of the rat *Bdnf* gene[7], which are involved in different functions. For example, the selective activation of dendritic spines of neurons is based on the spatial segregation of different *BDNF* transcripts. Splice variants 1 and 4 control the architecture of proximal dendrites, whereas variants 2 and 6 regulate distal ones, which leads to differentiated and localized translation into the protein (Baj et al., 2011).

In contrast to the well-studied mechanisms of the antibacterial effect of CEF, its role in neuroprotection remains poorly understood. Although modulating effects of CEF on the expression of many genes in the brain are known, regulating pathways have been studied only for few. One of the known regulatory effects involves NF-κB-mediated activation of promoter of the gene encoding GLT-1 (Lee et al., 2008). However, further studies revealed that this mechanism could be structure-specific: in a rat model of cocaine abuse, CEF strongly upregulated GLT-1 both in the hippocampus and n. accumbens, whereas NF-κB involvement was found in the hippocampus but not in n. accumbens (Niedzielska-Andres et al., 2019). Here, we revealed for the first time a CEF effect on HDAC1 binding in a gene promoter. Indeed, CEF treatment significantly reduced HDAC1 enrichment at the *Bdnf* promoter IV in OXYS rats. We suggest that this mechanism might be involved in the above-mentioned CEF effect on GLT-1 upregulation in n. accumbens in the rat model of cocaine abuse, as GLT-1 expression was initially suppressed in n. accumbens in rats vulnerable to rewarding effects of cocaine prior the CEF treatment (Niedzielska-Andres et al., 2019). At the same time, this novel epigenetic CEF effect could not be attributed to the CEF-induced upregulation of *Mme*, *Ide*, and *Bdnf* we studied here in OXYS rats.

No HDAC1-mediated effect of CEF on the *Mme* or *Ide* promoters was detected. Previously obtained results in a cell culture of rat primary cortical neurons revealed no interaction of HDAC1 with the *Mme* promoter either (Belyaev et al., 2009). Moreover, in that study, an inverse correlation between HDAC1 enrichment at the *MME* promoter and *MME* mRNA levels was found. In cell cultures with low *MME* mRNA levels (SH-SY5Y, HUVEC), HDAC1 enrichment was the highest. In contrast, in cell cultures with high *MME* / *Mme* mRNA levels (NB7, rat cortical neurons), the enrichment was low or null. We did not find reports on HDAC1 enrichment at *Ide* promoters in rats or rat cells. HDAC1 involvement was also shown in the regulation of *IDE* in human cell cultures. HDAC1 binding varied in cells overexpressing different splice variants of APP: HDAC1 enrichment was lower in cells overexpressing APP751 and APP770 than in cells injected with APP695 cDNA. *IDE* mRNA expression was higher in cells with longer APP isoforms, and this observation was consistent with the influence of HDAC1 (Nalivaeva et al., 2016). Noteworthy, untreated 5-month-old OXYS rats did not differ from control Wistar rats in the *Mme* or *Ide* mRNA levels in the amygdala (Tikhonova et al., 2018); therefore, the HDAC-mediated gene suppression that might be reverted by HDAC inhibition is unlikely.

In this study, we did not find significant differences between 5-month-old OXYS and Wistar rats in the levels of *Bdnf* mRNA (*Bdnf-tr.var.5* and *Bdnf-tr.var.6*) in the amygdala. These results are consistent with previous findings about similar *Bdnf* mRNA levels in the frontal cortex and hippocampus in OXYS and Wistar rats at the age of 14 weeks (Alsallum et al., 2023). At the same time, we revealed the HDAC1 enrichment of promoter IV of the *Bdnf* gene in 5-month-old OXYS rats, although we observed no significant differences in the levels of *Bdnf-tr.var.5* (the only *Bdnf* transcript containing exon IV in rats) in the amygdala between OXYS and Wistar rats of this age. As a rule, in younger proliferating cells, chromatin is in a less condensed state, which facilitates the access of the cellular transcriptional apparatus. On the contrary, aging cells are characterized by the appearance of densely packed heterochromatin organized into specific structures (Narita et al., 2003). In neurons, which are not prone to proliferation, markers of both active (H3K27Ac) and repressive (H3K27Me3) chromatin may be present, but in aging neurons of the murine hippocampus, a general decrease in acetylation and an increase in deacetylation are observed (Palomer et al., 2016). In the model of accelerated senescence and sporadic AD, enrichment of the BDNF promoter in HDACs seems to be anticipated. Chromatin of glial cells in OXYS rats at the age of 18 months has a high degree of condensation (Stefanova et al., 2015). We are unaware of the degree of enrichment of the *Bdnf* promoter in HDACs in the

[7] National Library of Medicine. NCBI_Gene_Bdnf brain-derived neurotrophic factor [Rattus norvegicus (Norway rat)]. https://www.ncbi.nlm.nih.gov/gene/24225 (Accessed March, 20, 2026).

early postnatal period, but we could assume it from the state of chromatin in the brain of OXYS rats. For example, the size of the pyramidal neuron nucleus in the CA1 hippocampal area in OXYS rats decreases starting from the age of five months (Stefanova et al., 2014). Hence, we suggest that the activity of HDACs in the early postnatal period is low. With aging, this activity would increase. This is consistent with the present findings on the enrichment of the *Bdnf* promoter IV in HDAC1 in the amygdala of OXYS rats at the age of five months, when morphological changes in the neuron nuclei appear. Although this regulatory mechanism of gene transcription arises in 5-month-old OXYS rats, it seems to play a minor role at this age as no significant differences were found in the *Bdnf-tr.var.5* levels in the amygdala between OXYS and Wistar rats or under the CEF treatment, which significantly reduced HDAC1 binding to the *Bdnf* promoter IV but did not change *Bdnf-tr.var.5* levels in OXYS rats.

Conclusions

The study of the mechanisms of chromatin remodeling through histone acetylation/deacetylation is of great interest for cognitive and behavioral neuroscience research. Moreover, dysregulation of histone acetylation pathways has been found in the hippocampus and frontal cortex of AD patients (Schueller et al., 2020), while HDAC inhibitors are considered potential drugs in the treatment of AD (Bondarev et al., 2021). Here, we disclosed a novel mechanism of transcription regulation by CEF in the brain related to the inhibition of the HDAC1 enrichment of a gene promoter, which might underlie its neuroprotective activity. However, in 5-month-old OXYS rats, a rat model of sporadic AD, it seems to play a minor role at this age, as CEF treatment significantly reduced HDAC1 binding to *Bdnf* promoter IV but did not change *Bdnf-tr.var.5* (the only *Bdnf* transcript containing exon IV in rats) levels in the amygdala in OXYS rats. We are also the first to demonstrate the transcript-specific regulation of *BDNF* transcription by CEF. CEF significantly increased the levels of *Bdnf*-tr.var.-6 (containing exons VII, VIII, and IX) but not of *Bdnf*-tr.var.-5 in the amygdala of OXYS rats. The results of the study can be taken into account and used in AD treatment and the correction of cognitive deficits in neurodegenerative diseases.

References

Alhaddad H., Alasmari F., Alhamadani B., Wong W., Bell R.L., Sari Y. Effects of chronic ethanol consumption on the expression of GLT-1 and neuroplasticity-related proteins in the nucleus accumbens of alcohol-preferring rats. *Brain Res Bull*. 2020;165:272-280. doi 10.1016/j.brainresbull.2020.10.012

Alsallum M., Kaminskaya Y.P., Tsybko A., Kolosova N., Naumenko V. Patterns of expression of the key genes of the BDNF system and serotonin receptors in the brain of OXYS rats in the development of the signs of Alzheimer's disease. *Adv Gerontol*. 2023;13(2):84-93. doi 10.1134/S207905702360026X

Baj G., Leone E., Chao M.V., Tongiorgi E. Spatial segregation of BDNF transcripts enables BDNF to differentially shape distinct dendritic compartments. *Proc Natl Acad Sci USA*. 2011;108(40):16813-16818. doi 10.1073/pnas.1014168108

Belichenko V.M., Bashirzade A.A., Tenditnik M.V., Dubrovina N.I., Akopyan A.A., Ovsyukova M.V., Fedoseeva L.A., Pupyshev A.B., Aftanas L.I., Amstislavskaya T.G., Tikhonova M.A. Comparative analysis of early neurodegeneration signs in a mouse model of Alzheimer's disease-like pathology induced by two types of the central (Intracerebroventricular vs. Intrahippocampal) administration of $A\beta_{25-35}$ oligomers. *Behav Brain Res*. 2023;454:114651. doi 10.1016/j.bbr.2023.114651

Belyaev N.D., Nalivaeva N.N., Makova N.Z., Turner A.J. Neprilysin gene expression requires binding of the amyloid precursor protein intracellular domain to its promoter: implications for Alzheimer disease. *EMBO Rep*. 2009;10(1):94-100. doi 10.1038/embor.2008.222

Bondarev A.D., Attwood M.M., Jonsson J., Chubarev V.N., Tarasov V.V., Schioth H.B. Recent developments of HDAC inhibitors: Emerging indications and novel molecules. *Br J Clin Pharmacol*. 2021;87(12):4577-4597. doi 10.1111/bcp.14889

Cini N., Atasoy O., Uyanikgil Y., Yaprak G., Erdogan M.A., Erbas O. Ceftriaxone has a neuroprotective effect in a whole-brain irradiation-induced neurotoxicity model by increasing GLT-1 and reducing oxidative stress. *Strahlenther Onkol*. 2025;201(9):903-919. doi 10.1007/s00066-025-02405-z

Cudkowicz M.E., Titus S., Kearney M., Yu H., Sherman A., Schoenfeld D., Hayden D., … Simpson E., Tolkoff-Rubin N., Zinman L., Shefner J.M.; Ceftriaxone Study Investigators. Safety and efficacy of ceftriaxone for amyotrophic lateral sclerosis: a multi-stage, randomised, double-blind, placebo-controlled trial. *Lancet Neurol*. 2014;13(11):1083-1091. doi 10.1016/S1474-4422(14)70222-4

Du Y., Wu H.T., Qin X.Y., Cao C., Liu Y., Cao Z.Z., Cheng Y. Postmortem brain, cerebrospinal fluid, and blood neurotrophic factor levels in Alzheimer's disease: A systematic review and meta-analysis. *J Mol Neurosci*. 2018;65(3):289-300. doi 10.1007/s12031-018-1100-8

Gao R., Ali T., Liu Z., Li A., Hao L., He L., Yu X., Li S. Ceftriaxone averts neuroinflammation and relieves depressive-like behaviors via GLT-1/TrkB signaling. *Biochem Biophys Res Commun*. 2024;701:149550. doi 10.1016/j.bbrc.2024.149550

Ginzinger D.G. Gene quantification using real-time quantitative PCR: an emerging technology hits the mainstream. *Exp Hematol*. 2002;30(6):503-512. doi 10.1016/s0301-472x(02)00806-8

Hammad A.M., Swiss G.M.S., Hall F.S., Hikmat S., Sari Y., Al-Qirim T.M., Amawi H.A. Ceftriaxone reduces waterpipe tobacco smoke withdrawal-induced anxiety in rats via modulating the expression of TNF-α/NFkB, Nrf2, and GLT-1. *Neuroscience*. 2021;463:128-142. doi 10.1016/j.neuroscience.2021.03.030

Hefendehl J.K., LeDue J., Ko R.W., Mahler J., Murphy T.H., MacVicar B.A. Mapping synaptic glutamate transporter dysfunction in vivo to regions surrounding Aβ plaques by iGluSnFR two-photon imaging. *Nat Commun*. 2016;7:13441. doi 10.1038/ncomms13441

Idda M.L., Munk R., Abdelmohsen K., Gorospe M. Noncoding RNAs in Alzheimer's disease. *Wiley Interdiscip Rev RNA*. 2018;9(2):10. doi 10.1002/wrna.1463

Kaur B., Prakash A. Ceftriaxone attenuates glutamate-mediated neuroinflammation and restores BDNF in MPTP model of Parkinson's disease in rats. *Pathophysiology*. 2017;24(2):71-79. doi 10.1016/j.pathophys.2017.02.001

Kumari S., Deshmukh R. β-lactam antibiotics to tame down molecular pathways of Alzheimer's disease. *Eur J Pharmacol*. 2021;895:173877. doi 10.1016/j.ejphar.2021.173877

Kurochkin I.V., Guarnera E., Berezovsky I.N. Insulin-degrading enzyme in the fight against Alzheimer's disease. *Trends Pharmacol Sci*. 2018;39(1):49-58. doi 10.1016/j.tips.2017.10.008

Lee S.G., Su Z.Z., Emdad L., Gupta P., Sarkar D., Borjabad A., Volsky D.J., Fisher P.B. Mechanism of ceftriaxone induction of excitatory amino acid transporter-2 expression and glutamate uptake in primary human astrocytes. *J Biol Chem*. 2008;283(19):13116-13123. doi 10.1074/jbc.M707697200

Nalivaeva N.N., Belyaev N.D., Turner A.J. New insights into epigenetic and pharmacological regulation of amyloid-degrading enzymes. *Neurochem Res*. 2016;41(3):620-630. doi 10.1007/s11064-015-1703-1

Nalivaeva N.N., Zhuravin I.A., Turner A.J. Neprilysin expression and functions in development, ageing and disease. *Mech Ageing Dev*. 2020;192:111363. doi 10.1016/j.mad.2020.111363

Narita M., Nunez S., Heard E., Narita M., Lin A.W., Hearn S.A., Spector D.L., Hannon G.J., Lowe S.W. Rb-mediated heterochromatin formation and silencing of E2F target genes during cellular senescence. *Cell*. 2003;113(6):703-716. doi 10.1016/s0092-8674(03)00401-x

Ng T.K.S., Ho C.S.H., Tam W.W.S., Kua E.H., Ho R.C. Decreased serum brain-derived neurotrophic factor (BDNF) levels in patients with Alzheimer's disease (AD): A systematic review and meta-analysis. *Int J Mol Sci*. 2019;20(2):257. doi 10.3390/ijms20020257

Niedzielska-Andres E., Mizera J., Sadakierska-Chudy A., Pomierny-Chamiolo L., Filip M. Changes in the glutamate biomarker expression in rats vulnerable or resistant to the rewarding effects of cocaine and their reversal by ceftriaxone. *Behav Brain Res*. 2019;370:111945. doi 10.1016/j.bbr.2019.111945

Nikolac Perkovic M., Videtic Paska A., Konjevod M., Kouter K., Svob Strac D., Nedic Erjavec G., Pivac N. Epigenetics of Alzheimer's disease. *Biomolecules*. 2021;11(2):195. doi 10.3390/biom11020195

Palomer E., Martin-Segura A., Baliyan S., Ahmed T., Balschun D., Venero C., Martin M.G., Dotti C.G. Aging triggers a repressive chromatin state at *Bdnf* promoters in hippocampal neurons. *Cell Rep*. 2016;16(11):2889-2900. doi 10.1016/j.celrep.2016.08.028

Poon C.H., Tse L.S.R., Lim L.W. DNA methylation in the pathology of Alzheimer's disease: from gene to cognition. *Ann N Y Acad Sci*. 2020;1475(1):15-33. doi 10.1111/nyas.14373

Ramazi S., Allahverdi A., Zahiri J. Evaluation of post-translational modifications in histone proteins: A review on histone modification defects in developmental and neurological disorders. *J Biosci*. 2020;45(1):135

Rasero J., Alonso-Montes C., Diez I., Olabarrieta-Landa L., Remaki L., Escudero I., Mateos B., Bonifazi P., Fernandez M., Arango-Lasprilla J.C., Stramaglia S., Cortes J.M. Group-level progressive alterations in brain connectivity patterns revealed by diffusion-tensor brain networks across severity stages in Alzheimer's disease. *Front Aging Neurosci*. 2017;9:215. doi 10.3389/fnagi.2017.00215

Ratti E., Berry J.D., Greenblatt D.J., Loci L., Ellrodt A.S., Shefner J.M., Cudkowicz M.E. Preclinical rodent toxicity studies for long term use of ceftriaxone. *Toxicol Rep*. 2015;2:1396-1403. doi 10.1016/j.toxrep.2015.09.010

Rudnitskaya E.A., Kolosova N.G., Stefanova N.A. Impact of changes in neurotrophic supplementation on development of Alzheimer's disease-like pathology in Oxys rats. *Biochemistry* (*Mosc*). 2017;82(3):318-329. doi 10.1134/S0006297917030105

Sada N., Fujita Y., Mizuta N., Ueno M., Furukawa T., Yamashita T. Inhibition of HDAC increases BDNF expression and promotes neuronal rewiring and functional recovery after brain injury. *Cell Death Dis*. 2020;11(8):655. doi 10.1038/s41419-020-02897-w

Schueller E., Paiva I., Blanc F., Wang X.L., Cassel J.C., Boutillier A.L., Bousiges O. Dysregulation of histone acetylation pathways in hippocampus and frontal cortex of Alzheimer's disease patients. *Eur Neuropsychopharmacol*. 2020;33:101-116. doi 10.1016/j.euroneuro.2020.01.015

Shvedunova M., Akhtar A. Modulation of cellular processes by histone and non-histone protein acetylation. *Nat Rev Mol Cell Biol*. 2022;23(5):329-349. doi 10.1038/s41580-021-00441-y

Stefanova N.A., Kozhevnikova O.S., Vitovtov A.O., Maksimova K.Y., Logvinov S.V., Rudnitskaya E.A., Korbolina E.E., Muraleva N.A., Kolosova N.G. Senescence-accelerated OXYS rats: a model of age-related cognitive decline with relevance to abnormalities in Alzheimer disease. *Cell Cycle*. 2014;13(6):898-909. doi 10.4161/cc.28255

Stefanova N.A., Maksimova K.Y., Kiseleva E., Rudnitskaya E.A., Muraleva N.A., Kolosova N.G. Melatonin attenuates impairments of structural hippocampal neuroplasticity in OXYS rats during active progression of Alzheimer's disease-like pathology. *J Pineal Res*. 2015;59(2):163-177. doi 10.1111/jpi.12248

Tikhonova M.A., Ho S.C., Akopyan A.A., Kolosova N.G., Weng J.C., Meng W.Y., Lin C.L., Amstislavskaya T.G., Ho Y.J. Neuroprotective effects of ceftriaxone treatment on cognitive and neuronal deficits in a rat model of accelerated senescence. *Behav Brain Res*. 2017;330:8-16. doi 10.1016/j.bbr.2017.05.002

Tikhonova M.A., Amstislavskaya T.G., Belichenko V.M., Fedoseeva L.A., Kovalenko S.P., Pisareva E.E., Avdeeva A.S., Kolosova N.G., Belyaev N.D., Aftanas L.I. Modulation of the expression of genes related to the system of amyloid-beta metabolism in the brain as a novel mechanism of ceftriaxone neuroprotective properties. *BMC Neurosci*. 2018;19(Suppl. 1):13. doi 10.1186/s12868-018-0412-5

Tikhonova M.A., Amstislavskaya T.G., Ho Y.J., Akopyan A.A., Tenditnik M.V., Ovsyukova M.V., Bashirzade A.A., Dubrovina N.I., Aftanas L.I. Neuroprotective effects of ceftriaxone involve the reduction of Aβ burden and neuroinflammatory response in a mouse model of Alzheimer's disease. *Front Neurosci*. 2021;15:736786. doi 10.3389/fnins.2021.736786

Tran P.V., Kennedy B.C., Lien Y.C., Simmons R.A., Georgieff M.K. Fetal iron deficiency induces chromatin remodeling at the Bdnf locus in adult rat hippocampus. *Am J Physiol Regul Integr Comp Physiol*. 2015;308(4):R276-R282. doi 10.1152/ajpregu.00429.2014

Zhang Y., Chen H., Li R., Sterling K., Song W. Amyloid β-based therapy for Alzheimer's disease: challenges, successes and future. *Signal Transduct Target Ther*. 2023;8(1):248. doi 10.1038/s41392-023-01484-7

Zuccato C., Belyaev N., Conforti P., Ooi L., Tartari M., Papadimou E., MacDonald M., Fossale E., Zeitlin S., Buckley N., Cattaneo E. Widespread disruption of repressor element-1 silencing transcription factor/neuron-restrictive silencer factor occupancy at its target genes in Huntington's disease. *J Neurosci*. 2007;27(26):6972-6983. doi 10.1523/JNEUROSCI.4278-06.2007

Zumkehr J., Rodriguez-Ortiz C.J., Cheng D., Kieu Z., Wai T., Hawkins C., Kilian J., Lim S.L., Medeiros R., Kitazawa M. Ceftriaxone ameliorates tau pathology and cognitive decline via restoration of glial glutamate transporter in a mouse model of Alzheimer's disease. *Neurobiol Aging*. 2015;36(7):2260-2271. doi 10.1016/j.neurobiolaging.2015.04.005

Declaration of competing interest. The authors declare that they have no known competing financial interests or personal relationships that could have appeared to influence the work reported in this paper.

Received October 21, 2025. Revised May 14, 2026. Accepted May 25, 2026.

Vavilovskii Zhurnal Genetiki i Selektsii
Vavilov Journal of Genetics and Breeding. 2026;30(6):908-920

doi 10.18699/vjgb-26-92

The influence of mutant genes *APP* and *PSEN1* on hippocampal asymmetry in 5xFAD mice, transgenic model of Alzheimer disease

E.Yu. Brusentsev [1], I.N. Rozhkova[1], V.S. Kozeneva[1, 2], I.D. Chekashov [1, 2], T.A. Rakhmanova[1, 2], O.B. Shevelev[1], S.Ya. Amstislavsky [1]

[1] Institute of Cytology and Genetics of the Siberian Branch of the Russian Academy of Sciences, Novosibirsk, Russia
[2] Novosibirsk State University, Novosibirsk, Russia
amstis@yandex.ru

Abstract. Alzheimer's disease (AD) is an age-related neurodegenerative pathology and one of the primary causes of dementia associated with memory and cognitive impairment. The dentate gyrus (DG) of the hippocampus plays a crucial role in learning and memory encoding, and it undergoes significant changes in AD. To study the underlying mechanisms of AD and to test new therapeutic agents, mouse models of this pathology are developed. One of the most popular and relevant models for AD research is the 5xFAD transgenic mouse strain carrying mutant human genes, specifically: amyloid beta precursor protein (*APP*) and presenilin-1 (*PSEN1*). The aim of this study was to investigate the influence of mutant *APP* and *PSEN1* transgenes on the microstructure of the hippocampal DG in six-month-old heterozygous male 5xFAD transgenic mice using diffusion tensor magnetic resonance imaging (DTI-MRI) combined with immunohistochemical analysis. A special emphasis was placed on assessing hippocampal asymmetry, which had not been previously investigated in 5xFAD mice. In the hippocampal DG of both hemispheres in male 5xFAD mice, an elevated level of beta-amyloid was detected compared to the wild-type control group, combined with a higher density of microglia, but no differences were found in the level of neurogenesis. Along with this, hippocampal asymmetry was discovered in male 5xFAD mice, manifesting as an increased volume of the right hippocampus, a decreased level of fractional anisotropy in the right hippocampal DG, and a reduced neuron density in the left DG compared to the wild-type. Based on our results, it can be concluded that mutant human *APP* and *PSEN1* genes cause alterations in the hippocampal DG, which may open new possibilities for the early diagnosis of Alzheimer's disease. The identified changes in hippocampal volume and its asymmetry could become important biomarkers characterizing this pathology.

Key words: Alzheimer's disease; 5xFAD transgenic mice; *APP* and *PSEN1* genes; hippocampus; dentate gyrus; diffusion tensor imaging; immunohistochemistry; neuroinflammation; beta-amyloid; neurogenesis

For citation: Brusentsev E.Yu., Rozhkova I.N., Kozeneva V.S., Chekashov I.D., Rakhmanova T.A., Shevelev O.B., Amstislavsky S.Ya. The influence of mutant genes *APP* and *PSEN1* on hippocampal asymmetry in 5xFAD mice, transgenic model of Alzheimer disease. *Vavilovskii Zhurnal Genetiki i Selektsii = Vavilov J Genet Breed*. 2026;30(6):908-920. doi 10.18699/vjgb-26-92

Funding. This work was supported by the Russian Science Foundation (RSF) No. 25-24-00153.

Acknowledgements. The authors thank the Core Facility "Center for Genetic Resources of Laboratory Animals" of the Institute of Cytology and Genetics, SB RAS, and the Institute of Biomedicine of the Faculty of Biomedicine at the Pirogov's Russian National Research Medical University.

Authors' contribution. Conceptualization and experimental design – S.Ya.A., E.Yu.B., I.N.R.; hippocampal assessment – I.N.R., V.S.K., I.D.Ch.; data processing – O.B.Sh., V.S.K., T.A.R., E.Yu.B., S.Ya.A.; writing and editing of the manuscript – S.Ya.A., I.N.R., E.Yu.B., O.B.Sh., V.S.K., I.D.Ch.

Влияние мутантных генов *APP* и *PSEN1* на асимметрию гиппокампа у мышей 5xFAD – трансгенной модели болезни Альцгеймера

Е.Ю. Брусенцев [1], И.Н. Рожкова[1], В.С. Козенева[1, 2], И.Д. Чекашов [1, 2], Т.А. Рахманова[1, 2], О.Б. Шевелев[1], С.Я. Амстиславский [1]

[1] Федеральный исследовательский центр Институт цитологии и генетики Сибирского отделения Российской академии наук, Новосибирск, Россия
[2] Новосибирский национальный исследовательский государственный университет, Новосибирск, Россия
amstis@yandex.ru

© Brusentsev E.Yu., Rozhkova I.N., Kozeneva V.S., Chekashov I.D., Rakhmanova T.A., Shevelev O.B., Amstislavsky S.Ya., 2026
This work is licensed under a Creative Commons Attribution 4.0 License

Аннотация. Болезнь Альцгеймера (БА) – возрастная нейродегенеративная патология, а также одна из главных причин деменции с расстройством памяти и когнитивных функций. Важнейшую роль в процессе обучения и кодирования памяти играет зубчатая извилина гиппокампа (dentate gyrus, DG), которая подвергается существенным изменениям при БА. Для изучения механизмов, лежащих в основе БА, тестирования новых терапевтических средств создают модели этой патологии на мышах. Одной из наиболее популярных и актуальных моделей для исследования БА является трансгенная линия мышей 5xFAD с мутантными генами человека, а именно предшественника бета-амилоида (*APP*) и пресенилина-1 (*PSEN1*). Целью данной работы стало исследование влияния мутантных трансгенов *APP* и *PSEN1* на микроструктуру DG гиппокампа у гетерозиготных самцов мышей трансгенной линии 5xFAD в возрасте 6 месяцев при помощи магнитно-резонансной томографии с диффузионно-тензорной визуализацией в сочетании с иммуногистохимическим анализом. Особый акцент был сделан и на оценке асимметрии гиппокампа, что ранее на мышах 5xFAD не исследовали. В DG гиппокампа обоих полушарий самцов мышей 5xFAD выявлены повышенное содержание бета-амилоида по сравнению с контрольной группой дикого типа в сочетании с более высокой плотностью микроглии, но отсутствие различий по уровню нейрогенеза. Наряду с этим обнаружена асимметрия гиппокампа у самцов мышей 5xFAD, проявляющаяся в увеличении объема правого гиппокампа и снижении уровня фракционной анизотропии в DG правого гиппокампа, а также в уменьшении плотности нейронов в DG с левой стороны по сравнению с диким типом. Исходя из полученных нами результатов, можно сделать заключение, что мутантные гены *APP* и *PSEN1* человека вызывают изменение в DG гиппокампа, что может открыть новые возможности ранней диагностики болезни Альцгеймера. Выявленные нами изменения объема гиппокампа и его асимметрия могут стать важными биомаркерами, характеризующими данную патологию.

Ключевые слова: болезнь Альцгеймера; трансгенные мыши 5xFAD; гены *APP* и *PSEN1*; гиппокамп; зубчатая извилина; диффузионно-тензорная визуализация; иммуногистохимия; нейровоспаление; бета-амилоид; нейрогенез

Introduction

Alzheimer's disease (AD) is an age-related pathology and one of the primary causes of dementia associated with memory and cognitive impairment (Bermejo-Pareja, Del Ser, 2024; Nasb et al., 2024; Perneczky et al., 2024). Human AD is characterized by the abnormal accumulation of extracellular beta-amyloid and intracellular hyperphosphorylated tau protein (Koss et al., 2016; Wang L. et al., 2016; Nasb et al., 2024). Genetic studies have demonstrated that these brain changes, which precede dementia and other symptoms of AD, can be linked to mutations in the gene encoding the amyloid precursor protein (Amyloid Precursor Protein – *APP*) and the gene encoding presenilin-1 (presenilin-1 – *PSEN1*) (De Strooper et al., 2012; Pink et al., 2012; Petit et al., 2022). The formation of beta-amyloid plaques, which begins years before the onset of major clinical symptoms, is considered one of the earliest signs of AD pathology (Bloom, 2014; Bermejo-Pareja, Del Ser, 2024). The accumulation of beta-amyloid, as well as the resulting neuroinflammation in the central nervous system (CNS), serve as important biomarkers both for monitoring the progression of AD (Adlard et al., 2014; Long, Holtzman, 2019; Perneczky et al., 2024) and for tracking the outcomes of therapeutic interventions aimed at mitigating this disease (Perneczky et al., 2024).

Volumetric magnetic resonance imaging (MRI) methods detect functional and structural brain abnormalities, including those in AD patients (Roe et al., 2021; Wang C. et al., 2022; Ai et al., 2025). A characteristic feature of AD is the disruption of white matter fiber integrity in the brain, which may be identified using diffusion tensor magnetic resonance imaging (DTI-MRI) (Rose et al., 2000). The DTI-MRI method is more sensitive compared to volumetric magnetic resonance imaging and is widely used to detect microstructural brain changes, particularly for assessing white matter integrity (Rose et al., 2000; Wang N. et al., 2019; Harrison et al., 2020; Veale et al., 2021).

Previously, using DTI-MRI, a decrease in fractional anisotropy (FA) was detected in certain brain regions of individuals suffering from AD, specifically in the corpus callosum, medial and temporal lobes, fornix, cingulate gyrus, precuneus, and the white matter of the prefrontal cortex (Teipel et al., 2012). Moreover, DTI-MRI has been used to identify microstructural changes in specific subregions of the hippocampus (Beaujoin et al., 2018; Shih et al., 2023). Analysis of these studies confirms that this method is promising for the early detection and monitoring of changes in distinct brain structures during Alzheimer's disease.

To study the mechanisms underlying the development of the pathology and to test pharmaceuticals intended for the treatment of AD, animal models of this disease are applied (Jankowsky, Zheng, 2017; Sasaguri et al., 2017). In particular, one of the most popular models is the 5xFAD transgenic mouse strain (Research Models 5xFAD (C57BL6)), generated at The Jackson Laboratory (USA) on a C57BL/6 background. 5xFAD mice express human *APP* (with mutations: K670N/M671L, I716V, and V717I) and *PSEN1* (with mutations: M146L and L286V) (Oakley et al., 2006; Oblak et al., 2021). Previously, using manganese-enhanced MRI, it was demonstrated that mutant human *APP* and *PSEN1* genes alter regional brain activity in 5xFAD mice (Tang et al., 2016; Nie et al., 2019), while the application of DTI-MRI revealed a longer characteristic path length in weighted structural and functional elements of the connectome at minimum density (Kesler et al., 2018).

Mutant human *APP* and *PSEN1* genes induce various brain abnormalities in transgenic 5xFAD mice depending on the homozygosity/heterozygosity of the strain (Richard et al., 2015). Amyloid precursor protein in pyramidal neurons of homozygous 5xFAD mice is formed as early as 16 days of age, and intraneuronal beta-amyloid accumulates by the age of 1.5 months; however, in heterozygous 5xFAD mice, beta-amyloid is detected at a later age (Richard et al., 2015).

Along with beta-amyloid accumulation, mutant human *APP* and *PSEN1* genes cause abnormalities in the myelin sheaths of brain neurons in transgenic 5xFAD mice, and these pathological changes exacerbate as the animals ageing (Gu et al., 2018). Impairment of nerve fiber myelination, detectable particularly via MRI methods, is a critical marker of AD that manifests in the initial stages of the disease and represents a significant pathophysiological factor of this pathology (Butt et al., 2019; Bermejo-Pareja, Del Ser, 2024).

The hippocampus – a brain region playing a vital role in various processes, including learning, as well as memory formation and consolidation – undergoes substantial structural, morphological, and electrophysiological changes during aging and in neurodegenerative diseases such as Alzheimer's disease (Padurariu et al., 2012; Bartsch, Wulff, 2015). In patients with early symptoms of AD, atrophy of the hippocampal dentate gyrus was identified, indicating the role of this brain structure in the development of this pathology (Hari et al., 2024).

To date, studies investigating the hippocampal dentate gyrus of 5xFAD mice have not accounted for hemispheric asymmetry (Giannoni et al., 2016; Kantarci et al., 2020; Nairuz et al., 2024; Zhu, Liu, 2025). The aim of this study was to investigate the influence of mutant human *APP* and *PSEN1* genes on the microstructure of the dentate gyrus (DG region) of the hippocampus, as well as to evaluate hippocampal asymmetry in heterozygous mice of the 5xFAD transgenic strain using DTI-MRI and immunohistochemistry (IHC).

Materials and methods

Animals. Five male 5xFAD mice (heterozygous mice modeling AD) and five wild-type (WT) males were investigated in the experiment. The animals were housed in the SPF vivarium of the Institute of Cytology and Genetics, SB RAS (Novosibirsk, Russia) in individually ventilated OptiMice cages (AnimalCare, USA) measuring 34.3 × 29.2 × 15.5 cm, at a temperature of 22–24 °C and a humidity of 40–50 %, with an inverted 12:12-hour light-dark cycle (lights on at 3:00 AM); fractional birch chips for laboratory animals (TU 16.10.23-001-0084157135-2019) were used as bedding. The animals had *ad libitum* access to autoclaved standardized chow for laboratory rats and mice "Delta Feeds" LbK 120 R-22, GOST 34566-2019 (BioPro, Russia) and purified water enriched with mineral supplements.

Experimental design. The graphical layout of the experimental design is presented in Figure 1.

Diffusion tensor magnetic resonance imaging. Assessment of brain anatomy, as well as the continuity and density of nerve fibers in the hippocampus of 5xFAD and WT mouse strains, was performed using MRI according to protocols described previously (Naumenko et al., 2018; Lipengolts et al., 2022; Zhang C. et al., 2023). Mice were anesthetized using a mixture of oxygen and isoflurane (98.5/1.5 %) and then placed into the MR scanner on a specialized platform. Prior to scanning, each animal was secured on a custom cradle, after which a respiration sensor was attached to monitor the depth of anesthesia.

Magnetic resonance imaging was performed for 20–30 minutes per animal on a ClinScan 7T experimental scanner for small animals (Bruker BioSpin, Germany) using a volume mouse head coil and the following pulse sequences: 1) fast T1-weighted images based on a gradient echo pulse sequence in three orthogonal planes, repeated at least three times or until correct anatomical sections are obtained through the brain structure for sequential transmission of slices of the main pulse sequences; 2) a diffusion-weighted pulse sequence with b-factors of 0 and 1,200 s/mm^2, 64 diffusion directions, TE = 32 ms, TR = 8,000 ms, 4 averages, voxel size of 0.163542 × 0.163542 × 0.8 mm^3 (FOV = 13 × 15 mm) without an interslice gap, and images with the same resolution at a b-factor of 0 s/mm^2 with a 180-degree phase-encoding gradient reversal; 3) anatomical T2-weighted images with the following parameters: TE = 80 ms, TR = 3,430 ms, ETL = 14, voxel size of 0.083 × 0.083 × 0.8 mm^3 (FOV = 16 × 16 mm) without an interslice gap.

The obtained data processing was performed in the DSI-Studio software package using the following steps: 1) data conversion into the NIfTI (Neuroimaging Informatics Techno-

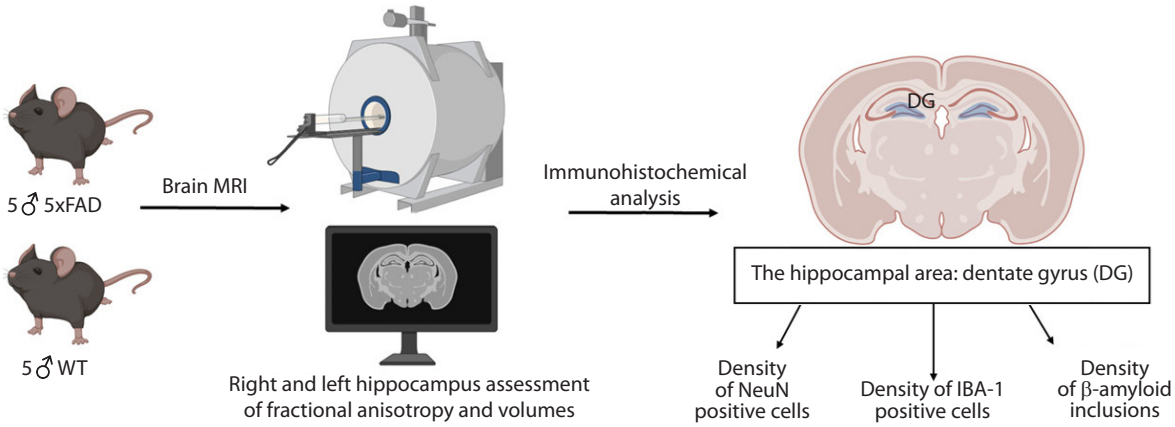


Fig. 1. The graphical layout of the experimental design.
WT – wild type.

logy Initiative) format; 2) TOPUP and EDDY inhomogeneity correction; 3) motion artifact correction; 4) data reconstruction using two methods: Generalized q-sampling imaging – GQI (Yeh et al., 2010) and Q-space diffeomorphic reconstruction – QSDR (Yeh, Tseng, 2011). For GQI, interpolation to an isotropic voxel of 0.1635 and reconstruction with the preservation of the original spatial orientation were performed. For QSDR, spatial orientation alignment of the images and reconstruction to the mouse atlas with an isotropic voxel of 0.1630 were conducted; 5) export of fractional anisotropy (FA) maps; 6) loading the DukeRCCF atlas (Johnson et al., 2022) and maps into a Python script; 7) calculation of the median, first, and third quartiles in target zones of the selected atlas via its registration onto the obtained FA maps using both methods (GQI and QSDR).

Hippocampal volume assessment. The volumes of the right and left parts of the hippocampus were calculated as the sum of the areas of the structures on brain slices obtained from T2-weighted images, multiplied by the slice thickness, using the ImageJ software (Zapara et al., 2018).

Intracardiac perfusion. Perfusion was performed through the circulatory system for brain tissue fixation, as described previously (Rozhkova et al., 2023). Immediately after completion of the MRI, mice were anesthetized with an intramuscular injection of 75 μL (per 10 g of body weight) of medetomidine hydrochloride (Meditin, 1 mg/mL; Api-San, Russia) and 60 μL (per 10 g of body weight) of Zoletil (Virbac, France). Next, 30–50 mL of phosphate-buffered saline (PBS) followed by 30–50 mL of a 10 % formalin solution prepared in PBS were infused through the circulatory system. Thereafter, the brains were harvested and stored in a 30 % sucrose solution prepared in PBS containing 10 % formalin at 4 °C for dehydration and subsequent fixation over the next two weeks until the tissue sank to the bottom of the container. Brain samples were embedded in Tissue-Tek O.C.T. (Sakura Finetek, USA), then frozen and stored at –70 °C.

Preparation of frozen brain slices. In accordance with the atlas coordinates (Paxinos et al., 2012), frozen sections of the left and right hippocampus (including the dentate gyrus – DG) were cut at a distance of –1.46 (–1.82) mm from bregma. Sections with a thickness of 20 μm were prepared at –25 °C using an HM550 OP cryostat (Thermo Scientific, USA) and placed on PCI adhesive-coated microscope slides with ground edges and a colored frosted end (CITOTEST, China).

Immunohistochemical staining. Sample staining was performed according to the manufacturers' kit protocols with minor modifications (Rozhkova et al., 2023). Prior to the staining procedure, sections were dehydrated followed by rehydration for five minutes in PBS. Then, after rehydration, heat-induced epitope retrieval was performed in 10 mM alkaline citrate buffer (pH = 9) at 95 °C in a TW-2.02 water bath (Elmi, Latvia) for 10 min. Following this, the sections were removed from the buffer and cooled to room temperature. The samples were then washed three times in PBS-Tween buffer: PBS supplemented with 0.1 % Tween-20 P9416-100ML (Merck, Germany). Next, ProteinBlock (ab64226; Abcam, UK) was added to each section for 30 min, and excess liquid was subsequently removed in accordance with the manufacturer's recommendation. After that, 50 μL of the primary antibody was added, and the sections were incubated overnight at 4 °C in a humidified dark chamber.

The primary antibody concentrations used were 1:750 for anti-NeuN (ab177487, Abcam, UK), 1:500 for AIF1/IBA1 Rabbit mAb (A19776, ABclonal, Germany), 1:500 for β-Amyloid(1-42) Rabbit mAb (A24422, ABclonal, Germany), and 1:750 for anti-DCX (ab18723, Abcam, UK). Sections were then washed with PBS-Tween buffer, excess liquid was removed, and 50 μL of secondary antibody Goat Anti-Rabbit IgGH & LAF488 (ab150077, Abcam, UK) at a 1:650 dilution was applied. Sections were incubated in a dark humidified chamber for two hours at 4 °C. Following incubation, the samples were washed with PBS-Tween buffer, excess fluid was removed, and sections were mounted on microscope slides in ProLong Glass Antifade Mountant (Thermo P36982, Thermo Fisher Scientific, USA).

To identify cell nuclei, sections stained with AIF1/IBA1 Rabbit mAb and β-Amyloid (1-42) Rabbit mAb were additionally treated with 80 μL of DAPI (Thermo Fisher Scientific, USA) at a concentration of 2 mg/mL, incubated in a dark humidified chamber for 15 minutes, and then washed twice in PBS for 3 min before applying the ProLong Glass Antifade Mountant.

Neuronal density analysis. Analysis of the density of antibody-labeled neurons in the DG region of the hippocampus was performed using a ZEISS AxioImager 2 upright fluorescent microscope (Carl Zeiss, Germany). The average number of antibody-labeled cells in the region of interest was calculated from at least four sections for each animal. Evaluation of the number of granular and DCX-positive cells was carried out in the granular layer of the DG. Beta-amyloid inclusions and IBA1-positive cells were counted simultaneously in two layers of the DG (granular and polymorphic). To evaluate the density of DCX-positive cells, beta-amyloid inclusions, and IBA1-positive cells, a field of view corresponding to the size of the studied area was used; to evaluate the density of NeuN-positive neurons, at least three fields of view (2,000 μm^2) on a single image were used (Zhang L. et al., 2021). ImageJ software was used to create the field of view. The density (millions of cells, $n \times 10^5$) in volume (mm^3) was calculated based on the average number of cells in the region, as described previously (Rozhkova et al., 2023).

Statistical analysis. Data analysis was performed using the STATISTICA v. 12.0 software package (StatSoft, Inc., USA). All data were tested for normality using the Shapiro–Wilk W-test. To evaluate the impact of the "hemispheric asymmetry" factor on the level of fractional anisotropy, hippocampal volumes, as well as the density of neurons, microglia, DCX, and beta-amyloid inclusions in the DG region of the hippocampus, the Wilcoxon signed-rank test was used, followed by pairwise comparisons between groups of different genotypes using the Mann–Whitney U-test. To evaluate the density of neurons, microglia, DCX, and beta-amyloid inclusions, the Kruskal–Wallis H-test was additionally applied for comparison based on the "genotype" factor. Data are presented as median with the first and third quartiles – Me [Q1;Q3]. The level of statistical significance was set at $p < 0.05$.

Results

Data on hippocampal volume are presented in Figure 2. Statistical analysis using the Wilcoxon test showed no effect of the "hemispheric asymmetry" factor [T = 23; $p > 0.05$] on this parameter. Nevertheless, the Mann–Whitney U-test revealed an effect of the "genotype" factor (U = 1; |Z| = 2.30; $p < 0.05$), specifically, a significantly larger hippocampal volume in 5xFAD mice than in WT mice (13.599 [13.583;14.834] *vs.* 12.445 [11.556;12.622] μL^3, respectively) in the right hemisphere of the brain.

Data on FA in the hippocampal DG are presented in Figure 3. The Wilcoxon test showed a significant effect of the "hemispheric asymmetry" factor [T = 2; $p < 0.01$] on FA in the DG region of the hippocampus. Comparison using the Mann–Whitney U-test revealed an effect of the "genotype" factor on the FA level (U = 2; |Z| = 2.09; $p < 0.05$) in the hippocampal DG region; FA was lower on the right side in 5xFAD mice compared to control WT mice (0.106 [0.010;0.115] *vs.* 0.126 [0.124;0.143], respectively) (Fig. 3*a*).

Statistical analysis using the Wilcoxon test demonstrated an effect of the "hemispheric asymmetry" factor [T = 5; $p < 0.05$] on FA in the granular layer of the hippocampal DG region. However, comparison using the Mann-Whitney U-test revealed no effect of the "genotype" factor either for the left hemisphere ([U = 10; |Z| = 0.42; $p > 0.05$]) or for the right hemisphere ([U = 3; |Z| = 1.89; $p > 0.05$]) in the granular layer of the hippocampal DG (Fig. 3*b*). The Wilcoxon test showed no significant effect of the "hemispheric asymmetry" factor [T = 10; $p > 0.05$] on FA in the polymorphic layer of the hippocampal DG region. Comparison using the Mann–Whitney U-test revealed an effect of the "genotype" factor on FA (U = 2; |Z| = 2.09; $p < 0.05$) in the polymorphic layer of the hippocampal DG region on the right side in 5xFAD mice compared to WT (0.096 [0.096;0.098] *vs.* 0.121 [0.116;0.130], respectively) (Fig. 3*c*).

Data on immunohistochemical staining are presented in Figures 4–6. Differences in total neuronal density within the granular layer of the DG are presented in Figure 4. Statistical analysis using the Wilcoxon test revealed no effect of the "hemispheric asymmetry" factor [T = 10; $p > 0.05$] on neuronal density in the granular layer of the DG. Analysis using the Kruskal–Wallis H-test demonstrated an effect of the "genotype" factor [$H_{(1.20)} = 7.20$; $p < 0.01$] on this parameter. Furthermore, comparison using the Mann–Whitney U-test revealed that within the granular layer of the DG in 5xFAD males, neuronal density in the left hemisphere was significantly lower (U = 2.5; |Z| = 1.98; $p < 0.05$) than in WT (10.15 [9.69;10.17] *vs.* 10.95 [10.70;11.21], respectively) (Fig. 4*f*).

Statistical analysis using the Wilcoxon test revealed an effect of the "hemispheric asymmetry" factor [T = 2; $p < 0.01$] on the level of neurogenesis in the granular layer of the DG. However, the Kruskal–Wallis H-test showed no effect of the "genotype" factor [$H_{(1.20)} = 1.46$; $p > 0.05$] on this parameter. Comparison using the Mann–Whitney U-test also revealed no differences ($p > 0.05$) in this parameter between 5xFAD and WT males in the hippocampal dentate gyrus either on the left (0.05 [0.04;0.05] *vs.* 0.05 [0.05;0.06], respectively) or on the right (0.05 [0.04;0.05] *vs.* 0.05 [0.04;0.05], respectively).

The results regarding the density of IBA1-expressing cells in the granular and polymorphic layers of the DG are presented in Figure 5. Statistical analysis using the Wilcoxon test revealed no significant effect of the "hemispheric asymmetry" factor [T = 22; $p > 0.05$] on the density of IBA1-expressing cells. Nevertheless, the Kruskal–Wallis H-test demonstrated an effect of the "genotype" factor [$H_{(1.20)} = 13.50$; $p < 0.001$] on this parameter. Comparison using the Mann–Whitney U-test revealed that within the DG, 5xFAD mice exhibited a higher density of IBA1-positive cells in both the left (U = 0; |Z| = 2.51; $p < 0.05$) and right hemispheres (U = 0; |Z| = 2.51; $p < 0.05$) compared to control WT mice (0.10 [0.10;0.12] *vs.* 0.06 [0.05;0.06] for the left side; 0.11 [0.11;0.11] *vs.* 0.05 [0.04;0.05] for the right side, respectively) (Fig. 5*f*).

Differences in the total density of beta-amyloid inclusions in the granular and polymorphic layers of the DG are presented in Figure 6. Statistical analysis using the Wilcoxon test revealed no effect of the "hemispheric asymmetry" factor [T = 19;

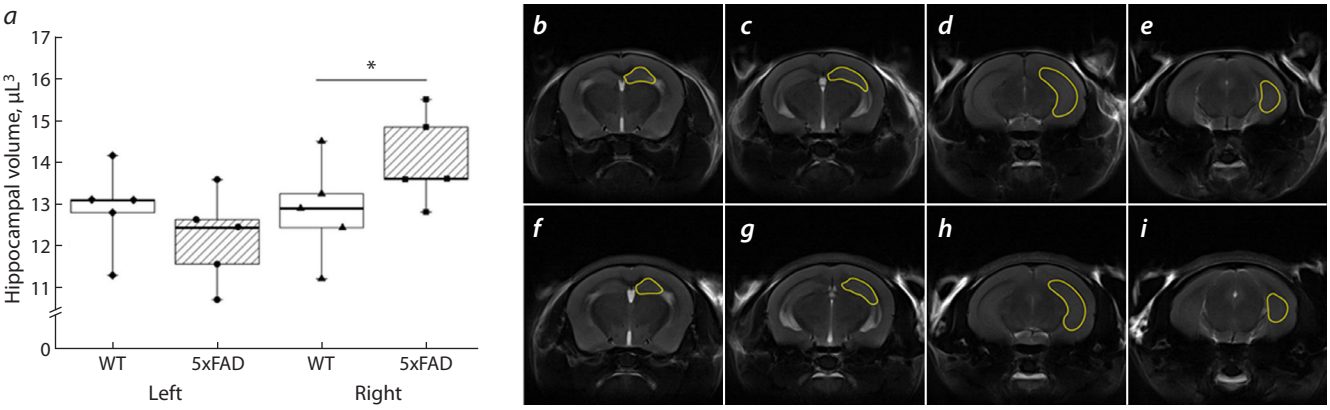


Fig. 2. Hippocampal volume in 5xFAD and WT mouse strains.
a – volumes of the left and right hippocampi of 5xFAD and WT mice; *b–e* – T2-weighted images of hippocampal slices of 5xFAD mice in the right hemisphere of the brain; *f–i* – T2-weighted images of hippocampal slices of WT mice in the right hemisphere of the brain.
* $p < 0.05$ between WT and 5xFAD.

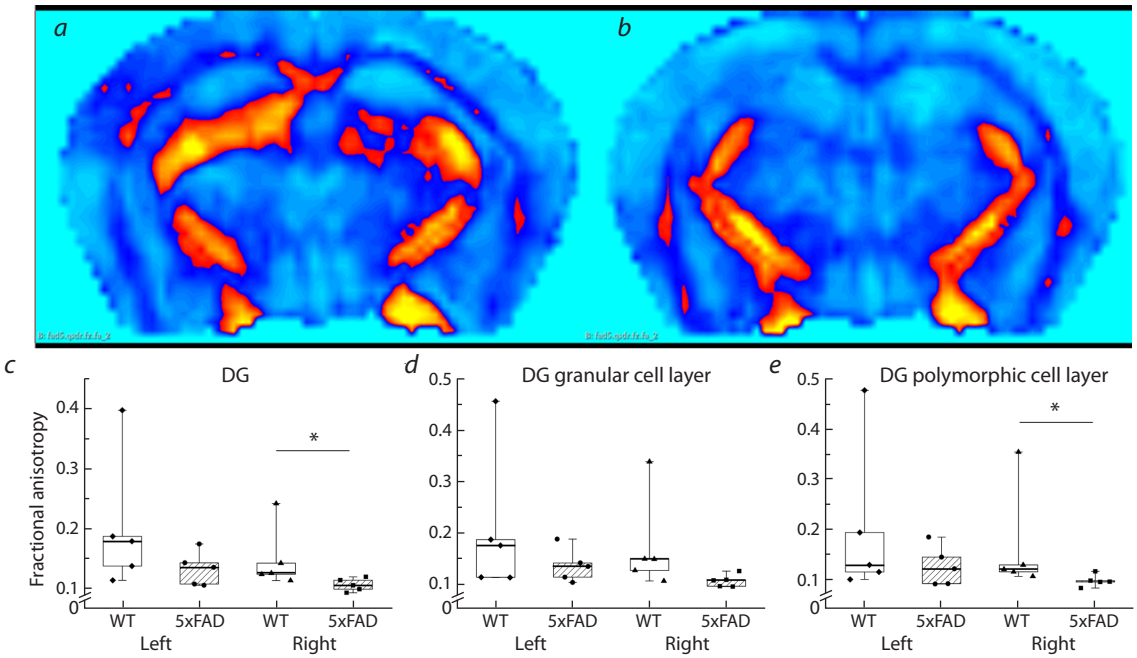


Fig. 3. Fractional anisotropy (FA) levels in the hippocampal DG region of WT (*a*) and 5xFAD (*b*) mouse strains.
c – FA in the DG; *d* – FA in the granular layer of the DG; *e* – FA in the polymorphic layer of the DG.
* $p < 0.05$ between WT and 5xFAD.

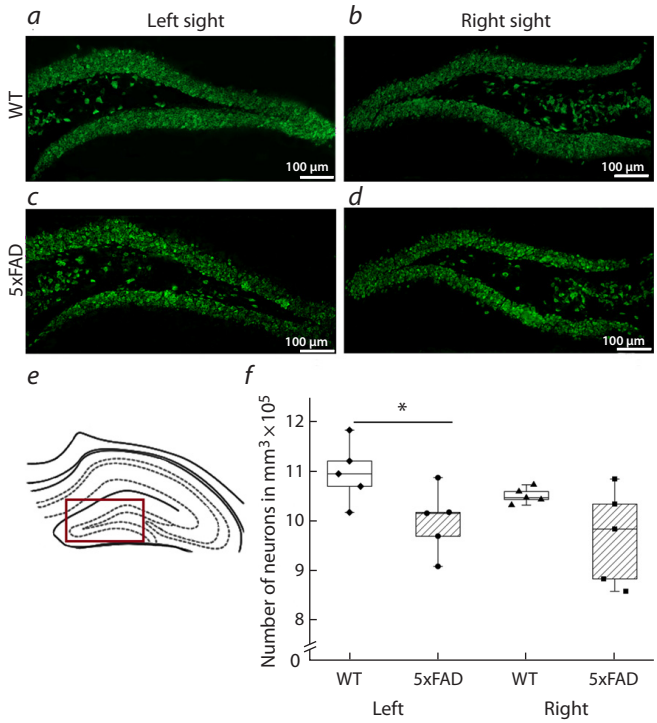


Fig. 4. Neuronal density in the granular layer of the DG; neurons are labeled with antibodies against the neuronal marker (NeuN).
a–d – microphotographs of DG sections; *a* – left hemisphere of the brain of wild-type (WT) males; *b* – right hemisphere of the brain of wild-type (WT) males; *c* – left hemisphere of the brain of 5xFAD males; *d* – right hemisphere of the brain of 5xFAD males; *e* – schematic representation of the studied hippocampal region; *f* – number of neurons per mm³. Magnification 400x.
* $p < 0.05$ between WT and 5xFAD in the left hemisphere of the brain.

$p > 0.05$] on the density of beta-amyloid inclusions in the DG. The Kruskal–Wallis H-test demonstrated an effect of the "genotype" factor [$H_{(1.20)} = 14.28$; $p < 0.001$] on this parameter. Comparison using the Mann–Whitney U-test revealed that in the hippocampal dentate gyrus of 5xFAD mice, the density of beta-amyloid was higher than in the corresponding region of wild-type mice, both on the left ($U = 0$; $|Z| = 2.51$; $p < 0.05$) and on the right ($U = 0$; $|Z| = 2.51$; $p < 0.05$) compared to the corresponding region of wild-type mice (0.12 [0.12;0.13] *vs.* 0.06 [0.05;0.07] for the left side; 0.12 [0.12;0.13] *vs.* 0.05 [0.04;0.07] for the right side, respectively) (Fig. 6*f*).

Discussion

Mutant *APP* and *PSEN1* genes induce beta-amyloid accumulation in the CNS, which is one of the most significant hallmark features of AD (Petit et al., 2022; Nasb et al., 2024; Perneczky et al., 2024). In our study, a substantial increase in beta-amyloid inclusions was detected in the hippocampal dentate gyrus of heterozygous 5xFAD mice carrying mutant human *APP* and *PSEN1* genes in both the right and left hemispheres of the brain, which aligns with the results of previous studies demonstrating elevated beta-amyloid levels in the hippocampal DG of this AD model (Giannoni et al., 2016; Kantarci et al., 2020; Nairuz et al., 2024; Zhu, Liu, 2025).

In particular, a study by T. Nairuz et al. (2024) showed that at 6 and 12 months of age, the density of beta-amyloid inclusions in male 5xFAD mice was significantly increased in the CA1, CA3, and DG regions of the hippocampus. Furthermore, at six months of age, among the three investigated hippocampal subfields, the maximum level of beta-amyloid inclusions was observed precisely in the DG of 5xFAD mice

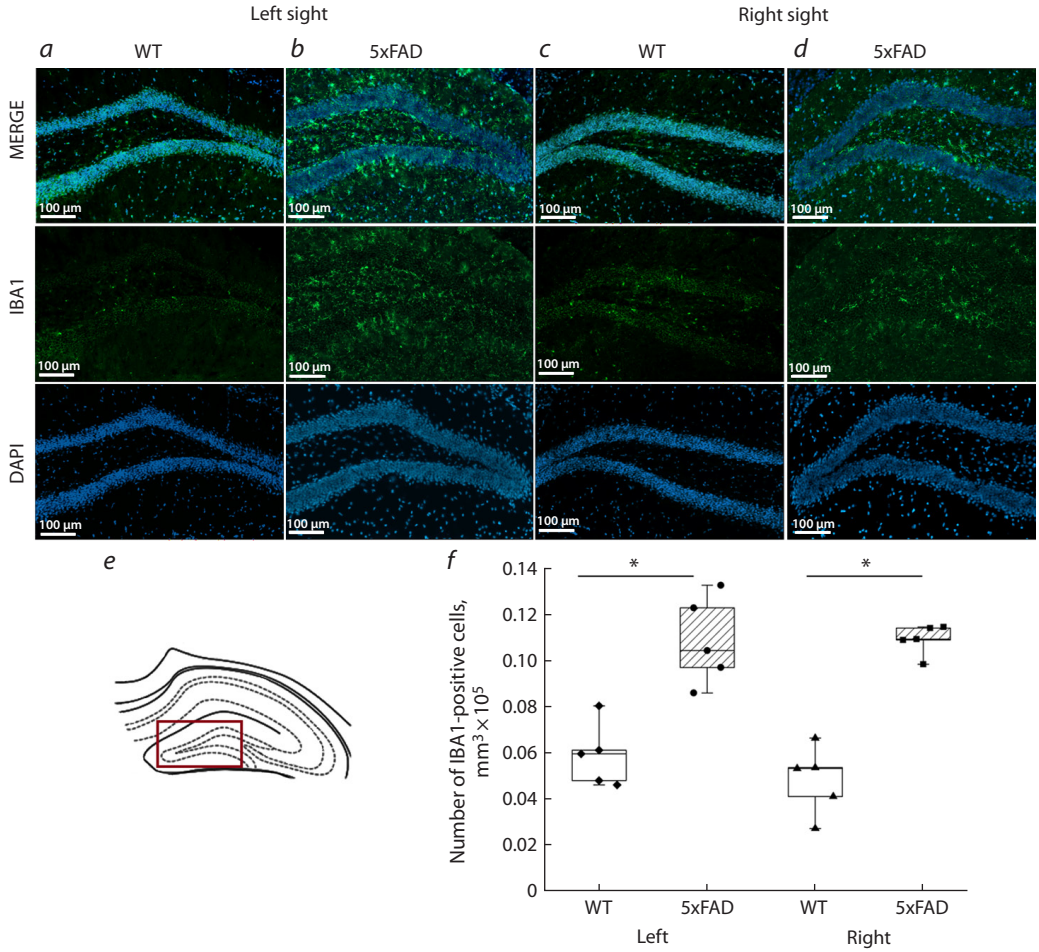


Fig. 5. Microglia density in the DG; cells are labeled with antibodies against IBA1 (ionized calcium-binding adapter molecule 1); cell nuclei are counterstained with DAPI.

a–d – microphotographs of DG sections; *a* – left hemisphere of the brain of wild-type (WT) males; *b* – left hemisphere of the brain of 5xFAD males; *c* – right hemisphere of the brain of wild-type (WT) males; *d* – right hemisphere of the brain of 5xFAD males; *e* – schematic representation of the studied hippocampal region; *f* – number of IBA-1 positive cells per mm³. Magnification 200x.
* $p < 0.05$ between WT and 5xFAD in the left hemisphere of the brain.

compared to control wild-type mice (Nairuz et al., 2024). A recently published study demonstrated that in female 5xFAD mice at an even earlier age of four months, a similar increase in beta-amyloid inclusions was observed in the hippocampal dentate gyrus compared to control wild-type animals (Zhu, Liu, 2025). The accumulation of beta-amyloid in the frontal, parietal, entorhinal cortex, and the hippocampal dentate gyrus of 5xFAD mice is accompanied by blood vessel damage in these brain regions (Giannoni et al., 2016).

Beta-amyloid accumulation can induce neuroinflammation in various brain regions of AD patients (Long, Holtzman, 2019; Perneczky et al., 2024). Microglial cells are activated in response to beta-amyloid accumulation in the brain and cluster around beta-amyloid plaques (Meyer-Luehman et al., 2008).

In our study, a substantial increase in microglia density was detected in both the right and left parts of the hippocampal dentate gyrus in male 5xFAD mice carrying mutant human *APP* and *PSEN1* genes, which aligns with the results of other studies that identified neuroinflammation in the hippocampus of 5xFAD mice starting from two months of age (Oakley et al., 2006; Kantarci et al., 2020; Nairuz et al., 2024; Westi et al., 2024). In particular, at six months of age, the level of neuroinflammation in the hippocampal subiculum of heterozygous 5xFAD mice significantly increases compared to wild-type littermates (Westi et al., 2024). A substantial increase in microglial density at 6–8 months of age is also noted in the hippocampal DG region of 5xFAD mice (Kantarci et al., 2020; Nairuz et al., 2024), which is in good agreement with our findings.

Previously, it was established that neurogenesis impairment occurs in the hippocampal DG region of AD patients (Moreno-Jimenez et al., 2019; Disouky, Lazarov, 2021). However, we did not detect any changes in the level of neurogenesis in the dentate gyrus of 5xFAD mice at six months of age. In studies conducted at 2–4 months of age, a decrease in the level of hippocampal neurogenesis was shown in 5xFAD mice compared to control wild-type animals, as well as its increase during experimental forms of treatment (Moon et al., 2014; Ding et al., 2023; Lee et al., 2025). However, by seven months of age in 5xFAD mice, differences in this parameter compared to

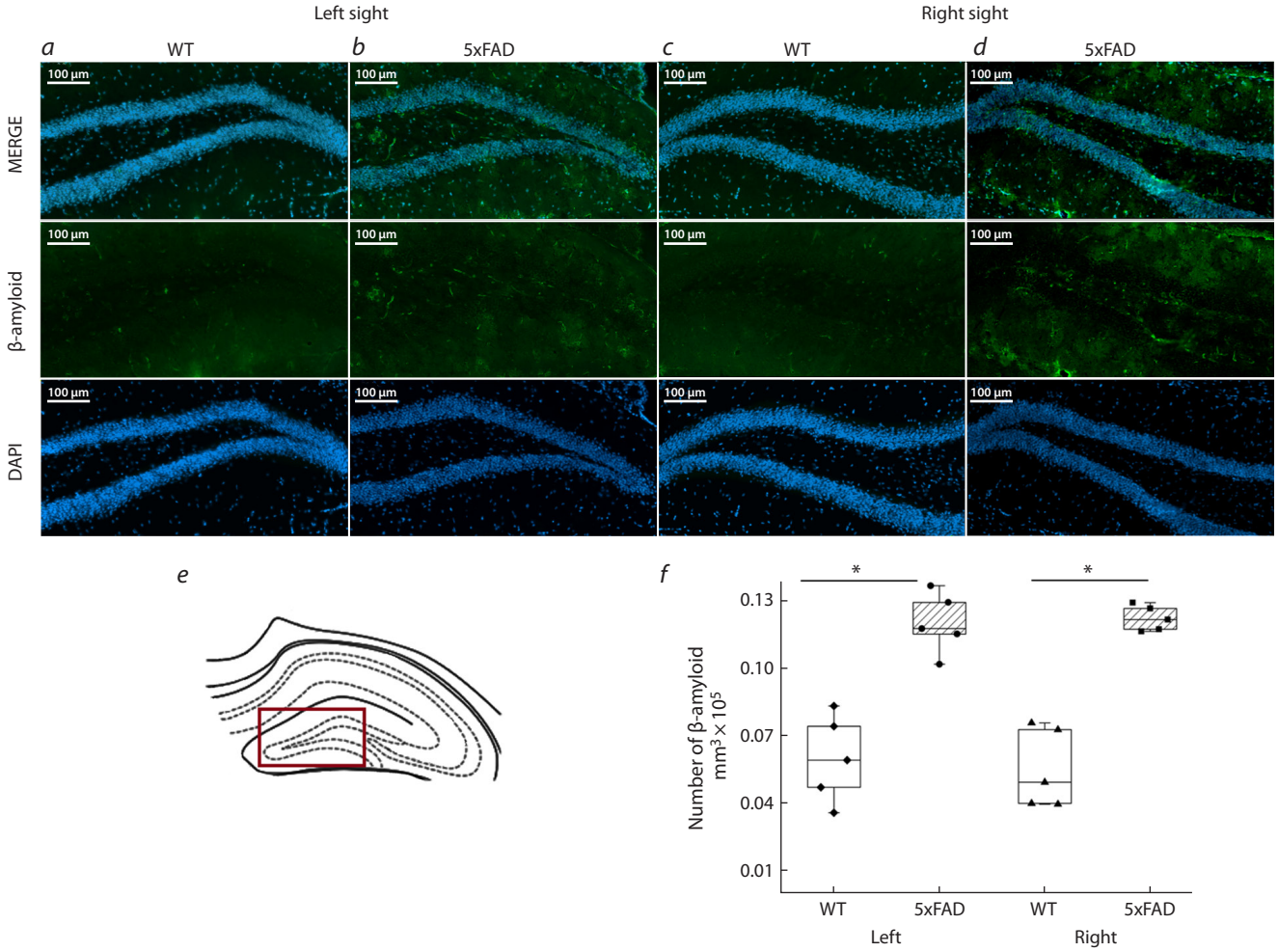


Fig. 6. Density of beta-amyloid inclusions in the DG; beta-amyloid is labeled with antibodies against β-amyloid (1-42); cell nuclei are counterstained with DAPI.

a–d – microphotographs of DG sections; *a* – left hemisphere of the brain of wild-type (WT) males; *b* – left hemisphere of the brain of 5xFAD males; *c* – right hemisphere of the brain of wild-type (WT) males; *d* – right hemisphere of the brain of 5xFAD males; *e* – schematic representation of the studied hippocampal region; *f* – number of beta-amyloid inclusions per mm^3. Magnification 200x.
* $p < 0.05$ between WT and 5xFAD.

wild-type littermates disappeared (Moon et al., 2014), which is possibly associated with a sharp decline in the level of neurogenesis in both 5xFAD mice and control wild-type mice.

Neuronal loss is characteristic of the late stages of AD (Braak H., Braak E., 1991). Meanwhile, neuronal loss in AD is not uniform throughout the brain: the entorhinal cortex and certain subfields of the hippocampus prove to be the most vulnerable (Braak H., Braak E., 1991; Shi et al., 2009; Shih et al., 2023).

Similar changes have also been detected in 5xFAD mice, which exhibited an age-dependent decline in the total number of neurons across various hippocampal zones, specifically CA1, CA3, and the DG (Jawhar et al., 2012; Kim et al., 2019; Zhang L. et al., 2021; Francis et al., 2024). In the present study, it was established that in six-month-old 5xFAD males, there were fewer neurons in the hippocampal DG of the left hemisphere compared to control wild-type animals, whereas no such changes were detected in the DG of the right hemisphere.

The results of previous studies evaluating neuronal density in the hippocampus of 5xFAD mice are ambiguous. At 4.5 months of age, no significant difference from the control is found in the number of neurons within the hippocampal DG of 5xFAD mice (Kim et al., 2019), but a decrease in the number of neurons in this structure is observed at 6–14 months of age (Kim et al., 2019; Zhang L. et al., 2021; Francis et al., 2024).

In modern neurobiology, issues of brain lateralization and asymmetry are actively studied, as they can be crucial for understanding functional differences between the hemispheres and responses to pathology (Francis et al., 2024). The asymmetrical decrease in the number of neurons in the left DG of 5xFAD mice discovered by us is of particular interest, because previous studies aimed at investigating this hippocampal region in this AD model overlooked this factor and evaluated the number of neurons in the DG as a whole, without distinguishing between the right and left hemispheres of the brain (Kim et al., 2019; Zhang L. et al., 2021; Francis et al., 2024).

Atrophy of various hippocampal subfields and the hippocampus as a whole, detected by MRI methods, is an important diagnostic sign of Alzheimer's disease (Shi et al., 2009; Jahanshahi et al., 2023; Hari et al., 2024). In patients with mild cognitive impairment, the volume of left hemisphere structures is typically altered less than that of the right hemisphere (right lateralization), although pronounced forms of AD exhibit a certain reduction in the prominence of right hippocampal lateralization (Shi et al., 2009; Jahanshahi et al., 2023).

In our study, it was revealed that mutant human *APP* and *PSEN1* genes in 5xFAD mice can influence changes in hippocampal volume; the volume of the right hippocampus in 5xFAD mice was larger than that of control wild-type mice. Meanwhile, no differences in hippocampal volume were detected in the left hemisphere.

In studies conducted on 5xFAD mice at 2–6 months of age, no changes in hippocampal volume were found in comparison with control wild-type animals (Girard et al., 2014; Westi et al., 2024). However, at 13 months of age, the hippocampal volume in 5xFAD mice decreased (Macdonald et al., 2014). The authors of the aforementioned studies evaluated the hippocampal volume as a whole, without distinguishing right and left parts and without assessing its individual zones. Meanwhile, our results obtained from 5xFAD mice indicate that measuring hippocampal volume while accounting for asymmetry may serve as a more reliable marker of changes characterizing AD, which aligns with the conclusions of a meta-analysis of clinical data (Shi et al., 2009).

Previously, using DTI-MRI, a decrease in fractional anisotropy was detected in certain brain regions of individuals suffering from AD, specifically in the *corpus callosum*, medial and temporal lobes, fornix, cingulate gyrus, precuneus, and the white matter of the prefrontal cortex (Teipel et al., 2012). The decrease in FA may be associated with an expansion of the extracellular space volume and neurodegeneration (Hong et al., 2013; Nowrangi et al., 2013), and it can indicate that water molecules move not in a single direction, i. e., along axons as they normally should, but more uniformly across the entire area due to nerve fiber damage. The reduction in FA detected via MRI is considered an indicator of beta-amyloid accumulation (Maharjan et al., 2022).

Brain studies in mice using genetic models such as 3xTg and 5xFAD have revealed a decrease in FA in several brain structures (Snow et al., 2017; Maharjan et al., 2022). Changes in FA levels can occur differently depending on the studied brain region, which may be associated with its complex microstructure and heterogeneous accumulation of beta-amyloid, and could also be driven by the associated neuroinflammation (Praet et al., 2018; Maharjan et al., 2022).

In the present study, a decrease in FA was revealed in the hippocampal dentate gyrus of the right hemisphere in male 5xFAD mice compared to control wild-type animals. Our data indicating asymmetry in FA changes in the brain of 5xFAD mice are consistent with the observation that different mouse strains modeling AD have shown asymmetry in the development of this pathology between the hemispheres regarding changes in the levels of beta-amyloid accumulation and neuroinflammation levels (Biechele et al., 2021; Shipton et al., 2022; Morrissey et al., 2023).

Previously, no FA impairments were found in the hippocampus of 5xFAD mice (Maharjan et al., 2022). However, in that study, FA was evaluated within the hippocampus as a whole without distinguishing the left and right hemispheres and without subdividing it into regions. Our data indicate that evaluating FA in specific hippocampal regions, in the DG particularly, can be a more sensitive indicator of AD-characteristic brain impairments. Moreover, it is necessary to account for the asymmetry of the right and left hemispheres regarding this feature. Nevertheless, it must be acknowledged that the small sample size in the present study imposes limitations on the interpretation of the results and requires verification in larger cohorts.

The hippocampus is a critical brain structure where various types of impairments occur in AD (Moreno-Jimenez et al., 2019; Disouky, Lazarov, 2021; Zeng et al., 2021; Jahanshahi et al., 2023; Shih et al., 2023). The functional anatomy of hippocampal subfields, as well as the role of each subfield in the storage and processing of visual and verbal information, episodic memory, navigation, and object recognition, has been studied in detail (Bartsch, Wulff, 2015; Zammit et al., 2017; Pang et al., 2019; Zeng et al., 2021). Meanwhile, it has been shown that during the progression of AD, the rate and extent of impairments differ significantly across different hippocampal subfields (Padurariu et al., 2012; Bartsch, Wulff, 2015). It has been suggested that alterations in individual hippocampal regions may serve as a more precise marker for AD than changes evaluated in the hippocampus as a whole without subfield distinguishing (Zilioli et al., 2025).

The DG plays a special role in the neural processes underlying learning and memory; information encoding processes occur within this structure, and it receives input and output signals from various hippocampal regions (CA1–CA4) and the neocortex (Amaral et al., 2007; Jonas, Lisman, 2014; Bartsch, Wulff, 2015; Jahanshahi et al., 2023; Shih et al., 2023). Adult neurogenesis in humans occurs within the dentate gyrus, continuing into old age but becoming impaired as AD progressed (Moreno-Jimenez et al., 2019), which makes the hippocampal dentate gyrus of particular interest in AD research (Shih et al., 2023).

In the present study, six-month-old heterozygous male 5xFAD mice carrying mutant human *APP* and *PSEN1* genes demonstrated a hemispheric asymmetry against a background of overall elevated beta-amyloid levels and neuroinflammation, alongside an unchanged level of neurogenesis in the hippocampal DG of both hemispheres. This asymmetry manifested as a difference in hippocampal volume between the right and left hemispheres, a decrease in FA within the right DG, and a reduction in neuronal density within the left DG.

Several studies have noted an asymmetry in the progression of features characteristic of AD between the brain hemispheres, particularly in the cortex (Derflinger et al., 2011; Roe et al., 2021), thalamus (McGeown et al., 2008), and hippocampus (Shi et al., 2009; Jahanshahi et al., 2023). Using volumetric MRI and subsequent analysis of T1-weighted images in AD

patients, changes in the hippocampal asymmetry index (the ratio of right-to-left hippocampal volumes) were observed, with alterations being more pronounced on the right side than on the left in several of its subfields (Jahanshahi et al., 2023).

Previously, it was established that under normal conditions, mice and rats exhibit a pronounced structural and functional left-right asymmetry of the hippocampus (El-Gaby et al., 2015; Sakaguchi, Sakurai, 2020), which could also influence the differing levels of AD progression between hemispheres in male 5xFAD mice. M. El-Gaby et al. (2015) point out in their review that the hippocampi of the left and right hemispheres possess distinct functional lateralization, and they analyze the mechanisms underlying this asymmetry. The left hippocampus specializes in associative long-term memory, while the right specializes in spatial orientation. Such functional differentiation is achieved through structural differences at the synaptic level (El-Gaby et al., 2015).

In our study, the hippocampal asymmetry revealed for the first time in 5xFAD mice with mutant human APP and PSEN1 genes, in particular the difference in hippocampal volume between the right and left hemispheres of the brain, may be associated with the accumulation of beta-amyloid in the DG observed in 5xFAD mice and the resulting increase in neuroinflammation on both sides, combined with a reduction in neuronal density only in the DG of the left hippocampus. It is possible that in male 5xFAD mice, the volume of the left hippocampus does not differ from the wild type because the reduction in the number of neurons within its DG is counterbalanced by the overall increase in the density of beta-amyloid plaques and microglia, whereas the right hippocampus expanded due to the preservation of cell density and, potentially, an expansion of the extracellular space associated with neuroinflammation. A second hypothesis is that the hippocampal volume in both the right and left hemispheres could have been larger at an earlier age in male 5xFAD mice, than in control WT mice due to early beta-amyloid accumulation and subsequent neuroinflammation; however, the later decrease in the number of neurons within the left DG eliminated the difference with control animals specifically on the left side.

Some studies revealed an asymmetry in the development of pathological changes characteristic for AD between the brain hemispheres, particularly in the cortex (Derflinger et al., 2011; Roe et al., 2021), thalamus (McGeown et al., 2008), and hippocampus (Shi et al., 2009; Jahanshahi et al., 2023). Previously, it was hypothesized that during the progression of AD, the rate of atrophy across different regions of the right and left hippocampi may differ (Shi et al., 2009). The results of our study support this hypothesis.

Conclusion

Based on our findings and the analysis of literature data, we believe that mutant human *APP* and *PSEN1* genes induce alterations in the dentate gyrus (DG region) of the hippocampus, and evaluating the microstructure of this brain area may serve as an indicator of AD-characteristic impairments and in the future might be used for the early diagnosis of AD (Shih et al., 2023). In particular, the changes in hippocampal volume and its asymmetry identified in our study could become a useful biomarker for AD diagnosis.

Compliance with ethical standards. All studies were approved by the Bioethics Commission of the Institute of Cytology and Genetics SB RAS (Protocol No. 215 dated February 25, 2025) and comply with the European Convention for the Protection of Vertebrate Animals used for Experimental and Other Scientific Purposes (ETS No. 123).

References

Adlard P.A., Tran B.A., Finkelstein D.I., Desmond P.M., Johnston L.A., Bush A.I., Egan G.F. A review of β-amyloid neuroimaging in Alzheimer's disease. *Front Neurosci*. 2014;8:327. doi 10.3389/fnins.2014.00327

Ai M., Liu Y., Liu D., Yan C., Wang X., Chen X. Research progress in predicting the conversion from mild cognitive impairment to Alzheimer's disease via multimodal MRI and artificial intelligence. *Front Neurol*. 2025;16:1596632. doi 10.3389/fneur.2025.1596632

Amaral D.G., Scharfman H.E., Lavenex P. The dentate gyrus: fundamental neuroanatomical organization (dentate gyrus for dummies). *Prog Brain Res*. 2007;163:3-22. doi 10.1016/S0079-6123(07)63001-5

Bartsch T., Wulff P. The hippocampus in aging and disease: from plasticity to vulnerability. *Neuroscience.* 2015;309:1-16. doi 10.1016/j.neuroscience.2015.07.084

Beaujoin J., Palomero-Gallagher N., Boumezbeur F., Axer M., Bernard J., Poupon F., Schmitz D., Mangin J.F., Poupon C. Post-mortem inference of the human hippocampal connectivity and microstructure using ultra-high field diffusion MRI at 11.7 T. *Brain Struct Funct*. 2018;223(5):2157-2179. doi 10.1007/s00429-018-1617-1

Bermejo-Pareja F., Del Ser T. Controversial past, splendid present, unpredictable future: a brief review of Alzheimer disease history. *J Clin Med*. 2024;13:536. doi 10.3390/jcm13020536

Biechele G., Wind K., Blume T., Sacher C., Beyer L., Eckenweber F., Franzmeier N., … Bartenstein P., Cumming P., Rominger A., Herms J., Brendel M. Microglial activation in the right amygdala-entorhinal-hippocampal complex is associated with preserved spatial learning in $App^{NL\text{-}G\text{-}F}$ mice. *NeuroImage*. 2021;230:117707. doi 10.1016/j.neuroimage.2020.117707

Bloom G.S. Amyloid-β and tau: the trigger and bullet in Alzheimer disease pathogenesis. *JAMA Neurol*. 2014;71(4):505-508. doi 10.1001/jamaneurol.2013.5847

Braak H., Braak E. Neuropathological stageing of Alzheimer-related changes. *Acta Neuropathol*. 1991;82:239-259. doi 10.1007/BF00308809

Butt A.M., De La Rocha I., Rivera A. Oligodendroglial cells in Alzheimer's disease. In: Verkhratsky A., Ho M., Zorec R., Parpura V. (Eds) Neuroglia in Neurodegenerative Diseases. Advances in Experimental Medicine and Biology. Vol. 1175. Springer, 2019;325-333. doi 10.1007/978-981-13-9913-8_12

De Strooper B., Iwatsubo T., Wolfe M.S. Presenilins and γ-secretase: structure, function, and role in Alzheimer disease. *Cold Spring Harb Perspect Med*. 2012;2(1):a006304. doi 10.1101/cshperspect.a006304

Derflinger S., Sorg C., Gaser C., Myers N., Arsic M., Kurz A., Zimmer C., Wohlschlager A., Muhlau M. Grey-matter atrophy in Alzheimer's disease is asymmetric but not lateralized. *J Alzheimers Dis*. 2011;25(2):347-357. doi 10.3233/JAD-2011-110041

Ding Y., Li L., Wang S., Cao Y., Yang M., Dai Y., Lin H., Li J., Liu Y., Wang Z., Liu W., Tao J. Electroacupuncture promotes neurogenesis in the dentate gyrus and improves pattern separation in an early Alzheimer's disease mouse model. *Biol Res*. 2023;56:65. doi 10.1186/s40659-023-00472-z

Disouky A., Lazarov O. Adult hippocampal neurogenesis in Alzheimer's disease. *Prog Mol Biol Transl Sci*. 2021;177:137-156. doi 10.1016/bs.pmbts.2020.09.002

El-Gaby M., Shipton O.A., Paulsen O. Synaptic plasticity and memory: new insights from hippocampal left-right asymmetries. *Neuroscientist*. 2015;21(5):490-502. doi 10.1177/1073858414550658

Francis J.S., Nguyen Q., Markov V., Leone P. Over-expression of N-acetylaspartate synthase exacerbates pathological energetic deficit and accelerates cognitive decline in the 5xFAD mouse. *J Neurochem*. 2024;168(2):69-82. doi 10.1111/jnc.16044

Giannoni P., Arango-Lievano M., Neves I.D., Rousset M.C., Baranger K., Rivera S., Jeanneteau F., Claeysen S., Marchi N. Cerebrovascular pathology during the progression of experimental Alzheimer's disease. *Neurobiol Dis*. 2016;88:107-117. doi 10.1016/j.nbd.2016.01.001

Girard S., Jacquet M., Baranger K., Migliorati M., Escoffier G., Bernard A., Khrestchatisky M., Feron F., Rivera S., Roman F., Marchetti1 E. Onset of hippocampus-dependent memory impairments in 5xFAD transgenic mouse model of Alzheimer's disease. *Hippocampus*. 2014;24(7):762-772. doi 10.1002/hipo.22267

Gu L., Wu D., Tang X., Qi X., Li X., Bai F., Chen X., Ren Q., Zhang Z. Myelin changes at the early stage of 5xFAD mice. *Brain Res Bull*. 2018;137:285-293. doi 10.1016/j.brainresbull.2017.12.013

Hari I., Adeyemi O.F., Gowland P., Bowtell R., Mougin O., Vesey P., Shah J., Mukaetova-Ladinska E.B., Hosseini A.A. Memory impairment in Amyloidβ-status Alzheimer's disease is associated with a reduction in CA1 and dentate gyrus volume: *in vivo* MRI at 7T. *NeuroImage*. 2024;292:120607. doi 10.1016/j.neuroimage.2024.120607

Harrison J.R., Bhatia S., Tan Z.X., Mirza-Davies A., Benkert H., Tax C.M.W., Jones D.K. Imaging Alzheimer's genetic risk using diffusion MRI: a systematic review. *NeuroImage Clin*. 2020;27:102359. doi 10.1016/j.nicl.2020.102359

Hong Y.J., Yoon B., Lim S.C., Shim Y.S., Kim J.Y., Ahn K.J., Han I.W., Yang D.W. Microstructural changes in the hippocampus and posterior cingulate in mild cognitive impairment and Alzheimer's disease: a diffusion tensor imaging study. *Neurol Sci*. 2013;34(7):1215-1221. doi 10.1007/s10072-012-1225-4

Jahanshahi A.R., Naghdi Sadeh R., Khezerloo D. Atrophy asymmetry in hippocampal subfields in patients with Alzheimer's disease and mild cognitive impairment. *Exp Brain Res*. 2023;241:495-504. doi 10.1007/s00221-022-06543-z

Jankowsky J.L., Zheng H. Practical considerations for choosing a mouse model of Alzheimer's disease. *Mol Neurodegener*. 2017;12(1):89. doi 10.1186/s13024-017-0231-7

Jawhar S., Trawicka A., Jenneckens C., Bayer T.A., Wirths O. Motor deficits, neuron loss, and reduced anxiety coinciding with axonal degeneration and intraneuronal Aβ aggregation in the 5xFAD mouse model of Alzheimer's disease. *Neurobiol Aging*. 2012;33:196.e29-196.e40. doi 10.1016/j.neurobiolaging.2010.05.027

Johnson G.A., Tian Y., Cofer G.P., Cook J.C., Gee J.C., Hall A., Hornburg K., Qi Y., Yeh F.-C., Wang N., White L.E., Williams R.W. HiDiver: a suite of methods to merge magnetic resonance histology, light sheet microscopy, and complete brain delineations. *bioRxiv*. 2022. doi 10.1101/2022.02.10.479607

Jonas P., Lisman J. Structure, function, and plasticity of hippocampal dentate gyrus microcircuits. *Front Neural Circuits*. 2014;8:107. doi 10.3389/fncir.2014.00107

Kantarci A., Tognoni C.M., Yaghmoor W., Marghalani A., Stephens D., Ahn J.Y., Carreras I., Dedeoglu A. Microglial response to experimental periodontitis in a murine model of Alzheimer's disease. *Sci Rep*. 2020;10:18561. doi 10.1038/s41598-020-75517-4

Kesler S.R., Acton P., Rao V., Ray W.J. Functional and structural connectome properties in the 5xFAD transgenic mouse model of Alzheimer's disease. *Netw Neurosci*. 2018;2(2):241-258. doi 10.1162/netn_a_00048

Kim S., Nam Y., Jeong Y.O., Park H.H., Lee S.K., Shin S.J., Jung H., … Yu J., Yoo D.H., Park S.H., Jeon S.G., Moon M. Topographical visualization of the reciprocal projection between the medial septum and the hippocampus in the 5xFAD mouse model of Alzheimer's disease. *Int J Mol Sci*. 2019;20:3992. doi 10.3390/ijms20163992

Koss D.J., Jones G., Cranston A., Gardner H., Kanaan N.M., Platt B. Soluble pre-fibrillar tau and β-amyloid species emerge in early human Alzheimer's disease and track disease progression and cognitive decline. *Acta Neuropathol*. 2016;132:875-895. doi 10.1007/s00401-016-1632-3

Lee H., Hossain M.K., Lee H.Y., Kumar V., Shin S.J., Kim B.H., Park H.H., Son J.G., Moon M., Kim H.R. Taurine suppresses Aβ aggregation and attenuates Alzheimer's disease pathologies in 5xFAD mice and patient-derived cerebral organoids. *Biomed Pharmacother*. 2025;191:118527. doi 10.1016/j.biopha.2025.118527

Lipengolts A.A., Finogenova Y.A., Skribitsky V.A., Shpakova K.E., Anaki A., Motiei M., Semkina A.S., Abakumov M.A., Smirnova A.V., Grigorieva E.Y., Popovtzer R. CT and MRI imaging of theranostic bimodal Fe3O4@Au NanoParticles in tumor bearing mice. *Int J Mol Sci*. 2022;24:70. doi 10.3390/ijms24010070

Long J.M., Holtzman D.M. Alzheimer disease: an update on pathobiology and treatment strategies. *Cell*. 2019;179:312-339. doi 10.1016/j.cell.2019.09.001

Macdonald I.R., DeBay D.R., Reid G.A., O'Leary T.P., Jollymore C.T., Mawko G., Burrell S., Martin E., Bowen C.V., Brown R.E., Darvesh S. Early detection of cerebral glucose uptake changes in the 5xFAD mouse. *Curr Alzheimer Res*. 2014;11(5):450-460. doi 10.2174/1567205011666140505111354

Maharjan S., Tsai A.P., Lin P.B., Ingraham C., Jewett M.R., Landreth G.E., Oblak A.L., Wang N. Age-dependent microstructure alterations in 5xFAD mice by high-resolution diffusion tensor imaging. *Front Neurosci*. 2022;16:964654. doi 10.3389/fnins.2022.964654

McGeown W.J., Shanks M.F., Venneri A. Prolonged cholinergic enrichment influences regional cortical activation in early Alzheimer's disease. *Neuropsychiatr Dis Treat*. 2008;4(2):465-476. doi 10.2147/ndt.s2461

Meyer-Luehmann M., Spires-Jones T.L., Prada C., Garcia-Alloza M., de Calignon A., Rozkalne A., Koenigsknecht-Talboo J., Holtzman D.M., Bacskai B.J., Hyman B.T. Rapid appearance and local toxicity of amyloid-beta plaques in a mouse model of Alzheimer's disease. *Nature*. 2008;451(7179):720-724. doi 10.1038/nature06616

Moon M., Cha M.Y., Mook-Jung I. Impaired hippocampal neurogenesis and its enhancement with ghrelin in 5xFAD mice. *J Alzheimers Dis*. 2014;41(1):233-241. doi 10.3233/JAD-132417

Moreno-Jimenez E.P., Flor-Garcia M., Terreros-Roncal J., Rabano A., Cafini F., Pallas-Bazarra N., Avila J., Llorens-Martin M. Adult hippocampal neurogenesis is abundant in neurologically healthy subjects and drops sharply in patients with Alzheimer's disease. *Nat Med*. 2019;25(4):554-560. doi 10.1038/s41591-019-0375-9

Morrissey Z.D., Gao J., Zhan L., Li W., Fortel I., Saido T., Saito T., Bakker A., Mackin S., Ajilore O., Lazarov O., Leow A.D. Hippocampal functional connectivity across age in an App knock-in mouse model of Alzheimer's disease. *Front Aging Neurosci*. 2023;14:1085989. doi 10.3389/fnagi.2022.1085989

Nairuz T., Heo J.C., Lee J.H. Differential glial response and neurodegenerative patterns in CA1, CA3, and DG hippocampal regions of 5xFAD mice. *Int J Mol Sci*. 2024;25(22):12156. doi 10.3390/ijms252212156

Nasb M., Tao W., Chen N. Alzheimer's disease puzzle: delving into pathogenesis hypotheses. *Aging Dis*. 2024;15:43-73. doi 10.14336/AD.2023.0608

Naumenko V., Garanina A., Nikitin A., Vodopyanov S., Vorobyeva N., Tsareva Y., Kunin M., Ilyasov A., Semkina A., Chekhonin V., Abakumov M., Majouga A. Biodistribution and tumors MRI contrast enhancement of magnetic nanocubes, nanoclusters, and nanorods in multiple mice models. *Contrast Media Mol Imaging*. 2018;2018:8264208. doi 10.1155/2018/8264208

Nie B., Wu D., Liang S., Liu H., Sun X., Li P., Huang Q., Zhang T., Feng T., Ye S., Zhang Z., Shan B. A stereotaxic MRI template set of mouse brain with fine sub-anatomical delineations: application to MEMRI studies of 5xFAD mice. *Magn Reson Imaging*. 2019;57:83-94. doi 10.1016/j.mri.2018.10.014

Nowrangi M.A., Lyketsos C.G., Leoutsakos J.M., Oishi K., Albert M., Mori S., Mielke M.M. Longitudinal, region-specific course of diffusion tensor imaging measures in mild cognitive impairment and Alzheimer's disease. *Alzheimers Dement*. 2013;9(5):519-528. doi 10.1016/j.jalz.2012.05.2186

Oakley H., Cole S.L., Logan S., Maus E., Shao P., Craft J., Guillozet-Bongaarts A., Ohno M., Disterhoft J., Van Eldik L., Berry R., Vassar R. Intraneuronal beta-amyloid aggregates, neurodegeneration, and neuron loss in transgenic mice with five familial Alzheimer's disease mutations: potential factors in amyloid plaque formation. *J Neurosci*. 2006;26(40):10129-10140. doi 10.1523/JNEUROSCI.1202-06.2006

Oblak A.L., Lin P.B., Kotredes K.P., Pandey R.S., Garceau D., Williams H.M., Uyar A., … Territo P.R., Carter G.W., Howell G.R., Sasner M., Lamb B.T. Comprehensive evaluation of the 5xFAD mouse model for preclinical testing applications: a MODEL-AD study. *Front Aging Neurosci*. 2021;13:713726. doi 10.3389/fnagi.2021.713726

Padurariu M., Ciobica A., Mavroudis I., Fotiou D., Baloyannis S. Hippocampal neuronal loss in the CA1 and CA3 areas of Alzheimer's disease patients. *Psychiatr Danub*. 2012;24(2):152-158

Pang C.C., Kiecker C., O'Brien J.T., Noble W., Chang R.C. Ammon's horn 2 (CA2) of the hippocampus: a long-known region with a new potential role in neurodegeneration. *Neuroscientist*. 2019;25(2):167-180. doi 10.1177/1073858418778747

Paxinos G., Franklin K. Mouse Brain in Stereotaxic Coordinates. Academic Press, 2012

Perneczky R., Dom G., Chan A., Falkai P., Bassetti C. Anti-amyloid antibody treatments for Alzheimer's disease. *Eur J Neurol*. 2024;31:e16049. doi 10.1111/ene.16049

Petit D., Fernandez S.G., Zoltowska K.M., Enzlein T., Ryan N.S., O'Connor A., Szaruga M., Hill E., Vandenberghe R., Fox N.C., Chavez-Gutiérrez L. Aβ profiles generated by Alzheimer's disease causing *PSEN1* variants determine the pathogenicity of the mutation and predict age at disease onset. *Mol Psychiatry*. 2022;27(6):2821-2832. doi 10.1038/s41380-022-01518-6

Pink A.E., Simpson M.A., Desai N., Dafou D., Hills A., Mortimer P., Smith C.H., Trembath R.C., Barker J.N.W. Mutations in the γ-secretase genes *NCSTN*, *PSENEN*, and *PSEN1* underlie rare forms of hidradenitis suppurativa (acne inversa). *J Invest Dermatol*. 2012;132(10):2459-2461. doi 10.1038/jid.2012.162

Praet J., Manyakov N.V., Muchene L., Mai Z., Terzopoulos V., de Backer S., Torremans A., … Bijnens L., Pemberton D.J., Schmidt M.E., Van der Linden A., Verhoye M. Diffusion kurtosis imaging allows the early detection and longitudinal follow-up of amyloid-β-induced pathology. *Alzheimers Res Ther*. 2018;10(1):1. doi 10.1186/s13195-017-0329-8

Research Models 5xFAD (C57BL6) [Database]. URL: https://www.alzforum.org/research-models/5xfad-c57bl6

Richard B.C., Kurdakova A., Baches S., Bayer T.A., Weggen S., Wirths O. Gene dosage dependent aggravation of the neurological phenotype in the 5XFAD mouse model of Alzheimer's disease. *J Alzheimers Dis*. 2015;45(4):1223-1236. doi 10.3233/JAD-143120

Roe J.M., Vidal-Piñeiro D., Sørensen Ø., Brandmaier A.M., Düzel S., Gonzalez H.A., Kievit R.A., … Rundle M.M., Walhovd K.B., Fjell A.M., Westerhausen R.; Australian Imaging Biomarkers and Lifestyle Flagship Study of Ageing. Asymmetric thinning of the cerebral cortex across the adult lifespan is accelerated in Alzheimer's disease. *Nat Commun*. 2021;12(1):721. doi 10.1038/s41467-021-21057-y (Erratum in: *Nat Commun*. 2022;13(1):834. doi 10.1038/s41467-022-28514-2)

Rose S.E., Chen F., Chalk J.B., Zelaya F.O., Strugnell W.E., Benson M., Semple J., Doddrell D.M. Loss of connectivity in Alzheimer's disease: an evaluation of white matter tract integrity with colour coded MR diffusion tensor imaging. *J Neurol Neurosurg Psychiatry*. 2000;69(4):528-530. doi 10.1136/jnnp.69.4.528

Rozhkova I.N., Okotrub S.V., Brusentsev E.Yu., Uldanova K.E., Chuyko E.A., Naprimerov V.A., Lipina T.V., Amstislavskaya T.G., Amstislavsky S.Ya. Alterations in the social-conditioned place preference and density of dopaminergic neurons in the ventral tegmental area in Clsnt2-KO mice. *Vavilovskii Zhurnal Genetiki i Selektsii = Vavilov J Genet Breed*. 2023;27(2):177-184. doi 10.18699/VJGB-23-14

Sakaguchi Y., Sakurai Y. Left-right functional difference of the rat dorsal hippocampus for short-term memory and long-term memory. *Behav Brain Res*. 2020;382:112478. doi 10.1016/j.bbr.2020.112478

Sasaguri H., Nilsson P., Hashimoto S., Nagata K., Saito T., De Strooper B., Hardy J., Vassar R., Winblad B., Saido T.C. APP mouse models for Alzheimer's disease preclinical studies. *EMBO J*. 2017;36(17):2473-2487. doi 10.15252/embj.201797397

Shi F., Liu B., Zhou Y., Yu C., Jiang T. Hippocampal volume and asymmetry in mild cognitive impairment and Alzheimer's disease: meta-analyses of MRI studies. *Hippocampus*. 2009;19:1055-1064. doi 10.1002/hipo.20573

Shih N.C., Kurniawan N.D., Cabeen R.P., Korobkova L., Wong E., Chui H.C., Clark K.A., Miller C.A., Hawes D., Jones K.T., Sepehrband F. Microstructural mapping of dentate gyrus pathology in Alzheimer's disease: a 16.4 Tesla MRI study. *NeuroImage Clin*. 2023;37:103318. doi 10.1016/j.nicl.2023.103318

Shipton O.A., Tang C.S., Paulsen O., Vargas-Caballero M. Differential vulnerability of hippocampal CA3-CA1 synapses to Aβ. *Acta Neuropathol Commun*. 2022;10:45. doi 10.1186/s40478-022-01350-7

Snow W.M., Dale R., O'Brien-Moran Z., Buist R., Peirson D., Martin M., Albensi B.C. *In vivo* detection of gray matter neuropathology in the 3xTg mouse model of Alzheimer's disease with diffusion tensor imaging. *J Alzheimers Dis*. 2017;58(3):841-853. doi 10.3233/JAD-170136

Tang X., Wu D., Gu L.H., Nie B.B., Qi X.Y., Wang Y.J., Wu F.F., Li X.L., Bai F., Chen X.C., Xu L., Ren Q.G., Zhang Z.J. Spatial learning and memory impairments are associated with increased neuronal activity in 5xFAD mouse as measured by manganese-enhanced magnetic resonance imaging. *Oncotarget*. 2016;7(36):57556-57570. doi 10.18632/oncotarget.11353

Teipel S.J., Wegrzyn M., Meindl T., Frisoni G., Bokde A.L., Fellgiebel A., Filippi M., Hampel H., Kloppel S., Hauenstein K., Ewers M.; EDSD study group. Anatomical MRI and DTI in the diagnosis of Alzheimer's disease: a European multicenter study. *J Alzheimers Dis*. 2012;31:33-47. doi 10.3233/JAD-2012-112118

Veale T., Malone I.B., Poole T., Parker T.D., Slattery C.F., Paterson R.W., Foulkes A.J.M., Thomas D.L., Schott J.M., Zhang H., Fox N.C., Cash D.M. Loss and dispersion of superficial white matter in Alzheimer's disease: a diffusion MRI study. *Brain Commun*. 2021;3:fcab272. doi 10.1093/braincomms/fcab272

Wang C., Wei Y., Li J., Li X., Liu Y., Hu Q., Wang Y.; Alzheimer's Disease Neuroimaging Initiative. Asymmetry-enhanced attention network for Alzheimer's diagnosis with structural Magnetic Resonance Imaging. *Comput Biol Med*. 2022;151:106282. doi 10.1016/j.compbiomed.2022.106282

Wang L., Benzinger T.L., Su Y., Christensen J., Friedrichsen K., Aldea P., McConathy J., Cairns N.J., Fagan A.M., Morris J.C., Ances B.M. Evaluation of Tau imaging in staging Alzheimer disease and revealing interactions between β-amyloid and tauopathy. *JAMA Neurol*. 2016;73(9):1070-1077. doi 10.1001/jamaneurol.2016.2078

Wang N., Zhuang J., Wei H., Dibb R., Qi Y., Liu C. Probing demyelination and remyelination of the cuprizone mouse model using multimodality MRI. *J Magn Reson Imaging*. 2019;50(6):1852-1865. doi 10.1002/jmri.26758

Westi E.W., Molhemi S., Hansen C.T., Skoven C.S., Knopper R.W., Ahmad D.A., Rindshøj M.B., Ameen A.O., Hansen B., Kohlmeier K.A., Aldana B.I. Comprehensive analysis of the 5xFAD mouse model of Alzheimer's disease using dMRI, immunohistochemistry, and neuronal and glial functional metabolic mapping. *Biomolecules*. 2024;14:1294. doi 10.3390/biom14101294

Yeh F.C., Tseng W.Y. NTU-90: a high angular resolution brain atlas constructed by q-space diffeomorphic reconstruction. *NeuroImage*. 2011;58:91-99. doi 10.1016/j.neuroimage.2011.06.021

Yeh F.C., Wedeen V.J., Tseng W.Y. Generalized *q*-sampling imaging. *IEEE Trans Med Imaging*. 2010;29(9):1626-1635. doi 10.1109/TMI.2010.2045126

Zammit A.R., Ezzati A., Zimmerman M.E., Lipton R.B., Lipton M.L., Katz M.J. Roles of hippocampal subfields in verbal and visual episodic memory. *Behav Brain Res*. 2017;317:157-162. doi 10.1016/j.bbr.2016.09.038

Zapara T.A., Romashchenko A.V., Proskura A.L., Ratushnyak A.S. Effect of physical activity on structural asymmetry of mouse hippocampus. *Vavilovskii Zhurnal Genetiki i Selektsii = Vavilov J Genet Breed*. 2018;22(8):1084-1089. doi 10.18699/VJ18.454 (in Russian)

Zeng Q., Li K., Luo X., Wang S., Xu X., Li Z., Zhang T., … Liu Z., Chen Y., Huang P., Zhang M.; The Alzheimer's Disease Neuroimaging Initiative. Distinct atrophy pattern of hippocampal subfields in patients with progressive and stable mild cognitive impairment: a longitudinal MRI study. *J Alzheimers Dis*. 2021;79(1):237-247. doi 10.3233/JAD-200775

Zhang C., Morozova A.Y., Abakumov M.A., Mel'nikov P.A., Gabashvili A.N., Chekhonin V.P. Evaluation of the optimal number of implanted mesenchymal stem cells for the treatment of post-traumatic syrinx and recovery of motor activity after chronic spinal cord injury. *Bull Exp Biol Med*. 2023;175(4):557-568. doi 10.1007/s10517-023-05904-0

Zhang L., Li J., Lin A. Assessment of neurodegeneration and neuronal loss in aged 5xFAD mice. *STAR Protoc*. 2021;2(4):100915. doi 10.1016/j.xpro.2021.100915

Zhu C., Liu X. Behavioral and pathological characteristics of 5xFAD female mice in the early stage. *Sci Rep*. 2025;15(1):6924. doi 10.1038/s41598-025-90335-2

Zilioli A., Pancaldi B., Baumeister H., Busi G., Misirocchi F., Mutti C., Florindo I., Morelli N., Mohanty R., Berron D., Westman E., Spallazzi M. Unveiling the hippocampal subfield changes across the Alzheimer's disease continuum: a systematic review of neuroimaging studies. *Brain Imaging Behav*. 2025;19(1):253-267. doi 10.1007/s11682-024-00952-0

Conflict of interest. The authors declare no conflict of interest.

Received October 31, 2025. Revised May 13, 2026. Accepted May 14, 2026.

Vavilovskii Zhurnal Genetiki i Selektsii
Vavilov Journal of Genetics and Breeding. 2026;30(6):921-937

doi 10.18699/vjgb-26-93

Assessment of taxonomic and genetic diversity of wood mice of the genus *Apodemus* in the steppe zone of the Central Ciscaucasia

F.A. Tembotova, A.Kh. Amshokova, M.S. Gudova, E.P. Kononenko

Tembotov Institute of Ecology of Mountain Territories of the Russian Academy of Sciences, Nalchik, Russia
mpapieva@inbox.ru

Abstract. Steppe ecosystems are among the most heavily modified habitats due to anthropogenic pressure and rapid land-use changes. Over the course of several decades of the 20th century, the biogeocenoses of the steppe plains and a significant portion of the forest-steppe of the Central Ciscaucasia have almost completely lost their original appearance. Anthropogenic impact resulted in the reduction of suitable habitats, their fragmentation, and so on. It is known that prolonged isolation of a population, caused by natural or anthropogenic habitat fragmentation, can lead to changes in the genetic structure of the population, specifically to a decrease in genetic diversity and a reduction in the total effective population size, which is particularly detrimental to small populations. The relevance of this study is due to the lack of current data on the species composition, genetic structure, genetic diversity, habitat distribution, and abundance of *Apodemus* wood mice in the steppe zone of the Central Ciscaucasia. Based on an analysis of the mitochondrial DNA *cytochrome b* (*cyt b*) gene fragment variability, the species composition and genetic diversity of sibling species of wood mice of the genus *Apodemus* have been studied for the first time in the steppe zone of the Central Ciscaucasia. Molecular genetic analysis revealed that the genus *Apodemus* is represented by three species: *A. uralensis*, *A. witherbyi*, and *A. flavicollis*. *A. flavicollis* and *A. witherbyi* are described for the first time in this area. Of the three taxa, *A. uralensis* exhibits the highest level of genetic diversity. Molecular dating results suggest that of the three species, *A. uralensis* was the first to colonize the Central Ciscaucasia in two stages: approximately 370–350 thousand years ago and approximately 256 thousand years ago. Subsequently, *A. witherbyi* entered the area in two stages: approximately 166–154 thousand years ago and 125–115 thousand years ago. *A. flavicollis* is the youngest inhabitant of the Central Ciscaucasia, with an evolutionary age of approximately 100 thousand years. This study identifies the distribution patterns and landscape-biotopic distribution of representatives of the genus *Apodemus* in the study areas of the Central Ciscaucasia.

Key words: Central Ciscaucasia; steppe zone; *cytochrome b*; genus *Apodemus*; genetic diversity

For citation: Tembotova F.A., Amshokova A.Kh., Gudova M.S., Kononenko E.P. Assessment of taxonomic and genetic diversity of wood mice of the genus *Apodemus* in the steppe zone of the Central Ciscaucasia. *Vavilovskii Zhurnal Genetiki i Selektsii = Vavilov J Genet Breed*. 2026;30(6):921-937. doi 10.18699/vjgb-26-93

Funding. This work was carried out under the state assignment program of the Tembotov Institute of Ecology of Mountain Territories of the Russian Academy of Sciences (FMEU-2026-0001: "Vertebrate diversity (genetic, morphological, taxonomic) as a basis for the long-term monitoring of natural and anthropogenic ecosystems").

Оценка таксономического и генетического разнообразия лесных мышей рода *Apodemus* степной зоны Центрального Предкавказья

Ф.А. Темботова, А.Х. Амшокова, М.С. Гудова, Е.П. Кононенко

Институт экологии горных территорий им. А.К. Темботова Российской академии наук, Нальчик, Россия
mpapieva@inbox.ru

Аннотация. Степные экосистемы – одни из наиболее измененных местообитаний из-за антропогенного давления и быстрых изменений в землепользовании. За несколько десятилетий XX в. биогеоценозы степных равнин и значительной части лесостепи Центрального Предкавказья почти полностью утратили свой первоначальный облик. Результатом антропогенного воздействия являются сокращение пригодных местообитаний, их фрагментация и т. д. При этом известно, что длительная изоляция популяции, вызванная естественной или антропогенной фрагментацией среды обитания, может привести к изменению генетической структуры популяции, в частности к уменьшению генетического разнообразия и сокращению общей эффективной численности

© Tembotova F.A., Amshokova A.Kh., Gudova M.S., Kononenko E.P., 2026
This work is licensed under a Creative Commons Attribution 4.0 License

популяции, что особенно губительно для популяции небольшого размера. Актуальность проведения настоящего исследования связана с отсутствием современных данных, касающихся видового состава, генетической структуры, генетического разнообразия, биотопического распространения и численности представителей лесных мышей рода *Apodemus* в условиях степной зоны Центрального Предкавказья. На основании анализа изменчивости фрагмента гена цитохрома *b* (*cyt b*) митохондриальной ДНК впервые изучены видовой состав и генетическое разнообразие видов-двойников лесных мышей рода *Apodemus* в условиях степной зоны Центрального Предкавказья. По результатам молекулярно-генетического анализа род *Apodemus* представлен тремя видами: *A. uralensis*, *A. witherbyi* и *A. flavicollis*. На рассматриваемой территории *A. flavicollis* и *A. witherbyi* описаны впервые. Из трех таксонов наиболее высоким уровнем генетического разнообразия характеризуется *A. uralensis*. Результаты молекулярного датирования позволяют предположить, что из трех видов первым заселил территорию Центрального Предкавказья *A. uralensis* в два этапа: примерно 370–350 тыс. лет назад и около 256 тыс. лет назад. Позднее на данную территорию в два этапа проник *A. witherbyi*: примерно 166–154 тыс. лет назад и 125–115 тыс. лет назад. *A. flavicollis* является самым молодым вселенцем на Центральном Предкавказье. Его эволюционный возраст составляет примерно 100 тыс. лет. В работе приведены особенности распространения и ландшафтно-биотопического распределения представителей рода *Apodemus* на исследованных территориях Центрального Предкавказья.

Ключевые слова: Центральное Предкавказье; степная зона; цитохром *b*; род *Apodemus*; генетическое разнообразие

Introduction

The study of genetic differentiation and phylogeography of widespread species is important for the study of modern biodiversity, the formation of species ranges, the consequences of global climate change and anthropogenic impacts, and issues of biological expansion and invasion (Yalkovskaya et al., 2022). Genetic diversity is considered one of the many important factors determining species adaptation to changing environmental conditions (Soulé, Simberloff, 1986). The higher the genetic diversity of species living in both undisturbed and highly disturbed environments, the more successful the adaptation, the more capable the populations are of evolving in response to the pressure of external environmental factors and the less likely they are to disappear if environmental conditions change (cited in Poliakova, 2022).

Currently, due to anthropogenic pressure and rapid land-use changes, steppe ecosystems are among the most heavily modified habitats. As S.I. Sigida (2010) rightly notes, as a result of human impact, the biogeocenoses of the steppe plains and a significant portion of the forest-steppe of the Central Ciscaucasia have almost completely lost their original appearance over the course of several decades of the 20th century. The planting of shelterbelts, artificial forests, irrigation, and water supply facilitated the expansion of forest and aquatic animal groups into the steppe regions, as well as the emergence of migrants from neighboring regions (cited in Pushkin, 2015). Clearly, such changes impact the species diversity of steppe ecosystems.

It should also be noted that anthropogenic impact results in the reduction of suitable habitats, their fragmentation, etc. Also, as is known, long-term isolation of a population caused by natural or anthropogenic fragmentation of the habitat can lead to a change in the genetic structure of the population, in particular, to a decrease in genetic diversity and a reduction in the total effective population size (Radespiel, Bruford, 2014; Wang et al., 2017).

The relevance of this study stems from the lack of modern data on the species composition of members of the genus *Apodemus* in the steppe zone of the Central Ciscaucasia, obtained through molecular genetic analysis. Existing studies were conducted before the advent of these methods in the second half of the 20th century (Tembotov, 1972). It should be noted that cryptic species, which include members of the genus *Apodemus*, are virtually indistinguishable based on morphological characteristics. Incorrect identification of biologically important species creates false perceptions of biological diversity (Sukhikh, 2013).

It is also important to note that for some representatives of the genus *Apodemus*, genetic data are represented by single sequences of the *cytochrome b* (*cyt b*) gene of mtDNA. For example, only 18 sequences of the Caucasian wood mouse have been deposited in the international genetic database GenBank, some of which are from Iran. Regarding *Apodemus witherbyi* Thomas, 1902, the 26 *cyt b* gene sequences submitted come only from Ukraine and Iran. As can be seen, sequences from the study area are missing from the GenBank database.

In light of the above, it was of interest to study the species composition, genetic structure, and genetic diversity of members of the genus *Apodemus* in the steppe zone of the Central Ciscaucasia. The selection of members of the genus *Apodemus* was deliberate: firstly, they constitute a significant proportion of the catches; secondly, they represent species with diverse ecological preferences, which can be found in both natural (untouched virgin steppe areas, intrazonal forests) and anthropogenically transformed landscapes (haystacks in row crop fields, canal banks, shelterbelts, etc.).

Materials and methods

Tissue samples from 153 *Apodemus* wood mice collected from various locations in the steppe zone of the Central Ciscaucasia were used in the work.

The study was conducted in the Maysky, Prokhladnensky, and Tersky districts of the Kabardino-Balkarian Republic (KBR) (Fig. 1). In the Maysky district, the study covered biotopes in the vicinity of three settlements (Novoivanovka village, khutor Baksansky, and khutor Novokursky). Due to

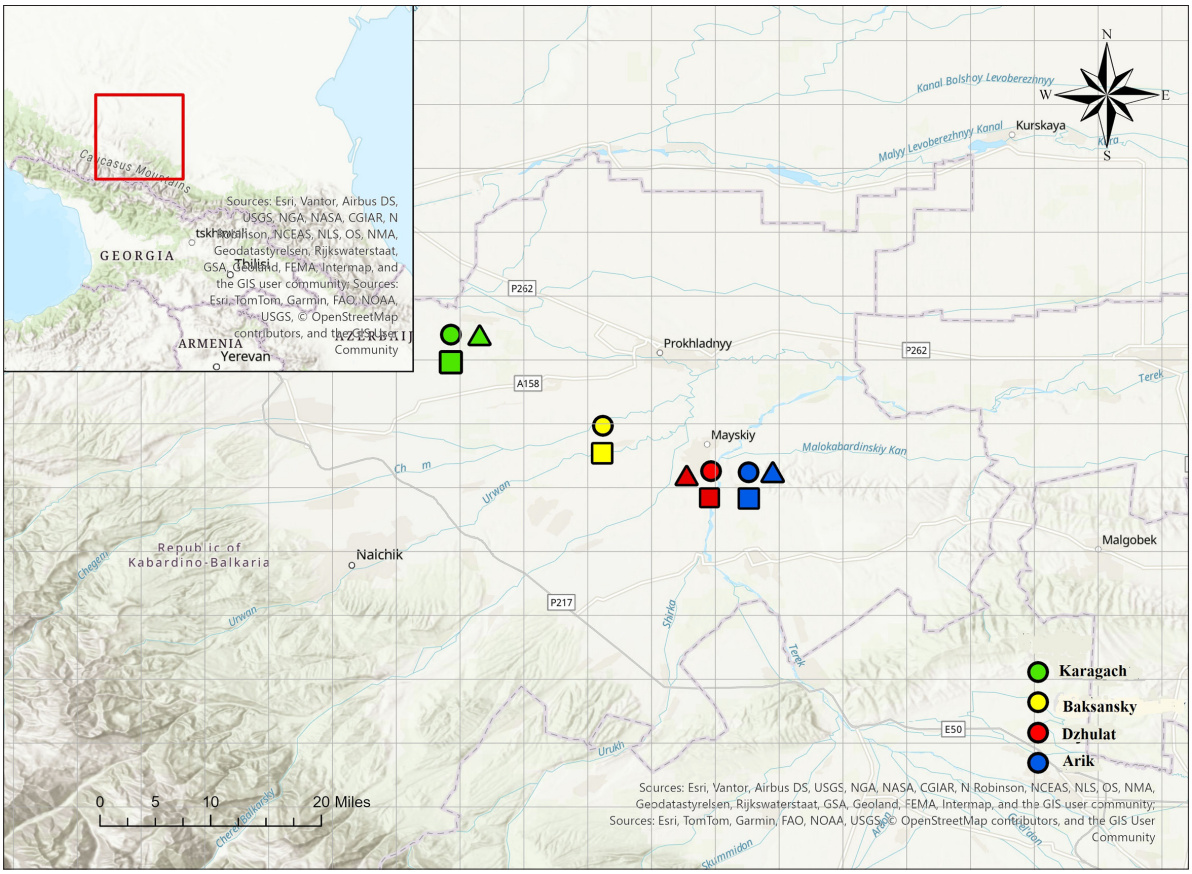


Fig. 1. Map of the origin of the material of representatives of the genus *Apodemus* from the steppe zone of the Central Ciscaucasia: circles – *Apodemus uralensis* Pallas, 1811, squares – *Apodemus flavicollis* Melchior, 1834, triangles – *Apodemus witherbyi* Thomas, 1902.

their proximity, we considered it appropriate to combine them, and this area is designated as khutor Baksansky (N 43.6640° E 043.9362°, h – 224 m above sea level) in this study.

The material was collected in three biotopes: 1. Forest shelterbelts; 2. Haystacks located in winter crop fields; 3. A boundary directly adjacent to irrigation canals, located between agricultural crop fields.

In the Prokhladnensky district, in the vicinity of the Karagach village (N 43.7838° E 43.7369°, h – 290 m above sea level), the research covered two biotopes: 1. Lowland forest; 2. Meadow located between the road and the agrocenosis. In the Tersky district, the material was collected at two geographical points: in the vicinity of the Dzhulat village (N 43.6050° E 44.0077°, h – 215 m above sea level) – two biotopes: 1. Virgin steppe areas unsuitable for agricultural cultivation; 2. Lowland forest; and in the vicinity of the Arik village (Arik ridge N 43.6036° E 44.1268°, h – 233 m above sea level) – three biotopes: 1. Steppe area: undisturbed forb-fescue community on the slope of the ridge; 2. Shelterbelt; 3. Bank of the Small Kabardian irrigation canal.

Tissue samples were fixed in 96 % ethanol and used for manual DNA extraction using the Diatom™ DNA Prep 100 reagent kit (Isogen Laboratory, Moscow) according to the manufacturer's instructions. Amplification of the *cyt b* gene was performed by polymerase chain reaction (PCR), using primers from (Yasuda et al., 2005) with the PCR cycle parameters recommended in the cited work. The resulting PCR products were purified by reprecipitation in 0.15 M sodium acetate in 90 % ethanol, followed by washing with 70 % ethanol. The result was visualized by electrophoresis in 1.5 % agarose gel in the presence of ethidium bromide. Sequencing of nucleotide sequences was performed in both directions at Syntol (Moscow).

Alignment of the obtained sequences was performed using the ClustalW module in the BioEdit software package (Hall, 1999). Weighted (net distance) intergroup genetic distances using the Kimura two-parameter model (K2P) (Kimura, 1980) were calculated in the Mega 6 program (Tamura et al., 2013).

The Bayesian algorithm was implemented in MrBayes v3.2.6 using the Markov chain Monte Carlo (MCMC) algorithm (Ronquist, Huelsenbeck, 2003). The Bayesian information criterion (BIC) was used to find optimal models. Nucleotide substitution models were selected using Mega 6. The analysis generated 5×10^6 Markov chain trees, with tree selection performed every 1,000 generations. The first 25 % were discarded as "burnout". Phylogenetic trees were visualized using FigTree.

To estimate the divergence time, an additional analysis was performed in BEAST version 1.10.4 (Suchard et al., 2018). For each species, nucleotide substitution models calculated in the Mega 6 program are presented: HKY+G+I for *A. uralensis* and *A. flavicollis*, and HKY+G for *A. witherbyi*. The analysis was performed using an uncorrelated lognormal relaxed molecular clock model and a constant-size coalescence model. The MCMC chain length was 60 million generations, with a sampling step of one thousand and discarding the first 10 % of generations (burn-in); the effective sample size (ESS) for all parameters was greater than 200. Convergence of parameters was confirmed by ESS values >200, estimated in the Tracer 1.7 program (Rambaut et al., 2018).

The calibration points were taken from the work of Y. Amir Afzali and R. López-Antoñanzas (2024), performed on Iranian rodents, including representatives of the Muridae family. According to the data of the noted authors, the species *Mus* Linnaeus, 1758 and *Apodemus* Kaup, 1829 diverged from *Rattus* Fischer, 1803 approximately 12.28 million years ago (mya). The time estimate of 12.28 mya for the root node of divergence between *Rattus* and *Mus* + *Apodemus* was used as the first calibration point. We also used a second calibration point of 2.09 mya – the time of divergence of *Mus macedonicus* Petrov & Ruzic, 1983 from *M. musculus musculus* and *M. musculus domesticus*. Additional calibration points were used for the species *A. uralensis* and *A. flavicollis*. For *A. uralensis*, the time of divergence of the European and Asian races was approximately 1.5 mya (Chelomina, Atopkin, 2010), and 2.6 mya was the time of separation for *A. flavicollis* and *A. f. ponticus* (Darvish et al., 2015).

In this study, results were obtained using a mutation rate of 2.4–3.1 % (Suzuki et al., 2015).

The median haplotype network was constructed using Network 4.6.1 using the Median Joining algorithm (Bandelt et al., 1999).

Molecular diversity indices – the number of haplotypes, haplotype (h) and nucleotide diversity (π) values, as well as the Tajima (1989) and Fu (1996) neutrality tests – were calculated using Arlequin v.3.5 (Excoffier, Lischer, 2010).

For genetic diversity assessment, the analyzed sequence length was 960 bp for all three taxa studied.

Information on the original material is provided in in Table S1 in Supplementary Material[1], and the data obtained from GenBank can be found in Table S2.

Results

This paper presents the results of an analysis of the variability of the mtDNA *cyt b* gene fragment in representatives of the subgenus *Apodemus* from geographical samples from the steppe zone of the Central Ciscaucasia (Arik village, Dzhulat settlement, Karagach village, khutor Baksansky), which have not been previously studied. Molecular genetic analysis yielded 153 nucleotide sequences of the mtDNA *cyt b* gene fragment, of which 73 belonged to *A. uralensis*, 37 to *A. flavicollis*, and 43 to *A. witherbyi* = *A. fulvipectus*. Within the alignment, 225 polymorphic sites were detected.

[1] Supplementary Tables S1 and S2 are available at:
https://vavilov.elpub.ru/jour/manager/files/Suppl_Tem_Engl_30_6.pdf

Genetic characterization of *A. uralensis*

Nucleotide sequences of a 960-bp mtDNA *cytochrome b* gene fragment were obtained for 73 *A. uralensis* samples. Based on the analysis of 73 mtDNA *cytochrome b* gene fragment sequences from four *A. uralensis* populations, 75 polymorphic sites were identified, 40 of which were parsimony-informative.

To construct the phylogenetic tree, in addition to the *A. uralensis* sequences obtained in this study, another 98 from the GenBank database (948 bp) were included in the alignment. Figure 2 shows the Bayesian tree obtained for 116 *A. uralensis* haplotypes. As can be seen from the resulting dendrogram, two statistically supported clusters can be identified within the *A. uralensis* group: *A. uralensis 1* and *A. uralensis 2*, with a distance of 6.2 % (Fig. 2). The first cluster corresponds to the so-called European race, the second, to the Asian one, which is consistent with publications based on the use of karyotypic and biochemical as well as molecular genetic data (Chelomina et al., 2007; Chelomina, Atopkin, 2010). Remarkably, out of the 27 European *A. uralensis* sequences from the GenBank database included in the analysis, not a single haplotype was identical to the mitotypes of *A. uralensis* from the steppe Ciscaucasia. Haplotypes of *A. uralensis* from the Central Ciscaucasia occupy a somewhat isolated position on the phylogenetic tree, but with a low posterior probability.

Haplotypes of mice from Iran and the Russian Plain also do not form distinct clusters with high posterior probability values, and the presence of mitotypes from Iran and the Kurgan region among haplotypes of mice from the Central Ciscaucasia likely indicates ongoing gene flow. This is also supported by the low genetic distances between mice from the Central Ciscaucasia and Iran (0.12 %), and mice from the Russian Plain (0.26 %).

To achieve more precise clustering, a median network (Fig. 3) was constructed based on 99 European *A. uralensis* sequences. The median network also demonstrates a lack of clear differentiation between haplotypes of mice from different regions, including those from the GenBank database included in the analysis.

In the Central Ciscaucasian species *A. uralensis*, 50 haplotypes were described among 73 sequenced sequences, of which 40 are unique (80 %). The remaining 20 % of haplotypes were found in 2–7 individuals. A characteristic feature of the median network of *A. uralensis* is the large number of alternative connections that arise as a result of reverse or parallel mutations (Fig. 3).

Genetic distances between geographic samples of *A. uralensis* from the Ciscaucasian steppe also revealed no differences. The maximum distance (K2D) in a pairwise comparison of four samples (Karagach, Dzhulat, Baksansky, and Arik) did not exceed 0.06 %.

Haplotype diversity was quite high in all samples, with nucleotide diversity ranging from 0.0044 to 0.0089 (Table 1). The lowest values were observed in the sample from Dzhulat, and the highest, in the one from Baksansky. Almost all *A. uralensis* samples studied showed significantly negative values for the Fu and Tajima tests for evolutionary neutrality.

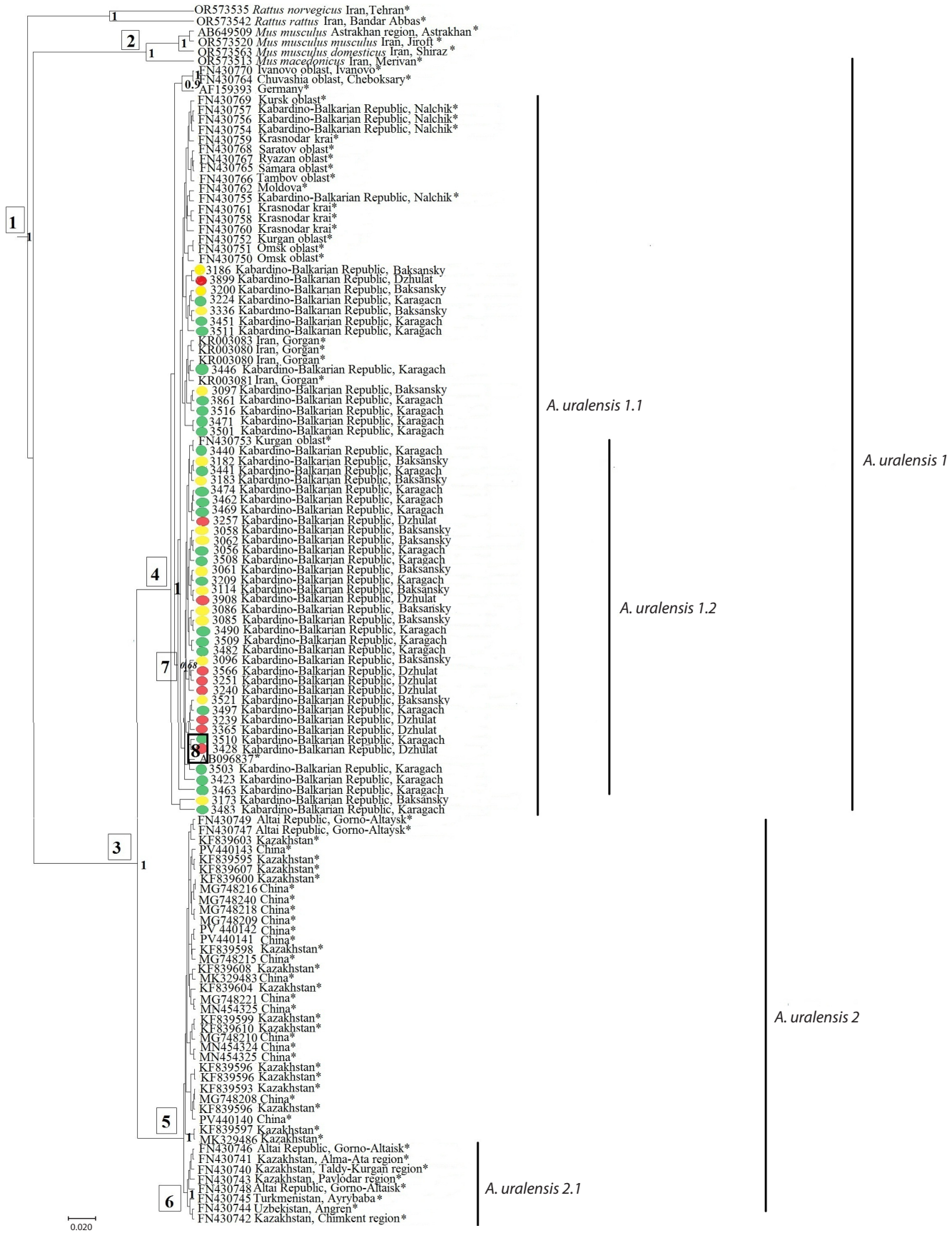


Fig. 2. Bayesian phylogenetic tree of *A. uralensis* based on the analysis of haplotypes of the mtDNA *cyt b* gene fragment (948 bp).

Here and in Figures 4 and 6: numbers at branch nodes are posterior probabilities; numbers in squares are node numbers. Haplotypes from GenBank are marked with an asterisk (*).

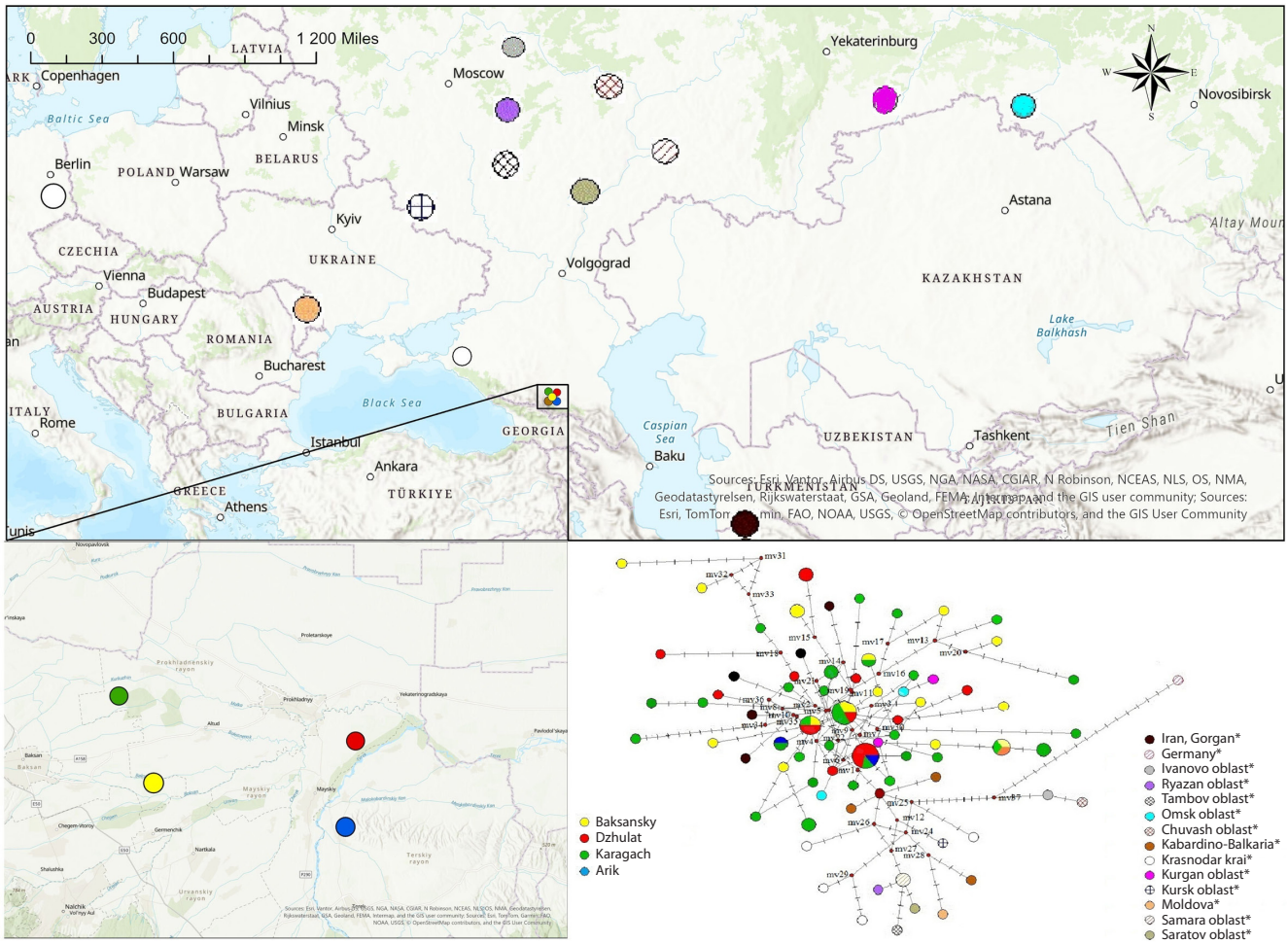


Fig. 3. Median haplotype network of *A. uralensis* based on 73 sequences of the 948-bp *cyt b* gene fragment obtained in this study and 26 sequences from the GenBank database.

Here and in Figures 5 and 7: the circle size is proportional to the number of identical haplotypes; dashes indicate mutations, mv denotes hypothetical haplotypes, and asterisk (*) denotes haplotypes from GenBank.

Table 1. Haplotype (h) and nucleotide (π) diversity indices and Tajima and Fu test values for *A. uralensis* from the Central Ciscaucasia

Geographic groupings (sample size)	*N*	$\pi \pm$ S.E.	h ± S.E.	Tajima's D	Fu's F
KBR, Prokhladnensky district					
Karagach (*n* = 34)	30	0.0075 ± 0.0040	0.991 ± 0.010	**–1.731**	**–22.74**
KBR, Maysky district					
Baksansky (*n* = 16)	15	0.0089 ± 0.0049	0.992 ± 0.025	–1.146	**–6.655**
KBR, Tersky district					
Dzhulat (*n* = 21)	13	0.0044 ± 0.0025	0.929 ± 0.039	**–1.603**	**–4.334**
For *A. uralensis* (*n* = 73) in general	50	0.0069 ± 0.0037	0.978 ± 0.008	**–2.015**	**–25.10**

Note. Here and in Tables 3 and 5: *N* – number of haplotypes; S.E. – standard error. KBR – Kabardino-Balkarian Republic. Statistically significant test values are highlighted in bold.

Divergence time of the main *A. uralensis* clusters

According to our calculations, the separation of the two races, *A. uralensis 1* and *A. uralensis 2*, i. e. the European and Asian, occurred approximately 1.475 million years ago (95 % HPD: 0.930–2.076) (Table 2, node 3). Our date does not contradict the data of G.N. Chelomina and D.M. Atopkin (2010), who showed the divergence of the Asian and European races approximately 1.5 million years ago. The most recent common ancestor of the European race of *A. uralensis* (*A. uralensis 1*) existed approximately more than 600 thousand years ago (95 %

Table 2. Time of existence (in million years) of the last common ancestor (TMRCA) in the main clades of *A. uralensis* based on the results of the analysis of differences in *cyt b* sequences

Node number on the tree. Genus, species	2.4 %		3.1 %	
	Mean (Mya)	95 % HPD Interval	Mean (Mya)	95 % HPD Interval
1. ingroup *Mus* + *Apodemus* + *Rattus*	9.624	6.374–13.14	9.329	6.191–12.81
2. *Mus m. musculus* + *M. m. domesticus* / *M. macedonicus*	1.726	1.087–2.439	1.692	1.059–2.381
3. *A. uralensis 1* european race / *A. uralensis 2* azian race	1.475	0.930–2.076	1.426	0.898–2.016
4. *A. uralensis 1* european race	0.629	0.346–0.951	0.598	0.332–0.901
5. *A. uralensis 2* azian race	0.252	0.121–0.424	0.236	0.108–0.401
6. *A. uralensis 2.1* azian race	0.126	0.051–0.212	0.117	0.048–0.197
7. *A. uralensis 1.1* european race	0.372	0.212–0.566	0.346	0.193–0.528
8. *A. uralensis 1.2* european race	0.256	0.122–0.403	0.239	0.115–0.377

HPD: 0.346–0.951) (Table 2, node 4), and that of the Asian race (*A. uralensis 2*), approximately 252 thousand years ago (95 % HPD: 0.121–0.424) (Table 2, node 5). The age of the cluster (*A. uralensis 1.1*), which included almost all haplotypes from the Russian Plain and the Central Ciscaucasia (from FN430769 to 3463), averaged approximately 400 thousand years (95 % HPD: 0.212–0.566) (Table 2, node 7). The age of the haplogroup *A. uralensis 1.2*, represented only by haplotypes *A. uralensis* of the Central Ciscaucasia, was approximately 260 thousand years (Table 2, node 8).

Genetic characteristics of *A. flavicollis*

The phylogenetic tree obtained from the Bayesian analysis clearly demonstrates the division of *A. flavicollis* haplotypes into two clusters with high posterior probabilities (Fig. 4). The first cluster, *A. flavicollis 1*, is formed by haplotypes of mice from Iran, Turkey, Israel, and the Central Ciscaucasia. The second, largest cluster, *A. flavicollis 2*, includes several haplogroups: *A. flavicollis 2.1*, *2.2*, and *2.3*. Haplogroup *A. flavicollis 2.1* includes animals from France, Bosnia and Herzegovina, and Belarus, Italy, Greece, Spain, Sweden, Turkey, the Czech Republic, Iberian Peninsula, Germany, Macedonia, Austria, Switzerland, Hungary, Russia (Samara). Haplogroup *A. flavicollis 2.2* is represented primarily by haplotypes of mice from Russia (Urals), Ukraine (Chernobyl), Macedonia, Romania, Lithuania, Belarus, Estonia, and France. Haplogroup *A. flavicollis 2.3* includes animals from Russia (Voronezh, Urals, Volgograd), Yugoslavia, and Romania. The distance between clusters *A. flavicollis 1* and *A. flavicollis 2* is 5.3 %. It should be noted that the taxonomic status of *A. flavicollis 1*, the distribution of which covers Georgia, Dagestan, Krasnodar Krai, Azerbaijan, Armenia, and territories bordering the Caucasus (Turkey and Iran), remains disputed.

The median network (Fig. 5), constructed using additional data on 13 nucleotide sequences of the homologous region of mtDNA of *A. flavicollis* from Iran, Turkey, and Israel, shows that the haplotypes of mice from the Central Ciscaucasia are represented by one dominant haplotype and a fan of haplotypes with minor frequencies of occurrence, differing from each other by 1–4 nucleotide substitutions, which indicates the absence of subdivision of the samples.

The 50 analyzed mtDNA *cyt b* gene fragment sequences formed 21 haplotypes. The fragment under study was found to contain 41 variable sites. The dominant haplotype was observed in 29 individuals and was widely represented in all studied localities: Arik, Dzhulat, Karagach, and Baksansky. Of the 37 haplotypes in the identified area, only six were unique, accounting for only 16 %. Overall, the network had a fairly extensive structure with a significant number of median vectors representing hypothetical, likely ancestral haplotypes. No completely identical haplotypes were identified when compared with sequences from Iran and Turkey (Genbank). The genetic distances in pairwise comparison of *A. flavicollis* samples were zero, indicating that they belong to the same population; however, when compared with the grouping from Iran and Turkey, they were 0.16 and 0.14 %, respectively.

The phylogenetic structure we discovered, characterized by a small number of haplotypes and their close proximity, likely indicates that the study area was populated by a small number of founder individuals originating from a single ancestral population.

Table 3 shows that virtually all samples were characterized by low nucleotide and haplotype diversity.

The observed values in the overall *A. flavicollis* sample were also low. The sample from the village of Arik was characterized by zero values, as it was monomorphic, likely due to its small size. Nearly all samples showed significantly negative values for the Tajima and Fu tests. In the overall sample, both neutrality tests were also significantly negative.

Divergence time of the main clusters of *A. flavicollis*

As can be seen from Table 4, the split between *A. flavicollis 1* and *A. flavicollis 2* occurred approximately two million years ago (Table 4). The age of the most recent common ancestor of the *A. flavicollis 1* cluster, which includes haplotypes from Iran, Turkey, Israel, and the Central Ciscaucasia, is ap-

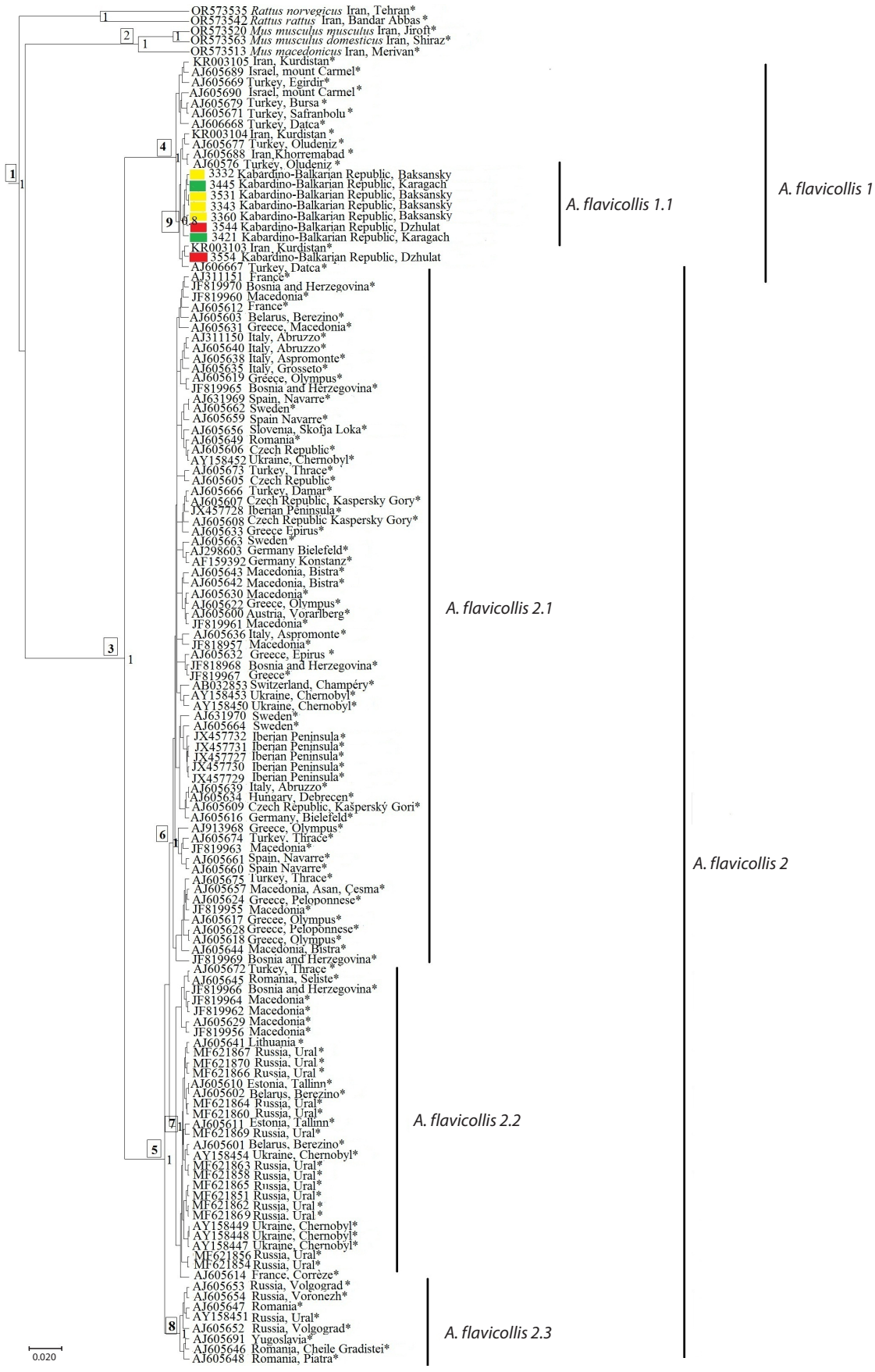


Fig. 4. Bayesian phylogenetic tree of *A. flavicollis* based on the analysis of haplotypes of the mtDNA *cyt b* gene fragment (870 bp).

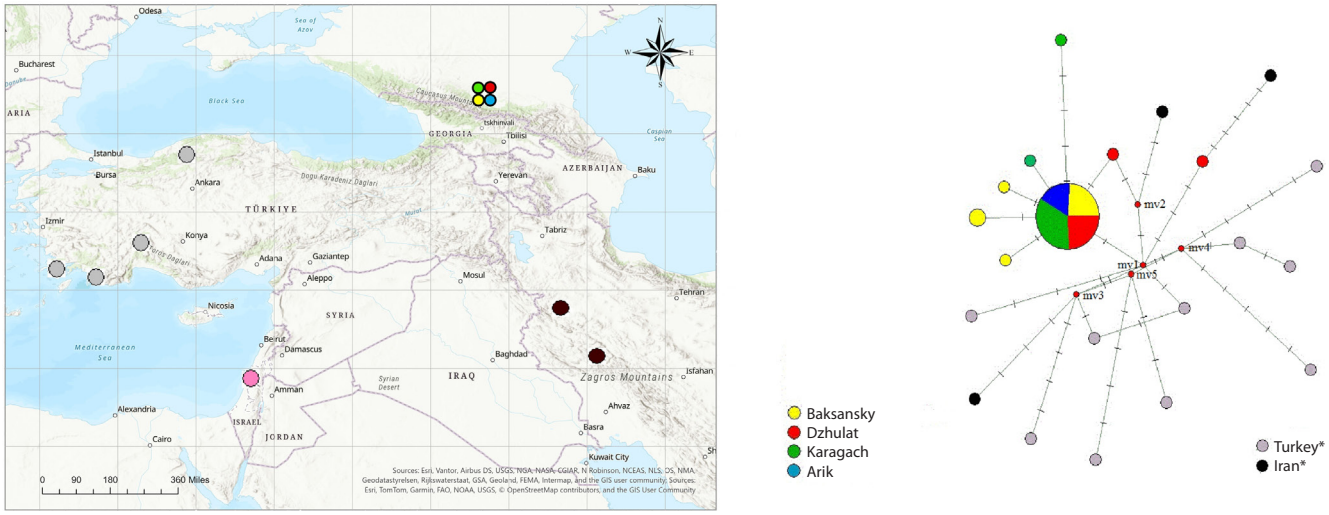


Fig. 5. Median haplotype network of *A. flavicollis* based on 37 *cyt b* gene fragment sequences obtained in this study and 13 sequences from the GenBank database.

Table 3. Haplotype (h) and nucleotide (π) diversity indices and Tajima and Fu test values for *A. flavicollis* from the Central Ciscaucasia

Geographic groupings (sample size)	*N*	$\pi \pm$ S.E.	h ± S.E.	Tajima's D	Fu's F
KBR, Prokhladnensky district					
Karagach (*n* = 12)	3	0.0009 ± 0.0008	0.318 ± 0.164	**–1.831**	0.325
KBR, Maysky district					
Baksansky (*n* = 11)	4	0.0008 ± 0.0007	0.636 ± 0.128	–1.451	–1.256
KBR, Tersky district					
Dzhulat (*n* = 9)	4	0.0014 ± 0.0011	0.583 ± 0.183	**–1.728**	–0.450
Arik (*n* = 5)	1	0	0		
For *A. flavicollis* (*n* = 37) in general	9	0.0008 ± 0.0007	0.431 ± 0.102	**–2.452**	**–5.951**

Table 4. Time of existence (in million years) of the last common ancestor (TMRCA) of the main clades of *A. flavicollis* based on the analysis of differences in *cyt b*

Node number on the tree. Genus, species	2.4 %		3.1 %	
	Mean (Mya)	95 % HPD Interval	Mean (Mya)	95 % HPD Interval
1. ingroup *Mus* + *Apodemus* + *Rattus*	9.744	6.518–13.47	9.509	6.334–13.14
2. *Mus m. musculus* + *M. m. domesticus* / *M. macedonicus*	1.754	1.088–2.480	1.727	1.076–2.420
3. *A. flavicollis 1* / *A. flavicollis 2*	2.007	1.218–2.926	1.951	1.159–2.814
4. *A. flavicollis 1*	0.303	0.123–0.525	0.281	0.119–0.492
5. *A. flavicollis 2*	0.638	0.304–1.060	0.599	0.288–1.011
6. *A. flavicollis 2.1*	0.322	0.186–0.478	0.300	0.176–0.446
7. *A. flavicollis 2.2*	0.254	0.109–0.427	0.236	0.104–0.402
8. *A. flavicollis 2.3*	0.169	0.050–0.332	0.157	0.045–0.309
9. *A. flavicollis 1.1*	0.100	0.019–0.268	0.085	0.017–0.195

proximately 300 thousand years (95 % HPD: 0.123–0.525) (Table 4, node 4).

The age of the most recent common ancestor of the *A. flavicollis 1.1* cluster, represented only by haplotypes of mice from the Central Ciscaucasia, averaged approximately 100 thousand years (95 % HPD: 0.019–0.268) (Table 4, node 9). Within the larger *A. flavicollis 2* cluster, which includes haplotypes from all regions of the Western Palearctic, including western (France), northern (Sweden), and eastern Europe to Ukraine, as well as three Mediterranean peninsulas (Spain, Italy, and the Balkans), several groups with different evolutionary ages were distinguished. The age of the *A. flavicollis 2* cluster was approximately 640–600 thousand years (Table 4, node 5), and that of haplogroups *A. flavicollis* 2.1, *A. flavicollis* 2.2, and *A. flavicollis* 2.3 ranged from 330 to 160 thousand years (Table 4, nodes 6–8).

Genetic characteristics of *A. witherbyi*

As Figure 6 shows, all of the analysed *A. witherbyi* haplotypes formed a single large cluster, *A. witherbyi 1*, which included haplotypes from Iran, Israel, Turkey, and the Central Ciscaucasia. Within this cluster, two haplogroups emerged, represented only by animals from the Central Ciscaucasus: *A. witherbyi 1.1* with a low posterior probability value of >0.6 and *A. witherbyi 1.2* with a high posterior probability value of 0.9.

The median network of *A. witherbyi* is characterized by a rather complex structure with a large number of hypothetical haplotypes through which the transition from one haplotype to another could occur. A total of 36 haplotypes have been described, of which two are dominant (Fig. 7). The majority of haplotypes (32 of 36) are unique. The most common haplotype was observed in 21 individuals (48.8 %) from Dzhulat and Karagach, and the second most frequent haplotype was observed in five individuals from the same localities. As can be seen, the distribution of haplotypes in this species, as in others, is not associated with geographic localization.

As with the previous species, the genetic distances between the studied samples were very low and did not exceed 0.0009. The total sample from the Ciscaucasia differed from the sample from Iran with a distance of 0.0017, from Turkey – 0.0028, from Israel – 0.0035.

Among individual groups, the highest values of both haplotype and nucleotide diversity were observed in *A. witherbyi* from the vicinity of the village of Karagach (Table 5). The remaining two samples, from the villages of Dzhulat and Arik, were characterized by similar values of haplotype diversity, with higher nucleotide diversity in the latter sample. Overall, low values of both indices were observed for the species: h = 0.759, π = 0.0037.

Divergence time of the main clades of *A. witherbyi*

The age of the *A. witherbyi 1* cluster, represented by haplotypes from the territory of Israel, Iran, Turkey, and the Central Ciscaucasia, was on average about 350–330 thousand years (95 % HPD: 0.200–0.530 and HPD: 0.184–0.503, respectively) (Table 6, node 3). In the territory of the Central Ciscaucasia, two haplogroups were distinguished: with a low posterior probability value – *A. witherbyi 1.1* and with a high one – *A. witherbyi 1.2*. The most recent common ancestor of haplogroup *A. witherbyi 1.1* existed between 166 and 154 thou-

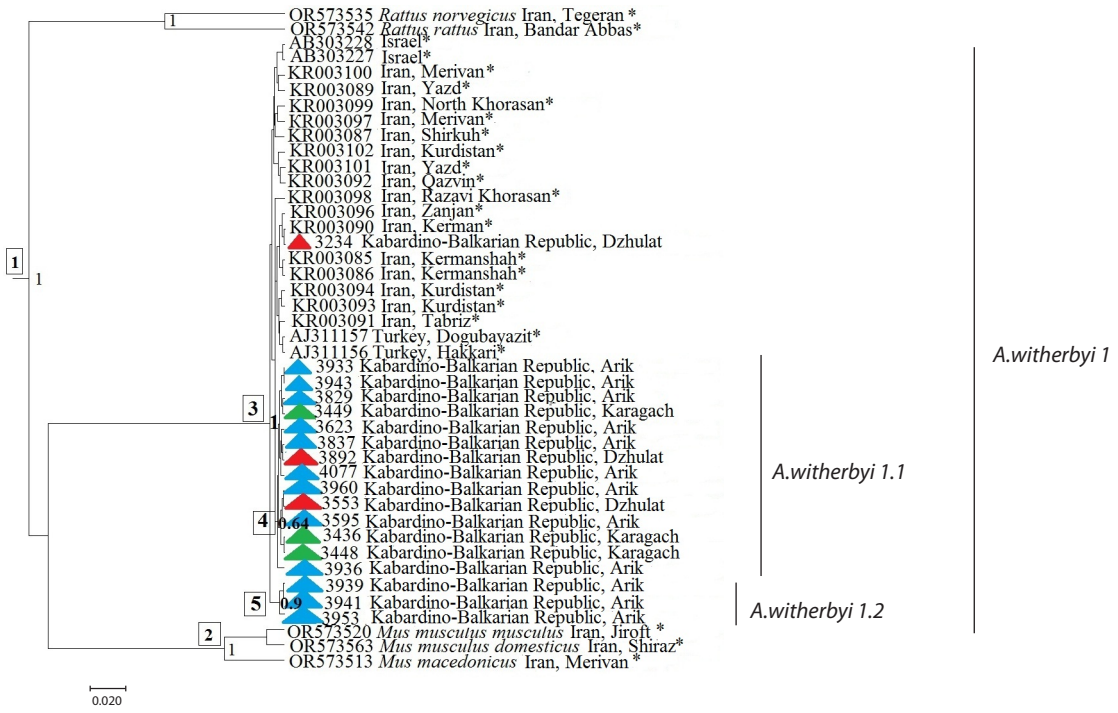


Fig. 6. Bayesian phylogenetic tree of *A. witherbyi* based on the analysis of haplotypes of the mtDNA *cyt b* gene fragment (870 bp).

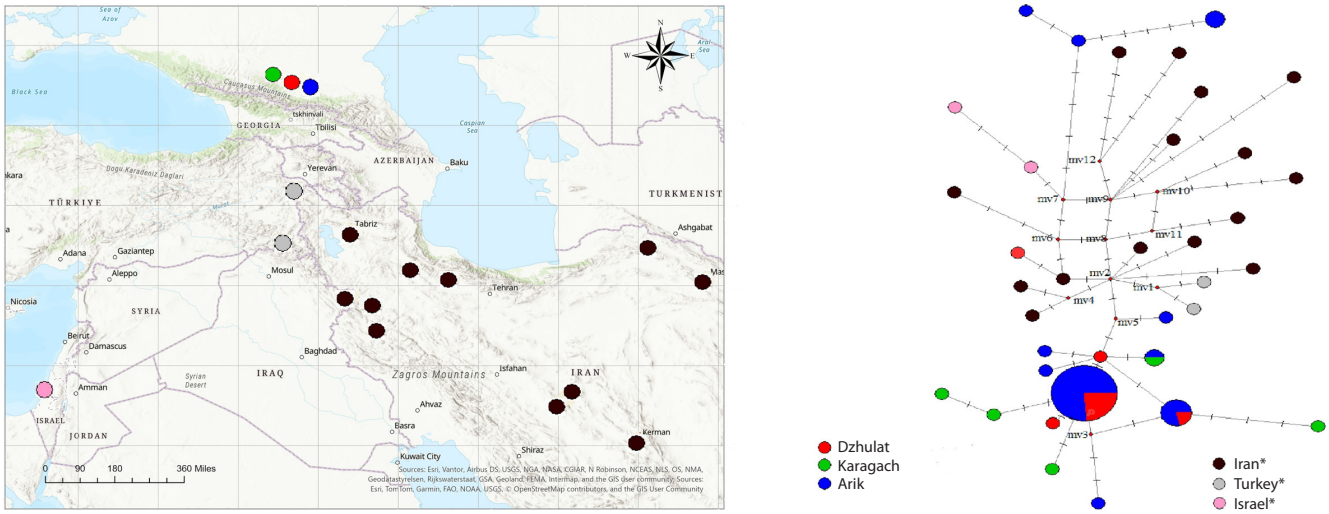


Fig. 7. Median haplotype network of *A. witherbyi* based on 43 *cyt b* gene fragment sequences obtained in this study and 19 sequences from the GenBank database.

Table 5. Haplotype (h) and nucleotide (π) diversity indices and Tajima and Fu test values for *A. witherbyi* from the Central Ciscaucasia

Geographic groupings (sample size)	*N*	$\pi \pm$ S.E.	h ± S.E.	Tajima's D	Fu's F
KBR, Prokhladnensky district					
Karagach (*n* = 4)	4	0.0052 ± 0.0038	1.000 ± 0.177	0.1843	–0.5235
KBR, Tersky district					
Dzhulat (*n* = 9)	5	0.0016 ± 0.0012	0.722 ± 0.159	–1.398	–1.504
Arik (*n* = 30)	12	0.0041 ± 0.0023	0.715 ± 0.089	–1.270	–1.220
For *A. witherbyi* (*n* = 43) in general	18	0.0037 ± 0.0021	0.759 ±0.069	**–1.720**	**–5.616**

Table 6. Time of existence (million years) of the last common ancestor (TMRCA) of the main clades of *A. witherbyi* based on the analysis of differences in *cyt b*

Node number on the tree. Genus, species	2.4 %		3.1 %	
	Mean (Mya)	95 % HPD Interval	Mean (Mya)	95 % HPD Interval
1. ingroup *Mus* + *Apodemus* + *Rattus*	9.150	6.397–12.118	8.684	5.995–11.54
2. *Mus m. musculus* + *M. m. domesticus* / *M. macedonicus*	1.706	1.149–2.295	1.641	1.102–2.233
3. *A. witherbyi 1*	0.354	0.200–0.530	0.330	0.184–0.503
4. *A. witherbyi 1.1*	0.166	0.071–0.292	0.154	0.064–0.268
5. *A. witherbyi 1.2*	0.125	0.031–0.245	0.115	0.027–0.029

sand years ago (95 % HPD: 0.071–0.292) (Table 6, node 4), and that of haplogroup *A. witherbyi* 1.2, approximately 125–115 thousand years ago (95 % HPD: 0.031–0.245) (Table 6, node 5).

Biotopic distribution and abundance of representatives of the genus *Apodemus* in the Central Ciscaucasia

In the Central Ciscaucasia, in the studied steppe regions (Maysky, Tersky, and Prokhladnensky districts), representatives of the genus *Apodemus* (*A. uralensis*, *A. witherbyi* and *A. flavicollis*) are observed to coexist almost everywhere, sympatrically and in places symbiotically, with the exception of the Maysky district, where *A. witherbyi* has not been recorded. All three *Apodemus* species were observed in all the studied biotopes: forest, shelterbelt, banks of an irrigation canal, open habitats, meadow areas (virgin lands), and wastelands between agrocenoses. However, in relation to the study area, along with the symbiotopic habitation of the species, the division of their habitats and the greatest or least gravitation of species to certain biotopes are noted.

The abundance of species varies depending on the type of habitat, year and season. So, the values for *A. uralensis* range from common to numerous (1–18.1 ind./100 trap-days). It is found in forest shelterbelts with pedunculate oak and on the banks of irrigation canals with a cereal-legume phytocenosis, in the vicinity of khutor Baksansky, Maysky district, where the abundance in some years reaches 8.3 and 10.6 ind./100 trap-days, respectively. In general, the relative abundance of *A. uralensis* in the studied biotopes was on average (ind./100 trap-days): in the forest – 4.9–9.6; in the shelterbelt – 8.3; on the bank of an irrigation canal – 1.4–6.6; in the meadow – 4.2.

A. flavicollis was recorded in all biotopes of the studied area; in the forests and shelterbelts near khutor Baksansky and Karagach village, the relative abundance of the species reached its maximum values (14 and 14.8 ind./100 trap-days, respectively). The species was common on the banks of irrigation canals with a cereal-legume phytocenosis near khutor Baksansky and Arik village. The average relative abundance values of *A. flavicollis* were (ind./100 trap-days): in the forest – 2.6–7.6; in the shelterbelt – 8.8; on the bank of an irrigation canal – 1.9–4.9; in the meadow – 1.7.

The third species of the genus *Apodemus*, *A. witherbyi*, is present in all studied biotopes of the surveyed areas, with the exception of Maysky district. *A. witherbyi* is most often found in meadows and virgin lands unsuitable for plowing, with wormwood-grass-forb phytocenoses, where the relative abundance ranges from 1.7 to 4.2 ind./100 trap-days. However, in the forest shelterbelt around Arik, its abundance reaches its highest levels.

Discussion

Genetic structure of representatives of the genus *Apodemus*

Based on an analysis of the mitochondrial DNA *cyt b* gene fragment variability, the species composition and genetic diversity of sibling species of wood mice of the genus *Apodemus* in the steppe zone of the Central Ciscaucasia were studied for the first time. Molecular genetic methods revealed the presence of three species of the genus in the designated area: *A. uralensis*, *A. flavicollis* and *A. witherbyi*, with genetic distances ranging from 10 to 13 %. The maximum level of differences was observed when comparing *A. witherbyi* with two other taxa: *A. uralensis* and *A. flavicollis*. Intraspecific genetic distances among the studied taxa were minimal, not exceeding 0.06 %.

Among the three species, *A. uralensis* exhibits the greatest genetic diversity (Table 1). *A. witherbyi* occupies an intermediate position (Table 5), while *A. flavicollis* exhibits the lowest level of molecular genetic variability among the studied species (Table 3). Inclusion of sequences of suitable length from the GenBank database in the analysis revealed no completely identical haplotypes in all three taxa studied.

For comparison, we note that in previously studied *A. flavicollis* samples from the Western and Eastern Caucasus, haplotype diversity ranged from 0.867 to 0.978, and nucleotide diversity, from 0.0044 to 0.0051, while in the combined sample, these values were 0.918 and 0.0050, respectively (Amshokova et al., 2024). The haplotype and nucleotide diversity values in the combined sample of *A. flavicollis* from the Central Ciscaucasia are lower than those obtained previously. Negative and significant values of the Tajima and Fu tests observed in the combined sample provide evidence of population expansion of *A. flavicollis*. The dominant haplotype of *A. flavicollis* is found in 78.3 % of individuals across all geographic samples. This median network structure, as well as genetic diversity indicators, likely indicate a recent colonization of the studied area by a limited number of founder individuals carrying the dominant haplotype. The absence of genetic differences between the four samples also serves as evidence of a common origin.

A. uralensis, unlike *A. flavicollis*, is characterized by a more complex haplotype network structure and the highest values of the haplotype and nucleotide diversity indices (Fig. 3). In this case, we observe the presence of a large number of alternative links of varying lengths, which are the result of back or parallel mutations, leading to the formation of multiple closed loops. In *A. uralensis*, as in other species, the haplotype distribution does not demonstrate a clear, reliable relationship with the geographic location of the samples. This network structure, along with high values of haplotype and nucleotide diversity, indicates long-term population evolution under stable conditions, likely indicating significant gene flow with neighboring areas.

A comparison of the level of genetic variability of *A. uralensis* with known literature data suggests a relatively high level of genetic diversity characteristic of the species as a whole. Similar results were obtained by other authors when analyzing the *cyt b* gene region of *A. uralensis* in the Kabardino-Balkarian Republic – $h = 1.000$, $\pi = 0.0131$; Krasnodar Krai – $h = 0.900$, $\pi = 0.0079$ (Chelomina, Atopkin, 2010); and the Lower Don – $h = 0.933$, $\pi = 0.0056$ (Stakheev, 2024).

The combined sample of *A. witherbyi* occupies an intermediate position in terms of genetic variability among the studied representatives of the genus *Apodemus*. Compared with data reported in the literature, the species in the study area is characterized by lower values of genetic diversity. So, according to data from N. Shad et al. (2016), in the combined sample of *A. witherbyi* from Iran, the haplotype diversity was 0.914, and the nucleotide diversity was 0.0043. The relatively low genetic diversity of *A. witherbyi* from the Central Ciscaucasia is likely due to its late introduction to the study area.

Divergence time of the main clades of representatives of the genus *Apodemus*

Speciation within the subgenus *Sylvaemus* occurred between 1.2 and 5.7 million years ago, i. e. in the Pliocene-Pleistocene, and its divergence from the genus *Apodemus* occurred more than 7.5 million years ago, i. e. in the Miocene (Chelomina, Suzuki, 2006).

According to the results of our molecular dating, the separation of the two races of *A. uralensis* – European and Asian – occurred approximately 1.5 million years ago (95 % HPD: 0.929–2.076) (Fig. 2, Table 2), which is consistent with the data of G.N. Chelomina and D.M. Atopkin (2010).

The divergence time between *A. flavicollis 1* (Fig. 4), which is distinguished by some authors as an independent species (*A. ponticus* (Bogdanov et al., 2012)), and by others as a subspecies (*A. flavicollis ponticus* (Gromov, Erbaeva, 1995)), and *A. flavicollis 2* (Fig. 4) is about two million years. Our data are close to the results of foreign authors (Michaux et al., 2004), who showed the separation of clade 1 (Turkey, Iran, Israel) and clade 2, which includes all populations of the Western Palearctic, from the Iberian Peninsula in the west to the south of Russia (Samara) in the east and Estonia in the north, 2.2–2.4 million years ago. According to J.R. Michaux et al. (2004), this tree structure can be explained by the isolation of two *A. flavicollis* groups in two different refugia: one in the Middle East and the other in the Balkan region during one of the first Quaternary climatic fluctuations. The authors believe that the entire Western Palearctic was recolonized not from the Middle Eastern, but from the Balkan population, a finding they tentatively attributed to the presence of strong biogeographic barriers, such as the Black Sea and the Caucasus, which prevented contact between Palearctic and Middle Eastern animals.

According to literature data, the divergence between *A. witherbyi* and other closely related species occurred 6 million years ago (Darvish et al., 2015).

Before discussing the data obtained on the evolutionary age of *Apodemus* mice in the Central Ciscaucasia, it is necessary to highlight some key points in the evolution of the Caucasus itself, which forms the isthmus between Europe and Asia. According to the literature, approximately 1.8–0.7 million years ago, during the Eopleistocene (Middle Pleistocene), the Caucasus was a peninsula. During this period, it was washed by the Absheron Sea, which existed in the territories of today's Black Sea, Azov, Caspian, Aral, lower Volga regions, Turkmenistan, and Kazakhstan. During this period, fauna, including mammals, was closely connected with that of Asia Minor via Transcaucasia. The formation of the isthmus resulted from the repeated merging of the Pontus and Caspian basins during the Pleistocene. So, A.A. Svitoch and V.M. Sobolev (2011), while studying the Pleistocene Manych Straits, which is the natural boundary between the Russian Plain and the North Caucasus, identified the following periods of merging of the Pontus and Caspian Seas during the Pleistocene.

1. In the second half of the Early (Lower) Pleistocene (Gelazian: 2.58–1.80 million years ago, according to the Russian stratigraphic scale approved in March 2024), the Baku (Late Chaudinian) Strait existed, through which the waters of the Baku transgression of the Caspian Sea discharged into the Late Chaudinian basin of Pontus.
2. In the middle of the Middle Pleistocene (Eopleistocene, 1.80–0.781 million years ago), a second junction of the Caspian and Black Sea basins was noted, resulting in the formation of the Early Khazar Strait, which was caused by the high level of the Early Khazarian transgression of the Caspian Sea and the overflow of its waters into Pontus.
3. At the beginning of the Late (Upper) Pleistocene (Neopleistocene, 0.781–0.129 million years ago), the Late Khazar (Karangat) Strait emerged in the Manych Depression, caused by the major Karangat transgression of the Pontus and the relatively small Late Khazar transgression of the Caspian.
4. In the middle of the Late Pleistocene, after the regression of the Karangat and Late Khazar basins, a vast freshwater reservoir existed in the Manych Depression. It occupied the entire lowland portion of the depression, filling the troughs of the ancient straits. Compared to the preceding Late Khazar (Karangat) Strait, the lake had a larger area and depth.

Summarizing the presented data on the paleogeography of Pontus, the Caspian Sea and Manych, it can be assumed that the penetration of mammal fauna from the Russian Plain to the North Caucasus periodically occurred in the Neopleistocene starting from 780 thousand years ago.

No less interesting and important, in addition to the history of the formation of the modern territory of the Caucasus, are the paleontological data of A.K. Markova (2016). The author studied the fauna of small mammals in Europe, including Eastern Europe, in the first half of the Middle Pleistocene in the range of 0.76–0.42 million years ago, and then in the second half in the range of 0.424–0.13 million years ago (Markova, 2017). It should be clarified here that, according to the Russian stratigraphic scale, these intervals correspond to the Late Pleistocene (Neopleistocene). According to the author, in the first half of the Middle Pleistocene, remains of mice of the genus *Apodemus* from 26 sections in European Russia and Belarus were found in only two sections: *Apodemus* cf. *flavicollis* in Belarus (Korchevo locality), and remains of *Apodemus* ex gr. *sylvaticus* in Tambov Oblast (Kuznetsovka locality). Of the 35 sections studied in the European part of Russia during the second half of the Middle Pleistocene (~0.424–0.13 million years ago, according to the author), remains of *Apodemus* ex gr. *sylvaticus* were found in only one section (the Chekalin locality, Tula Oblast). It is worth clarifying here that, according to modern taxonomy, *A. uralensis* inhabits the European part of Russia (Gromov, Erbaeva, 1995) and the North Caucasus (Tembotova, 2015). Based on the data of A.K. Markova (2016, 2017), it can be concluded that mice of the genus *Apodemus* were not widespread or numerous in the European part of Russia during the Middle Pleistocene (in sections, both species were represented by an insignificant number of remains). This is also consistent with the data of N.K. Vereshchagin (1959). The author claimed that paleontological data from Pleistocene deposits in the Caucasus are absent. For example, *Apodemus agrarius* Pallas (1771) is known in the Caucasus only from Upper Quaternary deposits of the lower Don. The author does not provide any information on other species of the genus, nor does she provide data on representatives of two other closely related genera: *Rattus* and *Mus* of the family Muridae Illiger (1811).

Thus, the paleontological data of A.K. Markova (2016, 2017) on small mammals of the European part of Russia allow us to assume that only in the middle of the Late Pleistocene (Neopleistocene), less than 400 thousand years ago, corresponding to the optimum of the Likhvin interglacial (350–300 thousand years ago), did the possibility arise for

the penetration of European fauna into the Ciscaucasia from the Russian Plain.

Turning to the evolutionary age of the three mouse species (*A. uralensis*, *A. witherbyi* and *A. flavicollis*) from the study area, the following can be noted in the context of the above. As reflected in the results, the *A. uralensis* haplotypes from the Central Ciscaucasia do not form a distinct cluster with a high level of support; however, some structure is evident. Therefore, the age was calculated for a cluster combining haplotypes from the Central Ciscaucasia and the Russian Plain, which also included three haplotypes from Iran. The formation time of this mitochondrial clade of *A. uralensis* is approximately 370–350 thousand years ago (Fig. 2, node 7), corresponding to the so-called Middle Neopleistocene. The cluster represented solely by *A. uralensis* haplotypes from the Central Ciscaucasia (Fig. 2, node 8) is younger, dating to approximately 256 thousand years ago, corresponding to the Late Neopleistocene. Considering the fact that an insurmountable water barrier regularly appeared between the Russian Plain and the North Caucasus in the Manych region, the little wood mouse penetrated the North Caucasus in at least two stages.

The age of the most recent common ancestor (MRCA) of haplogroup *A. witherbyi 1.1* in the Central Ciscaucasia falls between 166 and 154 thousand years, while that of haplogroup *A. witherbyi 1.2* falls between 125 and 115 thousand years. The absence of *cyt b* gene sequences in the GenBank database from other areas of *A. witherbyi* distribution precludes any speculation about the possible routes of this species' introduction into the Central Ciscaucasia. Based on the data obtained, the species most likely also entered the North Caucasus in two stages: the late Neopleistocene and early Holocene.

According to data obtained for the Caucasian wood mouse, the age of the most recent common ancestor of haplogroup *A. flavicollis 1*, represented only by haplotypes of mice from the Central Ciscaucasia, is approximately 100–85 thousand years. These data indicate that *A. flavicollis* is the youngest invader to the Central Ciscaucasia, with an evolutionary age corresponding to the Middle Holocene. mDNA variability indicates a close relationship with representatives from Asia Minor, suggesting that the mouse entered the Caucasus via the Black Sea coast from Turkey, which is consistent with paleontological data from A.S. Tesakov (2021) on the Black Sea coast.

Distribution and habitat distribution of representatives of the genus *Apodemus*

According to I.V. Zagorodniuk et al. (1997), the range of *A. witherbyi* extends north from the Main Caucasus Range, to the Don and the Kuma-Manych Depression, and is known throughout the area from the Black Sea (Don, Kuban) to the Caspian Sea (Kuma, Terek). Regarding the yellow-necked mouse, which inhabits the Caucasus, there are two points of view: some authors distinguish it as an independent species, others as a subspecies. *Sylvaemus flavicollis ponticus* is endemic to the Caucasus Mountains and is common in the broad-leaved forests of the Ciscaucasia, Caucasus, and Transcaucasia (Pavlinov, Lisovsky, 2012). As for *A. uralensis*, electrophoretically typed specimens have been described almost everywhere in the Caucasus and Transcaucasia (Vorontsov, 1992), as well as in the European part of Russia (Chelomina, Atopkin, 2010; Stakheev et al., 2011).

There are differing opinions regarding the biotopic preferences of the studied species. According to E.I. Lashkova and I.I. Dzeverin (2004), *A. uralensis* is the most polymorphic species, the biotopic and geographic distribution of which is difficult to characterize. Biotopic preferences vary slightly depending on the region. It is believed that in some parts of its range, *A. uralensis* clearly avoids forests, preferring open habitats such as dry shrublands and even virgin steppe areas. In others, on the contrary, it prefers forests and moist areas with dense vegetation, avoiding dry, open spaces. One of the factors determining the species' habitat distribution in the Caucasus is humidity. The species avoids dry habitats, giving way to *S. arianus* (steppe mouse) = *A. witherbyi*. It is found in lowland and mountain forests, meadows, reed beds along water bodies, and in gardens and vegetable plots (https://biodiversity.ru). It is abundant in the dark coniferous mountain forests of the Caucasus on rocky scree, where it lives in symbiosis with *Chionomys gud*. Previous studies conducted in the North Caucasus also showed that of the three wood mouse species inhabiting the study area – *A. uralensis*, *A. witherbyi*, and *A. flavicollis* – the former is the most widespread, occurring in all studied biotopes, with the exception of the xerophytic landscapes of the protected areas of the Eastern Caucasus and Rostov Oblast, where the species has not been recorded (Gudova et al., 2021; Amshokova et al., 2024). The range of *A. uralensis* extends in altitudinal, longitudinal, and latitudinal directions.

A. uralensis is widespread in the steppe regions of the Central Ciscaucasia, inhabiting all studied biotopes. The species accounts for a significant proportion of catches: of 153 genetically dated specimens, 72 (47 %) belonged to this taxon. It prefers forested areas; more than half (approximately 65 %) were captured in the oak-poplar forest near the village of Karagach, where the highest numbers are recorded. The species is also abundant in the maple-elm forest near the village of Dzhulat. At the same time, *A. uralensis* avoids xerophytic areas; in all the years of research in the Central Ciscaucasia, it was recorded once in a steppe grass-forb biotope (meadow) adjacent to an agrocenosis, in the vicinity of the village of Karagach.

Sympatric and almost universal symbiotopic habitation is noted with *A. uralensis* and *A. flavicollis*. Although *A. flavicollis* is present in all regions of the Central Ciscaucasia, its most preferred biotopes are lowland forests and shelterbelts, consisting of mixed stands of common oak and poplar, where a significant portion of the animals (25 %) were collected in the vicinity of khutor Baksansky and Karagach village. Like *A. uralensis*, the Caucasian wood mouse avoids meadows and virgin steppe areas adjacent to agrocenoses; a single individual was recorded near the village of Dzhulat, in an open station – a virgin area between agrocenoses. In general, *A. flavicollis* is a mesophilic species, the optimum range of which is confined to beech forests (Amshokova et al., 2024).

According to a number of authors, the most typical biotope for *A. flavicollis* is a broad-leaved forest, where the seeds of beech, hornbeam, oak, and some shrubs make up the bulk of its diet; it also reaches high numbers in mountain beech forests and inhabits mixed forests in the presence of broad-leaved species (Popov, 1960; Mammalian…, 1963; Tatarinov, 1973; Pavlinov, 2002). In the Caucasus, *A. flavicollis* is also found in broad-leaved forests; in the Alazani Valley, it has also been recorded in dry small-leaved forests (Vorontsov et al., 1992); in Krasnodar Krai and the Republic of Adygea, the Caucasian wood mouse gravitates toward low-mountain, highly productive, nut-bearing broad-leaved forests (beech, hornbeam, oak, chestnut) (Okulova et al., 2007).

A genetic study of mice in the North Caucasus also revealed that *A. flavicollis* is confined to forested (broadleaf) landscapes of the Western and Eastern Caucasus. The species has not been found in the foothills and mid-mountains of the Central Caucasus (Amshokova et al., 2024).

Although *A. witherbyi* is present in all the studied biotopes of the Tersky District (vicinity of Arik village and Dzhulat settlement) – where it reaches high population densities in shelterbelts – in the Prokhladnensky District (vicinity of Karagach village), it is recorded exclusively in open habitats, such as meadows, and has not been observed in forests. The species accounts for 28 % of the total catch. It is frequently associated with dry habitats.

In the Ciscaucasia, *A. witherbyi* inhabits open and forest-edge biotopes, fields, and in the North Caucasus and Transcaucasia, steppe habitats, including steppe areas, along the edges of broad-leaved forests, and shrub thickets (Zagorodniuk et al., 1997; Stakheev, 2024). Based on our previously obtained data, we also concluded that *A. witherbyi* is a stenobiont inhabiting xerophytic landscapes (steppe, semi-desert) of the Eastern Caucasus and on the southern border of the Russian Plain (Rostov Nature Reserve) (Gudova, 2021; Amshokova et al., 2024). We recorded the species in the Tlyaratinsky Nature Reserve at an altitude of 1,800 m above sea level, where it lived sympatrically and symbiotopically with *A. uralensis*, inhabiting a variety of biotopes: rocky slopes with a forb-clover community and oak areas with sparse herbaceous vegetation, cereal-forb biotopes, forest edges and birch forest clearings (Amshokova et al., 2024; Gudova et al., 2026).

Conclusion

The species composition and genetic diversity of representatives of the genus *Apodemus* in the steppe zone of the Central Ciscaucasia were studied. Three cryptic species were identified in the designated area: *A. uralensis*, *A. witherbyi* and *A. flavicollis*, with distances ranging from 10 to 13 %. For the study area, the species *A. flavicollis* and *A. witherbyi* were described for the first time based on genetically dated material. *A. flavicollis* and *A. uralensis* were recorded in all four studied locations: the vicinity of the Arik and Karagach villages, the village of Dzhulat, and khutor Baksansky. *A. witherbyi* was found in three out of the four geographical locations (the vicinity of the Arik and Karagach villages, and the village of Dzhulat).

Considering the general features of distribution, landscape-biotopic distribution and abundance of representatives of the genus *Apodemus*, it can be concluded that in the conditions of the steppe zone of the Central Ciscaucasia, *A. uralensis*, having a wide distribution, is most attracted to forest areas, reaching maximum abundance here, less often – to forest shelterbelts; the species is also numerous in the coastal phytocenoses of irrigation canals, avoiding the most xerophytic meadow stations – virgin wastelands adjacent to agrocenosis. *A. flavicollis* shares a symbiotic relationship with *A. uralensis*. It is also most often found in forests and shelterbelts. In addition, it is recorded in moist areas, such as along canal banks, but is absent from open steppe areas, slopes, and wastelands. The habitats of *A. uralensis* and *A. flavicollis* are most similar. *A. witherbyi* exhibits a narrower range than the other two species, preferring open habitats, meadow areas, the banks of irrigation canals, and virgin lands and wastelands, where it is common. However, its highest populations are found in shelterbelts.

A. uralensis is most often dominant in forests, whereas *A. flavicollis* is a codominant species relative to the year and season studied. Sometimes, a shift in dominance is observed, with the second species predominating. *A. witherbyi* is most often the absolute dominant species, and less frequently codominant with *A. uralensis* in meadows and virgin, uncultivated areas. In isolated cases, it is monodominant or codominant with *A. flavicollis* in shelterbelts and along the banks of irrigation canals.

A. uralensis was the first to penetrate into the Central Ciscaucasia from the Russian Plain in geological time, likely in two stages. The first occurred approximately 370–350 thousand years ago, and the second, approximately 256 thousand years ago, which, according to the latest version of the Russian stratigraphic scale (2024), corresponds to the mid-Pleistocene. This period coincides with the optimum of the Likhvin interglacial. The obtained data on the genetic diversity of *A. uralensis* suggest that gene exchange with individuals from European Russia is actively ongoing.

A. witherbyi likely also entered the Central Ciscaucasia in two stages: 1) the late Neopleistocene, approximately 166–154 thousand years ago; 2) the early Holocene, approximately 125–115 thousand years ago. It would be premature to determine the species' origin in the Caucasus due to a lack of material from other regions.

A. flavicollis is the youngest invader in the Central Ciscaucasia. Its evolutionary age is approximately 100 thousand years; the species is a representative of the Holocene fauna in the region. Variability in mDNA indicates a close relationship with species from Asia Minor, suggesting that the mouse entered the Caucasus via the Black Sea coast from Asia Minor.

References

Amir Afzali Y., López-Antoñanzas R. Molecular phylogeny and historical biogeography of Iranian murids (Rodentia: Muridae). *Mamm Biol*. 2024;104:79-89. doi 10.1007/s42991-023-00390-3

Amshokova A.Kh., Tembotova F.A., Kononenko E.P., Gudova M.S. Molecular genetic analysis of representatives of the subgenus *Sylvaemus* (Rodentia, Muridae) in specially guarding natural areas in the southern of Russia according to data analysis of a fragment of

the cytochrome *b* gene. *Biol Bull Russ Acad Sci.* 2024;51(Suppl.2): 127- 148. doi 10.1134/S1062359024611649

Bandelt H.J., Forster P., Röhl A. Median-joining networks for inferring intraspecific phylogenies. *Mol Biol Evol*. 1999;16(1):37-48. doi 10.1093/oxfordjournals.molbev.a026036

Bogdanov A.S., Stakheev V.V., Zykov A.E., Yakimenko V.V., Mal'kova M.G. Genetic variation and differentiation of wood mice from the genus *Sylvaemus* inferred from sequencing of the cytochrome oxidase subunit 1 gene fragment. *Russ J Genet.* 2012;48(2):186-198. doi 10.1134/S1022795412020044

Chelomina G.N., Atopkin D.M., Molecular genetic evidences of a deep phylogenetic discontinuity between the Asian and European races of pygmy wood mouse based on the mitochondrial cytochrome *b* gene variability. *Mol Biol*. 2010;44(5):699-708. doi 10.1134/S0026893310050043

Chelomina G.N., Suzuki H. Molecular evolution and phylogeography of west-Palaearctic wood mice of the genus *Sylvaemus* based on the data on variation of nuclear (*IRBP*) and mitochondrial (*cyt b*) DNA genes. *Zoologicheskiy Zhurnal.* 2006;85(2):219-234 (in Russian)

Chelomina G.N., Atopkin D.M., Bogdanov A.S. Phylogenetic relationships between species and intraspecific forms of forest mice from the genus *Sylvaemus* as determined by partial sequencing of the cytochrome *b* gene of mitochondrial DNA. *Dokl Biol Sci.* 2007;416: 356-359. doi 10.1134/S0012496607050092

Darvish J., Mohammadi Z., Ghorbani F., Mahmoudi A., Dubey S. Phylogenetic relationships of *Apodemus* Kaup, 1829 (Rodentia: Muridae) species in the Eastern Mediterranean inferred from mitochondrial DNA, with emphasis on Iranian species. *J Mamm Evol*. 2015; 22(4):583-595. doi 10.1007/s10914-015-9294-9

Excoffier L., Lischer H. Arlequin suite ver 3.5: a new series of programs to perform population genetics analyses under Linux and Windows. *Mol Ecol Resour*. 2010;10(3):564-567. doi 10.1111/j.1755-0998.2010.02847.x

Fu Y. New statistical test of neutrality for DNA sample from a population. *Genetics.* 1996;143(1):557-570. doi 10.1093/genetics/143.1.557

Gromov I.M., Erbaeva M.A. Mammals of the Fauna of Russia and Adjacent Territories. Hares and Rodents. St. Petersburg, 1995 (in Russian)

Gudova M.S., Tembotova F.A., Emkuzheva M., Amshokova A.Kh., Kuchinova E.A. Current diversity of small mammals of the "Sarykum Barkhans" of Dagestan Reserve. *BIO Web Conf.* 2021;35: 00010. doi 10.1051/bioconf/20213500010

Gudova M.S., Amshokova A.Kh., Bottaeva Z.Kh. Current state of species diversity and community structure of small mammals in the Tlyaratinsky Wildlife Sanctuary of the Dagestansky State Nature Reserve. *Amurian Zoological Journal*. 2026;18(1):190-206. doi 10.33910/2686-9519-2026-18-1-190-206 (in Russian)

Hall T.A. BioEdit: a user-friendly biological sequence alignment editor and analysis program for Windows 95/98/NT. *Nucleic Acids Symp Ser*. 1999;41:95-98

Kimura M. A simple method for estimating evolutionary rates of base substitutions through comparative studies of nucleotide sequences. *J Mol Evol.* 1980;16(2):111-120. doi 10.1007/BF01731581

Lashkova E.I., Dzeverin I.I. The possible role of interspecific competition in the formation of specific geographic ranges in wood mice *Sylvaemus* (Rodentia, Muridae). *Vestnik Zoologii*. 2004;38(6):41-46 (in Russian)

Mammalian Fauna of the USSR. Moscow; Leningrad: Nauka Publ., 1963 (in Russian)

Markova A.K. Faunas of small mammals of the first half of the Middle Pleistocene in Europe. *Izvestiya Rossiiskoy Akademii Nauk. Seriya Geograficheskaya = Bulletin of the RAS. Geographical series.* 2016; 1:87-102. doi 10.15356/0373-2444-2016-1-87-102 (in Russian)

Markova A.K. European faunas of small mammals in the second half of the Mid-Pleistocene: species spectra, spatial distribution, correlation. *Byulleten' Komissii po Izucheniyu Chetvertichnogo Perioda = Bulletin of Comission for Study of Quaternary.* 2017;75:11-33 (in Russian)

Michaux J.R., Libois R., Filippucci M.G. Phylogeographic history of the yellow-necked fieldmouse (*Apodemus flavicollis*) in Europe and in the near and Middle East. *Mol Phylogenet Evol.* 2004;32(3):788-798. doi 10.1016/j.ympev.2004.02.018

Okulova N.M., Ryabova T.E., Vasilenko L.E., Yunicheva Yu.V. Biotopic distribution of small mammals in mountains and foothills of Krasnodar region and Republic of Adygea. In: Mammals of Mountainous Territories: Proceedings of the international conference. Moscow, 2007;234-239 (in Russian)

Pavlinov I.Ya. Brief Guide to Land Animals of Russia. Moscow: Moscow State University Press, 2002 (in Russian)

Pavlinov I.Ya., Lisovsky A.A. The Mammals of Russia: a taxonomic and geographic reference. Moscow, 2012 (in Russian)

Poliakova T.A. Adaptive strategies and genetic stability of species of the genus *Spiraea* (Rosaceae) in natural population systems. *Uspekhi Sovremennoi Biologii = Advances in Current Biology.* 2022; 142(5):530-542. doi 10.31857/S0042132422050118 (in Russian)

Popov V.A. Mammals of the Volga-Kama Region: Insects, Bats, Rodents. Kazan, 1960 (in Russian)

Pushkin S.V. Rare and Endangered Species of Insects of the Central Ciscaucasia: Insects. Moscow; Berlin: Direct-Media Publ., 2015 (in Russian)

Radespiel U., Bruford M.W. Fragmentation genetics of rainforest animals: insights from recent studies. *Conserv Genet*. 2014;15:245-260. doi 10.1007/s10592-013-0550-3

Rambaut A., Drummond A.J., Xie D., Baele G., Suchard M.A. Posterior summarization in Bayesian phylogenetics using Tracer 1.7. *Syst Biol.* 2018:67(5):901-904. doi 10.1093/sysbio/syy032

Ronquist F., Huelsenbeck J.P. MrBayes 3: Bayesian phylogenetic inference under mixed models. *Bioinformatics*. 2003;19(12):1572-1574. doi 10.1093/bioinformatics/btg180

Shad H.H., Darvish J., Pouyani E.R. Genetic variation in populations of field mouse *Apodemus witherbyi* (Thomas, 1902) (Rodentia: Muridae) in Iran inferred from mitochondrial cytochrome *b* gene sequences and geometric morphometrics. *Acta Zool Bulg*. 2016;68(3): 311-320

Sigida R.S. Adaptations of Ground Beetles to Edaphic Factors under the Conditions of Anthropogenic Landscapes of Central Ciscaucasia. Extended Abstract of Dr. Biol. Sci. Diss. Astrakhan, 2010 (in Russian)

Soulé M.E., Simberloff D. What do genetics and ecology tell us about the design of nature reserves? *Biol Conserv*. 1986;35(1):9-40. doi 10.1016/0006-3207(86)90025-X

Stakheev V.V. The Role of Historical and Ecological Factors in the Formation of the Fauna and Population Dynamics of Insectivores and Rodents in the Plains of Southern European Russia. Dr. Biol. Sci. Diss. Rostov-on-Don, 2024 (in Russian)

Stakheev V.V., Bogdanov A.S., Vodolazhskiĭ D.I. Revision of the species composition of the wood mice from the genus *Sylvaemus* from the territory of Rostov oblast using karyological, allozyme and molecular genetic analysis. *Russ J Genet.* 2011;47(5):579-589. doi 10.1134/S1022795411050152

Suchard M.A., Lemey P., Baele G., Ayres D.L., Drummond A.J., Rambaut A. Bayesian phylogenetic and phylodynamic data integration using BEAST 1.10. *Virus Evol*. 2018;4(1):vey016. doi 10.1093/ve/vey016

Sukhikh N.M. Molecular and Morphological Studies of Cryptic Species of *Copepoda* in Continental Waters of Russia and Adjacent Territories. Extended Abstract of Cand. Biol. Sci. Diss. St. Petersburg, 2013 (in Russian)

Suzuki Y., Tomozawa M., Koizumi Y., Tsuchiya K., Suzuki H. Estimating the molecular evolutionary rates of mitochondrial genes referring to Quaternary ice age events with inferred population expansions and

dispersals in Japanese *Apodemus. BMC Evol Biol*. 2015;15:187. doi 10.1186/s12862-015-0463-5

Svitoch A.A., Sobolev V.M. Pleistocene straits of the Manych river: morphology, structure and evolution. *Vestnik Moskovskogo Universiteta. Seria 5. Geografiya = Moscow University Bulletin. Series 5. Geography*. 2011;4:70-77 (in Russian)

Tajima F. Statistical method for testing the neutral mutation hypothesis by DNA polymorphism. *Genetics*. 1989;123(3):585-595. doi 10.1093/genetics/123.3.585

Tamura K., Stecher G., Peterson D., Filipski A., Kumar S. MEGA6: Molecular Evolutionary Genetics Analysis version 6.0. *Mol Biol Evol.* 2013;30(12):2725-2729. doi 10.1093/molbev/mst197

Tatarinov K.A. Fauna of the Ridges of Ukraine. Lviv: Lviv University Publ., 1973 (in Russian)

Tembotov A.K. Geography of Mammals of the North Caucasus. Nalchik: Elbrus Publ., 1972 (in Russian)

Tembotova F.A. Mammals of the Caucasus and the Surrounding Seas. Moscow, 2005 (in Russian)

Tesakov A.S. Evolution of Small Mammal Faunas and Continental Biostratigraphy of the Late Cenozoic in Southern Eastern Europe and Western Asia. Dr. Geol.-Miner. Sci. Diss. Moscow, 2021 (in Russian)

Vereshchagin N.K. The Mammals of the Caucasus. A History of the Evolution of the Fauna. Moscow; Leningrad, 1959 (in Russian)

Vorontsov N.N., Boyeskorov G.G., Mezhzherin S.V., Lyapunova E.A., Kandaurov A.S. Systematics of the Caucasian wood mice of the subgenus *Sylvaemus* (Mammalia, Rodentia, *Apodemus*). *Zoologicheskiy Zhurnal*. 1992;71(3):119-131 (in Russian)

Wang W., Qiao Y., Li S., Pan W., Yao M. Low genetic diversity and strong population structure shaped by anthropogenic habitat fragmentation in a critically endangered primate, *Trachypithecus leucocephalus. Heredity.* 2017;118(6):542-553. doi 10.1038/hdy.2017.2

Yalkovskaya L., Sibiryakov P., Borodin A. Phylogeography of the striped field mouse (*Apodemus agrarius* Pallas, 1771) in light of new data from central part of Northern Eurasia. *PLoS One*. 2022;17(10):e0276466. doi 10.1371/journal.pone.0276466

Yasuda S.P., Vogel P., Tsuchiya K., Han S.-H., Lin L.-K., Suzuki H. Phylogeographic patterning of mtDNA in the widely distributed harvest mouse (*Micromys minutus*) suggests dramatic cycles of range contraction and expansion during the mid-to-late Pleistocene. *Can J Zool.* 2005;83(11):1411-1420. doi 10.1139/z05-139

Zagorodniuk N.V., Boeyskorov G.G., Zykov A.E. Variability and taxonomic status of steppe forms of mice of the genus *Sylvaemus* (*falzfeini – fulvipectus – hermonensis – arianus*). *Vestnik Zoologii.* 1997;31(5-6):37-56 (in Russian)

Conflict of interest. The authors declare no conflict of interest.

Received September 18, 2025. Revised April 7, 2026. Accepted June 15, 2026.

Vavilovskii Zhurnal Genetiki i Selektsii
Vavilov Journal of Genetics and Breeding. 2026;30(6):938-948

doi 10.18699/vjgb-26-94

DNA methylation analysis of aortic wall tissue in ascending aortic dilatation/aneurysm and dissection

I.A. Goncharova, A.A. Zarubin, A.V. Markov, S.A. Shipulina, N.P. Babushkina, Iu.A. Koroleva, A.A. Sleptcov, M.S. Nazarenko

Research Institute of Medical Genetics, Tomsk National Research Medical Center of the Russian Academy of Sciences, Tomsk, Russia
irina.goncharova@medgenetics.ru

Abstract. Ascending aortic dilatation/aneurysm and dissection are life-threatening cardiovascular conditions. However, the epigenetic regulatory mechanisms within aortic cells underlying these pathologies remain poorly understood. This study aimed to identify differentially methylated genes (DMGs) in aortic tissues from patients with ascending aortic dilatation/aneurysm and dissection by performing a re-analysis of publicly available DNA methylation datasets. A re-analysis was conducted on three DNA methylation datasets (GSE50192, GSE202047, GSE84274) from the Illumina Infinium HumanMethylation450 BeadChip. To account for tissue heterogeneity, cellular deconvolution was performed using the HEpiDISH algorithm and a custom reference panel of cell-type-specific CpG sites for key vascular cell types (endothelial cells, fibroblasts, smooth muscle cells, immune cells). Our re-analysis revealed that aortic dissection and bicuspid aortic valve patients with aortic dilatation/aneurysm exhibit distinct DNA methylation profiles compared to intact aorta. These pathologies differ from each other in the number and the spectrum of DMGs. The adjustment for cellular heterogeneity eliminated the majority of the initially identified DMGs. However, this correction helped to make an assessment of vascular inflammation, characterize its impact on aortic wall stability, and identify genes with differential DNA methylation associated with the disease phenotypes, rather than with inter-group heterogeneity. The genes *NFIX*, *PCDH7*, *MED13L*, *LMO4*, *DIP2C*, *PLEKHF1*, *NKD1*, *C10orf41* (*ZNF503-AS2*), *ARAP2*, *TBX3*, and *TBX5*, which remained in the DMG status after adjustment for cellular composition and are expressed in individual cells/whole aortic tissue, can be considered as new candidate genes for the development of aortic dilatation/aneurysm in patients with bicuspid aortic valve. NFIX, LMO4, DIP2C, C10orf41 (ZNF503-AS2), MED13L, TBX3, TBX5 are transcriptional regulators or modulators; NKD1 is a recognized inhibitor of the Wnt pathway. Our findings highlight the necessity of a rigorous approach to cohort design, which includes comprehensive phenotyping (encompassing aortic valve morphology) and underscore the importance of future single-cell investigations.

Key words: ascending aortic dilatation/aneurysm; ascending aortic dissection; DNA methylation; HEpiDISH; cell-type adjustment

For citation: Goncharova I.A., Zarubin A.A., Markov A.V., Shipulina S.A., Babushkina N.P., Koroleva Iu.A., Sleptcov A.A., Nazarenko M.S. DNA methylation analysis of aortic wall tissue in ascending aortic dilatation/aneurysm and dissection. *Vavilovskii Zhurnal Genetiki i Selektsii = Vavilov J Genet Breed*. 2026;30(6):938-948. doi 10.18699/vjgb-26-94

Funding. The study was funded and conducted as part of a basic research program of the Research Institute of Medical Genetics (Tomsk NRMC), No. 122020300041-7.

Особенности метилирования ДНК в пораженных тканях аорты при дилатации/аневризме и расслоении восходящего отдела

И.А. Гончарова, А.А. Зарубин, А.В. Марков, С.А. Шипулина, Н.П. Бабушкина, Ю.А. Королёва, А.А. Слепцов, М.С. Назаренко

Научно-исследовательский институт медицинской генетики Томского национального исследовательского медицинского центра Российской академии наук, Томск, Россия
irina.goncharova@medgenetics.ru

Аннотация. Дилатация/аневризма и расслоение восходящей аорты относятся к жизнеугрожающим заболеваниям, и выявление эпигенетического ландшафта, регулирующего функционирование генома в клетках аорты при данной патологии, является актуальной задачей. В связи с этим в настоящем исследовании выполнена идентификация дифференциально метилированных генов (ДМГ) в тканях аорты при дилатации/аневризме и расслоении восходящего отдела с помощью реанализа данных по метилированию ДНК, представленных в открытом доступе в репозитории NCBI GEO (Gene Expression Omnibus). Проведен реанализ результатов исследований (GSE50192, GSE202047, GSE84274), реализованных на платформе Illumina Infinium HumanMethylation450 BeadChip. Биоинформатическая деконволюция клеточного состава тканей сосудов осуществлена с помощью алгоритма HEpiDISH, а также разработанного референса, включавшего набор CpG-сайтов, индекс метилирования которых специфичен для эндотелиальных клеток,

© Goncharova I.A., Zarubin A.A., Markov A.V., Shipulina S.A., Babushkina N.P., Koroleva Iu.A., Sleptcov A.A., Nazarenko M.S., 2026
This work is licensed under a Creative Commons Attribution 4.0 License

фибробластов, гладкомышечных и иммунных клеток. Реанализ данных показал, что расслоение аорты и ее дилатация/аневризма с двухстворчатым аортальным клапаном характеризуются специфическим профилем метилирования ДНК относительно интактной ткани аорты, поскольку различаются как по числу, так и по спектру ДМГ. Поправка на клеточный состав аннулирует основное количество ДМГ, но позволяет составить представление о наличии воспаления в ткани аорты, оцениваемого по степени инфильтрации ткани иммунными клетками, охарактеризовать роль воспалительного инфильтрата в нарушении целостности стенки аорты и выявить гены, отражающие различия, связанные с изучаемыми фенотипами, а не с межгрупповой гетерогенностью клеточных популяций. Гены *NFIX*, *PCDH7*, *MED13L*, *LMO4*, *DIP2C*, *PLEKHF1*, *NKD1*, *C10orf41* (*ZNF503-AS2*), *ARAP2*, *TBX3*, *TBX5*, оставшиеся в статусе ДМГ после поправки на клеточный состав и экспрессируемые в отдельных клетках/цельной ткани аорты, могут рассматриваться как новые гены-кандидаты развития дилатации/аневризмы аорты у пациентов с двухстворчатым аортальным клапаном. Белковые продукты генов *NFIX*, *LMO4*, *DIP2C*, *C10orf41* (*ZNF503-AS2*), *MED13L*, *TBX3* и *TBX5* являются транскрипционными факторами или регуляторами транскрипционной активности ДНК, а гена *NKD1* – ингибитором сигнального пути Wnt. Полученные данные подчеркивают необходимость строгого подхода к формированию групп сравнения с полным описанием исследуемого фенотипа, включающим морфологию аортального клапана, и проведения исследований на уровне отдельных клеток.

Ключевые слова: дилатация/аневризма восходящей аорты; расслоение восходящей аорты; метилирование ДНК; HEpiDISH; поправка на клеточный состав

Introduction

DNA methylation is one of the main mechanisms of epigenetic modifications of the genome, both under normal conditions and in pathology. Nevertheless, studies investigating DNA methylation in pathologically altered tissues from ascending aortic dilatation/aneurysm and dissection are scarce (Shah et al., 2015; Pan et al., 2017; Björck et al., 2018; Li N. et al., 2020; Liu et al., 2021; Chen Y. et al., 2022; Goncharova et al., 2024; Koroleva et al., 2024). The data obtained from these studies show little overlap, which is due to phenotypically heterogeneous patient groups, different tissues (fragments of various aortic segments, peripheral blood) used in the studies, and different methods for DNA methylation assessment. Nonetheless, a comprehensive analysis of the results permits several conclusions, including the following: differentially methylated regions between diseased and intact aortic tissue are enriched in genes implicated in cardiovascular system development; the MAPK, WNT, TGFβ, and HOX signaling pathways participate in the pathogenesis of aortic aneurysm; and aortic valve morphology constitutes a critical determinant of the pathogenetic mechanisms underlying ascending aortic dilatation/aneurysm progression.

It is well established that cellular heterogeneity constitutes one of the most significant factors influencing the outcomes of DNA methylation studies. The walls of blood vessels contain varying proportions of several cell types that comprise their layered structure, as well as immune cells. All of these cells exhibit distinct DNA methylation patterns. Hence, alterations in DNA methylation patterns may reflect changes in cellular composition rather than provide reliable information regarding aberrant DNA methylation. In the present study, we consider arterial cell composition as a variable that affects DNA methylation levels.

Therefore, the aim of the present study was to identify differentially methylated genes in diseased aortic tissues in ascending aortic dilatation/aneurysm and dissection, while adjusting for cell composition, by integrating and re-analyzing publicly available DNA methylation data from pathologically altered and control tissues of the ascending aorta deposited in the NCBI Gene Expression Omnibus (GEO) repository.

Materials and methods

We re-analyzed publicly available results of studies GSE50192, GSE202047, and GSE84274, which were performed using the Illumina Infinium HumanMethylation450 BeadChip platform.

A description of the studies GSE50192, GSE202047, and GSE84274, that were used for the re-analysis, is presented in Table 1. The samples analyzed in GSE50192 comprised autopsy material from seventeen somatic tissues obtained from four individuals: three males, two of whom died from myocardial infarction (aged 40 and 53 years) and one who died from hemorrhagic stroke at 54 years of age; and one female, who died from hemorrhagic stroke at 60 years of age. For subsequent analyses, we selected DNA methylation data from samples of coronary arteries, as well as from the ascending and abdominal aorta.

The samples included in GSE202047 are ascending aortic tissues from patients with Stanford type A dissection (TAAD) (n = 4) and from healthy organ donors (n = 4), hereinafter referred to as intact ascending aorta (IAA). Both patients and healthy donors were male, with mean ages of 49.10 ± 4.91 years and 47.92 ± 6.73 years, respectively.

In GSE84274, we analyzed ascending aortic tissue samples from patients with acute Stanford type A dissection and a tricuspid aortic valve (n = 12; 10 males (52.4 years), 2 females); from patients with aortic dilatation/aneurysm (d > 4.5 cm) and bicuspid aortic valve (TAA with BAV) (n = 6; 5 males (53.8 years), 1 female); and from healthy organ donors (IAA) (n = 6; all males, 36.7 years).

Statistical analysis of the data was performed using the *lumi* and *limma* packages within the R software environment (Bioconductor). Principal component analysis (PCA) was employed for dimensionality reduction. Correction for false discovery rate (FDR) in multiple comparisons was performed using the Benjamini–Hochberg method. β-values were used to assess DNA methylation levels.

CpG sites (DMS) were considered differentially methylated if they exhibited a difference in mean methylation levels between sample groups with FDR < 0.05 and $|\Delta\beta| \geq 0.2$. Genes containing DMS were defined as differentially methylated genes (DMGs). The first twenty sites with the greatest differen-

Table 1. Characteristics of the studies included in the re-analysis of DNA methylation data from tissues of the ascending and abdominal aorta, coronary arteries, and pathologically altered tissues of the ascending aorta

GEO DataSets accession number	Sample characteristics	Main findings	References
GSE50192	*n* = 4, 17 autopsy tissues, including paired samples of coronary arteries, ascending aorta, and abdominal aorta	The aorta and coronary arteries cluster together based on DNA methylation profiles and exhibit the highest number of tissue-specific differentially methylated regions within genes involved in vascular development processes	Lokk et al., 2014
GSE202047	*n* = 4, ascending aortic tissue from patients with Stanford type A dissection; *n* = 4, ascending aortic tissue from healthy organ donors	A total of 589 differentially methylated sites (*P*-value ≤ 0.05 and |β difference (Δβ)| ≥ 0.3) were identified within genes belonging to the MAPK (mitogen-activated protein kinases), TNF (tumor necrosis factor), apoptosis, angiogenesis, heart development, and other signaling pathways. The key genes identified were *FAS*, *ANGPT2*, *DUSP6*, *FARP1*, *CARD6*	Chen Y. et al., 2022
GSE84274	*n* = 12, ascending aortic tissue from patients with acute Stanford type A dissection and a tricuspid aortic valve (TAV); *n* = 6, ascending aortic tissue from patients with dilatation/aneurysm (*d* > 4.5 cm) and bicuspid aortic valve (BAV); *n* = 6, ascending aortic tissue from healthy organ donors	Dissection with TAV and dilatation/aneurysm of the ascending aorta with BAV are characterized by loss of DNA methylation at non-CpG sites and by distinct DNA methylation profiles at CpG sites. In aortic dilatation/aneurysm with BAV, EZH2 targets (histone-lysine N-methyltransferase EZH2) are predominantly hypermethylated. Aortic dissection is characterized by smooth muscle cell dedifferentiation, as well as by increased expression of the *RARA* gene (retinoic acid receptor alpha) associated with DNA hypomethylation	Pan et al., 2017

ces in DNA methylation level between the compared tissues, as determined by the |Δβ| value, were characterized in detail.

Identification of DMS in ascending aortic pathology with adjustment for cell composition was performed using the HEpiDISH algorithm for deconvolution of DNA methylation profiles (Hierarchical Epigenetic Dissection of Intra-Sample-Heterogeneity; Zheng et al., 2019), as well as a reference panel previously developed by our group and adapted for blood vessel tissues. This reference panel includes a set of CpG sites with methylation specific to endothelial cells (datasets GSE84395, GSE122126, GSE82234, GSE40699 from the GEO repository), fibroblasts (GSE40699), smooth muscle cells (SMCs) (GSE40699, GSE113061), immune cells (GSE35069), and the data ENCSR420WUN from the study ENCODE (Markov et al., 2020).

Functional annotation of the identified DMGs was performed using the gene expression database for aortic arch tissues (GTEx Portal; https://gtexportal.org), single-cell transcriptomic data from studies on ascending aortic aneurysm (PlaqView; https://plaqviewv2.pods.uvarc.io), gene expression data for ascending aortic aneurysm publicly available in the Gene Expression Omnibus database (GSE83675, GSE61128, GSE5180), as well as data from the scientific literature (Kim et al., 2010; Doppler et al., 2023; Huang M. et al., 2023).

We performed a comparative analysis between the set of DMGs and genes associated with coronary artery disease (CAD), myocardial infarction (MI), and bicuspid aortic valve (BAV) based on genome-wide association studies (GWAS) available in the GWAS Catalog database (https://www.ebi.ac.uk/gwas), as well as genes implicated in hereditary and syndromic forms of thoracic aortic aneurysm (Elbitar et al., 2021; Li Y. et al., 2021).

Results

Analysis of CpG site methylation profiles in aortic samples within the integrated dataset revealed that autopsy arterial samples (GSE50192) distinctly separate from arterial tissues collected during surgical treatment (GSE202047 and GSE84274) (Fig. 1).

Therefore, only the data from GSE202047 and GSE84274 were combined, including all samples. The data obtained from study GSE50192 were not analyzed further.

Identification of differentially methylated DNA sites in ascending aortic tissues: dilatation/aneurysm with valve anomaly and thoracic aortic dissection compared to intact aortic tissue

Comparative analysis of DNA methylation levels between tissues of TAA with BAV and IAA revealed 57 DMS (14 DMGs). Among all DMS, 22 were localized in CpG shores and 14 in CpG islands (Table 2; sheet "TAA with BAV_IAA" in the Supplementary Materials)[1]. The majority of DMS (84.2 %) were hypermethylated in TAA with BAV tissues relative to IAA.

Within the nucleotide sequences of annotated genes, 23 CpG sites were identified, eight of which were localized in promoters. Among the 23 CpG sites located within the sequences of known genes, the hypomethylated sites included those in the *DIP2C* (Δβ = –0.29), *TMEM132C* (Δβ = –0.29; Δβ = –0.25), *CD82* (Δβ = –0.23), and *ZFPM1* (Δβ = –0.22) genes, with the *CD82* CpG site (cg01889574) being located in the promoter. All of these hypomethylated DMS/DMGs, with the exception of *ZFPM1* (cg06099697), were among the top 10 sites with

[1] Supplementary Materials are available at: https://vavilov.elpub.ru/jour/manager/files/Suppl_Gonchar_Engl_30_6.xlsx

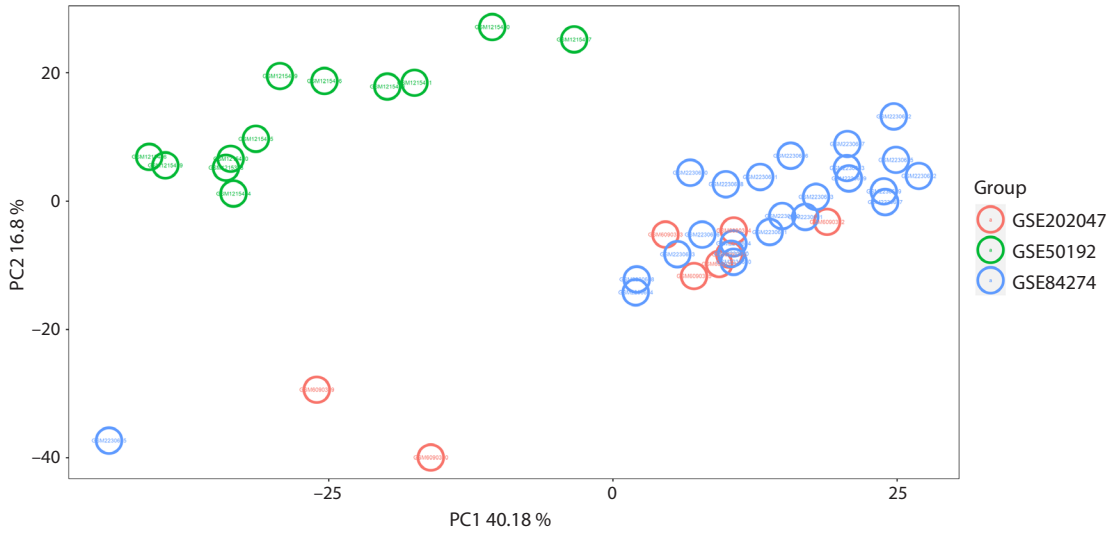


Fig. 1. Distribution of the analyzed samples in the space of the first two principal components according to the methylation level of CpG sites presented in GSE50192, GSE202047, and GSE84274.

Table 2. Characteristics of differentially methylated CpG sites/genes in the compared groups

Compared tissues	Number of DMS/DMGs	DMS localization (a/b/c/d/f)
TAA with BAV (*n* = 6) / IAA (*n* = 10)	Total 57/14	8/0/14/22/4
	Hyper 48 (84.2 %)/10	7/0/12/21/2
	Hypo 9 (15.8 %)/4	1/0/2/1/2
TAAD (*n* = 16) / IAA (*n* = 10)	Total 224/99	38/8/34/37/19
	Hyper 110 (49.1 %)/41	16/4/23/14/4
	Hypo 114 (50.9 %)/58	22/4/11/19/15
TAA with BAV (*n* = 6) / TAAD (*n* = 16)	Total 15/8	2/0/4/4/1
	Hyper 3 (20 %)/1	0/0/1/1/0
	Hypo 12 (80 %)/7	2/0/3/3/1

Note. BAV – bicuspid aortic valve, IAA – intact ascending aorta, TAA – thoracic aortic dilatation/aneurysm, TAAD – thoracic aortic aneurysm and dissection; DMS localization: a – promoter (TSS, 5′-UTR, 1st exon); b – 3′-UTR; c – CpG island; d – CpG shore (less than 2 kb from a CpG island); f – CpG shelf (2–4 kb from a CpG island).

the greatest differences in DNA methylation levels between the compared tissues (sheet "TAA with BAV_IAA" in the Supplementary Materials).

The remaining DMGs are characterized by the presence of CpG sites hypermethylated in TAA with BAV, with two DMS identified in each of the *ISL1* and *KCNN2* genes, and six DMS in the *TBX5* gene (sheet "TAA with BAV_IAA" in the Supplementary Materials). Among the top CpG sites with increased methylation levels in diseased aortic tissue were *ISL1* (Δβ = 0.32; Δβ = 0.25), *SNX25* (Δβ = 0.31), and *TBX5* (Δβ = 0.26; Δβ = 0.26; Δβ = 0.25). Site cg12836958 and two sites, cg23820885 and cg09042277, are located in the promoters of the *SNX25* and *TBX5* genes, respectively (sheet "TAA with BAV_IAA" in the Supplementary Materials).

Comparison of DNA methylation levels between ascending aortic tissues with dissection (TAAD) and IAA revealed 224 DMS (99 DMGs). Among all DMS, 37 were localized in CpG shores and 34 in CpG islands (Table 2; sheet "TAAD_IAA" in the Supplementary Materials). 130 CpG sites were identified within the nucleotide sequences of 99 genes, among them 38 CpG sites were localized in promoters. Hypermethylated DMS in TAAD samples accounted for 49.1 % of all DMS. Among the top 10 CpG sites, only those in the *ADARB2* (Δβ = 0.37; Δβ = 0.35) and *TTLL8* (Δβ = 0.28) genes were hypermethylated. Two hypomethylated sites, cg07162000 (Δβ = –0.24) and cg17861863 (Δβ = –0.23), were also identified in the *ADARB2* gene.

Among the top 10 CpG sites, four sites of the *TBX1* gene (Δβ = –0.34 to –0.29), located within a CpG island, as well as sites of the *FLJ42709* (*NR2F1-AS1*) (Δβ = –0.32), *COL21A1* (Δβ = –0.29), and *MAP3K5* (Δβ = –0.29) genes, were hypomethylated in TAAD samples (Table 2; sheet "TAAD_IAA" in the Supplementary Materials).

Comparison of DNA methylation levels between TAA with BAV and TAAD tissues revealed 15 DMS (8 DMGs). Among all DMS, four were localized in CpG shores and five in CpG

islands. In the *CYP2W1* and *PLEKHF1* genes, two CpG sites (cg09414673 and cg15561501, respectively) are located in the promoter (Table 2; sheet "TAA with BAV and TAAD" in the Supplementary Materials). Fifteen (80 %) of all DMS were hypomethylated in diseased aortic tissues from patients with TAA and BAV relative to aortic dissection (Table 2; sheet "TAA with BAV and TAAD" in the Supplementary Materials).

Among the CpG sites located within known genes, the greatest differences in methylation levels between the compared tissues were observed for sites hypomethylated in TAA with BAV tissues, specifically those in the *DIP2C* ($\Delta\beta = -0.27$) and *NFIX* ($\Delta\beta = -0.27$; $\Delta\beta = -0.24$) genes. Two sites, cg15561501 (*PLEKHF1*) and cg09414673 (*CYP2W1*), located in gene promoters, were also hypomethylated in TAA with BAV tissues ($\Delta\beta = -0.21$ each; sheet "TAA with BAV and TAAD" in the Supplementary Materials). A DMS in the *SLC1A3* gene was hypermethylated in diseased aortic tissues from patients with TAA and BAV ($\Delta\beta = 0.21$).

Reconstruction of the cellular composition of ascending aortic tissues in dilatation/aneurysm with valve anomaly, aortic dissection, and intact aortic tissue

Since tissue cellular composition is a significant factor for determining DMS (Houseman et al., 2015, 2016), bioinformatic deconvolution of the cellular composition of aortic tissues was also performed during data analysis (Fig. 2).

Application of the DNA methylation profile deconvolution algorithm to predict the proportions of expected cell types in ascending aortic tissues revealed that smooth muscle cells (SMCs) (33.7–88.7 %) and the leukocyte component (6.7–51.3 %) constitute a substantial proportion of cells, while vascular endothelial cells (ECs) are present to a lesser extent (4.2–21.2 %), and fibroblasts were not detected by the algorithm. Among leukocytes, monocytes account for a significant fraction (1.4–27.8 %).

The proportion of immune cells in IAA does not exceed 15 % (10.7 % on average). In TAA with BAV, this value ranges from 6 to 16 % (11.6 % on average). In TAAD, immune cell infiltration into the vascular wall ranges from 9 to 51 %, with a mean of 19.6 %, which is significantly higher than that in the intact aorta ($p = 0.003$) (Fig. 2).

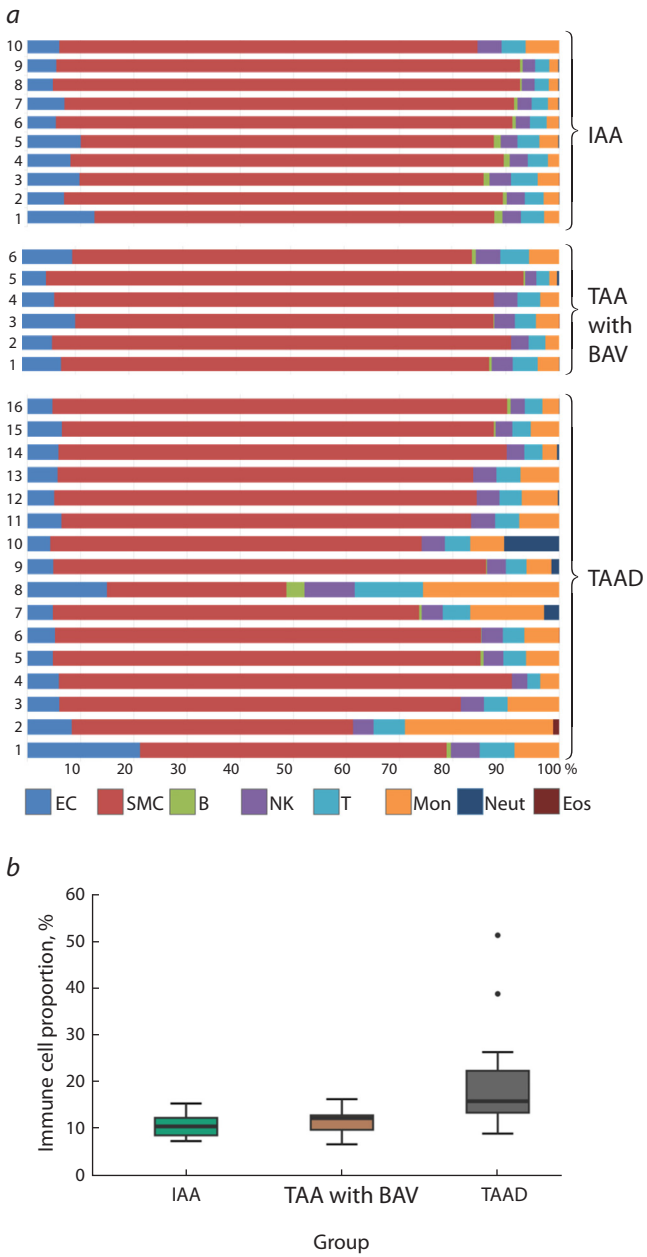


Fig. 2. Reconstruction of the cellular composition of the ascending aorta under normal and pathological conditions using the HEpiDISH algorithm and the developed methylome reference panel for vascular cells.

a – distribution of cell types in ascending aortic tissues in the studied groups (the vertical axis indicates the sample number within each group). EC – endothelial cells, SMC – smooth muscle cells, B – B lymphocytes, NK – natural killer cells, T – T lymphocytes, Mon – monocytes, Neut – neutrophils, Eos – eosinophils; *b* – proportion of immune cells in the studied sample groups according to the results of cellular composition assessment.

Identification of DMS and their host genes in ascending aortic pathology with adjustment for cell composition

After adjusting for cell composition, the list of CpG sites hypomethylated in TAA with BAV samples compared to IAA retained only site cg26561082 of the *DIP2C* gene ($\Delta\beta = -0.29$), located in a CpG shore region (Table 3).

Comparison of DNA methylation levels with adjustment for cell composition between the TAAD and IAA groups revealed no significant differences.

Comparison of DNA methylation levels between TAA with BAV and TAAD after adjustment for cell composition revealed 12 DMS, of which two were hypermethylated and ten were hypomethylated in the aorta with dilatation/aneurysm (Table 3). Seven differentially methylated genes (*LMO4*, *NFIX*, *CYP2W1*, *C10orf41* (*ZNF503-AS2*), *PLEKHF1*, *DIP2C*, *NKD1*) contained hypomethylated CpG sites in TAA with BAV relative to aortic dissection (Table 3).

Furthermore, three CpG sites were located in intergenic regions: cg02060919 (*PCDH7/ARAP2*) was hypomethylated in the TAA with BAV group compared to TAAD, while sites

Table 3. Differentially methylated CpG sites between the studied groups after adjustment for cell composition

CpG-site, genome coordinates (GRCh37/hg19)	Localization of the CpG site relative to the nearest CpG island	Δβ TAA with BAV/ IAA	Δβ TAA with BAV/ TAAD	Gene
cg26561082, chr10:410363	chr10:409201–409523/CpG-shore, no	**–0.29**	**–0.27**	*DIP2C*
cg22824635, chr19:13112283	chr19:13112170–13112809/CpG-island, no	–0.17	**–0.27**	*NFIX*
cg06744585, chr19:13135808	chr19:13135317–13136169/CpG-island, no	–0.14	**–0.24**	
cg01393939, chr1:87803705	chr1:87800835–87801252/CpG-shelf, no	–0.18	**–0.23**	*LMO4*
cg10642548, chr10:77165750	chr10:77155128–77169600/CpG-island, no	–0.23*	**–0.22**	*C10orf41* (*ZNF503-AS2)*
cg06262069, chr10:76835911	chr10:77155128–77169600/CpG-island, no	–0.21*	**–0.22**	
cg02015823, chr16:49142490	chr16:50583175–50583465/CpG-shore, no	–0.05	**–0.22**	*NKD1*
cg15561501, chr19:30160603	chr19:30156038–30156795/CpG-shelf, 5′ UTR	–0.07	**–0.21**	*PLEKHF1*
cg09414673, chr7:1022797	chr7:1024021–1024233/CpG-shore, TSS	–0.16	**–0.21**	*CYP2W1*
cg02060919, chr4:32932085	No	–0.072	**–0.24**	*PCDH7/ARAP2* intergenic
cg16945186, chr12:115103960	chr12:115102687–115103982/CpG-island, no	**0.26**	**0.24**	*TBX5/TBX3* intergenic
cg26343001, chr12:115104274	chr12:115104848–115105548/CpG-shore, no	**0.25**	**0.21**	*TBX3/MED13L* intergenic

Note. Values of Δβ for CpG sites meeting the DMS criteria (FDR < 0.05 and |Δβ| ≥ 0.2) are shown in bold; * Δβ for CpG sites with FDR > 0.05; TSS, 5′-UTR – promoter.

cg16945186 (*TBX5/TBX3*) and cg26343001 (*TBX3/MED13L*) were hypermethylated in ascending aortic dilatation/aneurysm relative to both aortic dissection and intact aortic tissue.

Thus, after adjustment for cell composition, TAA with BAV compared to both IAA and TAAD shows decreased methylation levels of the majority of identified DMGs. These include genes encoding functionally active molecules (transcription factors *DIP2C*, *LMO4*, *NFIX*; lncRNA *C10orf41* (*ZNF503-AS2*)), an inhibitor of the Wnt signaling pathway (*NKD1*), as well as genes whose protein products mediate apoptosis and autophagy (*PLEKHF1*), focal adhesion and intercellular interactions (*PCDH7*, *ARAP2*), or belong to the cytochrome P450 family (*CYP2W1*).

Elevated methylation levels were observed for intergenic CpG sites, which likely influence the functional activity of the transcription factor genes *TBX3* and *TBX5*, as well as the *MED13L* gene, whose protein product belongs to the mediator complex family (MED), a complex that plays a key role in the transcription of numerous eukaryotic genes.

Functional annotation of DMGs using databases and published studies

Analysis of expression of the DMGs identified after cell composition adjustment in aortic arch tissues according to the GTEx Portal data showed that, among the aforementioned genes, *NFIX* (131.7 TPM – transcripts per million) and *PCDH7* (65.4 TPM) exhibited the highest expression levels. The genes *MED13L*, *LMO4*, *DIP2C*, *PLEKHF1*, and *NKD1* were expressed at moderate levels (32.3; 29.6; 28.9; 27.1; and 16.5, respectively), whereas *C10orf41* (*ZNF503-AS2*), *TBX3*, *ARAP2*, *TBX5*, and *CYP2W1* showed almost no expression in the aortic arch (0.06–3.9 TPM).

Analysis of gene expression data for ascending aortic aneurysm in patients with BAV and TAV, available from public repositories (GSE5180, GSE83675, GSE61128 from the GEO repository) and scientific publications (Kim et al., 2010; Doppler et al., 2023), led to the conclusion that the DMGs identified in the present study do not significantly alter their functional activity either in the diseased aorta relative to intact tissues, or in dilated aortic tissues from patients with different aortic valve anatomy.

According to data from the PlaqView resource, in aortic tissue from 11 individuals, including eight patients with ascending aortic aneurysm and three healthy individuals (Li Y. et al., 2020), the *NFIX* and *LMO4* genes are expressed in a substantial number of SMCs and fibroblasts, with high expression levels for *NFIX* and approximately half that for *LMO4* (Fig. 3). Functional activity of the *PCDH7* gene was detected at high levels in a large percentage of SMCs and, to a lesser extent, in fibroblasts. The *DIP2C* gene is expressed at moderate levels, but in a small number of SMCs, fibroblasts, and mast cells. *ARAP2* activity was detected in T, B, and NK cells. The *MED13L* gene is expressed in a wide range of cells at moderate levels. The remaining DMGs are expressed in no more than 20 % of cells in ascending aortic tissues (Fig. 3).

Comparative analysis of the DMGs with lists of genes associated with coronary artery disease (CAD), thoracic aortic aneurysm based on GWAS results, bicuspid aortic valve, or genes implicated in hereditary aortic aneurysms revealed that rs543659530 in the *PCDH7* gene, encoding protocadherin 7, is associated with CAD in patients with type 2 diabetes mellitus (T2DM) (Song et al., 2021), and rs61937394 in the *MED13L* gene, whose protein product belongs to the mediator complex involved in transcription regulation, is associated with the development of ascending aortic aneurysm (Pirruccello et al., 2022). The remaining DMGs were not present in any of these lists.

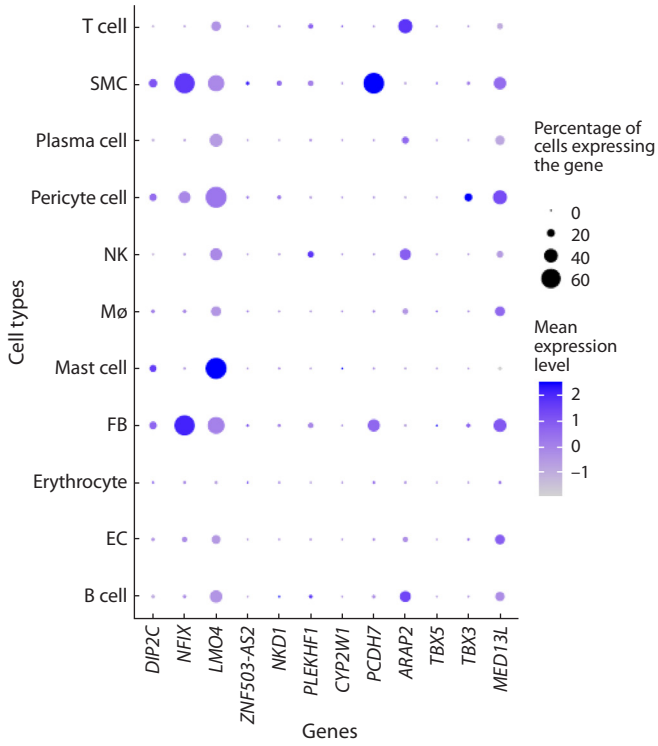


Fig. 3. Cell types and mean relative expression levels of the DMGs identified in the present study according to the PlaqView resource, in a single-cell dataset of the ascending aorta from 11 individuals, including eight patients with ascending aortic aneurysm and three healthy individuals (Li Y. et al., 2020).

DMG – differentially methylated genes. SMC – smooth muscle cells; NK – natural killer cells; Mø – macrophages; FB – fibroblasts; EC – endothelial cells.

Discussion

The use of a DNA methylation profile deconvolution algorithm and cellular composition assessment with a customized reference panel for vascular tissues allowed us to conclude that smooth muscle cells and immune cells constitute a substantial proportion of cells in the ascending aorta. The degree of immune cell infiltration into the vascular wall in ascending aortic dissection significantly exceeds that observed in intact vascular tissues.

Sun Pan et al. (2017) also performed adjustment for cell composition, albeit using a different algorithm (Houseman CP). The authors observed a decrease in the mean number of SMCs and an increase in the number of ECs in aortic dissection compared to normal aorta and dilated aorta/aneurysm with BAV (Pan et al., 2017). In the present study, the mean numbers of SMCs and ECs did not differ between groups, whereas immune cell infiltration was higher in aortic dissection. This finding may indicate a role of the inflammatory infiltrate in disrupting the integrity of the aortic wall.

It should also be noted that, according to the deconvolution algorithm results, fibroblasts were not detected in the studied samples, despite their expected abundance based on generally accepted knowledge of aortic wall structure.

Numerous studies employing transcriptome and epigenome analysis technologies in single cells from human artery samples and animal models have demonstrated that SMCs possess extensive phenotypic plasticity and, together with fibroblasts and pericytes, typically constitute a single supercluster of cells originating from mesenchymal stem cells (Mosquera et al., 2023; Zhao et al., 2025).

Thus, we believe that the "SMC component" in the deconvolution results may represent a mixture of different cell types (with the exception of pericytes) that are similar in their gene expression profiles and, apparently, DNA methylation patterns, including a spectrum of differentiated and modulated SMCs, as well as fibroblasts.

The re-analysis of DNA methylation data in aortic tissues revealed that dilatation/aneurysm with BAV and ascending aortic dissection exhibit distinct DNA methylation statuses relative to intact aortic tissue, as these phenotypes differ from each other both in the number and in the spectrum of DMGs. However, adjustment for cell composition eliminates the majority of DMS, leaving only one CpG site in the *DIP2C* gene and two sites in the intergenic regions *TBX5/TBX3* and *TBX3/MED13L* when comparing aortic dilatation/aneurysm with BAV and intact tissue. Comparison between dilatation/aneurysm and aortic dissection revealed ten differentially methylated CpG sites in the genes *DIP2C*, *LMO4*, *NFIX*, *C10orf41* (*ZNF503-AS2*), *PLEKHF1*, *NKD1*, *CYP2W1*, *PCDH7/ARAP2*, *TBX5/TBX3*, and *TBX3/MED13L*.

The obtained results likely reflect differences in DNA methylation patterns associated with sample cellular composition variability to a greater extent than significant epigenetic differences between diseased and intact aortic tissues. This is supported by earlier studies of gene expression conducted on different tissue types (intima-media and adventitia of the aorta, as well as intima-media of the internal thoracic artery), which demonstrated that between 22.5 and 52 % of all genes are differentially expressed in pairwise tissue comparisons (Folkersen et al., 2011).

Furthermore, the Gene Expression Omnibus data used for the re-analysis did not specify the aortic valve morphology in patients with dissection (GSE202047), or indicated a tricuspid aortic valve (GSE84274), as was also the case for healthy donors. In this context, the DMGs identified between the compared groups (TAA with BAV/IAA and TAA with BAV/TAAD), even after adjustment for cell composition, may reflect DNA methylation features of aortic tissues determined by aortic valve morphology rather than by aortic dilatation *per se*. This is indirectly supported by the observation that the largest number of DMGs, obtained when comparing groups with a tricuspid valve (TAAD/IAA), does not reflect differences in DNA methylation patterns between diseased and intact aortic tissue with the same aortic valve morphology, since these differences disappear after adjustment for cell composition.

DNA methylation analysis of aortic tissues conducted by other research groups has shown that, consistent with the present study, hypomethylated regions of the *DIP2C*, *LMO4*, *NFIX*, *NKD1*, and *CYP2W1* genes are detected in patients with BAV, both in aneurysmal and in intact ascending aortic tissues (Björck et al., 2018). Moreover, significantly more

hypomethylated regions are observed in ascending aortic tissues with bicuspid compared to tricuspid aortic valve, which is accompanied by a more active transcriptional profile in aortic tissues with BAV (Björck et al., 2018). At the same time, in atherosclerotic plaque of the aorta compared to intact aortic tissue from the same donors (where aortic valve morphology was not specified), hypermethylated CpG sites were identified in the *DIP2C*, *NFIX*, *NKD1*, and *ARAP2* genes (Zaina et al., 2014).

Differences in aortic valve morphology also result in altered ascending aortic function, which are largely determined by the asymmetric distribution of blood flow velocity by BAV, contributing to a higher frequency of ascending aortic pathologies (Viscardi et al., 2010). Hemodynamic disturbances are the primary factor leading to alterations in the structural organization of the vascular tissue and in genomic functioning, resulting in the formation of distinct patterns of expressed genes, microRNAs, and proteins in patients with BAV and TAV, which however drive the development of the same phenotype (Folkersen et al., 2011; Kjellqvist et al., 2013; Gallo et al., 2018; Freiholtz et al., 2023). Differences in gene expression profiles between BAV and TAV groups in ascending aortic aneurysm have been identified both in ascending aortic tissues and in individual cell types, but the lists of differentially expressed genes do not include the DMGs identified in the present study (Lei et al., 2022; Doppler et al., 2023; Huang M. et al., 2023).

Genetic factors play an important role in the etiology of BAV, with heritability estimates ranging from 47 to 89 % (Gehlen et al., 2023). Association studies, GWAS, and analyses of rare clinically significant variants have led to the identification of more than forty genes associated with BAV development (Gago-Díaz et al., 2017; Chen S. et al., 2022; Gehlen et al., 2023; Carlisle et al., 2024; Sticchi et al., 2025). However, the genes identified in the present study are not among those associated with BAV development. Nevertheless, evidence suggests an association between the DMGs identified in the present study and cardiovascular diseases (CVD). For instance, the *DIP2C* gene is involved in transcription factor binding, and its deficiency leads to the development of congenital heart defects (Xia et al., 2025).

The *NFIX* and *LMO4* genes encode transcription factors. Clinically significant variants of the *NFIX* gene are associated with thoracic aortic aneurysm and dissection in Malan syndrome (Oshima et al., 2017; Chevarin et al., 2020), whereas *LMO4* is overexpressed in regions of turbulent blood flow, including the carotid arteries, the lesser curvature of the aortic arch, and the coronary arteries, suggesting a potential role for this gene in mechanosensitivity and pro-atherogenic response (Ni et al., 2010). The *C10orf41* (*ZNF503-AS2*) gene encodes a long non-coding RNA (lncRNA). Increased methylation levels of the *ZNF503-AS2* gene were detected in the plasma of patients with myocardial infarction following percutaneous coronary intervention compared to healthy donors (Ren et al., 2022).

PLEKHF1 is a lysosome-associated protein that induces apoptosis and autophagy. It is known that autophagy is closely associated with the onset and progression of atherosclerosis, myocardial ischemia/reperfusion, heart failure, and aortopathy in combination with BAV (Forte et al., 2019; Jiang B. et al., 2023). *PLEKHF1* is one of eight genes associated with overall survival in dilated cardiomyopathy, and its expression is reduced in myocardial tissues of patients compared to the control group (Zhang et al., 2022). Overall, the *PLEKHF1* gene is considered a potential biomarker for the development of CAD in patients with T2DM and cardiomyopathy (Huang Q. et al., 2020; Zhang et al., 2022).

The protein product of the *NKD1* gene is an inhibitor of the Wnt signaling pathway, which is essential for the generation of cardiac progenitor cells, neural crest cell migration and differentiation, and the formation of the outflow tract and heart valves (Weerackoon et al., 2021). Dysregulation of the Wnt signaling pathway is one of the factors influencing the development of cardiovascular diseases, including structural abnormalities of the aorta, which is directly associated with a predisposition to aneurysms (Pozo-Vilumbrales et al., 2025).

Variants of the transcription factor gene *TBX5*, which is essential for the formation of the atrial and ventricular septa and the cardiac conduction system, are associated with the development of congenital heart defects, Holt–Oram and Brugada syndromes, atrial fibrillation, acute myocardial infarction, and BAV (Steimle, Moskowitz, 2017; Wang F. et al., 2017; Wang S. et al., 2019; Jiang W.F. et al., 2020). TBX3 is also a transcription factor important for the differentiation of the sinoatrial and atrioventricular nodes. Variants of the *TBX3* gene are associated with cardiac conduction abnormalities, the development of atrioventricular block, hypertrophic cardiomyopathy, atrial fibrillation, and heart failure (Lakda et al., 2025).

ARAP2 is a protein that activates the Arf6 GTPase and is involved in the regulation of focal adhesion, remodeling of actin fibers, and integrin recycling in vascular cells (Vitali et al., 2019). Altered *ARAP2* gene activity in the aorta in mouse models ($Eln^{-/-}$ line) reflects modulation of the cellular cytoskeleton and intercellular interactions in the aortic vascular wall under conditions of severe elastic fiber defects (Staiculescu et al., 2018). In humans, the single nucleotide variant rs116215256 of the *ARAP2* gene is associated with cardiac troponin I levels, which is known to be a regulator of myocardial contraction (Yang et al., 2021).

The *PCDH7* gene encodes protocadherin 7, a membrane protein involved in cell recognition and cell–cell adhesion. The cadherin family plays a key role in morphogenesis as well as in the development of various pathological conditions, including cardiovascular diseases such as dilated cardiomyopathy, atherosclerosis, and restenosis, which involve significant remodeling of tissue architecture leading to clinical manifestations of disease (Joshi et al., 2024).

The *MED13L* gene encodes one of the subunits of the large mediator complex, which is involved in regulating the transcriptional activity of genes in various signaling pathways during early development, including heart development (Henry et al., 2025). Pathogenic variants in the *MED13L* gene have been associated with transposition of the great arteries, coarctation of the aorta, and other cardiovascular diseases (Schiano, Napoli, 2025).

Thus, the genes identified in the present study play important roles in the development of the cardiovascular system, and disruption of their function may lead to the development of cardiovascular diseases. The association of these genes with aortic dilatation/aneurysm in patients with bicuspid aortic valve through alterations in their epigenetic regulation in diseased aortic tissues is reported for the first time in the present study.

Conclusion

Assessment of cellular composition based on DNA methylation profiles in aortic tissue samples allows us to evaluate the presence and extent of inflammation, as determined by the degree of immune cell infiltration into the arterial wall. This approach also characterizes the role of the inflammatory infiltrate in disrupting aortic wall integrity, as well as delineates genes that reflect differences associated with the studied phenotypes rather than sample cellular heterogeneity.

The genes *NFIX*, *PCDH7*, *MED13L*, *LMO4*, *DIP2C*, *PLEKHF1*, *NKD1*, *C10orf41* (*ZNF503-AS2*), *ARAP2*, *TBX3*, and *TBX5* may be considered novel candidate genes for the development of aortic dilatation/aneurysm in patients with bicuspid aortic valve. Particular attention should be paid to the genes *NFIX*, *LMO4*, *DIP2C*, *C10orf41* (*ZNF503-AS2*), *MED13L*, *TBX3*, and *TBX5*, which encode transcription factors or regulators of DNA transcriptional activity, as well as the gene *NKD1*, an inhibitor of the Wnt signaling pathway.

Furthermore, the obtained data once again underscore the need for a rigorous approach to forming comparison groups with a clear and complete description of the studied phenotype, as well as for conducting studies at the single-cell level.

References

Björck H.M., Du L., Pulignani S., Paloschi V., Lundströmer K., Kostina A.S., Österholm C., … Teixidó-Tura G., Maleki S., Franco-Cereceda A., Eriksson P.; Mechanistic Interrogation of Bicuspid Aortic Valve associated Aortopathy (MIBAVA) Leducq Consortium. Altered DNA methylation indicates an oscillatory flow mediated epithelial-to-mesenchymal transition signature in ascending aorta of patients with bicuspid aortic valve. *Sci Rep*. 2018;8(1):2777. doi 10.1038/s41598-018-20642-4

Carlisle S.G., Albasha H., Michelena H.I., Sabate-Rotes A., Bianco L., De Backer J., Mosquera L.M., … Milewicz D.M., Body S.C., Prakash S.K.; EBAV Investigators; BAVCon Investigators. Rare genomic copy number variants implicate new candidate genes for bicuspid aortic valve. *PLoS One*. 2024;19(9):e0304514. doi 10.1371/journal.pone.0304514

Chen S., Jin Q., Hou S., Li M., Zhang Y., Guan L., Pan W., Ge J., Zhou D. Identification of recurrent variants implicated in disease in bicuspid aortic valve patients through whole-exome sequencing. *Hum Genomics*. 2022;16(1):36. doi 10.1186/s40246-022-00405-z

Chen Y., Xu X., Chen Z., Huang B., Wang X., Fan X. DNA methylation alternation in Stanford – a acute aortic dissection. *BMC Cardiovasc Disord*. 2022;22(1):455. doi 10.1186/s12872-022-02882-5

Chevarin M., Duffourd Y., Barnard R.A., Moutton S., Lecoquierre F., Daoud F., Kuentz P., … Deleuze J.F., Thauvin-Robinet C., Rivière J.B., O'Roak B.J., Faivre L. Excess of de novo variants in genes involved in chromatin remodelling in patients with marfanoid habitus and intellectual disability. *J Med Genet*. 2020;57(7):466-474. doi 10.1136/jmedgenet-2019-106425

Doppler C., Messner B., Mimler T., Schachner B., Rezk M., Ganhör C., Wechselberger C., Müller M., Puh S., Pröll J., Arbeithuber B., Müller T., Zierer A., Bernhard D. Noncanonical atherosclerosis as the driving force in tricuspid aortic valve associated aneurysms – a trace collection. *J Lipid Res*. 2023;64(3):100338. doi 10.1016/j.jlr.2023.100338

Elbitar S., Renard M., Arnaud P., Hanna N., Jacob M.P., Guo D.C., Tsutsui K., … Michel J.B., Jondeau G., Sakai L.Y., Boileau C., Abifadel M. Pathogenic variants in *THSD4*, encoding the ADAMTS-like 6 protein, predispose to inherited thoracic aortic aneurysm. *Genet Med*. 2021;23(1):111-122. doi 10.1038/s41436-020-00947-4

Folkersen L., Wågsäter D., Paloschi V., Jackson V., Petrini J., Kurtovic S., Maleki S., … Michel J.B., Liska J., Gabrielsen A., Franco-Cereceda A., Eriksson P. Unraveling divergent gene expression profiles in bicuspid and tricuspid aortic valve patients with thoracic aortic dilatation: the ASAP study. *Mol Med*. 2011;17(11-12):1365-1373. doi 10.2119/molmed.2011.00286

Forte A., Cipollaro M., De Feo M., Della Corte A. Is there a role for autophagy in ascending aortopathy associated with tricuspid or bicuspid aortic valve? *Clin Sci* (*Lond*). 2019;133(7):805-819. doi 10.1042/CS20181092

Freiholtz D., Bergman O., Lång K., Poujade F.A., Paloschi V., Granath C., Lindeman J.H.N., Olsson C., Franco-Cereceda A., Eriksson P., Björck H.M. Bicuspid aortic valve aortopathy is characterized by embryonic epithelial to mesenchymal transition and endothelial instability. *J Mol Med* (*Berl*). 2023;101(7):801-811. doi 10.1007/s00109-023-02316-5

Gago-Díaz M., Brion M., Gallego P., Calvo F., Robledo-Carmona J., Saura D., Sánchez V., … Carracedo Á., Muehlschlegel J.D., García-Dorado D., Body S.C., Evangelista A. The genetic component of bicuspid aortic valve and aortic dilation. An exome-wide association study. *J Mol Cell Cardiol*. 2017;102:3-9. doi 10.1016/j.yjmcc.2016.11.012

Gallo A., Agnese V., Coronnello C., Raffa G.M., Bellavia D., Conaldi P.G., Pilato M., Pasta S. On the prospect of serum exosomal miRNA profiling and protein biomarkers for the diagnosis of ascending aortic dilatation in patients with bicuspid and tricuspid aortic valve. *Int J Cardiol*. 2018;273:230-236. doi 10.1016/j.ijcard.2018.10.005

Gehlen J., Stundl A., Debiec R., Fontana F., Krane M., Sharipova D., Nelson C.P., … Abdelilah-Seyfried S., Samani N.J., Erdmann J., Trenkwalder T., Schumacher J. Elucidation of the genetic causes of bicuspid aortic valve disease. *Cardiovasc Res*. 2023;119(3):857-866. doi 10.1093/cvr/cvac099

Goncharova I.A., Zarubin A.A., Shipulina S.A., Koroleva Iu.A., Panfilov D.S., Kozlov B.N., Nazarenko M.S. DNA methylation profiling in aneurysm and comorbid atherosclerosis of the ascending aorta. *Mol Biol*. 2024;58(3):439-449. doi 10.1134/s0026893324700079

Henry K.M., Gardner R.N., Oppman A.M., Daneshgar N., Rosales M., Martins I., Baskin K.K., Grueter C.E. Med13 and Med13L: critical redundant players in basal cardiac function and gene expression. *J Mol Cell Cardiol Plus*. 2025;13:100481. doi 10.1016/j.jmccpl.2025.100481

Houseman E.A., Kim S., Kelsey K.T., Wiencke J.K. DNA methylation in whole blood: uses and challenges. *Curr Environ Health Rep*. 2015;2(2):145-154. doi 10.1007/s40572-015-0050-3

Houseman E.A., Kile M.L., Christiani D.C., Ince T.A., Kelsey K.T., Marsit C.J. Reference-free deconvolution of DNA methylation data and mediation by cell composition effects. *BMC Bioinformatics*. 2016;17:259. doi 10.1186/s12859-016-1140-4

Huang M., Guan R., Qiu J., Gnamey A.J.E., Wang Y., Tian H., Sun H., Shi H., Sun W., Jia X., Wu J. Identification of immune-related signatures and pathogenesis differences between thoracic aortic aneurysm patients with bicuspid versus tricuspid valves via weighted gene co-expression network analysis. *PLoS One*. 2023;18(10):e0292673. doi 10.1371/journal.pone.0292673

Huang Q., Deng G., Wei R., Wang Q., Zou D., Wei J. Comprehensive identification of key genes involved in development of diabetes mellitus-related atherogenesis using weighted gene correlation net-

work analysis. *Front Cardiovasc Med*. 2020;7:580573. doi 10.3389/fcvm.2020.580573

Jiang B., Zhou X., Yang T., Wang L., Feng L., Wang Z., Xu J., Jing W., Wang T., Su H., Yang G., Zhang Z. The role of autophagy in cardiovascular disease: cross-interference of signaling pathways and underlying therapeutic targets. *Front Cardiovasc Med*. 2023;10:1088575. doi 10.3389/fcvm.2023.1088575

Jiang W.F., Xu Y.J., Zhao C.M., Wang X.H., Qiu X.B., Liu X., Wu S.H., Yang Y.Q. A novel TBX5 mutation predisposes to familial cardiac septal defects and atrial fibrillation as well as bicuspid aortic valve. *Genet Mol Biol*. 2020;43(4):e20200142. doi 10.1590/1678-4685-GMB-2020-0142

Joshi D., Coon B.G., Chakraborty R., Deng H., Yang Z., Babar M.U., Fernandez-Tussy P., … Traylor J.G., Jr., Orr A.W., Fernandez-Hernando C., Libreros S., Schwartz M.A. Endothelial γ-protocadherins inhibit KLF2 and KLF4 to promote atherosclerosis. *Nat Cardiovasc Res*. 2024;3(9):1035-1048. doi 10.1038/s44161-024-00522-z

Kim J.H., Na C.Y., Choi S.Y., Kim H.W., Du Kim Y., Kwon J.B., Chung M.Y., Hong J.M., Park C.B. Integration of gene-expression profiles and pathway analysis in ascending thoracic aortic aneurysms. *Ann Vasc Surg*. 2010;24(4):538-549. doi 10.1016/j.avsg.2010.01.007

Kjellqvist S., Maleki S., Olsson T., Chwastyniak M., Branca R.M., Lehtiö J., Pinet F., Franco-Cereceda A., Eriksson P. A combined proteomic and transcriptomic approach shows diverging molecular mechanisms in thoracic aortic aneurysm development in patients with tricuspid- and bicuspid aortic valve. *Mol Cell Proteomics*. 2013;12(2):407-425. doi 10.1074/mcp.M112.021873

Koroleva Iu.A., Goncharova I.A., Zarubin A.A., Shipulina S.A., Sleptsov A.A., Panfilov D.S., Kozlov B.N., Nazarenko M.S. Methylation levels in the 5′ region of the *TBX20* gene in the ascending aorta change in opposite direction in atherosclerosis and aneurysm. *Russ J Genet*. 2024;60(7):977-981. doi 10.1134/S102279542470042X

Lakda S., Davies R.H., Hingorani A.D., Paliwal N. A systematic review of GWAS on CMR imaging traits: genetic insights into cardiovascular structure, function, and diseases. *EBioMedicine*. 2025;121:105992. doi 10.1016/j.ebiom.2025.105992

Lei C., Kan H., Chen W., Yang D., Ren J., Xu F., Zhang H., Wang W., Zheng Y. Different gene co-expression patterns of aortic intima-media and adventitia in thoracic aortic aneurysm. *Gene*. 2022;819:146233. doi 10.1016/j.gene.2022.146233

Li N., Lin H., Zhou H., Zheng D., Xu G., Shi H., Zhu X., Gao J., Shao G., Sun L. Efficient detection of differentially methylated regions in the genome of patients with thoracic aortic dissection and association with MMP2 hypermethylation. *Exp Ther Med*. 2020;20(2):1073-1081. doi 10.3892/etm.2020.8753

Li Y., Ren P., Dawson A., Vasquez H.G., Ageedi W., Zhang C., Luo W., … Cassis L.A., Coselli J.S., Daugherty A., Shen Y.H., LeMaire S.A. Single-cell transcriptome analysis reveals dynamic cell populations and differential gene expression patterns in control and aneurysmal human aortic tissue. *Circulation*. 2020;142(14):1374-1388. doi 10.1161/CIRCULATIONAHA.120.046528

Li Y., Gao S., Han Y., Song L., Kong Y., Jiao Y., Huang S., Du J., Li Y. Variants of focal adhesion scaffold genes cause thoracic aortic aneurysm. *Circ Res*. 2021;128(1):8-23. doi 10.1161/CIRCRESAHA.120.317361

Liu P., Zhang J., Du D., Zhang D., Jin Z., Qiu W., Zhou X., … Ma J., Sun S., Fu W., Liu Y., Wang L. Altered DNA methylation pattern reveals epigenetic regulation of *Hox* genes in thoracic aortic dissection and serves as a biomarker in disease diagnosis. *Clin Epigenetics*. 2021;13(1):124. doi 10.1186/s13148-021-01110-9

Lokk K., Modhukur V., Rajashekar B., Märtens K., Mägi R., Kolde R., Koltšina M., Nilsson T.K., Vilo J., Salumets A., Tõnisson N. DNA methylome profiling of human tissues identifies global and tissue-specific methylation patterns. *Genome Biol*. 2014;15(4):r54. doi 10.1186/gb-2014-15-4-r54

Markov A.V., Zarubin A.A., Sharysh D.V., Nazarenko M.S. Evaluation of the ratio of different cell types in the study of DNA methylation in arterial samples from patients with atherosclerosis. In: Current Issues in Fundamental and Clinical Medicine. Tomsk, 2020;45-47 (in Russian)

Mosquera J.V., Auguste G., Wong D., Turner A.W., Hodonsky C.J., Alvarez-Yela A.C., Song Y., … Finn A.V., van der Laan S.W., Zang C., Sheffield N.C., Miller C.L. Integrative single-cell meta-analysis reveals disease-relevant vascular cell states and markers in human atherosclerosis. *Cell Rep*. 2023;42(11):113380. doi 10.1016/j.celrep.2023.113380

Ni C.W., Qiu H., Rezvan A., Kwon K., Nam D., Son D.J., Visvader J.E., Jo H. Discovery of novel mechanosensitive genes in vivo using mouse carotid artery endothelium exposed to disturbed flow. *Blood*. 2010;116(15):e66-e73. doi 10.1182/blood-2010-04-278192

Oshima T., Hara H., Takeda N., Hasumi E., Kuroda Y., Taniguchi G., Inuzuka R., Nawata K., Morita H., Komuro I. A novel mutation of *NFIX* causes Sotos-like syndrome (Malan syndrome) complicated with thoracic aortic aneurysm and dissection. *Hum Genome Var*. 2017;4:17022. doi 10.1038/hgv.2017.22

Pan S., Lai H., Shen Y., Breeze C., Beck S., Hong T., Wang C., Teschendorff A.E. DNA methylome analysis reveals distinct epigenetic patterns of ascending aortic dissection and bicuspid aortic valve. *Cardiovasc Res*. 2017;113(6):692-704. doi 10.1093/cvr/cvx050

Pirruccello J.P., Chaffin M.D., Chou E.L., Fleming S.J., Lin H., Nekoui M., Khurshid S., … Hoffmann U., Lubitz S.A., Philippakis A.A., Lindsay M.E., Ellinor P.T. Deep learning enables genetic analysis of the human thoracic aorta. *Nat Genet*. 2022;54(1):40-51. doi 10.1038/s41588-021-00962-4

Pozo-Vilumbrales B., Martín-Chaves L., López-Unzu M.A., Soto-Navarrete M.T., Pavón-Morón F.J., Rodríguez-Capitán J., Fernández B. Unraveling the molecular complexity of bicuspid aortopathy: lessons from comparative proteomics. *Biochim Biophys Acta Mol Basis Dis*. 2025;1871(3):167679. doi 10.1016/j.bbadis.2025.167679

Ren J., Jiang L., Liu X., Liao Y., Zhao X., Tang F., Yu H., Shao Y., Wang J., Wen L., Song L. Heart-specific DNA methylation analysis in plasma for the investigation of myocardial damage. *J Transl Med*. 2022;20(1):36. doi 10.1186/s12967-022-03234-9

Schiano C., Napoli C. Mediator complex: update of key insights into transcriptional regulation of ancestral framework and its role in cardiovascular diseases. *Eur J Med Res*. 2025;30(1):507. doi 10.1186/s40001-025-02720-2

Shah A.A., Gregory S.G., Krupp D., Feng S., Dorogi A., Haynes C., Grass E., Lin S.S., Hauser E.R., Kraus W.E., Shah S.H., Hughes G.C. Epigenetic profiling identifies novel genes for ascending aortic aneurysm formation with bicuspid aortic valves. *Heart Surg Forum*. 2015;18(4):E134-E139. doi 10.1532/hsf.1247

Song Y., Choi J.E., Kwon Y.J., Chang H.J., Kim J.O., Park D.H., Park J.M., Kim S.J., Lee J.W., Hong K.W. Identification of susceptibility loci for cardiovascular disease in adults with hypertension, diabetes, and dyslipidemia. *J Transl Med*. 2021;19(1):85. doi 10.1186/s12967-021-02751-3

Staiculescu M.C., Cocciolone A.J., Procknow J.D., Kim J., Wagenseil J.E. Comparative gene array analyses of severe elastic fiber defects in late embryonic and newborn mouse aorta. *Physiol Genomics*. 2018;50(11):988-1001. doi 10.1152/physiolgenomics.00080.2018

Steimle J.D., Moskowitz I.P. *TBX5*: a key regulator of heart development. *Curr Top Dev Biol*. 2017;122:195-221. doi 10.1016/bs.ctdb.2016.08.008

Sticchi E., De Cario R., Suraci S., Kura A., Berteotti M., Squillantini L., Barbieri G., … Gori A.M., Marcucci R., Pepe G., Nistri S., Giusti B. Bicuspid aortic valve: old and novel gene contribution to disease onset and complications. *Diagnostics* (*Basel*). 2025;16(1):104. doi 10.3390/diagnostics16010104

Viscardi F., Vergara C., Antiga L., Merelli S., Veneziani A., Puppini G., Faggian G., Mazzucco A., Luciani G.B. Comparative finite element model analysis of ascending aortic flow in bicuspid and tricuspid aortic valve. *Artif Organs*. 2010;34(12):1114-1120. doi 10.1111/j.1525-1594.2009.00989.x

Vitali T., Girald-Berlingeri S., Randazzo P.A., Chen P.W. Arf GAPs: a family of proteins with disparate functions that converge on a common structure, the integrin adhesion complex. *Small GTPases*. 2019; 10(4):280-288. doi 10.1080/21541248.2017.1299271

Wang F., Liu D., Zhang R.R., Yu L.W., Zhao J.Y., Yang X.Y., Jiang S.S., Ma D., Qiao B., Zhang F., Jin L., Gui Y.H., Wang H.Y. A TBX5 3′UTR variant increases the risk of congenital heart disease in the Han Chinese population. *Cell Discov*. 2017;3:17026. doi 10.1038/celldisc.2017.26

Wang S., Zhang J., He X., Zhang Y., Chen J., Su Q., Pang S., Zhang S., Cui Y., Yan B. Identification and functional analysis of genetic variants in TBX5 gene promoter in patients with acute myocardial infarction. *BMC Cardiovasc Disord*. 2019;19(1):265. doi 10.1186/s12872-019-1237-6

Weerackoon N., Gunawardhana K.L., Mani A. Wnt signaling cascades and their role in coronary artery health and disease. *J Cell Signal*. 2021;2(1):52-62. doi 10.33696/Signaling.2.035

Xia Y., Zhang M., Song R., Wu H., Deng J., Huang S., Yang Y. The deficiency of DIP2C leads to congenital heart defects in patients with 10p15.3 microdeletion syndrome. *Gene*. 2025;969:149753. doi 10.1016/j.gene.2025.149753

Yang Y., Bartz T.M., Brown M.R., Guo X., Zilhão N.R., Trompet S., Weiss S., … Rotter J.I., Boerwinkle E., Fornage M., Jun G., Yu B. Identification of functional genetic determinants of cardiac troponin T and I in a multiethnic population and causal associations with atrial fibrillation. *Circ Genom Precis Med*. 2021;14(6):e003460. doi 10.1161/CIRCGEN.121.003460

Zaina S., Heyn H., Carmona F.J., Varol N., Sayols S., Condom E., Ramírez-Ruz J., Gomez A., Gonçalves I., Moran S., Esteller M. DNA methylation map of human atherosclerosis. *Circ Cardiovasc Genet*. 2014;7(5):692-700. doi 10.1161/CIRCGENETICS.113.000441

Zhang F., Xia M., Jiang J., Wang S., Zhao Q., Yu C., Yu J., Xian D., Li X., Zhang L., Liu Y., Peng M. Machine learning and bioinformatics to identify 8 autophagy-related biomarkers and construct gene regulatory networks in dilated cardiomyopathy. *Sci Rep*. 2022;12(1):15030. doi 10.1038/s41598-022-19027-5

Zhao Q., Pedroza A., Sharma D., Gu W., Dalal A., Weldy C., Jackson W., … Kundaje A., Fischbein M., Wirka R., Quertermous T., Cheng P. A cell and transcriptome atlas of human arterial vasculature. *Cell Genom*. 2025;5(12):101034. doi 10.1016/j.xgen.2025.101034

Zheng S.C., Breeze C.E., Beck S., Dong D., Zhu T., Ma L., Ye W., Zhang G., Teschendorff A.E. EpiDISH web server: Epigenetic Dissection of Intra-Sample-Heterogeneity with online GUI. *Bioinformatics*. 2019;36(6):1950-1951. doi 10.1093/bioinformatics/btz833

Conflict of interest. The authors declare no conflict of interest.
Received February 20, 2026. Revised May 15, 2026. Accepted May 15, 2026.

Vavilovskii Zhurnal Genetiki i Selektsii
Vavilov Journal of Genetics and Breeding. 2026;30(6):949-954

doi 10.18699/vjgb-26-95

A clinical case of X-linked hypohidrotic ectodermal dysplasia caused by an Xq13.1 duplication affecting the *EDA* gene

V.I. Stepanenko [1], I.Zh. Zhalsanova [1], E.A. Fonova [1], A.S. Zuev [1], S.N. Gosudarkina [1], T.N. Kireeva [1], E.G. Ravzhaeva [1], A.A. Agafonova [1], G.N. Seitova [1], A.S. Monakhova [2], N.A. Skryabin [1]

[1] Research Institute of Medical Genetics, Tomsk National Research Medical Center of the Russian Academy of Sciences, Tomsk, Russia
[2] LLC "Biotech Campus", Moscow, Russia
vsevolod.stepanenko@medgenetics.ru

Abstract. X-linked hypohidrotic ectodermal dysplasia (XLHED; Christ–Siemens–Touraine syndrome, ICD-10: Q82.4) is the most common type of ectodermal dysplasia, caused by genetic disorders of ectodermal derivatives. The condition significantly impacts patients' quality of life, presenting with a classic triad of hypohidrosis, hypotrichosis and hypodontia, which creates a risk of impaired thermoregulation and necessitates complex dental rehabilitation. The molecular basis of the disease lies in alterations of the *EDA* gene, which encodes ectodysplasin A. This protein belongs to the tumor necrosis factor (TNF) family and plays a critical signaling role in ectodermal-mesenchymal interactions during embryonic development. The present case report describes a boy with an XLHED phenotype caused by a previously unreported structural rearrangement. Whole-genome sequencing (WGS) identified a ~397.3 kb microduplication at the Xq13.1 locus directly involving the *EDA* gene. Comprehensive bioinformatic analysis ruled out additional pathogenic or likely pathogenic variants in other genes that could account for the patient's phenotype. The Xq13.1 microduplication was confirmed in both the proband and his mother using quantitative real-time PCR (qPCR). Androgen receptor (*AR*) gene methylation analysis in the mother revealed a random X-chromosome inactivation (74/26 %), explaining her asymptomatic carrier status. The proband's clinical manifestations were also compared to those of literature-reported patients with overlapping genomic rearrangements. Based on international and Russian guidelines for the interpretation of massively parallel sequencing data, the identified variant was classified as pathogenic. Identification of this structural rearrangement expands the known mutational spectrum of the *EDA* gene. Establishing a precise molecular genetic diagnosis in this family is critical not only for disease verification but also for optimizing patient management through a multidisciplinary approach. Furthermore, it enables comprehensive genetic counseling, identification of female carriers among relatives and the development of timely primary and secondary prevention measures for the disease in this family.
Key words: ectodermal dysplasia; hypohidrotic; Christ–Siemens–Touraine syndrome; *EDA*; copy number variations (CNV); next-generation sequencing (NGS)

For citation: Stepanenko V.I., Zhalsanova I.Zh., Fonova E.A., Zuev A.S., Gosudarkina S.N., Kireeva T.N., Ravzhaeva E.G., Agafonova A.A., Seitova G.N., Monakhova A.S., Skryabin N.A. A clinical case of X-linked hypohidrotic ectodermal dysplasia caused by an Xq13.1 duplication affecting the *EDA* gene. *Vavilovskii Zhurnal Genetiki i Selektsii = Vavilov J Genet Breed*. 2026;30(6):949-954. doi 10.18699/vjgb-26-95

Funding. The study was supported by the Ministry of Science and Higher Education of the Russian Federation, project No. 122013100190-6.

Клинический случай Х-сцепленной гипогидротической эктодермальной дисплазии, вызванной дупликацией Xq13.1, затрагивающей ген *EDA*

В.И. Степаненко [1], И.Ж. Жалсанова [1], Е.А. Фонова [1], А.С. Зуев [1], С.Н. Государкина [1], Т.Н. Киреева [1], Е.Г. Равжаева [1], А.А. Агафонова [1], Г.Н. Сеитова [1], А.С. Монахова [2], Н.А. Скрябин [1]

[1] Научно-исследовательский институт медицинской генетики Томского национального исследовательского медицинского центра Российской академии наук, Томск, Россия
[2] ООО «Биотехнологический кампус», Москва, Россия
vsevolod.stepanenko@medgenetics.ru

Аннотация. Х-сцепленная гипогидротическая эктодермальная дисплазия (синдром Криста–Сименса–Турена, МКБ-10: Q82.4) представляет собой наиболее распространенную форму эктодермальной дисплазии, вызванной наследственными нарушениями развития производных эктодермы. Заболевание существенно влияет на качество

© Stepanenko V.I., Zhalsanova I.Zh., Fonova E.A., Zuev A.S., Gosudarkina S.N., Kireeva T.N., Ravzhaeva E.G., Agafonova A.A., Seitova G.N., Monakhova A.S., Skryabin N.A., 2026

This work is licensed under a Creative Commons Attribution 4.0 License

жизни пациентов, проявляясь классической триадой симптомов: гипогидрозом, гипотрихозом и гиподонтией, что создает риски нарушения терморегуляции и требует сложной стоматологической реабилитации. Молекулярной основой патологии служат нарушения в гене *EDA*, ответственном за синтез эктодисплазина-А. Данный белок принадлежит к семейству фактора некроза опухоли (TNF) и играет критическую сигнальную роль в процессе эктодермально-мезенхимальных взаимодействий во время эмбрионального развития. В настоящей работе описан клинический случай мальчика с фенотипом Х-сцепленной гипогидротической эктодермальной дисплазии, обусловленный ранее не описанной структурной перестройкой. Методом полногеномного секвенирования (WGS) была выявлена микродупликация локуса Xq13.1 размером приблизительно 397.3 Кб, непосредственно затрагивающая ген *EDA*. Комплексный биоинформатический анализ подтвердил отсутствие дополнительных патогенных или вероятно патогенных вариантов в других генах, которые могли обусловливать фенотип пациента. Микродупликация Xq13.1 подтверждена у пробанда и его матери методом количественной полимеразной цепной реакции в режиме реального времени. Анализ метилирования гена *AR* продемонстрировал у матери равновероятную инактивацию Х-хромосомы (74/26 %), что объясняет ее бессимптомное носительство. Проведено сравнение клинических проявлений пробанда с описанными в литературе пациентами, имеющими близкие по координатам структурные перестройки. На основании международных и российских руководств по интерпретации данных массового параллельного секвенирования обнаруженный вариант классифицирован как патогенный. Идентификация этой структурной перестройки расширяет известный мутационный спектр гена *EDA*. Уточнение молекулярно-генетического диагноза в описанной семье имеет критическое значение не только для верификации нозологии, но и для коррекции тактики ведения пациента, включая междисциплинарный подход к лечению. Кроме того, это позволяет провести качественное медико-генетическое консультирование, выявить носительство у родственников женского пола и разработать эффективные меры первичной и вторичной профилактики заболевания в данной семье.

Ключевые слова: эктодермальная дисплазия; гипогидротическая дисплазия; синдром Криста–Сименса–Турена; *EDA*; вариации числа копий участков ДНК (CNV); массовое параллельное секвенирование (МПС)

Introduction

Ectodermal dysplasia is a genetically and clinically heterogeneous group of disorders characterized by defects in two or more ectodermal derivatives, including sweat glands, hair, and teeth (Visinoni et al., 2009). Hypohidrotic ectodermal dysplasia is a subgroup of ectodermal dysplasias, whose characteristic clinical feature is reduced sweat gland function, leading to impaired thermoregulation (Anbouba et al., 2020; Wohlfart et al., 2020). Pathogenic variants in four genes account for approximately 90 % of hypohidrotic ectodermal dysplasia cases: *EDA* (X-linked forms), *EDAR* and *EDARADD* (responsible for both autosomal dominant and autosomal recessive forms), and *WNT10A* (autosomal recessive forms) (Cluzeau et al., 2011).

X-linked hypohidrotic ectodermal dysplasia (Christ–Siemens–Touraine syndrome, XLHED) (OMIM: #305100) is a hereditary disorder affecting structures of ectodermal origin, such as hair, teeth, nails, and sweat glands. The disease is caused by pathogenic variants in the *EDA* gene, responsible for the synthesis of the protein ectodysplasin A. This protein belongs to the tumor necrosis factor (TNF) family of ligands and plays an important role in the formation of ectoderm-derived structures during embryogenesis (Kere et al., 1996; Mikkola, Thesleff, 2003). According to the literature, X-linked hypohidrotic ectodermal dysplasia is the most common form of hypohidrotic ectodermal dysplasia worldwide (Lamartine, 2003). The prevalence of this disease is estimated to range from 1 to 22 per 100,000 individuals (Cañueto et al., 2011; Nguyen-Nielsen et al., 2013). The clinical presentation of this disease involves various combinations of the following features: hypohidrosis, hypotrichosis, and hypodontia (Itin, Fistarol, 2004; Bagdey et al., 2022). This paper presents a clinical case involving an Xq13.1 duplication not described hitherto.

Materials and methods

A family with a suspected case of ectodermal dysplasia in the son was enrolled in this study. The research was conducted in compliance with ethical standards as outlined in the World Medical Association's Declaration of Helsinki. Written informed consent was obtained from all participating family members. The study protocol was approved by the Biomedical Ethics Committee of the Research Institute of Medical Genetics, Tomsk National Research Medical Center (Protocol No. 10, dated January 20, 2021).

Peripheral blood samples were collected from the patient and his parents into EDTA-containing tubes for molecular genetic analysis. Genomic DNA was extracted from whole blood using the standard phenol-chloroform method.

Whole-genome sequencing of the proband was performed within the collaborative research program with the National Genetic Initiative "100,000+Me" at Biotech Campus Company. Whole-genome sequencing was carried out on DNBSEQ-T7 platforms (MGI) using the MGIEasy FS PCR-Free Library Prep Set (MGI) for library preparation, producing 2 × 150 bp paired-end reads. The bioinformatics pipeline included adapter trimming and quality filtering of raw data, followed by alignment of reads to the GRCh38 reference genome using BWA-MEM v0.7.17 (http://bio-bwa.sourceforge.net/). Duplicate reads were marked using GATK MarkDuplicates v4.3.0.0 (McKenna et al., 2010). Single nucleotide variants and small indels were called using DeepVariant v4.0.0. For each sample, the fraction of reads with a quality score of at least Q30 was ≥90 % of the total reads obtained by sequencing.

Variant annotation was performed using Annovar (Wang et al., 2010). The clinical relevance of identified variants was assessed using the OMIM (http://www.omim.org/), ClinVar (https://www.ncbi.nlm.nih.gov/clinvar/), gnomAD v4.1.0 exomes (https://gnomad.broadinstitute.org/), HPO (https://

hpo.jax.org/), and Decipher (https://www.deciphergenomics.org/) databases, as well as data from the scientific literature.

To validate the Xq13.1 microduplication, quantitative real-time PCR was performed on DNA from the proband and his parents using the following primer pairs (Syntol, Russia): targeting exon 2 of the *EDA* gene (F: 5′-TGGCT ATGACTGAGTGGGGT-3′; R: 5′-GCTTCTTTTATTGC GGCGAAC-3′) and targeting intron 1 of the *EDA* gene (F: 5′-GTGGGATGTTGGAGGAACT-3′; R: 5′-TGCGAAC TTTGGTGAAGAAGC-3′).

Primers were designed using the Primer-BLAST resource (https://www.ncbi.nlm.nih.gov/tools/primer-blast/). Selected primer sequences were tested for the formation of hairpins, self- and heterodimers using the OligoAnalyzer tool (https://eu.idtdna.com/calc/analyzer).

The X-chromosome inactivation status was determined by amplifying a highly polymorphic CAG repeat in the first exon of the androgen receptor gene (*AR*, Xq12) after DNA hydrolysis with the methylation-sensitive restriction endonuclease HpaII. PCR products were separated using fragment analysis. An inactivation skewing of less than 80 % was considered a random pattern of X-chromosome inactivation, whereas a skewing of more than 80 % was regarded as indicative of skewed (asymmetric) X-chromosome inactivation (sXCI) (Allen et al., 1992).

Results

Clinical case report. The proband, a 14-year-old male, was examined at the Genetic Clinic of the Research Institute of Medical Genetics, Tomsk National Research Medical Center, due to suspected anhidrotic ectodermal dysplasia. His medical history was significant for congenital absence of sweating and impaired thermoregulation. At the age of two months, he was diagnosed with atopic dermatitis and subsequently followed up for this condition, which was characterized by recurrent episodes of acute allergic manifestations, including atopic dermatitis and urticaria, requiring numerous hospitalizations in early childhood. His primary dentition erupted at 8 months of age and was notable for conical (awl-shaped) teeth.

The initial diagnosis of Christ–Siemens–Touraine syndrome with an X-linked recessive inheritance pattern was established at the age of 1 year and 5 months following a consultation by a clinical geneticist, based on the characteristic clinical presentation.

At the age of 2 years, the patient developed phimosis with the formation of synechiae. At 6 years, the proband was admitted to a surgical hospital with a diagnosis of acute balanoposthitis and preputial synechiae. From the age of 7 years, he has been followed up by a neurologist for an obsessive-compulsive disorder and a localized motor tic involving the periorbital musculature.

During a follow-up examination by a clinical geneticist at the age of 14, the following phenotypic features were noted: hypodontia of the upper jaw with conical teeth, anodontia of the lower jaw, hypotrichosis, periorbital hyperpigmentation, and palmoplantar keratoderma. The patient was subsequently referred for molecular genetic confirmation of the diagnosis.

Whole-genome sequencing identified a hemizygous ~397.3 kb duplication on chromosome X, spanning approximate coordinates chrX:69,620,777–70,018,072 and affecting the disease-associated *EDA* gene (Fig. 1).

The Xq13.1 microduplication was confirmed in the proband and his mother by quantitative real-time PCR (Fig. 2). Neither of the proband's parents exhibited any clinical manifestations of the disease.

The proband's parents showed no clinical manifestations of the disease. Analysis of the X-chromosome inactivation status in the proband's mother demonstrated random X-chromosome inactivation (74/26 %).

Discussion

The *EDA* gene spans 419 kb, comprises eight exons, and encodes ectodysplasin A, a signaling ligand of the tumor necrosis factor (TNF) family, which plays a key role in the formation of ectodermal structures during embryogenesis. The function of ectodysplasin A is to transmit a positive signal supporting cell survival, proliferation, and differentiation during epithelial-mesenchymal interactions, particularly in the development of hair follicles (Laurikkala et al., 2002).

According to the literature, hypohidrotic ectodermal dysplasia is frequently associated with atopic conditions, including atopic dermatitis, allergic rhinitis, and bronchial asthma

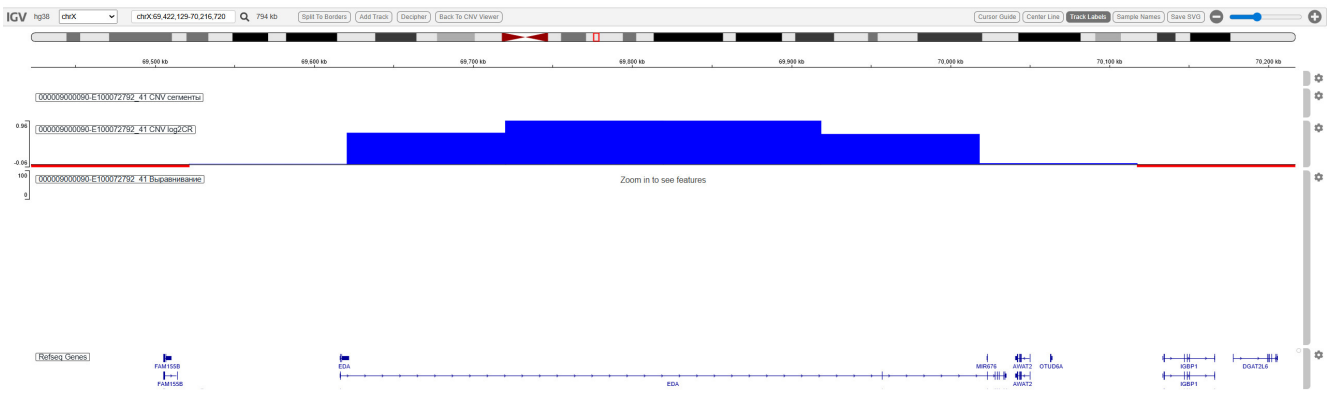


Fig. 1. Proband NGS sequencing (IGV browser).

Comparison of clinical features of the proband with literature data

Clinical feature	Proband	Patient-1[a]	Patient-2[b]	Patient-3[c]
Skin changes				
Superficial dry scaling skin at birth	+	N/A	+	+
Dry and often hypopigmented skin	+	N/A	+	+
Dermatitis resembling atopic skin disease	+	N/A	–	–
Impaired sweat gland function				
Absence or reduction of sweating	+	+	+	+
Hyperthermia under warm condition	+	+	+	+
Abnormalities in hair follicles				
Sparse, curly, and fair hair	+	+	+	+
Alopecia because of hypotrichosis or increased hair fragility	+	+	+	+
Eyebrows or eyelashes absent/sparse or malformed	+	+	+	+
Nail changes				
Leukonychia	–	–	–	–
Dystrophic and malformed nails	–	–	–	–
Dental changes				
Hypodontia or anodontia	+	N/A	+	+
Malformed teeth with cone- or pegshaped aspect	+	N/A	+	+
Prone to caries because of enamel defect or salivary gland malfunction with xerostomia	+	N/A	N/A	+
Facial changes				
Dysmorphic features	–	+	+	–
Numerous facial malformations	–	+	+	–
Eye abnormalities				
Corneal dysplasias	–	–	–	–
Cataract	–	–	–	–
Displaced or stenotic lacrimal puncta	–	–	–	–
Defective or decreased lacrimation	–	–	–	–

Note. Sources: [a] (Hayashi et al., 2013); [b] (Li et al., 2008); [c] (Al Marzouqi et al., 2014); N/A – Not Assessed.

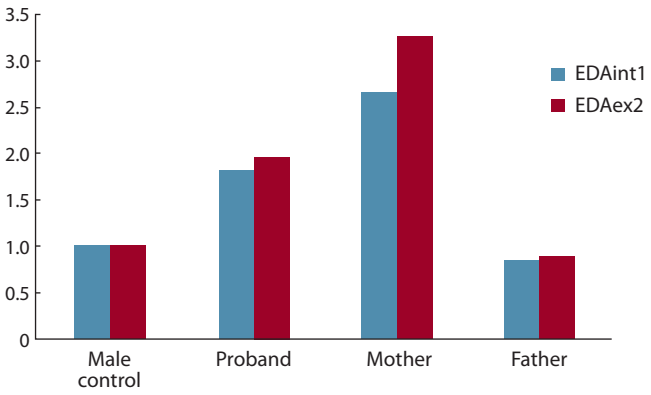


Fig. 2. Copy number analysis of the Xq13.1 region in the proband and his parents. Results of real-time PCR assays targeting intron 1 and exon 2 of the *EDA* gene.

The *X*-axis represents the male control sample, proband, mother, and father; the *Y*-axis shows the relative DNA copy number change.

(Stein, 2007). This association may be explained by impaired barrier function of the skin and mucous membranes, leading to xerosis (dry skin), as well as by thermoregulatory dysfunction resulting from sweat gland abnormalities. Dysfunction of bronchial glands has also been reported, which may predispose individuals to recurrent respiratory infections and bronchitis. In our clinical case, the patient showed signs of atopic dermatitis from the first months of life, requiring medical management.

The clinical presentation in the proband is consistent with the classical phenotype of X-linked hypohidrotic ectodermal dysplasia (Itin, Fistarol, 2004). In addition, the clinical features are similar to previously reported cases associated with pathogenic copy number variations (CNVs) affecting the *EDA* gene, including both deletions (Patient-1, Patient-2) and a duplication (Patient-3) (see the Table).

According to the literature and genomic databases, three cases of intragenic copy number variations (CNVs) have been described to date: two microdeletions and one microduplica-

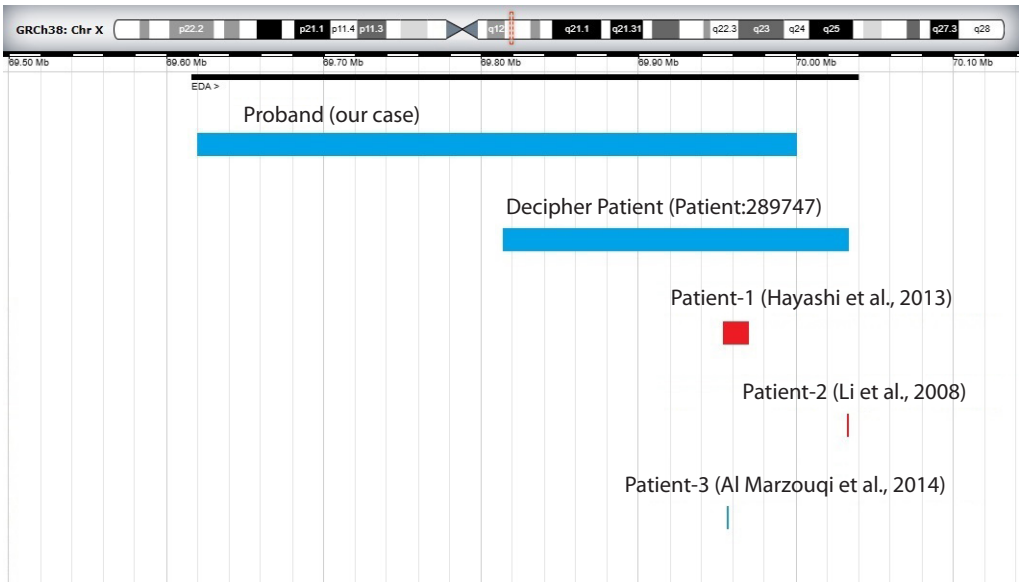


Fig. 3. Schematic scale-fitted representation of rearrangements in previously reported patients with duplications (blue bars), deletions (red bars), and the proband within the *EDA* gene.

tion. All of these cases were reported in patients presenting with a pronounced clinical picture consistent with the specific disease phenotype.

In Patient-1 (Hayashi et al., 2013), a deletion was identified and designated as NC_000023.11(NM_001399.5):c.397-1589_502+13848del. This rearrangement corresponds to an intragenic deletion within the Xq13.1 region, spanning genomic coordinates chrX:69955438-69970980 and involving exon 2 of the *EDA* gene. In Patient-2 (Li et al., 2008), a 22-bp intragenic deletion was identified within exon 8 of the *EDA* gene, resulting in a frameshift. In Patient-3 (Al Marzouqi et al., 2014), an intragenic duplication of *EDA* exon 2 was reported. In addition, a duplication with similar coordinates is registered in the Decipher database (Patient:289747) and classified as pathogenic (Fig. 3).

Structural variants with similar coordinates are not observed in the population frequency databases gnomAD CNVs/SVs v4.1.0.

According to the ACMG criteria established for the assessment of CNV pathogenicity, this rearrangement is classified as pathogenic, receiving a score of 1.0 (criteria 1A, 2A, 3A) (Riggs et al., 2020). Based on the refined ACMG/AMP criteria adapted for the evaluation of monogenic CNVs, this rearrangement is also classified as pathogenic (PVS1, PM2, PP4) (Brandt et al., 2020).

X-linked hypohidrotic ectodermal dysplasia is known to exhibit incomplete penetrance in female carriers due to its X-linked recessive inheritance pattern (Munoz et al., 1997; Cambiaghi et al., 2000). The identified variant was inherited from the mother, who is a heterozygous asymptomatic carrier. Clinical manifestations of X-linked recessive disorders in women may be absent due to the heterozygous state of the X chromosome and random X-chromosome inactivation (Vincent et al., 2001). However, if skewed X-chromosome inactivation is present, female carriers may exhibit clinical symptoms when the homologue carrying the pathogenic variant remains active. In this case, we found random X-chromosome inactivation in the proband's mother, which explains the absence of clinical manifestations of the disease. This rearrangement is assessed as pathogenic based on a combination of clinical data, pathogenicity criteria, and literature reports.

An important aspect of the presented clinical case is the utilization of whole-genome sequencing for the diagnosis of this disease. Verifying an intragenic microduplication on the X chromosome in a male patient using standard NGS approaches (such as targeted gene sequencing or whole-exome sequencing) is extremely challenging. In a male, the hemizygous state of the X chromosome, combined with a copy number gain in a specific region, could be misinterpreted as increased gene coverage, potentially leading to a false negative diagnosis. Furthermore, methods designed to determine DNA copy number, such as MLPA, array CGH, or real-time PCR, are not routinely used in the diagnosis of Christ–Siemens–Touraine syndrome, because pathogenic variants are represented by various single nucleotide variants (SNVs) in up to 90 % of cases.

Conclusion

This report presents a clinical case of X-linked hypohidrotic ectodermal dysplasia caused by a previously unreported ~397.3 kb duplication at Xq13.1, affecting the *EDA* gene. The duplication breakpoints map to approximately chrX:69,620,777–70,018,072. The diagnosis was established based on the characteristic clinical presentation. Molecular genetic confirmation allowed us to clarify the etiology and identify carrier status in the asymptomatic mother with random X-chromosome inactivation. This finding enables preconception and prenatal diagnostic options for future pregnancies in this family, given the potential for transmission by female carriers.

References

Al Marzouqi F., Michot C., Dos Santos S., Bonnefont J.P., Bodemer C., Hadj-Rabia S. Bilateral amastia in a female with X-linked hypohidrotic ectodermal dysplasia. *Br J Dermatol*. 2014;171(3):671-673. doi 10.1111/bjd.13023

Allen R.C., Zoghbi H.Y., Moseley A.B., Rosenblatt H.M., Belmont J.W. Methylation of HpaII and HhaI sites near the polymorphic CAG repeat in the human androgen-receptor gene correlates with X chromosome inactivation. *Am J Hum Genet*. 1992;51(6):1229-1239

Anbouba G.M., Carmany E.P., Natoli J.L. The characterization of hypodontia, hypohidrosis, and hypotrichosis associated with X-linked hypohidrotic ectodermal dysplasia: A systematic review. *Am J Med Genet A*. 2020;182(4):831-841. doi 10.1002/ajmg.a.61493

Bagdey S.P., Moharil R.B., Dive A., Bodhade A. Hypohidrotic ectodermal dysplasia: A case report with review and latest updates. *J Oral Maxillofac Pathol*. 2022;26(Suppl. 1):S12-S16. doi 10.4103/jomfp.jomfp_287_21

Brandt T., Sack L.M., Arjona D., Tan D., Mei H., Cui H., Gao H., … Vincent L.M., Reavey C., Lai A., Richard G., Meck J.M. Adapting ACMG/AMP sequence variant classification guidelines for single-gene copy number variants. *Genet Med*. 2020;22(2):336-344. doi 10.1038/s41436-019-0655-2

Cambiaghi S., Restano L., Pääkkönen K., Caputo R., Kere J. Clinical findings in mosaic carriers of hypohidrotic ectodermal dysplasia. *Arch Dermatol*. 2000;136(2):217-224. doi 10.1001/archderm.136.2.217

Cañueto J., Zafra-Cobo M.I., Ciria S., Unamuno P., González-Sarmiento R. A novel *EDA* gene mutation in a Spanish family with X-linked hypohidrotic ectodermal dysplasia. *Actas Dermosifiliogr*. 2011;102(9):722-725. doi 10.1016/j.ad.2011.04.004

Cluzeau C., Hadj-Rabia S., Jambou M., Mansour S., Guigue P., Masmoudi S., Bal E., … de Prost Y., Munnich A., Bonnefont J.P., Bodemer C., Smahi A. Only four genes (*EDA1*, *EDAR*, *EDARADD*, and *WNT10A*) account for 90 % of hypohidrotic/anhidrotic ectodermal dysplasia cases. *Hum Mutat*. 2011;32(1):70-72. doi 10.1002/humu.21384

Hayashi R., Farooq M., Fujikawa H., Fujimoto A., Hashimoto T., Ito M., Shimomura Y. Case of hypohidrotic ectodermal dysplasia caused by a large deletion mutation in the *EDA* gene. *J Dermatol*. 2013;40(4):281-283. doi 10.1111/1346-8138.12077

Itin P.H., Fistarol S.K. Ectodermal dysplasias. *Am J Med Genet C Semin Med Genet*. 2004;131C(1):45-51. doi 10.1002/ajmg.c.30033

Kere J., Srivastava A.K., Montonen O., Zonana J., Thomas N., Ferguson B., Munoz F., … Chen E.Y., Ezer S., Saarialho-Kere U., de la Chapelle A., Schlessinger D. X-linked anhidrotic (hypohidrotic) ectodermal dysplasia is caused by mutation in a novel transmembrane protein. *Nat Genet*. 1996;13(4):409-416. doi 10.1038/ng0895-409

Lamartine J. Towards a new classification of ectodermal dysplasias. *Clin Exp Dermatol*. 2003;28(4):351-355. doi 10.1046/j.1365-2230.2003.01319.x

Laurikkala J., Pispa J., Jung H.S., Nieminen P., Mikkola M., Wang X., Saarialho-Kere U., Galceran J., Grosschedl R., Thesleff I. Regulation of hair follicle development by the TNF signal ectodysplasin and its receptor Edar. *Development*. 2002;129(10):2541-2553. doi 10.1242/dev.129.10.2541

Li M., Xu T.Y., Yang L.J., Zhu X.H. A novel 22-bp deletion mutation in a Chinese family with X-linked hypohidrotic ectodermal dysplasia. *Arch Dermatol Res*. 2008;300(7):389-391. doi 10.1007/s00403-008-0855-0

McKenna A., Hanna M., Banks E., Sivachenko A., Cibulskis K., KernytskyA., Garimella K., Altshuler D., Gabriel S., Daly M., DePristo M.A. The Genome Analysis Toolkit: a MapReduce framework-for analyzing next-generation DNA sequencing data. *Genome Res*. 2010;20(9):1297-1303. doi 10.1101/GR.107524.110

Mikkola M.L., Thesleff I. Ectodysplasin signaling in development. *Cytokine Growth Factor Rev*. 2003;14(3-4):211-224. doi 10.1016/s1359-6101(03)00020-0

Munoz F., Lestringant G., Sybert V., Frydman M., Alswaini A., Frossard P.M., Jorgenson R., Zonana J. Definitive evidence for an autosomal recessive form of hypohidrotic ectodermal dysplasia clinically indistinguishable from the more common X-linked disorder. *Am J Hum Genet*. 1997;61(1):94-100. doi 10.1086/513905

Nguyen-Nielsen M., Skovbo S., Svaneby D., Pedersen L., Fryzek J. The prevalence of X-linked hypohidrotic ectodermal dysplasia (XLHED) in Denmark, 1995-2010. *Eur J Med Genet*. 2013;56(5):236-242. doi 10.1016/j.ejmg.2013.01.012

Riggs E.R., Andersen E.F., Cherry A.M., Kantarci S., Kearney H., Patel A., Raca G., Ritter D.I., South S.T., Thorland E.C., Pineda-Alvarez D., Aradhya S., Martin C.L. Technical standards for the interpretation and reporting of constitutional copy-number variants: a joint consensus recommendation of the American College of Medical Genetics and Genomics (ACMG) and the Clinical Genome Resource (ClinGen). *Genet Med*. 2020;22(2):245-257. doi 10.1038/s41436-019-0686-8

Stein R.A. Smith's recognizable patterns of human malformation, 6th edition. *Arch Dis Child*. 2007;92(6):562

Vincent M.C., Biancalana V., Ginisty D., Mandel J.L., Calvas P. Mutational spectrum of the ED1 gene in X-linked hypohidrotic ectodermal dysplasia. *Eur J Hum Genet*. 2001;9(5):355-363. doi 10.1038/sj.ejhg.5200635

Visinoni A.F., Lisboa-Costa T., Pagnan N.A., Chautard-Freire-Maia E.A. Ectodermal dysplasias: clinical and molecular review. *Am J Med Genet A*. 2009;149A(9):1980-2002. doi 10.1002/ajmg.a.32864

Wang K., Li M., Hakonarson H. ANNOVAR: functional annotation of genetic variants from high-throughput sequencing data. *Nucleic Acids Res*. 2010;38(16):e164. doi 10.1093/nar/gkq603

Wohlfart S., Meiller R., Hammersen J., Park J., Menzel-Severing J., Melichar V.O., Huttner K., Johnson R., Porte F., Schneider H. Natural history of X-linked hypohidrotic ectodermal dysplasia: a 5-year follow-up study. *Orphanet J Rare Dis*. 2020;15(1):7. doi 10.1186/s13023-019-1288-x

Conflict of interest. The authors declare no conflict of interest.
Received March 7, 2026. Revised June 1, 2026. Accepted June 2, 2026.

Vavilovskii Zhurnal Genetiki i Selektsii
Vavilov Journal of Genetics and Breeding. 2026;30(6):955-963

doi 10.18699/vjgb-26-96

Genetic analysis of a representative of the military nobility from the Dal'niy (Vydrin) burial ground of the Chernyakhov culture in the Kursk region

E.V. Rozhdestvenskikh [1], T.V. Andreeva [1, 2, 3] ✉, S.S. Kunizheva [1, 2], A.D. Manakhov [1, 2], M.S. Gasheva [1], O.A. Radyush [4], I.K. Reshetova [4], M.V. Dobrovolskaya [4], E.I. Rogaev [5] ✉

[1] Sirius University of Science and Technology, Sirius Federal Territory, Krasnodar region, Russia
[2] Vavilov Institute of General Genetics of the Russian Academy of Sciences, Moscow, Russia
[3] Centre of Genetics and Genetic Technologies, Faculty of Biology, Lomonosov Moscow State University, Moscow, Russia
[4] Institute of Archaeology of the Russian Academy of Sciences, Moscow, Russia
[5] UMass Chan Medical School, Department of Psychiatry, Shrewsbury, USA
✉ andreeva@rogaevlab.ru; evivrecc@gmail.com

Abstract. During the late Roman period, the military and political conditions in Eastern Europe declined both along the frontier between the Roman Empire and Barbaricum and within those territories. The Chernyakhov culture played an important role in the dynamics of these events. According to historical and archaeological evidence, this society was formed by Germanic tribes that had moved into the region from northwestern Europe, as well as a nomadic population of the steppes. The Chernyakhov culture's funerary traditions included the placement of weapons, most likely solely in the graves of military nobles. In this context, human remains from these burials serve as a unique resource for archaeogenetic studies, enabling insights into the genetic origins of the military aristocracy within the Chernyakhov culture. In this paper, we present the results of a whole-genome analysis of a member of the military elite from a status burial of the Chernyakhov culture at the Dal'niy (Vydrin) burial ground, located on the northern border of the Chernyakhov culture area. According to archaeological data and previous anthropological analysis, the buried individual belonged to the military nobility of the late Chernyakhov culture, which lasted from the fourth to fifth centuries AD. The whole-genome sequences of this individual were generated by large-scale parallel sequencing. The individual was shown to be male. Analysis of haplogroup markers indicated the European origin of maternal and paternal lineages. The examination of autosomal markers clearly indicated a genetic link between this individual, associated with the warrior class of the Chernyakhov culture, and members of nomadic steppe groups, specifically the Scythians, Sarmatians, and Avars. The results contribute to our understanding of the complex picture of interethnic contacts that created the basis for the formation of the polyethnic Chernyakhov culture.

Key words: Chernyakhov culture; late Roman period; ancient DNA; nomads; archaeogenetics

For citation: Rozhdestvenskikh E.V., Andreeva T.V., Kunizheva S.S., Manakhov A.D., Gasheva M.S., Radyush O.A., Reshetova I.K., Dobrovolskaya M.V., Rogaev E.I. Genetic analysis of a representative of the military nobility from the Dal'niy (Vydrin) burial ground of the Chernyakhov culture in the Kursk region. *Vavilovskii Zhurnal Genetiki i Selektsii = Vavilov J Genet Breed*. 2026;30(6):955-963. doi 10.18699/vjgb-26-96

Funding. This work was supported by the grant of the state program of the "Sirius" Federal Territory "Paleogenetics of Krasnodar Krai", Agreement No. 18–03 date September 10, 2024 (EVR, TVA, ADM, MSG).

Генетический анализ представителя воинской знати из могильника черняховской культуры Дальний (Выдрин) в Курской области

Е.В. Рождественских [1], Т.В. Андреева [1, 2, 3] ✉, С.С. Кунижева [1, 2], А.Д. Манахов [1, 2], М.С. Гашева [1], О.А. Радюш [4], И.К. Решетова [4], М.В. Добровольская [4], Е.И. Рогаев [5] ✉

[1] Научно-технологический университет «Сириус», федеральная территория «Сириус», Краснодарский край, Россия
[2] Институт общей генетики им. Н.И. Вавилова Российской академии наук, Москва, Россия
[3] Центр генетики и генетических технологий, биологический факультет МГУ им. М.В. Ломоносова, Москва, Россия
[4] Институт археологии Российской академии наук, Москва, Россия
[5] Медицинская школа Чан Массачусетского университета, департамент психиатрии, Шрусбери, США
✉ andreeva@rogaevlab.ru; evivrecc@gmail.com

© Rozhdestvenskikh E.V., Andreeva T.V., Kunizheva S.S., Manakhov A.D., Gasheva M.S., Radyush O.A., Reshetova I.K., Dobrovolskaya M.V., Rogaev E.I., 2026
This work is licensed under a Creative Commons Attribution 4.0 License

Аннотация. В позднеримский период на территории Восточной Европы происходит обострение военно-политической обстановки как на границе Рима (Римской империи) и Барбарикума, так и внутри них. Значительную роль в динамике этих процессов играла черняховская культурная общность, формирование которой, согласно историко-археологическим данным, происходило при активном участии германских племен, продвинувшихся в этот регион с Северо-Запада Европы, причерноморского оседлого и отчасти степного кочевого населения. Погребальный обряд черняховской культуры предполагает крайне редкое помещение оружия, предположительно, только в могилы представителей воинской знати. В связи с чем антропологический материал из подобных погребений является ценным объектом для археогенетических исследований, позволяющим понять генетическое происхождение представителей воинской элиты черняховского общества. В данной работе мы впервые представляем результаты полногеномного анализа представителя воинской элиты из статусного захоронения черняховской культуры на могильнике Дальний (Выдрин), расположенного на северной границе ареала черняховской культуры. Совокупность археологических данных и проведенного ранее антропологического анализа указывает на то, что погребенный индивид принадлежал к воинской знати периода позднечерняховской культуры, который датируется концом IV в. н. э. С использованием масштабного параллельного секвенирования были определены полногеномные последовательности этого индивида. Показана принадлежность индивида к мужскому полу. Анализ однородительских маркеров свидетельствует о европейском происхождении материнской и отцовской линий исследованного мужчины. На основе анализа аутосомных маркеров мы впервые продемонстрировали генетическую связь этого индивида, представляющего воинское сословие черняховской культуры, с представителями кочевых степных групп: скифов, сарматов и авар. Полученные результаты вносят вклад в понимание сложной картины межэтнических контактов, лежавших в основе формирования населения полиэтничной черняховской общности.

Ключевые слова: черняховская культура; позднеримское время; древняя ДНК; кочевники; археогенетика

Introduction

During the Late Roman period (the 2nd–5th centuries AD), significant transformations occurred on the frontiers between Europe and the Great Steppe. This era witnessed large-scale migrations, military-political crises, and the formation of new cultural communities within the vast territories of Barbaricum, situated outside the borders of the Roman Empire (Heather, 2011). One of the most prominent among them was the Chernyakhov cultural-historical complex (or Sântana de Mureș–Chernyakhov complex, mid-3rd to early 5th century AD), which spanned extensive areas from the Lower Danube to the Seversky Donets and the Kursk region. Archaeological research confirms that the Chernyakhov culture emerged as a result of a complex polyethnic process involving the migration of Germanic tribes from Northwestern Europe and their interaction with the local populations inhabiting the forest and forest-steppe zones (Terpilovsky, 2000; Oblomskiy, 2002; Radyush, 2018, 2023). Anthropological data further indicate the possible existence of a genetic link between the Chernyakhov culture and populations from the steppe regions, specifically groups belonging to the Scythian–Sarmatian cultural circle (Scythians, Sarmatians, and Alans) (Rudich, 2006, 2010).

Despite the relative homogeneity of material culture, the funerary ritual practiced by the Chernyakhov society provides clear evidence of social hierarchy. Burials containing weapons are extremely rare and, according to the consensus view in archaeology, are attributed to representatives of the military aristocracy (Radyush, 2012, 2019; Radyush, Vasil'ev, 2022). Consequently, the anthropological remains recovered from such burials constitute a unique data source for investigating the genetic profile and biological origins of the Chernyakhov military elite, who played a pivotal role in the military-political processes that characterized the Migration Period.

In 2021, archaeological excavations at the Chernyakhov burial site of Dal'niy (Vydrin) in the upper Sudzha River basin (the Kursk region) revealed a of a male aged 35–40 that was unique in the richness of its grave goods (Radyush, Vasil'ev, 2022; Radyush et al., 2025). The burial, dating back to the late 4th century, contained a significant collection of high-quality grave goods, including a large number of refined ceramic vessels, such as a massive black-polished vase, a jug, a glass goblet, belt buckles, and a fibula. A blade approximately 40 cm in length was recovered near the head of the deceased. The exceptional preservation of organic materials made it possible to establish that the weapon was in a wooden scabbard and was made of Damascus steel. Consistent with Chernyakhov funerary traditions, the individual was identified as a member of the military elite. This classification is further supported by anthropological analysis, which revealed a complex of physical characteristics typical of an experienced horseman who was regularly subjected to physical and military loads (Radyush et al., 2025). This burial is unparalleled among Chernyakhov sites on the left bank of the Dnieper, and its location in close proximity to the so-called "Knyazhye" burial near the village of Bolshoy Kamenets in the Kursk region further emphasises the high social status of the deceased male (Radyush, Vasil'ev, 2022).

Although historical scholarship traditionally recognizes the polyethnic nature of the Chernyakhov culture, the origin of its military elite, particularly in the peripheral the Left Bank Dnieper region, remains a subject of ongoing debate. Archaeogenetic research provides a powerful tool to test historical and archaeological hypotheses through the genetic analysis of individual human remains.

Within the framework of this study, we present for the first time the results of a whole-genome analysis of a Chernyakhov military aristocrat, excavated from a grave at the Dal'niy (Vydrin) burial ground in the Bolshesoldatsky District of the Kursk region.

Materials and methods

Ancient DNA (aDNA) was extracted at Sirius University in special laboratories designed to work with ancient materials. The molecular genetic work was conducted in accordance with previously developed methods (Gansauge, Meyer, 2013; Andreeva et al., 2022). Bone powder obtained from the tooth root of an individual from burial 12 at the Dal'niy burial ground (Vydrin) was used as an aDNA source. For this sample (hereinafter referred to as Dch08), two genomic libraries were prepared: one from native DNA and one from DNA treated with the PreCR Repair Mix (NEB) enzymes to repair postmortem modifications (Mouttham et al., 2015). Sequencing was performed using the Illumina MiSeq and Illumina NovaSeq 6000 platforms, generating single-end reads with a read length of 56 bp.

The initial data obtained from sequencing were analyzed using a bioinformatics pipeline, which included the following programs: FastQC, AdapterRemoval v2, mapDamage v2, BWA, SAMtools, BCFtools, BEDTools, and BamUtil (Li et al., 2009; Schubert et al., 2012, 2016; Jónsson et al., 2013; Picard Tools – By Broad Institute, 2019; Danecek et al., 2021). The trimmed reads were mapped to the reference sequence of the human mitochondrial genome (mtDNA, NC_012920.1) and to the human reference genome (GRCh37 assembly). The degree of contamination in the analyzed DNA was evaluated using two approaches: calculating mitochondrial genome heterozygosity via the Schmutzi program (Renaud et al., 2015) and examining X-chromosome polymorphisms using the ANGSD (Rasmussen et al., 2011). The genetic sex was determined for the studied individual using the karyo_RxRy program (Anastasiadou et al., 2024).

The mitochondrial genome sequence was reconstructed from a BAM file. The haplogroup was determined using HaploGrep 3 (Phylotree build 17), as described by S. Schönherr et al. (2023). The outcome was verified using YFull MTree 1.02 (YFull, 2025). We conducted a phylogeographic analysis using sequences from modern and ancient samples. The sequences were retrieved from the NCBI databases and selected via BLAST with 100 % query cover and 99.95 % identity. We also used the AmtDB dataset (Ehler et al., 2019). The phylogenetic tree was created using the mtPhyl program (Eltsov, Volodko, 2016), excluding highly variable sites.

The yhaplo program (Poznik et al, 2016) was used to determine the Y-chromosome haplogroup. To confirm the result, the identified single-nucleotide variants (SNVs) were cross-checked with the ISOGG Y-DNA Haplogroup Tree 2019–2020 data (International Society…, 2024, https://isogg.org/tree/index.html) and YFull YTree v.11.01.00 (YFull, 2025).

We generated a set of pseudohaploid genotypes for the 1240K panel for population genetic analyses (Mathieson et al., 2015). Genotype calling was performed using SAMtools mpileup and the --randomHaploid option from the pileupCaller package (Schiffels, 2025). Our dataset included individuals from the AADR (Allen Ancient DNA Resource) database dating from 6050 BC to 1326 AD. We restricted the analysis to genotypes derived from whole-genome sequencing data. In addition, we incorporated individuals from the Chernyakhov culture and those associated with the Scythian–Sarmatian groups (Andreeva et al., 2025; Saag et al., 2025; Schütz et al., 2025). Related individuals, as well as samples with fewer than 10,000 marker genotypes, were excluded from the analysis.

To perform a principal component analysis (PCA), we combined the selected ancient samples with modern samples from the Human Origins (HO) panel, which contains approximately 600,000 genetic markers (Lazaridis et al., 2014). Transitions, variants with a low minor allele frequency (--maf 0.01), and variants with a high percentage of missing genotypes (--geno 0.95), were excluded from the resultant file. Principal components were computed using the smartpca module in EIGENSOFT v.6.1.4 (Patterson et al., 2006). Ancient samples were then projected onto the principal component space defined by modern populations for visualization on the PCA plot.

To prepare the dataset for ADMIXTURE analysis, we supplemented it with reference populations that maximized genetic components. The transition variants, SNPs with low minor allele frequency, and those in linkage disequilibrium were pruned using the --indep-pairwise 200 5 0.5 option in PLINK v1.9 (Chang et al., 2015). To determine the optimal number of genetic components (K), we performed 10 independent ADMIXTURE runs for each K value ranging from 2 to 20, with cross-validation error estimation (--cv) enabled. The K value corresponding to the lowest cross-validation error was chosen as optimal.

Results and discussion

DNA sequencing from bone powder and subsequent mapping against reference genomes yielded an average nuclear genome coverage of approximately 1x and an average mitochondrial DNA (mtDNA) coverage exceeding 100x (see the Table). An elevated frequency of cytosine-to-thymine (C-to-T) transitions was observed at the ends of molecules, confirming the authenticity of the ancient DNA (aDNA) (Fig. 1). The individual's genetic sex was determined to be male (XY), with an estimated contamination level below 4 %.

The mitochondrial sequence belongs to haplogroup U5a1 and harbors additional variants at positions 12,811 and 8,610. Based on these variants, the individual clusters with a Bronze Age individual from the Late Minoan necropolis of Armenoi (Crete, Greece, 1370–1340 BC) (Lazaridis et al., 2017) as well as with modern individuals from Spain and Italy (Fig. 2). Notably, the mitochondrial genome of sample Dch08 represents

Summary statistics for the genomic data obtained from the Dch08 sample

Total reads	The proportion of reads mapped to the human genome (GRCh37)	Mean genome coverage (GRCh37)	Mean coverage of the human mitochondrial genome (NC_012920)	mtDNA contamination level (Schmutzi)	X-chromosome contamination level (ANGSD)
241 112 513	41.31 %	x0.9	x118.1	4 %	0.42 %

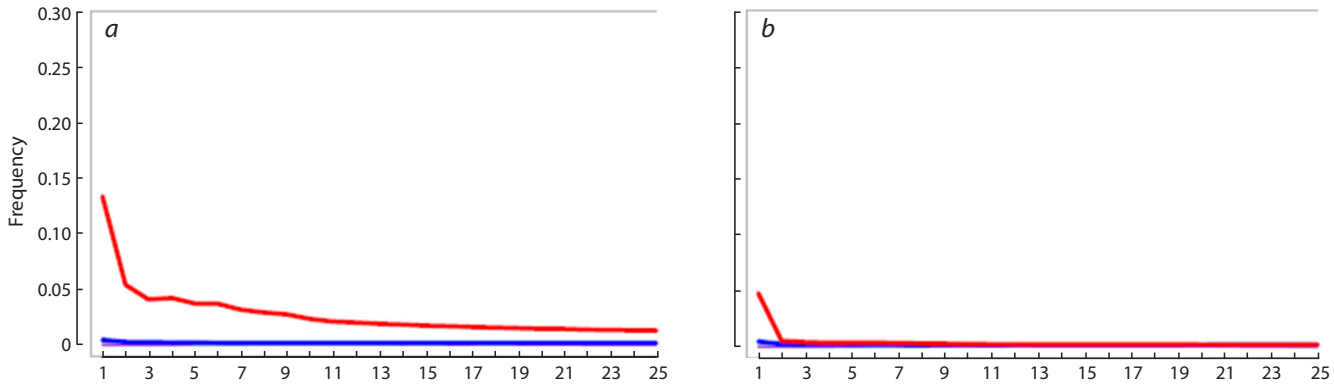


Fig. 1. Profile of C→T substitutions (red curve) in reads mapped onto the human reference genome GRCh37.
a – genomic library prepared from untreated DNA; *b* – genomic library prepared from repaired DNA.

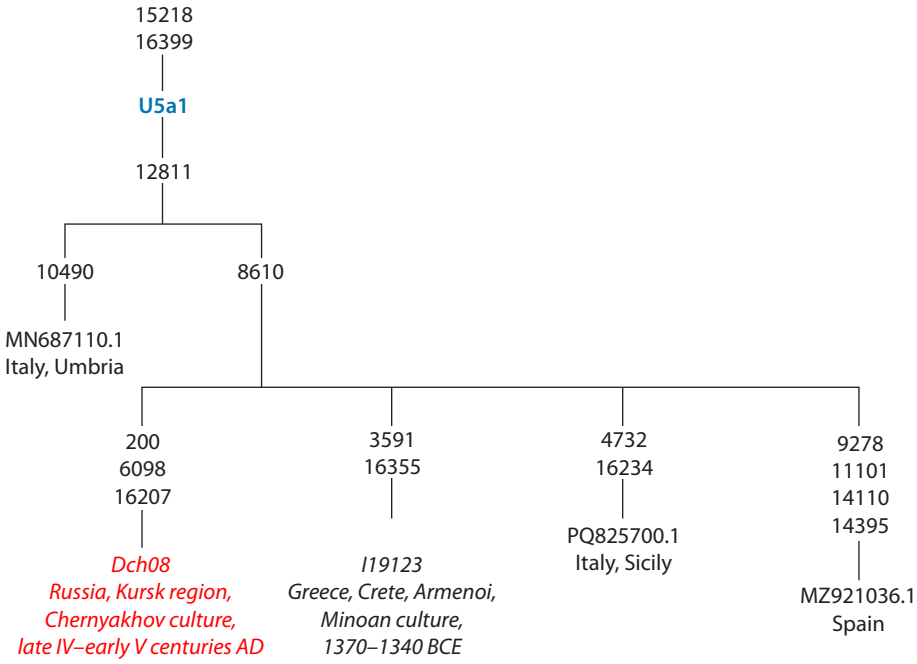


Fig. 2. A fragment of the phylogenetic tree for haplogroup U5a1.
The numbers indicate the positions of single-nucleotide substitutions. The geographical/ethnic origins of each sample are indicated, as well as the dating information for ancient samples. The test sample Dch08 is highlighted in red, and ancient samples are shown in italics.

a unique lineage within haplogroup U5a1, distinguished by specific variants at positions 200, 6,098, and 16,207 that are absent in both ancient and modern representatives of this clade.

According to YFull data, haplogroup U5a1 diverged approximately 15.4 thousand years ago and has been identified in Mesolithic populations of Northern and Eastern Europe (Skoglund et al., 2014; Mathieson et al., 2015, 2018; Günther et al., 2018; Allentoft et al., 2024), in Late Neolithic Corded Ware and Bell Beaker cultures (Linderholm et al., 2020), in Bronze Age cultures including Srubnaya (Krzewińska et al., 2018; Mathieson et al., 2018) and Minoan (Lazaridis et al., 2017), in Iron Age individuals from Italy (Emery et al., 2018)

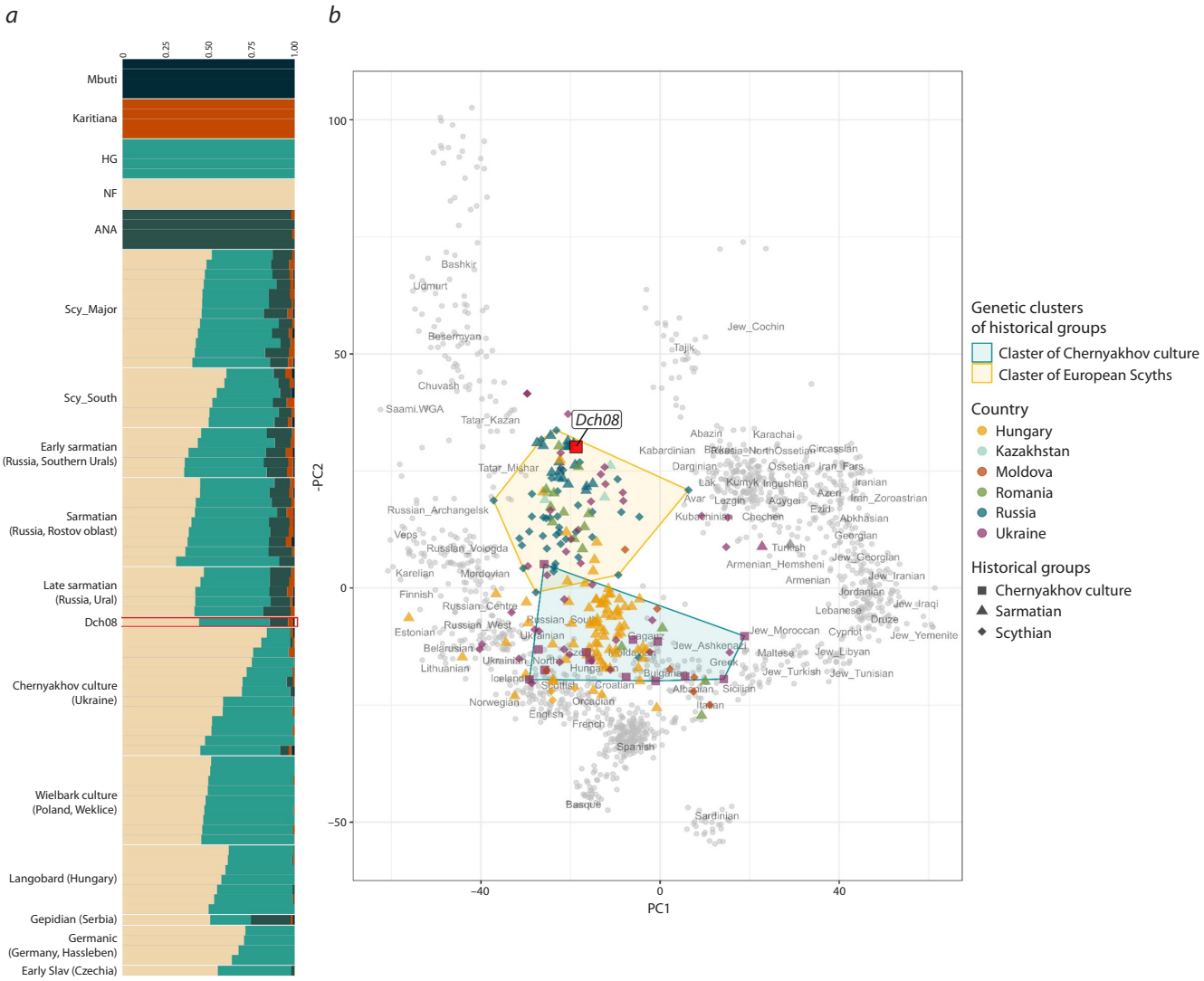


Fig. 3. The results of ADMIXTURE (*a*) and PCA (*b*) analyses for the individual under study from the Dal'niy (Vydrin) burial ground and previously published ancient individuals.

Ancient group names follow the AADR database (Mallick et al., 2024) and the publications (Andreeva et al., 2025; Saag et al., 2025): NF (Neolithic Farmers) – Austria_N_LBK.SG, Turkey_Marmara_Barcin_N.SG, Germany_Saxony_LBK_N.SG; ANA (Ancient North Asian) – Mongolia_Xiongnu.SG, Russia_DevilsCave_N.SG; HG (Hunter-gatherers) – Italy_Epigravettian.SG, Russia_Mesolithic_Veretye.SG.

and Poland (Stolarek et al., 2023), and in Sarmatians from Kazakhstan (Damgaard et al., 2018). Currently, this lineage occurs in Italy, Spain, and Russia (in particular, in certain populations of the North Caucasus), which indicates its wide distribution in Western Eurasia.

The Y-chromosome haplotype of individual Dch08 belongs to haplogroup R1a1a1b1 (R1a-Z283). No derived markers defining downstream subclades were detected. This lineage dates to approximately 5–6 thousand years ago, and its wide distribution in Europe is associated with the expansion of bearers of the Corded Ware culture (Haak et al., 2008; Underhill et al., 2010; Saag et al., 2019). The earliest samples associated with this culture and carrying the ancestral haplogroup R1a were found at the Eulau burial ground (Eastern Germany, ~2600 BC) and in Estonia (2702 BC) (Haak et al., 2008; Saag et al., 2019). In a later period, including the Early Middle Ages, carriers of haplogroup R1a-Z283 were identified in Scandinavia and other European regions (McColl et al., 2024).

According to the FamilyTreeDNA database (https://www.familytreedna.com/public/y-dna-haplotree/R), this subclade is most widespread in modern European populations, predominantly in Poland (14.37 %), Sweden (11.62 %), and Russia (10.72 %). This result indicates the genetic continuity of the Dch08 sample along the paternal line from populations that formed in Europe during the Late Neolithic.

PCA and ADMIXTURE analyses of the Dch08 sample show a genetic profile distinct from those of previously studied Chernyakhov individuals from the Legedzine, Shyshaky, Zolochiv, and Komariv-1 sites (Järve et al., 2019; Saag et al., 2025) (Fig. 3). On the PCA plot, the individual Dch08 under

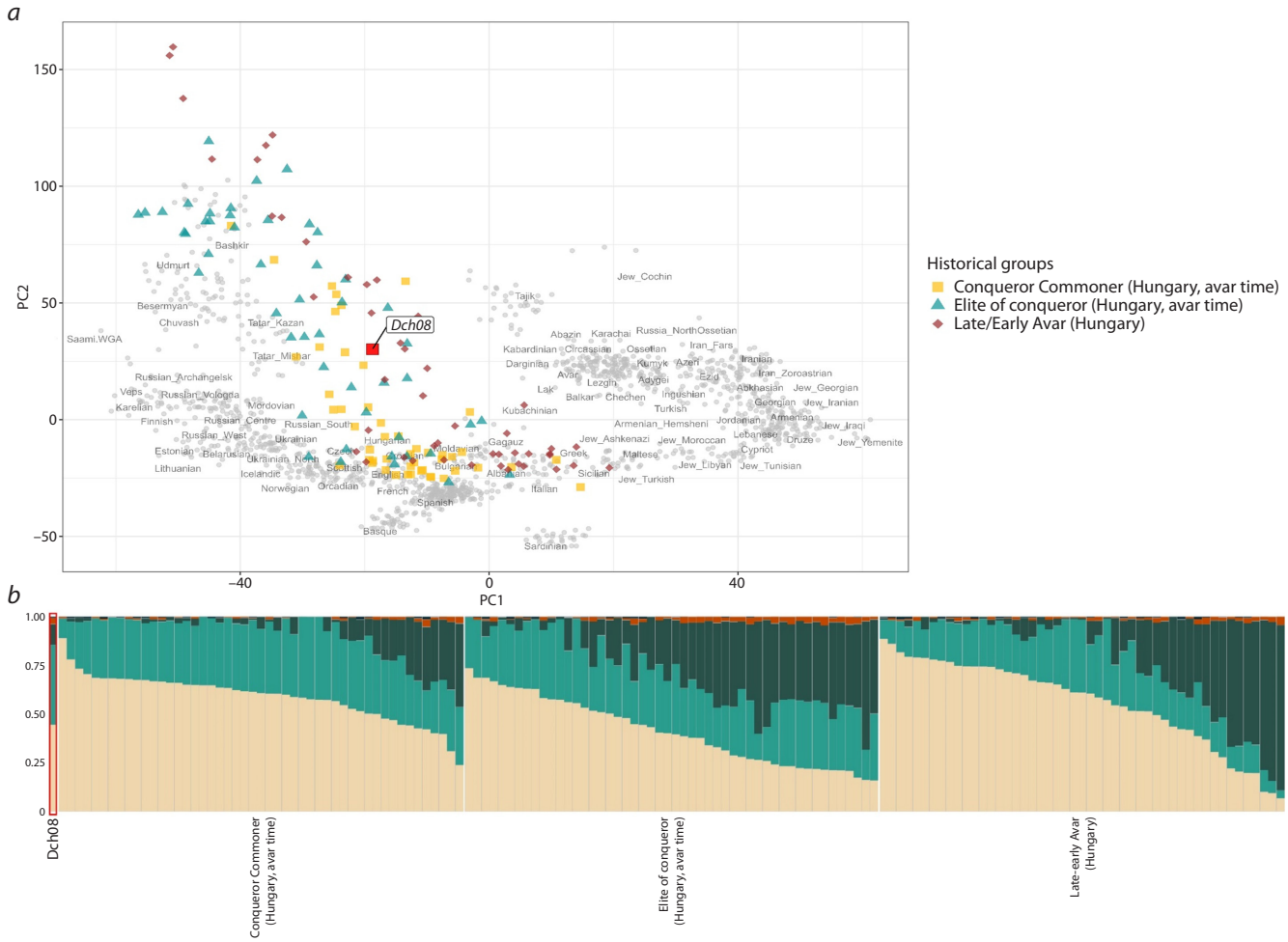


Fig. 4. PCA (*a*) and ADMIXTURE (*b*) results for the individual from the Dal'niy (Vydrin) burial ground and previously published Avar-period individuals from Hungary.

For group designations, see Figure 3.

study falls into the cluster of Early Iron Age nomads (Scythians and Sarmatians) and also demonstrates similarity with them according to the ADMIXTURE analysis results. Previous analyses of archaeological materials from Chernyakhov sites, as well as craniological analysis of its representatives, indicate the likely presence in this cultural community of a small fraction of individuals genetically linked to populations of the Scythian–Sarmatian groups, in the eastern and southern parts of the area (Lower Dnieper, Northern Pontic steppe regions) (Rudich, 2010, 2014; Radyush, 2023).

Our results support these hypotheses. Notably, unlike all previously published Chernyakhov culture individuals, the Dch08 individual carries Asian-related ancestry components (ANA) that are consistently present in the Early Iron Age nomadic populations. Importantly, similar genetic profiles have also been observed in Avar-period individuals from Hungary (6th–9th centuries AD) (Fig. 4), whose ancestry has been attributed to Scythian–Sarmatian sources (Maróti et al., 2022).

Historical and archaeological data suggest that migrants from Northern Europe, represented by the tribes of the Goths and the related Gepids and Heruli, as well as possibly other East Germanic groups, contributed to the formation of the Chernyakhov cultural community (Sedov, 1979; Magomedov, 2001; Shchukin, 2005). However, our analysis did not reveal any genetic similarity between Dch08 and any of these candidate groups for which whole-genome data were available at the time of this study. Specifically, no genetic link was found with individuals associated with the Wielbark culture (Stolarek et al., 2023; Antonio et al., 2024), the Lombards (Amorim et al., 2018), or the Gepids (Veeramah et al., 2018) (Fig. 3). The combination of uniparental inheritance markers of Western Eurasian origin (Y: R1a-Z283; mtDNA: U5a1) and an autosomal profile more characteristic of representatives of nomadic groups (Scythians, Sarmatians, and Avars) indicates the possible origin of individual Dch08 from a population that experienced genetic influence from nomads.

Conclusion

Our results demonstrate the first direct genetic link between a member of the Chernyakhov warrior elite and early 1st-millennium AD steppe nomads, revealed through whole-genome sequencing of an individual from the Dal'niy (Vydrin) burial ground. The evolution of weaponry among Eastern European forest-steppe tribes, including Chernyakhov groups, was predominantly shaped by Central European and Roman cultural horizons, whereas steppe nomadic influence was initially marginal. However, during the terminal phase of the Chernyakhov culture documented at the Dal'niy (Vydrin) site, interaction with steppe groups accelerated (Radyush, 2023). This shift is explicitly supported by the steppe-derived ancestry components identified in this late-period individual's genomic profile.

Ultimately, this study expands the empirical source base for reconstructing the mechanisms of ethnogenesis and social stratification in Eastern Europe during the pre-Hunnic and Hunnic periods, highlighting the value of integrating paleogenetic, archaeological, and historical records.

References

Allentoft M.E., Sikora M., Refoyo-Martínez A., Irving-Pease E.K., Fischer A., Barrie W., Ingason A., … Delaneau O., Werge T., Racimo F., Kristiansen K., Willerslev E. Population genomics of post-glacial western Eurasia. *Nature*. 2024;625(7994):301-311. doi 10.1038/s41586-023-06865-0

Amorim C.E.G., Vai S., Posth C., Modi A., Koncz I., Hakenbeck S., La Rocca M.C., … Barbujani G., Krause J., Caramelli D., Geary P.J., Veeramah K.R. Understanding 6th-century barbarian social organization and migration through paleogenomics. *Nat Commun*. 2018;9(1):3547. doi 10.1038/s41467-018-06024-4

Anastasiadou K., Silva M., Booth T., Speidel L., Audsley T., Barrington C., Buckberry J., … Holst M., Loe L., Armit I., Schulting R., Skoglund P. Detection of chromosomal aneuploidy in ancient genomes. *Commun Biol*. 2024;7:14. doi 10.1038/s42003-023-05642-z

Andreeva T.V., Manakhov A.D., Gusev F.E., Patrikeev A.D., Golovanova L.V., Doronichev V.B., Shirobokov I.G., Rogaev E.I. Genomic analysis of a novel Neanderthal from Mezmaiskaya Cave provides insights into the genetic relationships of Middle Palaeolithic populations. *Sci Rep*. 2022;12(1):13016. doi 10.1038/s41598-022-16164-9

Andreeva T.V., Soshkina A.D., Gusev F.E., Malyarchuk A.B., Dotsenko G.S., Dudko N.A., Plotnikova M.Yu., … Kantorovich A.R., Maslov V.E., Barinov D.G., Dobrovolskaya M.V., Rogaev E.I. Genetic history of Scythia. *Sci Adv*. 2025;11(30):eads8179. doi 10.1126/sciadv.ads8179

Antonio M.L., Weiß C.L., Gao Z., Sawyer S., Oberreiter V., Moots H.M., Spence J.P., … Borić D., Novak M., Coppa A., Pinhasi R., Pritchard J.K. Stable population structure in Europe since the Iron Age, despite high mobility. *eLife*. 2024;13:e79714. doi 10.7554/eLife.79714

Chang C.C., Chow C.C., Tellier L.C., Vattikuti S., Purcell S.M., Lee J.J. Second-generation PLINK: rising to the challenge of larger and richer datasets. *GigaScience*. 2015;4(1):7. doi 10.1186/s13742-015-0047-8

Damgaard P.B., Marchi N., Rasmussen S., Peyrot M., Renaud G., Korneliussen T., Moreno-Mayar J.V., … Nielsen R., Sikora M., Heyer E., Kristiansen K., Willerslev E. 137 ancient human genomes from across the Eurasian steppes. *Nature*. 2018;557(7705):369-374. doi 10.1038/s41586-018-0094-2

Danecek P., Bonfield J.K., Liddle J., Marshall J., Ohan V., Pollard M.O., Whitwham A., Keane T., McCarthy S.A., Davies R.M., Li H. Twelve years of SAMtools and BCFtools. *GigaScience*. 2021;10(2):giab008. doi 10.1093/gigascience/giab008

Ehler E., Novotný J., Juras A., Chyleński M., Moravčík O., Pačes J. AmtDB: a database of ancient human mitochondrial genomes. *Nucleic Acids Res*. 2019;47(D1):D29-D32. doi 10.1093/nar/gky843

Eltsov N., Volodko N. MtPhyl: Software tool for human mtDNA analysis and phylogeny reconstruction. 2016

Emery M.V., Duggan A.T., Murchie T.J., Stark R.J., Klunk J., Hider J., Eaton K., Karpinski E., Schwarcz H.P., Poinar H.N., Prowse T.L. Ancient Roman mitochondrial genomes and isotopes reveal relationships and geographic origins at the local and pan-Mediterranean scales. *J Archaeol Sci Rep*. 2018;20:200-209. doi 10.1016/j.jasrep.2018.04.036

Gansauge M.-T., Meyer M. Single-stranded DNA library preparation for the sequencing of ancient or damaged DNA. *Nat Protoc*. 2013;8(4):737-748. doi 10.1038/nprot.2013.038

Günther T., Malmström H., Svensson E.M., Omrak A., Sánchez-Quinto F., Kılınç G.M., Krzewińska M., … Lidén K., Skar B., Storå J., Götherström A., Jakobsson M. Population genomics of Mesolithic Scandinavia: investigating early postglacial migration routes and high-latitude adaptation. *PLoS Biol*. 2018;16(1):e2003703. doi 10.1371/journal.pbio.2003703

Haak W., Brandt G., de Jong H.N., Meyer C., Ganslmeier R., Heyd V., Hawkesworth C., Pike A.W.G., Meller H., Alt K.W. Ancient DNA, Strontium isotopes, and osteological analyses shed light on social and kinship organization of the Later Stone Age. *Proc Natl Acad Sci*. 2008;105(47):18226-18231. doi 10.1073/pnas.0807592105

Heather P. The Fall of the Roman Empire: a New History of Rome and the Barbarians. Oxford: Oxford University Press, 2005

International Society of Genetic Genealogy (ISOGG v15.73). 2024. URL: https://isogg.org/tree/index.html (accessed 12.24.2025)

Järve M., Saag L., Scheib C.L., Pathak A.K., Montinaro F., Pagani L., Flores R., … Metspalu M., Savelev N., Kriiska A., Kivisild T., Villems R. Shifts in the genetic landscape of the Western Eurasian Steppe associated with the beginning and end of the Scythian dominance. *Curr Biol*. 2019;29(14):2430-2441.e10. doi 10.1016/j.cub.2019.06.019

Jónsson H., Ginolhac A., Schubert M., Johnson P.L.F., Orlando L. mapDamage2.0: fast approximate Bayesian estimates of ancient DNA damage parameters. *Bioinformatics*. 2013;29(13):1682-1684. doi 10.1093/bioinformatics/btt193

Krzewińska M., Kılınç G.M., Juras A., Koptekin D., Chyleński M., Nikitin A.G., Shcherbakov N., … Dalén L., Sinika V., Jakobsson M., Storå J., Götherström A. Ancient genomes suggest the eastern Pontic-Caspian steppe as the source of western Iron Age nomads. *Sci Adv*. 2018;4(10):eaat4457. doi 10.1126/sciadv.aat4457

Lazaridis I., Patterson N., Mittnik A., Renaud G., Mallick S., Kirsanow K., Sudmant P.H., … Slatkin M., Pääbo S., Kelso J., Reich D., Krause J. Ancient human genomes suggest three ancestral populations for present-day Europeans. *Nature*. 2014;513(7518):409-413. doi 10.1038/nature13673

Lazaridis I., Mittnik A., Patterson N., Mallick S., Rohland N., Pfrengle S., Furtwängler A., … Stockhammer P., Pinhasi R., Reich D., Krause J., Stamatoyannopoulos G. Genetic origins of the Minoans and Mycenaeans. *Nature*. 2017;548(7666):214-218. doi 10.1038/nature23310

Li H., Handsaker B., Wysoker A., Fennell T., Ruan J., Homer N., Marth G., Abecasis G., Durbin R.; 1000 Genome Project Data Processing Subgroup. The Sequence Alignment/Map format and SAMtools. *Bioinformatics*. 2009;25(16):2078-2079. doi 10.1093/bioinformatics/btp352

Linderholm A., Kılınç G.M., Szczepanek A., Włodarczak P., Jarosz P., Belka Z., Dopieralska J., … Koman W., Rodríguez-Varela R.,

Storå J., Götherström A., Krzewińska M. Corded Ware cultural complexity uncovered using genomic and isotopic analysis from southeastern Poland. *Sci Rep*. 2020;10(1):6885. doi 10.1038/s41598-020-63138-w

Magomedov B.V. Chernyakhov Culture. The Problem of Ethnicity. Lublin, 2001;140-143. Available: http://archaeology.ru/Download/Magomedov/Magomedov_2001_Czerniachov_ethnos.pdf (in Russian)

Mallick S., Micco A., Mah M., Ringbauer H., Lazaridis I., Olalde I., Patterson N., Reich D. The Allen Ancient DNA Resource (AADR) a curated compendium of ancient human genomes. *Sci Data*. 2024; 11(1):182. doi 10.1038/s41597-024-03031-7

Maróti Z., Neparáczki E., Schütz O., Maár K., Varga G.I.B., Kovács B., Kalmár T., … Gulyás B., Kovacsóczy B.N., Gál S.S., Tomka P., Török T. The genetic origin of Huns, Avars, and conquering Hungarians. *Curr Biol*. 2022;32(13):2858-2870.e7. doi 10.1016/j.cub.2022.04.093

Mathieson I., Lazaridis I., Rohland N., Mallick S., Patterson N., Roodenberg S.A., Harney E., … Anthony D., Lalueza-Fox C., Haak W., Pinhasi R., Reich D. Genome-wide patterns of selection in 230 ancient Eurasians. *Nature*. 2015;528(7583):499-503. doi 10.1038/nature16152

Mathieson I., Alpaslan-Roodenberg S., Posth C., Szécsényi-Nagy A., Rohland N., Mallick S., Olalde I., … Borić D., Bonsall C., Krause J., Pinhasi R., Reich D. The genomic history of southeastern Europe. *Nature*. 2018;555(7695):197-203. doi 10.1038/nature25778

McColl H., Kroonen G., Moreno-Mayar J.V., Seersholm F.V., Scorrano G., Pinotti T., Vimala T., … Nielsen R., Hedeager L., Kristiansen K., Sikora M., Willerslev E. Steppe ancestry in Western Eurasia and the spread of the Germanic languages. *bioRxiv*. 2024. doi 10.1101/2024.03.13.584607

Mouttham N., Klunk J., Kuch M., Fourney R., Poinar H. Surveying the repair of ancient DNA from bones via high-throughput sequencing. *BioTechniques*. 2015;59(1):19-25. doi 10.2144/000114307

Oblomskiy A.M. The Forest-steppe Dnieper Left Bank Area in the Late Roman and Hun Ages (middle III–first half of V centuries A.D.). Moscow: Nauka Publ., 2002 (in Russian)

Patterson N., Price A.L., Reich D. Population structure and eigenanalysis. *PLoS Genet*. 2006;2(12):e190. doi 10.1371/journal.pgen.0020190

Picard Tools – By Broad Institute [WWW Document]. 2019. URL https://broadinstitute.github.io/picard/ (accessed 12.1.2025)

Poznik G.D. Identifying Y-chromosome haplogroups in arbitrarily large samples of sequenced or genotyped men. *bioRxiv*. 2016. doi 10.1101/088716

Radyush O.A. Armament of 3rd–5th centuries AD from Chernyakhov culture settlements from the Sejm river basin in the Kursk region. *Stratum Plus. Archaeol Cultural Anthropol.* 2012;4:139-155 (in Russian)

Radyush O.A. The Chernyaknov and Kiev cultures: correlations and problems in the interpretation of artifacts in the eastern Dnieper left bank area. In: Early Iron Age in Eurasia from the Turn of Eras to the Middle 1st Millennium A.D.: Dynamics of Cultural Arena Expansion. St. Petersburg: Skifiya-Print Publ., 2018;119-125 (in Russian)

Radyush O.A. Top-quality weapon and armor in the eastern Early Slavic world in the 5th–6th centuries. In: Balkans, Danube Region, and Eastern Europe in the Roman and Early Middle Ages. Novi-Sad, 2019;261-288 (in Russian)

Radyush O.A. "Sarmatian" elements in the armament of the Chernyakhov culture? (Some controversial issues in the study of weapons of the late Roman period and the beginning of the migration era of peoples in Eastern Europe). *Nizhnevolzhskii Arkheologicheskii Vestnik = Lower Volga Archaeological Bulletin*. 2023;22(2):126-166. doi 10.15688/nav.jvolsu.2023.2.7 (in Russian)

Radyush O.A., Vasil'ev A.A. Burial with weapons at the burial ground of the Chernyakhov culture Dal'niy (Vydrin) in the Kursk region. *Nizhnevolzhskii Arkheologicheskii Vestnik = Lower Volga Archaeological Bulletin.* 2022;21(2):208-242. doi 10.15688/nav.jvolsu.2022.2.13 (in Russian)

Radyush O.A., Reshetova I.K., Rasskazova A.V. Interdisciplinary research of Chernyakhov culture materials of the 4th century AD from the Dal'niy (Vydrin) burial ground in the upper reaches of the Sudzha river. *Stratum Plus. Archaeol Cultural Anthropol.* 2025;4: 171-220. doi 10.55086/sp254171220 (in Russian)

Rasmussen M., Guo X., Wang Y., Lohmueller K.E., Rasmussen S., Albrechtsen A., Skotte L., … Sicheritz-Pontén T., Villems R., Nielsen R., Wang J., Willerslev E. An Aboriginal Australian genome reveals separate human dispersals into Asia. *Science*. 2011; 334(6052):94-98. doi 10.1126/science.1211177

Renaud G., Slon V., Duggan A.T., Kelso J. Schmutzi: estimation of contamination and endogenous mitochondrial consensus calling for ancient DNA. *Genome Biol*. 2015:16;224. doi 10.1186/s13059-015-0776-0

Rudich T.A. Sarmatians in the Chernyakhov culture according to anthropological data. In: The Goths and Rome. Kiev, Biblioteka Vita Antiqua Publ., 2006;73-86 (in Russian)

Rudich T.A. Chernyakhov culture population on the territories between the Danube and Dniester rivers according to the anthropological data. *Stratum Plus. Archaeol Cultural Anthropol.* 2010;4:223-231 (in Russian)

Rudich T.O. Inhabitants of the Middle Dnieper Region in the 1st and 2nd Millennia According to Anthropological Data. Kyiv: Maidan Publ., 2014 (in Ukrainian)

Saag L., Laneman M., Varul L., Malve M., Valk H., Razzak M.A., Shirobokov I.G., … Kivisild T., Villems R., Lang V., Metspalu M., Tambets K. The arrival of Siberian ancestry connecting the Eastern Baltic to Uralic speakers further east. *Curr Biol*. 2019;29(10):1701-1711.e16. doi 10.1016/j.cub.2019.04.026

Saag L., Utevska O., Zadnikov S., Shramko I., Gorbenko K., Bandrivskyi M., Pavliv D., … Barrington C., Gilardet A., Macleod R., Skoglund P., Thomas M.G. North Pontic crossroads: mobility in Ukraine from the Bronze Age to the early modern period. *Sci Adv*. 2025;11(2):eadr0695. doi 10.1126/sciadv.adr0695

Schiffels S. stschiff/sequenceTools. 2025

Schönherr S., Weissensteiner H., Kronenberg F., Forer L. Haplogrep 3 – an interactive haplogroup classification and analysis platform. *Nucleic Acids Res*. 2023;51(W1):W263-W268. doi 10.1093/nar/gkad284

Schubert M., Ginolhac A., Lindgreen S., Thompson J.F., AL-Rasheid K.A., Willerslev E., Krogh A., Orlando L. Improving ancient DNA read mapping against modern reference genomes. *BMC Genomics*. 2012;13:178. doi 10.1186/1471-2164-13-178

Schubert M., Lindgreen S., Orlando L. AdapterRemoval v2: rapid adapter trimming, identification, and read merging. *BMC Res Notes*. 2016;9:88. doi 10.1186/s13104-016-1900-2

Schütz O., Maróti Z., Tihanyi B., Kiss A.P., Nyerki E., Gînguță A., Kiss P., … Soficaru A.D., Spekker O., Varga S., Neparáczki E., Török T. Unveiling the origins and genetic makeup of the "forgotten people": a study of the Sarmatian-period population in the Carpathian Basin. *Cell*. 2025;188(15):4074-4090.e11. doi 10.1016/j.cell.2025.05.009

Sedov V.V. The Origin and Early History of Slavs. Moscow: Nauka Publ., 1979 (in Russian)

Shchukin M.B. The Gothic Way (Goths, Rome and the Culture of Chernjakhov). Saint-Petersburg, 2005 (in Russian)

Skoglund P., Malmström H., Omrak A., Raghavan M., Valdiosera C., Günther T., Hall P., … Apel J., Willerslev E., Storå J., Götherström A., Jakobsson M. Genomic diversity and admixture differs for stone-age Scandinavian foragers and farmers. *Science*. 2014;344(6185):747-750. doi 10.1126/science.1253448

Stolarek I., Zenczak M., Handschuh L., Juras A., Marcinkowska-Swojak M., Spinek A., Dębski A., Matla M., Kóčka-Krenz H., Piontek J.; Polish Archaeogenomics Consortium Team; Figlerowicz M. Genetic history of East-Central Europe in the first millennium CE. *Genome Biol*. 2023;24(1):173. doi 10.1186/s13059-023-03013-9

Terpilovsky R.V. Kiev and Cherniakhov cultures: the problem of contacts. *Stratum Plus. Archaeol Cultural Anthropol.* 2000;4:303-311 (in Russian)

Underhill P.A., Myres N.M., Rootsi S., Metspalu M., Zhivotovsky L.A., King R.J., Lin A.A., … Majumder P., Rudan P., Primorac D., Villems R., Kivisild T. Separating the post-Glacial coancestry of European and Asian Y chromosomes within haplogroup R1a. *Eur J Hum Genet*. 2010;18(4):479-484. doi 10.1038/ejhg.2009.194

Veeramah K.R., Rott A., Groß M., Van Dorp L., López S., Kirsanow K., Sell C., … Päffgen B., Hellenthal G., Haas-Gebhard B., Harbeck M., Burger J. Population genomic analysis of elongated skulls reveals extensive female-biased immigration in Early Medieval Bavaria. *Proc Natl Acad Sci USA*. 2018;115(13):3494-3499. doi 10.1073/pnas.1719880115

YFull [WWW Document]. 2025. URL https://www.yfull.com/ (accessed 12.1.2025)

Conflict of interest. The authors declare no conflict of interest.
Received December 24, 2025. Revised December 29, 2025. Accepted December 29, 2025.

Vavilovskii Zhurnal Genetiki i Selektsii
Vavilov Journal of Genetics and Breeding. 2026;30(6):964-972

doi 10.18699/vjgb-26-97

UAV-based disease detection in strawberry by multispectral image segmentation invoking deep learning

A.F. Cheshkova, V.S. Riksen, O.V. Elkin

Siberian Federal Scientific Center of AgroBioTechnologies of the Russian Academy of Sciences, Krasnoobsk, Novosibirsk region, Russia
riksenvs@sfsca.ru

Abstract. Accurate and timely diagnosis of strawberry diseases is crucial for minimizing crop loss and reducing the cost of plant treatment. The use of unmanned aerial vehicles (UAVs) equipped with multispectral cameras opens up new possibilities for noninvasive plant health monitoring. The objective of this research is to explore the feasibility of detecting diseases in strawberries through multispectral imagery obtained from UAVs combined with deep learning techniques. Leaf spot disease, caused by *Ramularia tulasnei* Sacc., was chosen as a case study. A DJI Phantom 4 Multispectral quadcopter was used to survey an experimental plot (37×22 m) from an altitude of 3 m, achieving a resolution of 2.2 mm per pixel. Preprocessing of the acquired data involved orthomosaic building using Agisoft Metashape Pro and manual region-of-interest (ROI) extraction in ENVI 5.2. A dataset comprising 360 multispectral images, each of size 64×64×5 (with spectral bands at 450, 560, 650, 730, and 840 nm), was created and separated into three classes: healthy plants, diseased plants, and soil. Using this dataset, a U-Net-based model – supplemented with the attention gate, squeeze-and-excitation, and residual connections modules – was trained. Additionally, to assess the contribution of multispectral channels, another U-Net model was trained on RGB images, as well as a classic Random Forest model based on 40 GLCM texture features. The U-Net model trained on multispectral data achieved an overall classification accuracy of 96.04 %, which is significantly higher than the performance of Random Forest (76.64 %) and the U-Net on RGB images (94.14 %). The resulting disease distribution maps enable site-specific fungicide application. The proposed approach confirmed the effectiveness of deep learning for diagnosing leaf spot disease in strawberries. Future research will focus on expanding the dataset (different cultivars and disease stages), testing more advanced segmentation architectures, and scaling the method to commercial plantations.

Key words: strawberry; leaf spot disease; UAV; multispectral imaging; deep learning; U-Net; semantic segmentation; precision agriculture

For citation: Cheshkova A.F., Riksen V.S., Elkin O.V. UAV-based disease detection in strawberry by multispectral image segmentation invoking deep learning. *Vavilovskii Zhurnal Genetiki i Selektsii = Vavilov J Genet Breed*. 2026;30(6):964-972. doi 10.18699/vjgb-26-97

Обнаружение болезней земляники садовой с помощью БПЛА на основе сегментации мультиспектральных изображений методами глубокого машинного обучения

А.Ф. Чешкова, В.С. Риксен, О.В. Елкин

Сибирский федеральный научный центр агробиотехнологий Российской академии наук, р. п. Краснообск, Новосибирская область, Россия
riksenvs@sfsca.ru

Аннотация. Точная и своевременная диагностика болезней земляники садовой является важной задачей, позволяющей минимизировать потери урожая и снизить затраты на обработку растений. Использование беспилотных летательных аппаратов (БПЛА) с мультиспектральными камерами открывает новые возможности для неинвазивного мониторинга состояния растений. Цель настоящего исследования – анализ возможности выявления заболеваний земляники садовой (на примере белой пятнистости, возбудитель *Ramularia tulasnei* Sacc.) по мультиспектральным изображениям, полученным с БПЛА, с использованием методов глубокого машинного обучения. Съемка опытного участка (37×22 м) проводилась квадрокоптером DJI Phantom 4 Multispectral на высоте 3 м (разрешение 2.2 мм/пиксель). Полученные данные прошли предварительную обработку, включая построение ортофотоплана в программе Agisoft Metashape Pro и ручное выделение областей интереса (ROI) в ENVI 5.2. Сформирован набор из 360 мультиспектральных изображений размером 64×64×5 (каналы 450, 560, 650, 730, 840 нм) с тремя классами: здоровые растения, больные растения и почва.

© Cheshkova A.F., Riksen V.S., Elkin O.V., 2026
This work is licensed under a Creative Commons Attribution 4.0 License

На данном наборе была обучена модель архитектуры U-Net (с модулями attention gate, squeeze-and-excitation и residual connections). Дополнительно для оценки вклада мультиспектральных каналов обучены U-Net модель на RGB-изображениях, а также классическая модель Random Forest на основе 40 текстурных признаков GLCM. Модель U-Net, обученная на мультиспектральных данных, достигла общей точности классификации 96.04 %, что существенно выше показателей Random Forest (76.64 %) и U-Net на RGB-изображениях (94.14 %). Полученные карты распространения болезни позволяют проводить точечное применение фунгицидов. Предложенный подход подтвердил эффективность глубокого обучения для диагностики белой пятнистости земляники. Дальнейшие исследования будут направлены на расширение набора данных (разные сорта и стадии болезней), апробацию более современных архитектур сегментации и масштабирование метода на промышленные плантации.

Ключевые слова: земляника садовая; белая пятнистость; БПЛА; мультиспектральная съемка; глубокое обучение; U-Net; семантическая сегментация; точное земледелие

Introduction

Crop health monitoring using unmanned aerial vehicles (UAVs) is a key technology in modern precision agriculture (Radoglou-Grammatikis et al., 2020). The potential of UAVs has been demonstrated in a number of applications, such as plant stress detection, field mapping, biomass estimation, weed control, and plant population counting (Toscano et al., 2024). High efficiency, stability, accuracy, and productivity are the advantages of UAVs, enabling farmers and experts to make more informed and timely management decisions (Phang et al., 2023).

The use of various types of sensors mounted on UAVs allows farmers to monitor multiple aspects of plant condition.

For example, RGB and near-infrared images enable evaluation of organ and whole-plant morphology, growth dynamics, biomass accumulation, yield traits, and pest/disease severity (Cheshkova, 2022; Zahir et al., 2022). Chlorophyll fluorescence imaging helps the assessment of plant bioenergetic status and genetic stress tolerance (Moustakas et al., 2021). Thermal infrared imaging is used to measure plant temperature, water status, and insect damage (Hou et al., 2022). Laser scanning and 3D imaging are applied to determine seed morphology, leaf orientation, canopy structure, root architecture, and linear plant dimensions (Jin et al., 2021).

One of the important and common tasks in field monitoring is the detection of plant diseases in images acquired by UAVs (Neupane, Baysal-Gurel, 2021). Among UAV-mounted sensors, multispectral cameras are the primary tool for disease identification. The spectral data from these cameras enable the computation of various vegetation indices (VIs) that reflect the biophysical and biochemical properties of plants affected by stress (Candiago et al., 2015). Vegetation indices allow quantitation of these changes and are an important factor for identifying crop diseases (Mahlein et al., 2013).

Use of multispectral data goes beyond just calculating spectral indices. A more powerful and precise way to analyze images is through machine learning. These techniques can be broadly split into two categories.

In traditional machine learning methods (e. g., SVM, Random Forest, KNN), an expert manually creates and selects features from raw data (Behmann et al., 2015; Singh et al., 2016). The quality of the model is strongly dependent on the quality of these features. Despite their advantages, these algorithms can only be applied to tabular data, which limits their utility for detecting plant diseases in images or videos (Benos et al., 2021).

Deep learning methods (U-Net, SegNet, ResNet), in contrast, perform automatic feature extraction. The neural network learns feature hierarchies directly from raw data without manual intervention (Mudarisov, Miftakhov, 2024; Sajitha et al., 2024). These methods can process images and videos to detect and classify plant disease symptoms (Loey et al., 2020; Nagaraju, Chawla, 2020; Abade et al., 2021).

The main tasks in machine-learning-based image analysis are segmentation, classification, and detection (Saleem et al., 2019; Ding et al., 2024).

Detecting plant stress from UAV imagery is a semantic segmentation problem: each pixel is labeled as soil, healthy plant, or diseased plant, resulting in a field-wide map of disease spread.

Among berry crops, strawberry (*Fragaria* × *ananassa*) holds the leading position in global production and consumption, accounting for over 70 % of the world's berry production (Ozherelev et al., 2019). Precise, rapid, and noninvasive detection of diseases and abiotic stress in strawberries is essential for commercial production, enabling reduced crop losses and lower plant management costs (Zheng et al., 2021).

The aim of this study is to analyze the feasibility of detecting diseases in strawberries (*Fragaria* × *ananassa*) using multispectral images acquired by UAVs and deep learning methods.

Materials and methods

Plant material. The research was carried out on strawberry plants growing in an experimental plot of the Siberian Federal Research Center of Agro-BioTechnologies, Russian Academy of Sciences (Krasnoobsk, Novosibirsk region, Russia). The 37 × 22 m plot contained three-year-old

cv. Festivalnaya plants planted in 50-cm wide rows spaced 70 cm apart. At the time of imaging, most plants were affected by leaf spot disease (caused by *Ramularia tulasnei* Sacc.) Through visual inspection, 80 healthy plants and 80 plants with visible leaf lesions were selected. The selected plants were tagged with pink and blue labels, respectively (Fig. 1).

Image acquisition. A DJI Phantom 4 Multispectral quadcopter (SZ DJI Technology Co., Ltd., Shenzhen, China) was used for image acquisition. Its camera has one RGB (visible light) sensor and five monochrome sensors (blue, green, red, red edge, near-infrared) at wavelengths of 450, 560, 650, 730, and 840 nm, respectively.

The flight took place on July 15, 2025, under cloudy skies at an altitude of 3 m, yielding a resolution of 2.2 mm/pixel. The mission produced 2,170 images with 75 % forward overlap and 60 % side overlap.

Image preprocessing and dataset generation. Monochrome multispectral cameras capture each spectral band using a separate sensor at different points in time. Due to drone movement and vibrations, these channels are not pixel-aligned in the raw frames. Prior to model training, it is necessary to bind all spectral channels to a common coordinate system and create a multispectral raster in which each pixel contains all the required wavelengths. This step is mandatory for a neural network being able to correctly extract spectral features; otherwise, pixels from different channels would correspond to different points on the ground.

The first step in processing the images acquired by the five monochrome PM4 cameras was to construct a unified multispectral image (orthomosaic) of the experimental plot. For this purpose, the Agisoft Metashape Pro software (Agisoft LLC, Russia) was used. The final orthomosaic was output as a GeoTIFF file with a resolution of 15,000 × 20,000 × 5 pixels and a size of 2.9 GB.

The second step was image labeling. Axis-aligned rectangular regions of interest (ROIs) of 64 × 64 × 5 pixels in size were manually drawn on the resulting orthomosaic. These ROIs contained tagged diseased plants, tagged healthy plants, and soil areas (the tags themselves were not included in the ROIs). Each ROI was saved as a separate image file (Fig. 2). ROI extraction and image generation were carried out in ENVI 5.2 (ITT Visual Information Solutions).

A dataset of 360 multispectral images (120 per class) was generated in this way: 240 for training, 60 for validation, and 60 for testing.

To enable model accuracy comparisons, a second, RGB-based, dataset was prepared. Here, ROIs were drawn directly on raw PM4 RGB camera images, without orthomosaic generation. The RGB dataset also comprised 360 images of size 64 × 64 × 3.

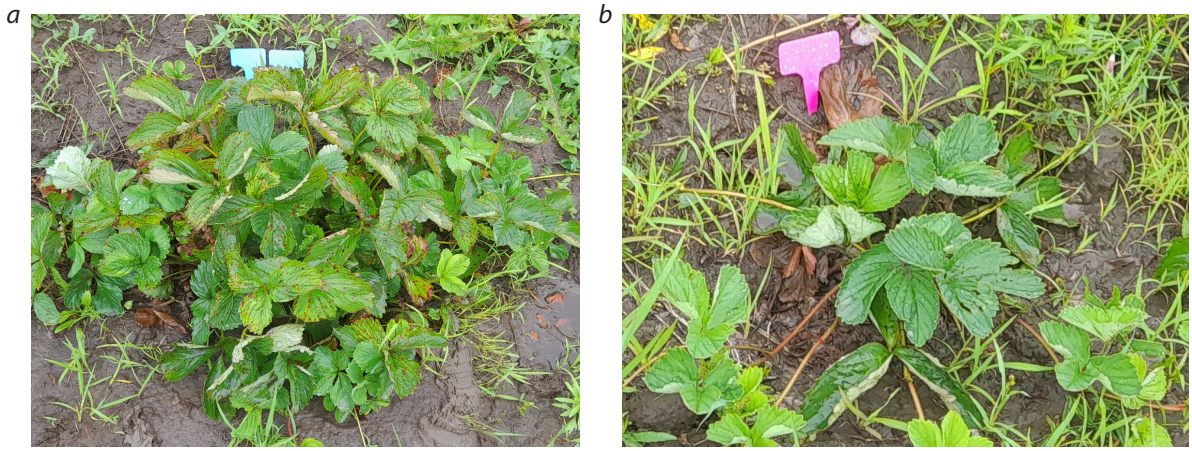


Fig. 1. Strawberry plants: *a* – affected by leaf spot disease; *b* – healthy.



Fig. 2. ROI extraction: *a* – strawberry plants affected by leaf spot disease; *b* – healthy plants; *c* – soil.

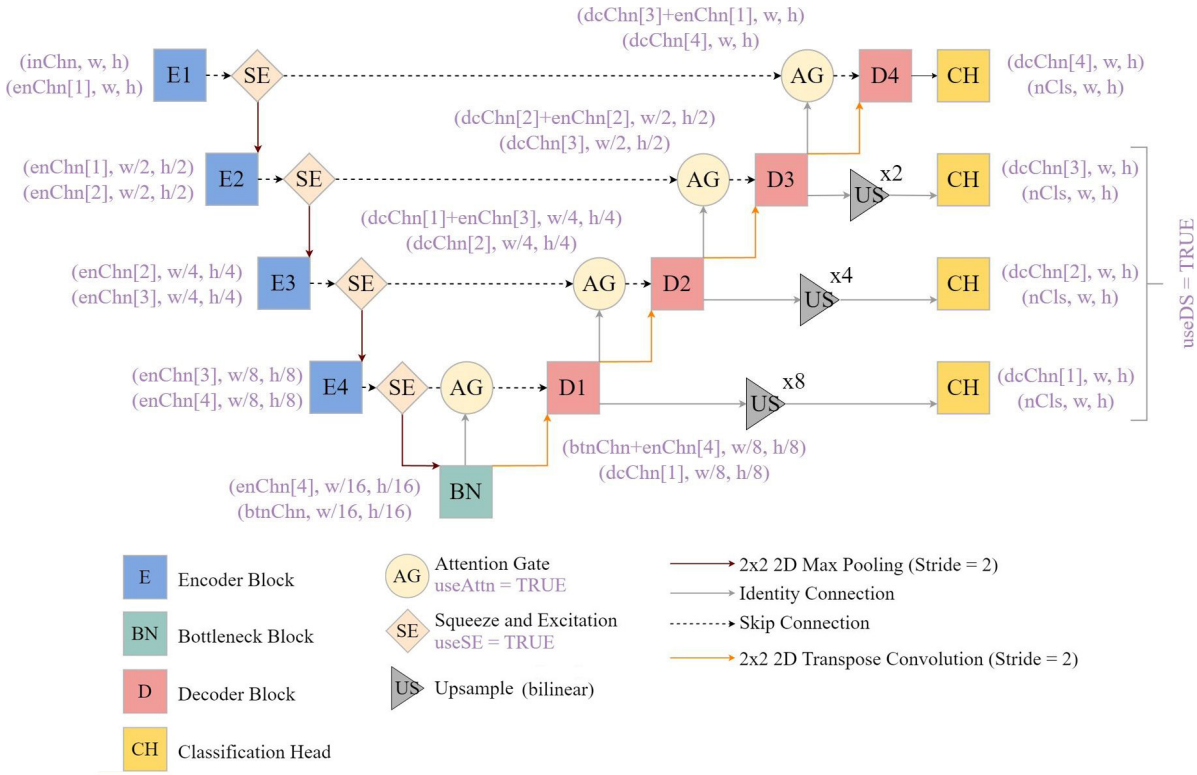


Fig. 3. U-Net architecture implemented in geodl.

Blocks prefixed with E represent encoder blocks while those prefixed with D represent decoder blocks; w – width, h – height.

For comparison with classical machine learning, an additional tabular dataset was created as follows. For each training multispectral image (64 × 64 × 5), eight GLCM-based texture features (mean, variance, homogeneity, contrast, dissimilarity, entropy, second moment, and correlation) were computed pixel-wise per channel (Li et al., 2019; Guo et al., 2021; Zhou et al., 2022) using a sliding window of (3×3) px.

For pixels whose local neighborhood extended beyond the image boundaries, the texture feature values were set to NA (not available). The relative distance measured in pixels (d) in the GLCM was set to 1 (d = 1). Matrices were computed for four directions (Θ = 0°, 45°, 90°, 135°), and the feature values were averaged across these directions. Each image yielded a table with 4,096 rows (64 × 64), 40 feature columns (8 features × 5 bands), and a class column (healthy, diseased, soil). From each table, 1,000 pixels were randomly sampled. The final training set had 240,000 rows (80,000 per class), with validation and test sets of 60,000 rows each.

Modeling and data analysis methods. All calculations and data analysis were performed in R environment using the torch, geodl, randomForest, and terra packages.

Two machine learning models were considered in this study: the U-Net deep learning model (Ronneberger et al., 2015) and the classical Random Forest model (Breiman et al., 2001).

The U-Net convolutional neural network is one of the most popular architectures for solving semantic segmentation tasks (Kerkech et al., 2020; Zhang T. et al., 2021). The U-shaped architecture of the network, consisting of a downsizing path (encoder) for capturing context and a symmetrically upsizing path (decoder) for precise localization, along with skip connections between the encoder and decoder, enables the network to combine high-level features with detailed spatial information. This method produces highly accurate segmentation maps even when training data are limited.

We used the U-Net architecture shown in Figure 3, implemented in the geodl package (Maxwell et al., 2024). This architecture can accept a variable number of input predictor variables, making it suitable for both RGB and multispectral images. The architecture comprises four encoding blocks, one bottleneck block, and four decoding blocks. The number of output feature maps was set to (16, 32, 64, 128) in the encoding blocks and (128, 64, 32, 16) in the decoding blocks. Rectified linear unit (ReLU) activation functions were implemented throughout the architecture to incorporate nonlinearity, and batch normalization was used to combat gradient issues and aid in convergence.

In the encoder, the size of the array in the spatial dimensions is reduced by half following each block using 2 × 2 max pooling with a stride of 2. In the decoder, 2D transpose convolution is used to double the spatial resolu-

tion of the feature maps provided from the prior block, also using a stride of 2. The final class logits are predicted using 1 × 1 2D convolution. Attention gate, squeeze-and-excitation, and residual connection modules were added to the main blocks of the U-Net architecture.

The classical Random Forest model, which is based on an ensemble of decision trees, is also frequently applied to remote sensing tasks, including the detection and classification of plant diseases (Lan et al., 2020; Liao et al., 2022; Zhang S. et al., 2022). In our previous work, we found that for detecting strawberry diseases from multispectral images using Random Forest, texture features perform best as predictors (Cheshkova, Riksen, 2025).

Model performance metrics. Segmentation quality was evaluated using standard per-class metrics: Accuracy, Precision, Recall, F1-score и IoU. Their calculation is based on the elements of the confusion matrix: TP (true positive) is the number of pixels belonging to the class under consideration that were correctly assigned to this class by the model; TN (true negative) is the number of pixels belonging to all other classes that were correctly not assigned to the class under consideration; FP (false positive) is the number of pixels from other classes that were incorrectly assigned to the class under consideration; and FN (false negative) is the number of pixels belonging to the class under consideration that were incorrectly assigned to other classes.

Accuracy (the proportion of correct classifications) represents the proportion of all pixels that were classified correctly when evaluating a particular class using a one-vs-rest scheme. It accounts for both the pixels of the class under consideration that were correctly identified and the pixels correctly assigned to all other classes. The closer the Accuracy value is to 1 (100 %), the higher the classification accuracy.

$$\text{Accuracy} = \frac{TP + TN}{TP + TN + FP + FN}.$$

Precision indicates the proportion of pixels assigned by the model to the class under consideration that actually belong to that class. A high Precision value corresponds to a low number of false-positive classifications.

$$\text{Precision} = \frac{TP}{TP + FP}.$$

Recall (sensitivity) characterizes the proportion of pixels belonging to the class under consideration that were correctly identified by the model among all pixels actually belonging to that class. A high Recall value indicates a low number of false-negative results, i. e., few missed pixels of the class under consideration.

$$\text{Recall} = \frac{TP}{TP + FN}.$$

The F1-score is the harmonic mean of Precision and Recall and is used to assess these two metrics jointly. A high F1-score can only be achieved when both Precision and Recall are high; therefore, this metric accounts for both false-positive and false-negative errors.

$$\text{F1 score} = \frac{2TP}{2TP + FN + FP}.$$

IoU (Intersection over Union) characterizes the degree of overlap between the class mask predicted by the model and the reference mask. The numerator represents the area of intersection between the predicted and reference masks, while the denominator represents the area of their union. An IoU value close to 1 indicates a high degree of spatial agreement between the predicted segmentation and the reference annotation.

$$\text{IoU} = \frac{TP}{TP + FN + FP}.$$

Overall Accuracy (OA) evaluates classification performance across all classes simultaneously and is defined as the ratio of the total number of correctly classified pixels from all classes to the total number of pixels. Unlike Accuracy, which is calculated separately for each class, Overall Accuracy provides a single summary measure of multiclass image classification performance.

Results

Model training and validation

U-Net models were trained using the Adam optimizer and CrossEntropyLoss. The training involved Z-score normalization and data augmentation (horizontal/vertical flip with 0.5 probability, random rotation by 0°, 90°, 180°, or 270°). Models were run for 50 epochs with an initial learning rate of 0.001.

Two training datasets were compared: multispectral and RGB images. Figures 4 and 5 illustrate the U-Net training dynamics for each dataset.

The Random Forest model was trained with the following hyperparameters: number of trees = 500, minimum terminal node size = 1, and number of candidate variables per split = 6.

The trained models were evaluated on the test sets. Tables 1–3 summarize the quality metrics.

The overall classification accuracy of the U-Net model trained on multispectral imagery reached 96.04 %. A slightly lower accuracy was observed for the U-Net model trained on RGB imagery – 94.14 %. In contrast, the Random Forest model performed considerably worse at 76.64 %.

The trained models were then applied to segment the images and produce disease distribution maps for the experimental strawberry plot (Fig. 6).

Discussion

This study evaluated the feasibility of detecting diseases in strawberries (with leaf spot as an example) from UAV-acquired multispectral imagery using the U-Net deep learning

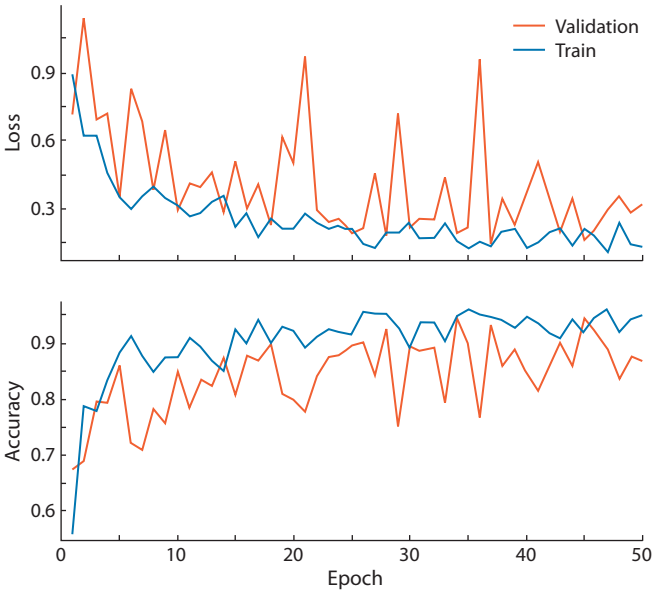


Fig. 4. U-Net training accuracy and loss curves on multispectral images.

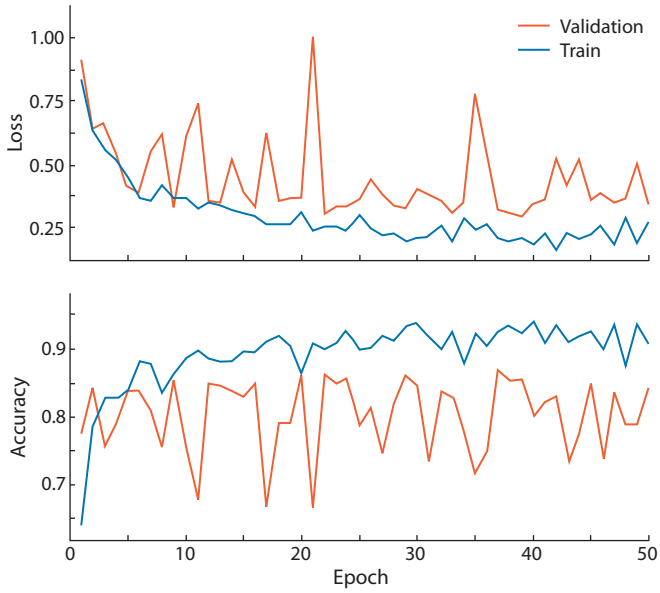


Fig. 5. U-Net training accuracy and loss curves on RGB images.

Table 1. Performance metrics of the U-Net model trained on multispectral images

Class/metric	Accuracy	Precision	Recall	F1	IoU
Soil	0.9996	0.9994	0.9994	0.9994	0.9989
Diseased	0.9603	0.9370	0.9445	0.9408	0.8882
Healthy	0.9607	0.9446	0.9370	0.9408	0.8883
Average	0.9735	0.9603	0.9603	0.9603	0.9251

Overall Accuracy – 96.04 %.

Table 2. Performance metrics of the U-Net model trained on RGB images

Class/metric	Accuracy	Precision	Recall	F1	IoU
Soil	1	1	1	1	1
Diseased	0.9414	0.9211	0.9015	0.9112	0.8370
Healthy	0.9414	0.9036	0.9228	0.9131	0.8401
Average	0.9609	0.9416	0.9414	0.9414	0.8923

Overall Accuracy – 94.14 %.

Table 3. Performance metrics of the Random Forest model trained on texture features of multispectral images

Class/metric	Accuracy	Precision	Recall	F1	IoU
Soil	0.9563	0.9174	0.9549	0.9358	0.8794
Diseased	0.7968	0.7364	0.6078	0.6660	0.4992
Healthy	0.7798	0.6496	0.7365	0.6903	0.5271
Average	0.8443	0.7678	0.7664	0.7641	0.6352

Overall Accuracy – 76.64 %.

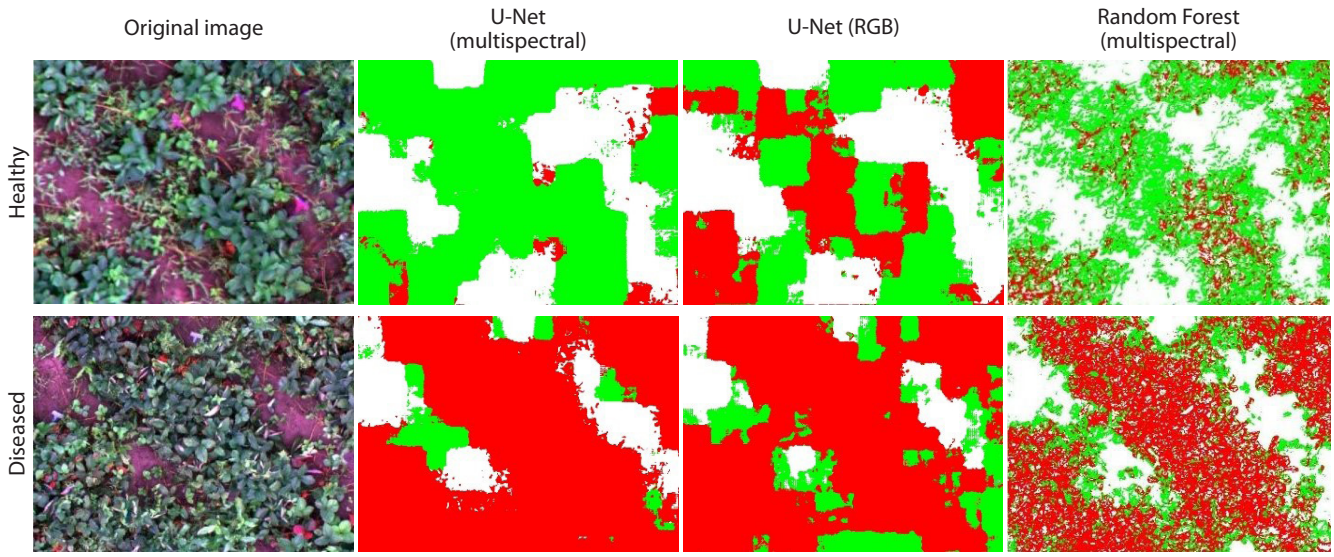


Fig. 6. Image segmentation results from the trained models.
Green – healthy plants, red – diseased plants, white – soil.

architecture and the traditional Random Forest method. The results obtained demonstrated that the U-Net model trained on multispectral data (five channels at 450, 560, 650, 730, and 840 nm) achieved an overall classification accuracy of 96.04 %, surpassing the accuracy of the Random Forest model (76.64 %) as well as that of the U-Net model trained solely on RGB images (94.14 %).

The accuracy achieved by our U-Net model (96.04 %) is comparable to, or exceeds, the results reported in other studies on crop disease detection using UAVs and deep learning. For instance, J. Su et al. (2020) and T. Zhang et al. (2021) achieved accuracies of 91 and 97 %, respectively, in detecting yellow rust in wheat using modified U-Net architectures. M. Kerkech et al. (2020) achieved 85–94 % accuracy with SegNet, DeepLabv3+, and PSPNet for grapevine diseases. Thus, our model lies at the upper end of this range, confirming the suitability of U-Net for phytopathological tasks in strawberry cultivation.

The multispectral U-Net outperformed the RGB version (96.04 *vs.* 94.14 %) because the additional red-edge (730 nm) and near-infrared (840 nm) bands are sensitive to changes in chlorophyll, mesophyll structure, and leaf water content – changes that occur during early fungal infection before visible spots appear. This inference agrees with A.-K. Mahlein et al. (2013) and S. Candiago et al. (2015), who emphasized the value of nonvisible spectral bands for early stress detection.

The Random Forest model, built on 40 GLCM texture features, achieved only 76.64 % accuracy. This is much lower than what other researchers have achieved with Random Forest for plant diseases: 90 % for eucalyptus disease (Liao et al., 2022) and 97 % for banana Fusarium wilt (Zhang S. et al., 2022). We attribute this to the specific symptomatology of leaf spot in strawberries: the disease produces small (1–5 mm) necrotic lesions on leaves that do not lead to a global change in the color or texture of the entire leaf. By contrast, banana Fusarium wilt and eucalyptus disease cause massive discoloration of whole leaves, obvious from GLCM features at the pixel-neighborhood level. GLCM features calculated for a local window (in our case, around each pixel) proved insufficiently sensitive to small-scale, scattered lesions.

These results clearly show that deep learning with multispectral UAV images is effective for detecting strawberry white leaf spot. U-Net outperformed both Random Forest and RGB-only models, confirming the value of nonvisible spectral bands and automatic feature extraction architectures.

Suggested future research directions:

- enlarge the dataset with more varieties, disease stages, and other strawberry diseases;
- compare U-Net with newer segmentation models (Swin-UNet, TransUNet, Mask2Former) for gauge accuracy gains;
- explore transfer learning using pretrained models (PlantCLEF, Agrivision) to reduce labeled data requirements;
- use multispectral time series (every 3–5 days) for early detection before visible symptoms appear.

Conclusion

The study confirmed the feasibility of automated detection of leaf spot in garden strawberries using multispectral UAV imagery. The deep learning U-Net model achieved an overall classification accuracy of 96.04 %, significantly

surpassing the performance of the Random Forest model (76.64 %) and the U-Net model trained solely on RGB images (94.14 %). This demonstrates that the U-Net architecture equipped with attention mechanisms and residual connections, together with the use of the near-infrared (840 nm) and red-edge (730 nm) channels, is essential for diagnosing diseases with scattered small lesions, where traditional texture features fail.

The practical significance of this work lies in the ability to generate detailed infection distribution maps for targeted fungicide application.

References

Abade A., Ferreira P.A., Vidal F.B. Plant diseases recognition on images using convolutional neural networks: a systematic review. *Comput Electron Agric.* 2021;185:106125. doi 10.1016/j.compag.2021.106125

Behmann J., Mahlein A.K., Rumpf T., Römer C., Plümer L. A review of advanced machine learning methods for the detection of biotic stress in precision crop protection. *Precis Agric.* 2015;16:239-260. doi 10.1007/s11119-014-9372-7

Benos L., Tagarakis A.C., Dolias G., Berruto R., Kateris D., Bochtis D. Machine learning in agriculture: a comprehensive updated review. *Sensors*. 2021;21(11):3758. doi 10.3390/s21113758

Breiman L. Random forest. *Mach Learn*. 2001;45:5-32. doi 10.1023/A:1010933404324

Candiago S., Remondino F., De Giglio M., Dubbini M., Gattelli M. Evaluating multispectral images and vegetation indices for precision farming applications from UAV images. *Remote Sens.* 2015;7(4):4026-4047. doi 10.3390/rs70404026

Cheshkova A.F. A review of hyperspectral image analysis techniques for plant disease detection and identification. *Vavilovskii Zhurnal Genetiki i Selektsii = Vavilov J Genet Breed.* 2022;26(2): 202-213. doi 10.18699/VJGB-22-25

Cheshkova A.F., Riksen V.S. Strawberry disease detection using multispectral UAV imagery. *Sel'skokhozyajstvennye Mashiny i Technologii = Agricultural Machinery and Technologies*. 2025;19(2):45-52. doi 10.22314/2073-7599-2025-19-2-45-52 (in Russian)

Ding W., Abdel-Basset M., Alrashdi I., Hawas H. Next generation of computer vision for plant disease monitoring in precision agriculture: a contemporary survey, taxonomy, experiments, and future direction. *Inf Sci.* 2024;665:120338. doi 10.1016/j.ins.2024.120338

Guo A., Huang W., Dong Y., Ye H., Ma H., Liu B., Wu W., Ren Y., Ruan C., Geng Y. Wheat yellow rust detection using UAV-based hyperspectral technology. *Remote Sens.* 2021;13(1):123. doi 10.3390/rs13010123

Hou F.J., Zhang Y., Zhou Y., Zhang M., Lv B., Wu J.Q. Review on infrared imaging technology. *Sustainability*. 2022;14(18):26. doi 10.3390/su141811161

Jin S.C., Sun X.L., Wu F.F., Su Y.J., Li Y.M., Song S.L., Xu K.X., Ma Q., Baret F., Jiang D. Lidar sheds new light on plant phenomics for plant breeding and management: recent advances and future prospects. *ISPRS J Photogramm Remote Sens.* 2021;171:202-223. doi 10.1016/j.isprsjprs.2020.11.006

Kerkech M., Hafiane A., Canals R. VddNet: Vine Disease Detection Network based on multispectral images and depth map. *Remote Sens.* 2020;12(20):3305. doi 10.3390/rs12203305

Lan Y., Huang Z., Deng X., Zhu Z., Huang H., Zheng Z., Lian B., Zeng G., Tong Z. Comparison of machine learning methods for citrus greening detection on UAV multispectral images. *Comput Electron Agric.* 2020;171:105234. doi 10.1016/j.compag.2020.105234

Li S., Yuan F., Ata-UI-Karim S.T., Zheng H., Cheng T., Liu X., Tian Y., Zhu Y., Cao W., Cao Q. Combining color indices and textures of UAV-based digital imagery for rice LAI estimation. *Remote Sens.* 2019;11(15):1763. doi 10.3390/rs11151763

Liao K., Yang F., Dang H., Wu Y., Luo K., Li G. Detection of eucalyptus leaf disease with UAV multispectral imagery. *Forests*. 2022;13(8):1322. doi 10.3390/f13081322

Loey M., Elsawy A., Afify M. Deep learning in plant diseases detection for agricultural crops: a survey. *Int J Serv Sci Manage Eng Technol.* 2020;11(2):18. doi 10.4018/IJSSMET.2020040103

Mahlein A.-K., Rumpf T., Welke P., Dehne H.-W., Plümer L., Steiner U., Oerke E.-C. Development of spectral indices for detecting and identifying plant diseases. *Remote Sens Environ.* 2013;128:21-30. doi 10.1016/j.rse.2012.09.019

Maxwell A.E., Farhadpour S., Das S., Yang Y. geodl: an R package for geospatial deep learning semantic segmentation using torch and terra. *PLoS One.* 2024;19(12):e0315127. doi 10.1371/journal.pone.0315127

Moustakas M., Calatayud Á., Guidi L. Chlorophyll fluorescence imaging analysis in biotic and abiotic stress. *Front Plant Sci.* 2021;12:658500. doi 10.3389/fpls.2021.658500

Mudarisov S.G., Miftakhov I.R. Deep learning methods and UAV technologies for crop disease detection. *Sel'skokhozyajstvennye Mashiny i Technologii = Agricultural Machinery and Technologies*. 2024;18(4):24-33. doi 10.22314/2073-7599-2024-18-4-24-33 (in Russian)

Nagaraju M., Chawla P. Systematic review of deep learning techniques in plant disease detection. *Int J Syst Assur Eng Manage.* 2020;11(3):547-560. doi 10.1007/s13198-020-00972-1

Neupane K., Baysal-Gurel F. Automatic identification and monitoring of plant diseases using unmanned aerial vehicles: a review. *Remote Sens.* 2021;13(19):3841. doi 10.3390/rs13193841

Ozherelev V.N., Ozhereleva M.V., Grin A.M., Somin V.V. Dynamics of garden strawberries production all over the world. *Vestnik of the Bryansk State Agricultural Academy*. 2019;4(74):60-66 (in Russian)

Phang S.K., Chiang T.H.A., Happonen A., Chang M.M.L. From satellite to UAV-based remote sensing: a review on precision agriculture. *IEEE Access.* 2023;11:127057-127076. doi 10.1109/ACCESS.2023.3330886

Radoglou-Grammatikis P., Sarigiannidis P., Lagkas T., Moscholios I. A compilation of UAV applications for precision agriculture. *Comput Networks.* 2020;172:107148. doi 10.1016/j.comnet.2020.107148

Ronneberger O., Fischer P., Brox T. U-net: convolutional networks for biomedical image segmentation. In: Medical Image Computing and Computer-Assisted Intervention – MICCAI 2015. Lecture Notes in Computer Science. Vol. 9351. Springer, 2015;234-241. doi 10.1007/978-3-319-24574-4_28

Sajitha P., Andrushia A.D., Anand N., Naser M.Z. A review on machine learning and deep learning image-based plant disease classification for industrial farming systems. *J Ind Inf Integr.* 2024;38:100572. doi 10.1016/j.jii.2024.100572

Saleem M.H., Potgieter J., Arif K.M. plant disease detection and classification by deep learning. *Plants*. 2019;8(11):468. doi 10.3390/plants8110468

Singh A., Ganapathysubramanian B., Singh A.K., Sarkar S. Machine learning for high-throughput stress phenotyping in plants. *Trends Plant Sci.* 2016;21(2):110-124. doi 10.1016/j.tplants.2015.10.015

Su J., Yi D., Su B., Mi Z., Liu C., Hu X., Xu X., Guo L., Chen W.H. Aerial visual perception in smart farming: field study of wheat yellow rust monitoring. *IEEE Trans Ind Inf.* 2020;17(3):2242-2249. doi 10.1109/TII.2020.2979237

Toscano F., Fiorentino C., Capece N., Erra U., Travascia D., Scopa A., Drosos M., D'Antonio P. Unmanned aerial vehicle for precision agriculture: a review. *IEEE Access.* 2024;12:69188-69205. doi 10.1109/ACCESS.2024.3401018

Zahir S.A.D.M., Omar A.F., Jamlos M.F., Azmi M.A.M., Muncan J. A review of visible and near-infrared (Vis-NIR) spectroscopy application in plant stress detection. *Sens Actuators A*. 2022;338:113468. doi 10.1016/j.sna.2022.113468

Zhang S., Li X., Ba Y., Lyu X., Zhang M., Li M. Banana fusarium wilt disease detection by supervised and unsupervised methods from UAV-based multispectral imagery. *Remote Sens.* 2022;14(5):1231. doi 10.3390/rs14051231

Zhang T., Xu Z., Su J., Yang Z., Liu C., Chen W.-H., Li J. Ir-UNet: irregular segmentation U-shape network for wheat yellow rust detection by UAV multispectral imagery. *Remote Sens.* 2021;13(19):3892. doi 10.3390/rs13193892

Zheng C., Abd-Elrahman A., Whitaker V. Remote sensing and machine learning in crop phenotyping and management, with an emphasis on applications in strawberry farming. *Remote Sens.* 2021;13(3):531. doi 10.3390/rs13030531

Zhou C., Gong Y., Fang S., Yang K., Peng Y., Wu X., Zhu R. Combining spectral and wavelet texture features for unmanned aerial vehicles remote estimation of rice leaf area index. *Front Plant Sci.* 2022;13:957870. doi 10.3389/fpls.2022.957870

Conflict of interest. The authors declare no conflict of interest.
Received April 13, 2026. Revised June 15, 2026. Accepted June 16, 2026.

BIOINFORMATICS AND SYSTEMS BIOLOGY
Original article

Vavilovskii Zhurnal Genetiki i Selektsii
Vavilov Journal of Genetics and Breeding. 2026;30(6):973-980

doi 10.18699/vjgb-26-98

Visual analysis of sorrel (*Rumex* spp.) genotypes by the biplot method using morphological characters

N. Sabaghnia [1] ✉, M. Mohebodini [2], M. Janmohammadi [1], M. Erfani [2], K. Farmanpour-Kalalagh [3]

[1] Department of Plant Production and Genetics, Faculty of Agriculture, University of Maragheh, Maragheh, Iran
[2] Department of Horticultural Science, Faculty of Agricultural Science and Natural Resources, University of Mohaghegh Ardabili, Ardabil, Iran
[3] Department of Horticultural Science, Faculty of Agriculture, Tarbiat Modares University, Tehran, Iran
✉ sabaghnia@maragheh.ac.ir

Abstract. Sorrel (*Rumex* spp.) belongs to Polygonaceae. It is distributed worldwide and used as vegetable crop and medicinal plant, so considerable research has been dedicated to its cultivation. Forty-four accessions from the Institut für Pflanzengenetik und Kulturpflanzenforschung (IPK), Germany, and ten genotypes collected from some areas of Iran were grown in two separate trials. The trials followed a completely randomized scheme with three replicates in a greenhouse environment. Seven traits were assessed: leaf length, blade length, lamina area, number of veins, petiole diameter, number of leaves, and dry leaf weight. The genotype × trait interaction (GTI) biplot model accounted for 77 and 78 % of the observed variability in the first and second trials, respectively. A nonagon and a heptagon were identified in trials, respectively, while genotypes 16 and 23 showed high mean values of dry leaf weight in the first and second trials, respectively. Genotypes 44 and 50 were identified as perfect genotypes, highly promising for sorrel genetic improvement programs, especially with regard to leaf yield. As for discriminative capacity, as well as typical potential, lamina area and petiole diameter best demonstrated differences among genotypes as perfect traits in both trials. There was a moderate positive correlation between dry leaf weight and lamina area across both trials ($r = 0.57$ for the first trial and $r = 0.49$ for the second trial). Therefore, lamina area can be considered an informative trait for constructing a selection index to improve leaf yield, along with dry leaf weight. The results demonstrate that lamina area and petiole diameter are key traits for selecting high-yielding sorrel genotypes, and the GTI biplot provides a practical visual approach to identify superior genotypes, facilitating efficient selection in breeding. Such a strategy can be recommended for future studies to describe prognostic and meticulous selection methods in order to recognize best traits for the breeding of sorrel and other vegetable crops.

Key words: dry leaf weight; discriminative capacity; perfect genotype; typical potential

For citation: Sabaghnia N., Mohebodini M., Janmohammadi M., Erfani M., Farmanpour-Kalalagh K. Visual analysis of sorrel (*Rumex* spp.) genotypes by the biplot method using morphological characters. *Vavilovskii Zhurnal Genetiki i Selektsii = Vavilov J Genet Breed*. 2026;30(6):973-980. doi 10.18699/vjgb-26-98

Acknowledgements. We are grateful to the Institute of Plant Genetics and Crop Plant Research, Germany, for supplying sorrel accessions. Also, we would like to express our gratitude to Dr. W. Yan (Agriculture and Agri-Food Canada) for providing the GGEbiplot application.

Визуальный анализ генотипов щавеля (*Rumex* spp.) биплот-методом с использованием морфологических признаков

Н. Сабагния [1] ✉, М. Мохебодини [2], М. Джанмохаммади [1], М. Эрфани [2], К. Фарманпур-Калалаг [3]

[1] Кафедра растениеводства и генетики, факультет сельского хозяйства, Университет Мараге, Мараге, Иран
[2] Кафедра садоводства, факультет сельскохозяйственных наук и природных ресурсов, Университет Мохаге Ардабили, Ардабил, Иран
[3] Кафедра садоводства, факультет сельского хозяйства, Университет Тарбиат Модарес, Тегеран, Иран
✉ sabaghnia@maragheh.ac.ir

Аннотация. Щавель (*Rumex* spp.) относится к семейству Polygonaceae, распространен по всему миру и используется как овощная культура и лекарственное растение, поэтому его культивирование стало предметом многочисленных исследований. В двух отдельных экспериментах были выращены 44 образца из Института генетики растений и исследований сельскохозяйственных культур (IPK, Германия) и 10 генотипов, собранных в разных районах Ирана. Эксперименты проводились в тепличных условиях по полностью рандомизированной схеме в трех повторениях, в ходе которых оценивались семь признаков: длина листа, длина листовой пластинки, площадь листовой пластинки, количество жилок, диаметр черешка, количество листьев и сухая масса листа. Оценка взаимодействия генотипа и признака (GTI) методом биплот-анализа объяснила 77 и 78 % наблюдаемой изменчивости в первом и втором экспериментах соответственно. В ходе испытаний были выявлены два типа расположения генотипов: нонагональное в первом и гептагональное во втором испытании, при этом генотипы 16 и 23 показали высокие средние значения сухой массы листьев в первом и втором испытаниях соответственно. Генотипы 44 и 50 были

© Sabaghnia N., Mohebodini M., Janmohammadi M., Erfani M., Farmanpour-Kalalagh K., 2026
This work is licensed under a Creative Commons Attribution 4.0 License

определены как идеальные, имеющие решающее значение для программы генетического улучшения щавеля, особенно с точки зрения урожайности листьев. Что касается дискриминационной способности, а также типичного потенциала, площадь листовой пластинки и диаметр черешка позволили выявить различия между генотипами как идеальными признаками в обоих испытаниях. Между сухой массой листьев и площадью листовой пластинки в обоих экспериментах наблюдалась умеренная положительная корреляция (r = 0.57 для первого эксперимента, r = 0.49 для второго эксперимента). Таким образом, площадь листовой пластинки можно считать информативным признаком для построения индекса отбора с целью повышения урожайности листьев, наряду с сухой массой. Результаты показывают, что площадь листовой пластинки и диаметр черешка являются ключевыми признаками для отбора высокоурожайных генотипов щавеля, а биплот-метод оценки GTI предоставляет практичный визуальный подход для выявления лучших генотипов, способствуя эффективному отбору в селекции. Подобная стратегия может быть рекомендована в будущих исследованиях для описания прогностических и тщательных методов отбора, которые помогут определить идеальные признаки для селекции щавеля и других овощных культур.

Ключевые слова: сухая масса листьев; дискриминационная способность; идеальный генотип; типичный потенциал

Introduction

One of the ways to evaluate genetic diversity is the examination of morphological traits, which is relatively simple and inexpensive, so it is used to analyze genetic diversity in different crops. There are about 200 species of sorrel (*Rumex* spp.) around the world, and some of them are known as edible vegetables or traditionally used for medicinal purposes. The genus *Rumex* belongs to the Polygonaceae family, whose species are scattered all over the world. Many sorrel species have high economic value. They are used as both vegetables and medicinal plants, where roots, leaves, seeds, and herbal extract are generally utilized. Sorrel leaves are used as food in some areas (Li et al., 2022). *Rumex rugosus* Campd. is a stable plant, which has a branched stem and relatively small leaves. Its rapid spread in nature is due to the fact that buds appear on its underground and creeping stems. *Rumex patientia* L. is a perennial plant with very large, long, heart-shaped leaves with wavy edges and its root contains anthraquinone glucosides and tannin, whereas *Rumex alpinus* L. is a large and stable plant with a thick, heart-shaped leaves. Its raw leaves are eaten like spinach in salads, and while its petiole is used like asparagus (Vasas et al., 2015). *Rumex pulcher* L. is a biennial plant with leaves with a noticeable depression near the wide base, so the leaf has a velvet-like appearance. In the context of herbal medicine, its root has an appetizing effect. *Rumex sculatus* L. has relatively woody stems with thick bushes, and it is usually found on old walls, stony ground, ditches and similar places (Bourang et al., 2023). *Rumex pseudonatronatus* Murb. is a perennial herb native to Europe and Asia, often branching above the middle. It grows in wet and disturbed locations along lake shores, roadsides, fields, meadows. *Rumex obtusifolius* L. is a perennial herb up of 40 to 150 cm in height. It has large oval leaves, which can be eaten as salad or cooked like spinach (Mohebodini et al., 2020). *Rumex kerneri* Borbas is native to Europe and has been observed in some areas as an introduced species and roadside weed. It produces a slender erect stem from a thick taproot (Mohebodini et al., 2020).

The species of sorrel are rich in ascorbic acid and secondary metabolites: oxalic acid, phenolic acids, flavonoid compounds, phenolic compounds, anthraquinone, naphthalene, sterols and triterpenes, etc. (Vasas et al., 2015). The important anthraquinone emodin is produced in many species of this genus in their roots, seeds, leaves, stems, and flowers (Li et al., 2022). Therefore, it is important to identify and choose a suitable species or modify and introduce a variety of this valuable plant. In plant breeding, the first step is to select the most suitable individuals, so it is necessary first to collect and evaluate the genetic material and then apply proper breeding methods to it. Due to the importance of this plant, studies have been conducted in various fields to investigate its genetic diversity. While previous studies have examined the fruit morphology of sorrel species (Shahla et al., 2014), these traits alone are insufficient to distinguish taxa due to overlapping characteristics. Therefore, our study focuses on leaf morphological traits critical for evaluating the leaf yield potential and for selecting superior genotypes in breeding programs. The genetic variation of some genotypes of five *Rumex* species has been assessed using morphological traits, and the highest variation coefficients have been found in fresh and dry yield of leaves and in leaf number (Bourang et al., 2023). Also, the contents of phenols and antioxidants are higher in *R. crispus* than in other species, whereas *R. tuberosus* shows lower amounts in the measured morphologic and chemical characteristics in comparison to other species examined.

One of the most effective ways to assess genetic diversity involves the analysis of morphological traits, which is simple, cost-effective, and informative for plant breeding programs. Sorrel (*Rumex* spp.) comprises about 200 species worldwide, some of which are cultivated as leafy vegetables or used for medicinal purposes. Despite its economic and nutritional importance, there is limited knowledge regarding the morphological diversity of sorrel genotypes, particularly in relation to leaf yield performance. Identifying superior genotypes and key traits is crucial for improving leaf production and guiding breeding programs.

The objectives of this study were to: (1) evaluate genetic variation among 54 sorrel genotypes from international and local collections using leaf morphological traits, (2) assess genotype × trait interactions using the GTI biplot method, (3) identify best genotypes for leaf yield, and (4) determine the most informative traits for discriminating genotypes. This knowledge is essential for selecting promising genotypes and traits to enhance leaf yield in sorrel breeding programs under greenhouse conditions. This study aims to provide practical guidance for sorrel breeding by identifying superior genotypes and key morphological traits, thereby enabling breeders to make informed decisions and accelerate the development of high-yielding cultivars.

Table 1. Codes and species types of sorrel genotypes (The first ten were collected in Iran, and the other were obtained from Genbank of the Leibniz Institute of Plant Genetics and Crop Plant Research, Germany)

Code	Species	Origin	Code	Species	Origin
1	*Rumex* spp.	Kashmar	28	*R. rugosus* Campd.	Hungary
2	*Rumex* spp.	Marand	29	*R. patientia* L.	DPRK
3	*Rumex* spp.	Ardabil	30	*R. rugosus* Campd.	Russian Federation
4	*Rumex* spp.	Hour	31	*R. pulcher* L.	Unknown
5	*Rumex* spp.	Nier	32	*R. rugosus* Campd.	
6	*Rumex* spp.	Namin	33	*R. patientia* L.	Germany
7	*Rumex* spp.	Khalkhal	34	*R. alpinus* L.	Poland
8	*Rumex* spp.	Dezfol	35	*R. rugosus* Campd.	Unknown
9	*Rumex* spp.	Ahwaz	36	*R. patientia* L.	Pakistan
10	*Rumex* spp.	Shiraz	37	*R. rugosus* Campd.	Unknown
11	*R. rugosus* Campd.	Germany	38	*R. rugosus* Campd.	
12	*R. rugosus* Campd.	Unknown	39	*R. rugosus* Campd.	
13	*R. rugosus* Campd.	Germany	40	*R. pseudonatronatus* Murb.	Russian Federation
14	*R. rugosus* Campd.	Tajikistan	41	*R. rugosus* Campd.	Unknown
15	*R. rugosus* Campd.	Slovakia	42	*R. scutatus* L.	Germany
16	*R. rugosus* Campd.	GDR	43	*R. rugosus* Campd.	Unknown
17	*R. rugosus* Campd.		44	*R. obtusifolius* L.	
18	*R. rugosus* Campd.	Kazakhstan	45	*R. kerneri* Borbas	Albania
19	*R. rugosus* Campd.	Ukraine	46	*R. patientia* L.	Unknown
20	*R. rugosus* Campd.	Tajikistan	47	*R. patientia* L.	
21	*R. rugosus* Campd.	USSR	48	*R. patientia* L.	Georgia
22	*R. rugosus* Campd.	Germany	49	*R. obtusifolius* L.	Unknown
23	*R. rugosus* Campd.	Unknown	50	*R. obtusifolius* L.	Romania
24	*R. rugosus* Campd.		51	*R. patientia* L.	Unknown
25	*R. rugosus* Campd.		52	*R. alpinus* L.	Italy
26	*R. rugosus* Campd.		53	*R. alpinus* L.	Georgia
27	*R. rugosus* Campd.		54	*R. patientia* L.	Unknown

Note. GDR, German Democratic Republic; USSR, Union of Soviet Socialist Republics; DPRK, Democratic People's Republic of Korea.

Materials and methods

Trials, plant materials and traits. Two independent trials were performed to discover the interrelationships between leaf dry yield and some morphologic traits in 54 sorrel genotypes (Table 1), which had been acquired from the Institut für Pflanzengenetik und Kulturpflanzenforschung (IPK), Germany, or collected from some regions of Iran; as the latter could not be reliably identified to species, they are referred to as *Rumex* spp.

The study was centered on genotype × trait interactions, and all accessions, regardless of species, were included to capture the phenotypic diversity relevant to leaf yield improvement. These species were *R. alpinus*, *R. kerneri*, *R. obtusifolius*, *R. patientia*, *R. pseudonatronatus*, *R. pulcher*, *R. rugosus*, *R. scutatus*, and *Rumex* spp. Seeds of each genotype were sown individually in 30-cm diameter pots, one plant per pot. The experiment was arranged in a completely randomized design with three replications. Each genotype was represented by three plants per replication, providing sufficient replication for reliable estimation of morphological traits and leaf dry weight. Plants were grown under greenhouse conditions with a 12/12 h day/night schedule at 25/15 °C, using a 1:2:1 mixture of loamy soil, sand, and organic fertilizer. Irrigation and weeding were performed regularly throughout the growth period.

The morphologic traits were estimated as recommended by Mohebodini et al. (2020): leaf length (LL), blade length (BL), lamina area (LA), number of veins (NV), petiole diameter (PD), number of leaves (NL), and leaf dry weight (DW) with the use of a laboratory caliper, leaf area meter device, and lab scales. Leaf dry weight (DW) was measured by harvesting all leaves from each plant at the end of the growth period. The leaves were then oven-dried at 70 °C until complete desiccation and weighed. Focusing on leaf dry weight allows breeders to select genotypes that maximize the most valuable component for consumption and breeding purposes. Although leaf dry weight was the primary trait of interest, additional morphological traits were measured as component traits contributing to leaf biomass. Separate analyses were performed for each trial to account for minor differences in greenhouse conditions that might influence trait manifestation.

Statistical data analysis. The normality of the measured traits was assessed using the Anderson–Darling test. All traits in both trials showed no significant deviation from normality ($p > 0.05$), confirming that the data were suitable for correlation analysis and subsequent GTI biplot modeling. Simple correlation coefficients between the traits were calculated using IBM-SPSS 25.0 (IBM-SPSS, Chicago, USA). For obtaining deeper insights into the interrelationships between traits and identifying those with the greatest impact on yield performance, the genotype × trait interaction (GTI) biplot model in the principal component analysis (PCA) layout was employed (Yan, Frégeau-Reid, 2018). The fitted model was generated with the GGEbiplot application, following the equation (Xu et al., 2017):

$$\frac{g_{ij} - t_j}{SD_j} = \sum_{n=1}^{2} \lambda_n \alpha_{in} \beta_{jn} + \theta_{ij},$$

where g_{ij} is the performance of genotype i for trait j, t_j is the means of all g_{ij}s in trait j, SD_j is the standard error for trait j, λ_n is the eigenvalue for PCAn, α_{in} and β_{jn} are the amounts for genotype i and trait j in PCAn, respectively, and θ_{ij} is the magnitude of model residuals.

To obtain symmetrical values of genotypes and traits in the biplot, the eigenvalues (λ) of the principal components were adjusted using a scaling procedure to balance genotype and trait scores, enabling a clear graphical representation of the relationships among genotypes, traits, and their interactions. The transformed dataset was processed to enable clear graphical interpretation of GTI. Data were centered by trait mean (centering), scaled to make trait variations comparable (scaling), and analyzed using singular value decomposition (SVD) to obtain principal components. The scores for genotypes and traits were adjusted to produce a symmetric biplot, allowing accurate visualization of relationships among genotypes, traits, and their interactions. In the polygon and vector-view plots, circles represent ideal or reference points; the perfect genotype or perfect trait, derived from maximum observed trait values. Orange and green lines indicate the directions and magnitudes of trait vectors, connecting each genotype or trait to the origin for visualizing relationships and correlations. Genotypes or traits closest to these circles are considered optimal or most informative, respectively.

Results and discussion

Model fitting

The PC1 and PC2 of the fitted GTI biplot model accounted for 60 to 17 % of the variation in the first trial and 60 to 18 % of the variation in the second trial within the datasets on sorrel (Fig. 1), indicating a substantial proportion of variation that demonstrated relationships among traits. Vectors were generated from the origin to the traits to explore such associations and to ease the explanations of interactions among traits (Yan, 2024). This fitted model pointed to the existence of the additive and crossover types of interaction, recommending that the rating of genotype in measured traits be altered. This is consistent with reports by Sabaghnia et al. (2015) on spinach and Sabaghnia et al. (2023) on garden cress, which emphasizes the complication of genotype selection without regarding

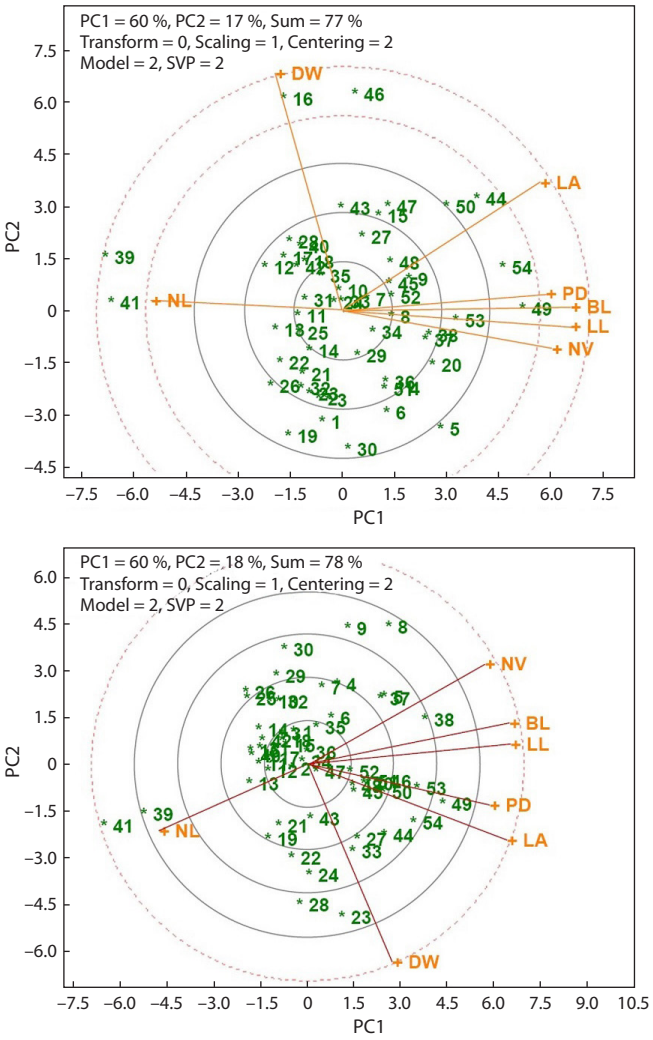


Fig. 1. The vector diagram showing relationships among traits of sorrel in (upper panel) the first trial and (lower panel) the second trial.

GTI. In this research, the fitted biplot model, as suggested by Xu et al. (2017), proved to be successful for surveying and envisaging genotypes by trait associations. The fitted biplot model explained a remarkable magnitude of variation, with trait correlations revealed by the cosines of vectors.

Vector-view analysis

According to Figure 1, outstanding relationships included: (i) positive correlations among leaf length (LL), blade length (BL), petiole diameter (PD) and number of veins (NV); cosine 0° = +1; (ii) negative correlations of number of leaves (NL) with LL, BL, PD, and NV; cosine 180° = –1; (iii) near-zero association between leaf dry weight (DW) and number of leaves (NL); cosine 90° = 0; and (iv) near-zero association of leaf DW with LL, BL, PD and NV in the first trial. Also, outstanding relationships in the second trial included: (i) positive correlations between leaf length (LL) and blade length (BL); (ii) positive correlations between lamina area (LA) and petiole diameter (PD); (iii) negative correlations between number of leaves (NL) and number of veins (NV); (iv) near-zero association between leaf dry weight (DW) and

Table 2. Correlations among traits of sorrels for (up diagonal) the first and (down diagonal) the second trial

	BL	LA	PD	NV	NL	LL	DW
BL		0.70	0.59	0.84	–0.42	0.83	0.20
LA	0.64		0.74	0.52	–0.56	0.68	0.57
PD	0.70	0.57		0.44	–0.47	0.68	0.33
NV	0.79	0.49	0.53		–0.49	0.70	0.01
NL	–0.47	–0.72	–0.43	–0.58		–0.52	0.01
LL	0.81	0.61	0.76	0.66	–0.58		0.27
DW	–0.19	0.49	–0.15	–0.27	0.30	–0.28	

Note. Significant magnitudes of correlation $p < 0.05$ and $p < 0.01$ (with degrees of freedom = 52) are 0.27 and 0.35, respectively.

number of leaves (NL); and (v) near-zero association between leaf dry weight (DW) and number of veins (NV). This agrees with findings by Mohebodini et al. (2020), who have shown positive correlations among leaf properties like leaf area and leaf length, as well as petiole diameter and number of veins, in various species of *Rumex*.

However, there was a moderate positive association between leaf dry weight (DW) with lamina area (LA) across both trials (Fig. 1), so lamina area should be considered in the determination of the selection index in sorrel breeding programs. Generally, the fitted biplot model provided an obvious visual indication of trait relations in sorrel, in agreement with the report by Bourang et al. (2023), who have found positive correlations between leaf dry weight and lamina area in some sorrel species. It should be noted that while the biplot method illustrates trait associations according to the structure of the dataset, correlation coefficients (Table 2) measure the direct interrelationship of traits and may not always directly align with the biplot results.

Polygon-view analysis

Figure 2 demonstrates how the GTI biplot model illustrates genotypes and their comparison with regard to certain traits and detects those superior in specific sections, identifying them as candidates for using in breeding programs or releasing as commercial cultivars. A nonagon was identified in the first trial (Fig. 2), while the perpendicular lines to its sides ease comparison of the vertex genotypes. However, only four vertex genotypes showed the highest values of some traits; genotype 49 had the largest averages for leaf length (LL), blade length (BL), number of veins (NV) and petiole diameter (PD); genotype 44 showed the largest lamina area (LA); genotype 39 demonstrated the greatest number of leaves (NL); and genotype 16 was superior in mean leaf dry weight (DW) in the first trial. Conversely, five vertex genotypes (5, 19, 30, 41, and 46) did not show superior performance in any of the measured traits in the first trial.

In the second trial, a heptagon was detected (Fig. 2), while only four vertex genotypes indicated the highest values for measured traits: genotype 49 had the large averages for leaf length (LL), blade length (BL), lamina area (LA) and petiole diameter (PD); genotype 41 showed a large number of leaves (NL); genotype 23 had a large leaf dry weight (DW); and genotype 8 showed a high mean for number of veins (NV) in the second trial. In contrast, three vertex genotypes (9, 30, and 38) did not manifest the most favorable performance in any of the traits in the second trial.

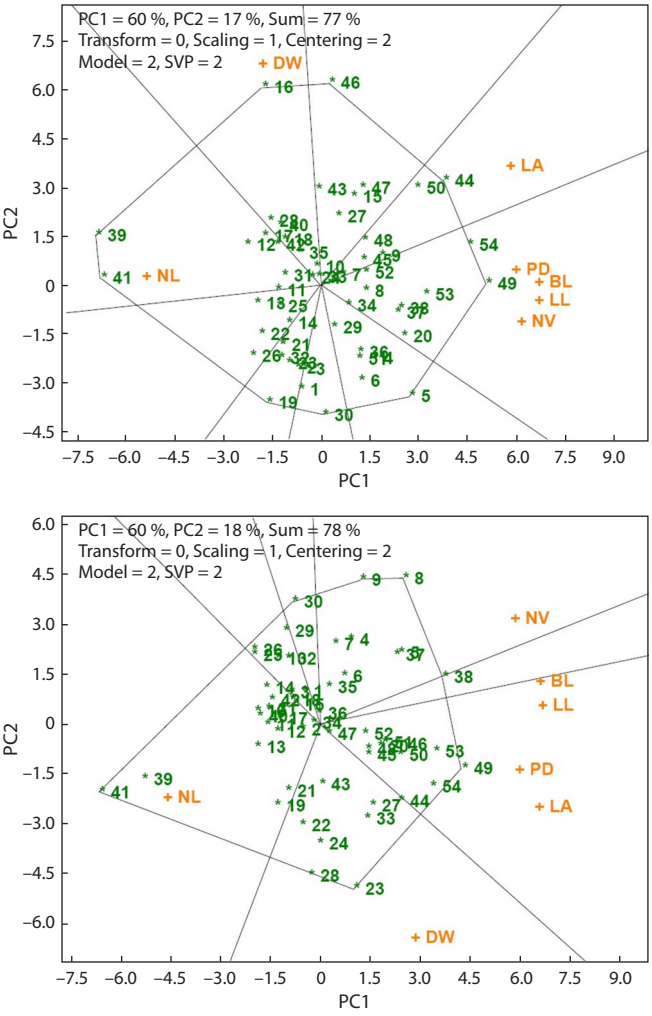


Fig. 2. The nonagon (upper panel) and the heptagon (lower panel) showing relationships among traits and genotypes of sorrel in the first and second trials, respectively.

The benefits of the applied GTI biplot model are similar to those reported in other vegetable and field crops like quince (Rahimi et al., 2019) and safflower (Ebrahimi et al., 2023), showing that the method used in our study should be successful in extraction of useful outputs. The differing polygon shapes observed in the two trials – nonagon in the first and heptagon

in the second – reflect the number of genotypes that were extreme for one or more traits in each trial. These differences likely result from minor variations in greenhouse conditions, which affected genotype performance and trait expression. This observation emphasizes that genotypes may respond differently to environmental conditions, even in controlled trials, and highlights the importance of multi-trial evaluation for reliable selection of superior genotypes.

Perfect genotype position

Figure 3 indicates the position of a perfect genotype, and the genotypes closest to this position are considered the best, so genotypes 44 and 50, followed by genotypes 47, 49, 53 and 54, were the closest to this position, indicating their superior performance in the first trial. Genotypes 39 and 41, although positioned farthest from the perfect genotype in the biplot, had the greatest number of leaves. However, this resulted in lower aggregate scores when considering multiple traits simultaneously. Hence, these genotypes can still be valuable in breeding programs, particularly for increasing leaf number in combination with traits such as lamina area and leaf dry weight.

Similarly, in the second trial, genotypes 44, 49, 50, 53 and 54 were close to the perfect genotype (Fig. 3), showing their favorable performance, while genotypes 39 and 41 were located farthest from this position, regarding them less favorable in the second trial. These identified perfect genotypes are crucial for a sorrel genetic improvement program, especially since leaf yield performance and yield components often show low correlations in many vegetable crops (Shukla et al., 2016); thus, the employment of graphic multivariate models is vital for determining perfect genotypes and enhancing sorrel breeding strategies.

While leaf dry weight is the ultimate trait of interest for sorrel breeding, component traits such as lamina area, petiole diameter, and number of veins provide valuable information on leaf structure, expansion, and resource allocation. In some cases, genotypes with a large number of small leaves showed lower dry weight, reflecting the natural compromise between leaf size and leaf number. The GTI biplot enables simultaneous evaluation of multiple traits, capturing both additive and crossover interactions, and helps in the identification of genotypes with balanced performance across all important leaf characteristics. Although dry weight can be used alone for selection, the multivariate approach provides a more comprehensive assessment for breeding programs. Minor differences in greenhouse conditions between the two trials, such as temperature and light intensity, influenced trait expression, which justifies separate trial analyses. The observed differences in vertex genotypes across trials highlight genotype sensitivity to environmental variation and emphasize the importance of multi-trial evaluation to identify stable high-performing genotypes.

Perfect trait position

The discriminative capacity for a trait is the magnitude of the standard deviation that marks genotypes as different and can be shown by a perfect trait with such a hypothetical position (Fig. 4) that traits closer to this position have better discriminative capacities and farther traits are inferior in discriminative

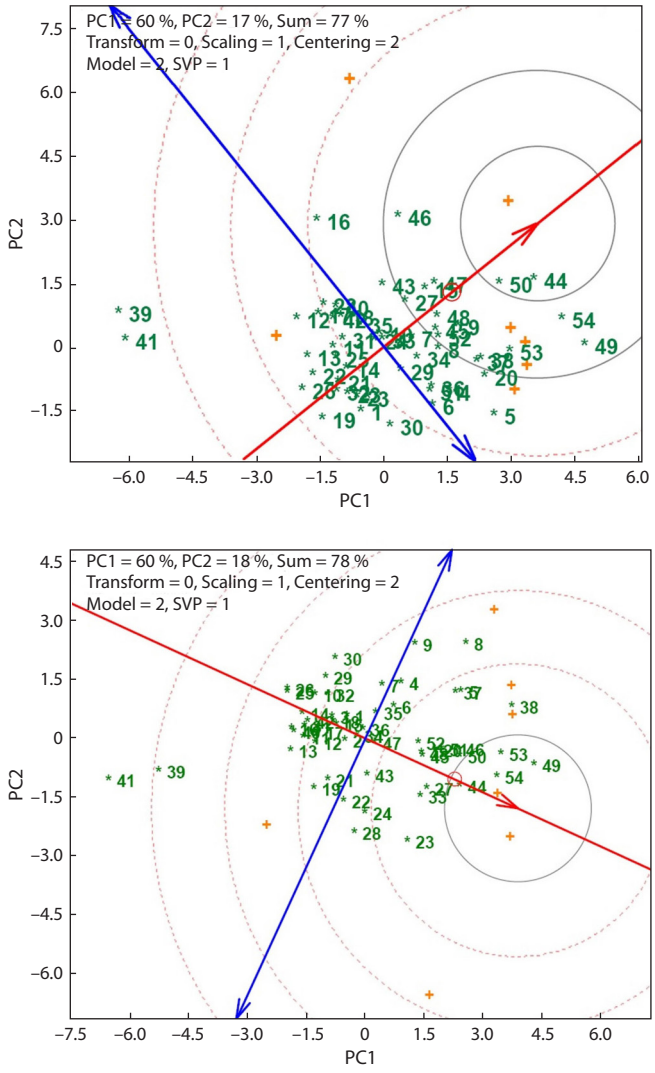


Fig. 3. The perfect genotype diagram showing the positions of sorrel genotypes in (upper panel) the first trial and (lower panel) the second trial.

capacity. Based on the perfect trait biplot of the first trial, the following (in the descending order) traits were identified as most discriminative: lamina area (LA) followed by petiole diameter (PD), blade length (BL), leaf length (LL), and number of veins (NV). In contrast, traits such as number of leaves (NL) and leaf dry weight (DW) had low discriminative potentials in the first trial (Fig. 4); thus, they are not advised for future studies for distinguishing differences among sorrel genotypes.

According to the perfect trait biplot of the second trial, lamina area (LA) and petiole diameter (PD), followed by blade length (BL) and leaf length (LL), were found to possess best discriminative capacities. Also, number of veins (NV) and leaf dry weight (DW) have a discriminative potential above average, indicating that they are effective in differentiating among sorrel genotypes in the second trial (Fig. 4). Finally, number of leaves (NL) had a low discriminative potential in the second trial, and it is not recommended for future investigations for revealing differences among sorrel genotypes.

The typical potential of a trait, showing its symbolic importance, is characterized by the angle between the trait's vector

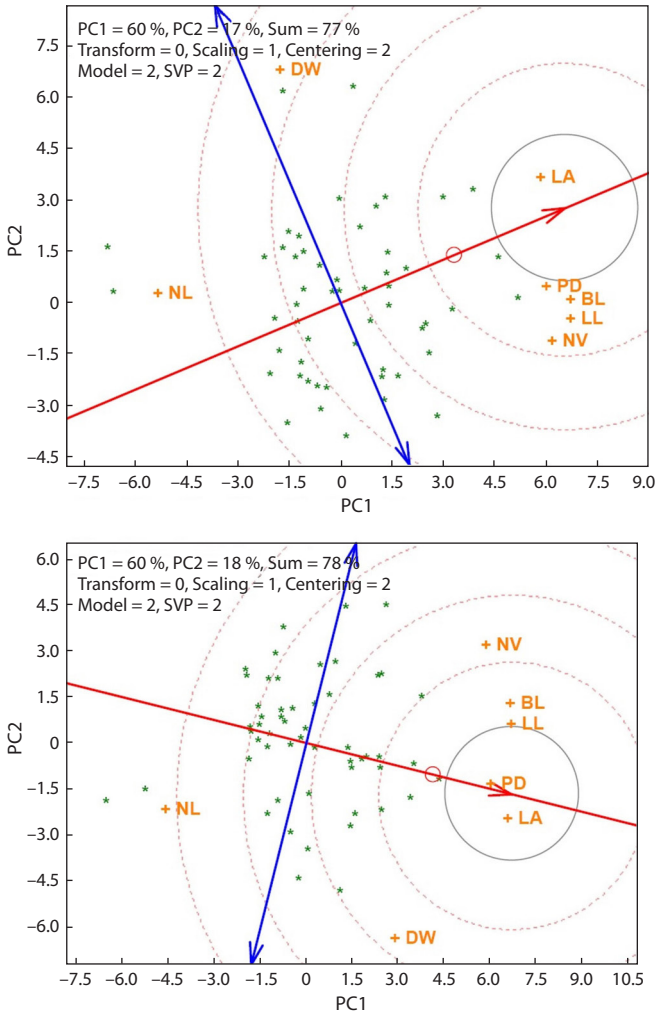


Fig. 4. The perfect trait diagram showing position of the measured traits of sorrel in (upper panel) the first trial and (lower panel) the second trial.

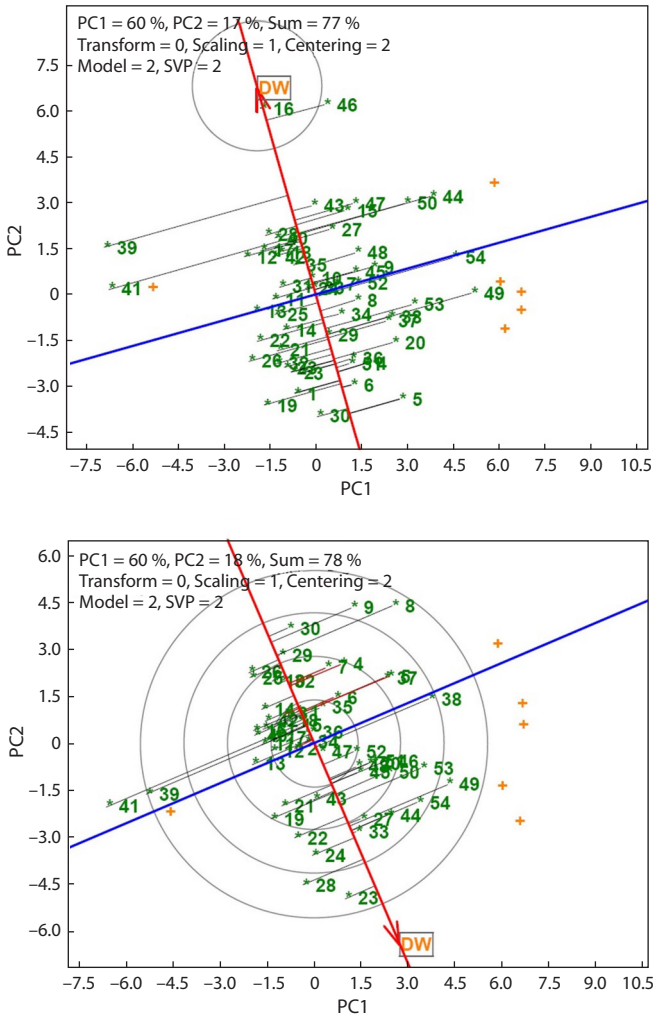


Fig. 5. Examination of leaf dry weight (DW) across sorrel genotypes in (upper panel) the first trial and (lower panel) the second trial.

and the axis of the average trait, smaller angles denoting greater typical potentials. Therefore, the traits with the smallest angles, such as lamina area (LA) and petiole diameter (PD), exhibit higher typical potential across both trials, while leaf dry weight (DW) had a larger angle with the axis, reflecting its lower typical potential in both trials.

Analysis of leaf dry weight

Figure 5 shows leaf dry weight (DW) along the horizontal axis, with distances from the axis reflecting variability among genotypes relative to the mean. Although accessions with the highest DW can be directly seen in Figure 2, Figure 5 highlights both mean performance and stability, assisting breeders in selecting genotypes with high and consistent leaf yield for further evaluation. Genotypes 16 and 46 were the most desirable for DW performance in the first trial, while genotypes 5 and 30 were the least favorable ones (Fig. 5). Genotypes with above-average performance of DW are situated above the average axis. The distance of genotypes from the horizontal axis serves as an index of standard deviation, and smaller distances indicate lower variability, so they are preferred for selection. Consequently, genotype 16 was recommended due to its low variability in comparison to genotype 30 in the first trial. In contrast, some genotypes located farther from the horizontal axis, such as 44 and 50, exhibit high variabilities and are considered less desirable.

In the second trial, genotypes 23 and 28 were the most desirable for DW performance, while genotypes 9 and 30 were the least favorable ones (Fig. 5). The effectiveness of using this option for identifying favorable genotypes for target traits has been demonstrated in studies on sweet corn (Stansluos et al., 2023) and safflower (Ebrahimi et al., 2023).

Sorrel genotype evaluation is crucial for preventing erosion in plant materials and effectively managing genetic improvement tasks. This study revealed substantial variation in leaf morphological traits among the 54 sorrel genotypes. While taxonomic identification was not available for all accessions, the observed phenotypic diversity provides useful information for selecting superior genotypes and identifying traits for breeding programs. These results should be interpreted as intrasample variation rather than interspecific diversity.

The GTI biplot model revealed a relatively high level of variation (77 and 78 % for the first and second trials, respectively) and confirmed the presence of both simple and complex interactions among the genotypes and traits. Similar interaction patterns have been documented in other vegetable crops, such as spinach (Sabaghnia et al., 2015) and green bean (de Oliveira et al., 2018). These interactions resulted in varying rankings of genotypes across traits, making it challenging to select the most superior genotypes. Ignoring genotype × trait interactions can complicate the selection process, because genetic differences among genotypes lead to varying performance across traits. The GTI highlights these differences, enabling breeders to select genotypes with consistently desirable trait profiles.

However, selection of high yielding genotypes needs genotypes with large lamina area, and it is similar in this respect to other leafy vegetable crops like spinach (Sabaghnia et al., 2013), so breeding for high leaf yield in sorrel should consider multiple traits, including lamina area, leaf number, and leaf dry weight (DW). Lamina area is particularly informative for selection because it moderately correlates with DW and can serve as a proxy at early steps of breeding. However, direct measurement of DW and consideration of leaf number are also important to ensure the development of high-yielding cultivars.

The GTI biplot proved effective for visualizing complex genotype × trait interactions, allowing breeders to identify superior genotypes and key traits for leaf yield, because this visual tool facilitates practical decision-making in breeding programs, enabling the selection of genotypes with optimal combinations of traits. While the present study focused on morphological traits of leaves to assess genetic diversity and leaf yield performance, we acknowledge that biochemical characteristics such as oxalate content, antioxidant capacity, and contents of other secondary metabolites are also important for evaluating the nutritional and medicinal value of sorrel. Integrating these biochemical traits in future studies could provide a more comprehensive assessment of genotype performance, allowing breeders to select genotypes that combine high leaf yield with superior nutritional or medicinal qualities. Such combined morphological and biochemical evaluations would further enhance the practical utility of the GTI biplot method in sorrel breeding programs.

Conclusions

The study demonstrates the practical utility of the GTI biplot for sorrel breeding. By identifying lamina area as a key trait and highlighting superior genotypes such as 16, 23, 28, 46, 44, and 50, breeders can optimize breeding strategies and efficiently raise high-yielding cultivars. The GTI biplot explained 77 and 78 % of the variation in the first and second trials, respectively, demonstrating its utility for evaluating multivariate morphological data. Lamina area and petiole diameter were identified as the most discriminative and typical traits across both trials, providing key selection criteria for leaf yield improvement. However, for breeding programs aimed at industrial conditions, further evaluation in the field is recommended to ensure stability and performance in those target environments.

References

Bourang M.K., Hassandokht M., Nazeri V., Rasoulnia A., Moghanloo G.D. Morphological evaluation of genetic diversity of wild populations of some *Rumex* species in Iran. *Iran J Hortic Sci*. 2023;53(4):823-836. doi 10.22059/ijhs.2020.305743.1819

de Oliveira T.R.A., Gravina G.A., de Oliveira G.H.F., Araújo K.C., de Araújo L.C., Daher R.F., Vivas M., Gravina L.M., da Cruz D.P. The GT biplot analysis of green bean traits. *Ciênc Rural*. 2018;48(6):e20170757. doi 10.1590/0103-8478cr20170757

Ebrahimi H., Sabaghnia N., Javanmard A., Abbasi A. Genotype by trait biplot analysis of trait relations in safflower. *Agrotech Ind Crops*. 2023;3(2):67-73. doi 10.22126/atic.2023.8906.1086

Li J.J., Li Y.X., Li N., Zhu H.T., Wang D., Zhang Y.J. The genus *Rumex* (Polygonaceae): an ethnobotanical, phytochemical and pharmacological review. *Nat Prod Bioprospect*. 2022;12(1):21. doi 10.1007/s13659-022-00346-z

Mohebodini M., Ghanbari A., Sabaghnia N. Genetic diversity of *Rumex* spp. accessions according to morphological traits. *Iran J Biol*. 2020;33(2):396-407. doi 20.1001.1.23832592.1399.33.2.10.2

Rahimi M., Asadi-Gharneh H.A., Sabaghnia N. Evaluation of some traits in local Iranian quince (*Cydonia oblonga* Miller) genotypes. *Int J Fruit Sci*. 2019;19(4):397-412. doi 10.1080/15538362.2018.1552231

Sabaghnia N., Asadi-Gharneh H.A., Janmohammadi M. Sequential path analysis of spinach yield using several quantitative and qualitative traits. *Nat Montenegrina*. 2013;12(1):205-216

Sabaghnia N., Behtash F., Janmohammadi M. Graphic analysis of trait relations of spinach (*Spinacia oleracea* L.) landraces using the biplot method. *Acta Univ Agric Silvic Mendelianae Brun*. 2015;63(4):1187-1194. doi 10.11118/actaun201563041187

Sabaghnia N., Yousefzadeh S., Janmohammadi M. Graphical evaluation of genetic diversity among some genotypes of *Lepidium sativum* L. using morphological traits. *Taxon Biosyst*. 2023;15:43-54. doi 10.22108/tbj.2024.139710.1243

Shahla S., Maasoumi A.A., Hamd S.M.M., Mehregan I., Nejadsattari T. Fruit morphology of the genus *Rumex* L. (Polygonaceae) in Iran. *J Biodivers Environ Sci*. 2014;5(1):655-663

Shukla S., Upadhyay K.K., Mishra B.K. Genetic relationship between foliage yield and its biochemical components in vegetable amaranth. *Int J Veg Sci.* 2016;22(4):322-332. doi 10.1080/19315260.2015.1042994

Stansluos A.A.L., Öztürk A., Niedbała G., Türkoğlu A., Haliloğlu K., Szulc P., Omrani A., Wojciechowski T., Piekutowska M. Genotype–trait (GT) biplot analysis for yield and quality stability in some sweet corn (*Zea mays* L. *saccharata* Sturt.) genotypes. *Agronomy.* 2023;13(6):1538. doi 10.3390/agronomy13061538

Vasas A., Orbán-Gyapai O., Hohmann J. The genus *Rumex*: review of traditional uses, phytochemistry and pharmacology. *J Ethnopharmacol*. 2015;175:198-228. doi 10.1016/j.jep.2015.09.001

Xu N., Fok M., Li J., Yang X., Yan W. Optimization of cotton variety registration criteria aided with a genotype-by-trait biplot analysis. *Sci Rep*. 2017;7(1):17237. doi 10.1038/s41598-017-17631-4

Yan W. Two types of biplots to integrate multi-trial and multi-trait information for genotype selection. *Crop Sci*. 2024;64(3):1608-1618. doi 10.1002/csc2.21231

Yan W., Frégeau-Reid J. Genotype by yield*trait (GYT) biplot: a novel approach for genotype selection based on multiple traits. *Sci Rep*. 2018;8(1):8242. doi 10.1038/s41598-018-26688-8

Conflict of interest. The authors declare no conflict of interest.
Received November 26, 2025. Revised June 16, 2026. Accepted June 16, 2026.

Прием статей через электронную редакцию на сайте http://vavilov.elpub.ru/index.php/jour
Предварительно нужно зарегистрироваться как автору, затем в правом верхнем углу страницы выбрать «Отправить рукопись». После завершения загрузки материалов обязательно выбрать опцию «Отправить письмо», в этом случае редакция автоматически будет уведомлена о получении новой рукописи.

«Вавиловский журнал генетики и селекции (Vavilov Journal of Genetics and Breeding)» до 2011 г. выходил под названием «Информационный вестник ВОГиС»/ "The Herald of Vavilov Society for Geneticists and Breeding Scientists".

Сетевое издание «Вавиловский журнал генетики и селекции (Vavilov Journal of Genetics and Breeding)» – реестровая запись СМИ Эл № ФС77-85772, зарегистрировано Федеральной службой по надзору в сфере связи, информационных технологий и массовых коммуникаций 14 августа 2023 г.

Издание включено ВАК Минобрнауки России в Перечень рецензируемых научных изданий, в которых должны быть опубликованы основные результаты диссертаций на соискание ученой степени кандидата наук, на соискание ученой степени доктора наук, Белый список (уровень 1), Russian Science Citation Index, Российский индекс научного цитирования, ВИНИТИ, Web of Science CC, Scopus, PubMed Central, DOAJ, ROAD, Ulrich's Periodicals Directory, Google Scholar.

Открытый доступ к полным текстам:
русскоязычная версия – на сайте https://vavilovj-icg.ru/
и платформе Научной электронной библиотеки, elibrary.ru/title_about.asp?id=32440

англоязычная версия – на сайте vavilov.elpub.ru/index.php/jour
и платформе PubMed Central, https://www.ncbi.nlm.nih.gov/pmc/journals/3805/

При перепечатке материалов ссылка обязательна.

✉ email: vavilov_journal@bionet.nsc.ru

Издатель: Федеральное государственное бюджетное научное учреждение
«Федеральный исследовательский центр Институт цитологии и генетики
Сибирского отделения Российской академии наук»,
проспект Академика Лаврентьева, 10, Новосибирск, 630090.
Адрес редакции: проспект Академика Лаврентьева, 10, Новосибирск, 630090.
Секретарь по организационным вопросам С.В. Зубова. Тел.: (383)3634977.
Издание подготовлено информационно-издательским отделом ИЦиГ СО РАН. Тел.: (383)3634963*5218.
Начальник отдела: Т.Ф. Чалкова. Редакторы: В.Д. Ахметова, И.Ю. Ануфриева. Дизайн: А.В. Харкевич.
Компьютерная графика и верстка: Т.Б. Коняхина, О.Н. Савватеева.
Дата выхода в свет 06.10.2026. Формат 60 × 84 1/8. Уч.-изд. л. 19.1.